

**BEHAVIOR OF AUTOCLAVED AERATED CONCRETE SHEAR  
WALLS WITH LOW-STRENGTH AAC**

**by**

**Ulises Max Cancino, B.S.E**

**Thesis**

Presented to the Faculty of the Graduate School of  
The University of Texas at Austin  
in Partial Fulfillment  
of the Requirements  
for the Degree of

**Master of Science in Engineering**

**The University of Texas at Austin  
December 2003**

**BEHAVIOR OF AUTOCLAVED AERATED CONCRETE SHEAR  
WALLS WITH LOW-STRENGTH AAC**

**Approved by  
Supervising Committee:**

---

**Richard E. Klingner, Supervisor**

---

**Oguzhan Bayrak**

## **Dedication**

To my family.

## **Acknowledgements**

The experience of working at Ferguson Laboratory in the University of Texas at Austin has been one of the most valuable experiences that I have had in my life.

I would like to thank Dr. Richard Klingner for his tremendous support and friendship during the entire process of the development of the project and after. While I was under his supervision, I learned how to conduct a research project professionally and also to understand the different theoretical aspects involved during this study. Also, I would like to thank Dr. Oguzhan Bayrak for his support, friendship and patience. As a result, I can evaluate this experience as an invaluable opportunity to deepen my knowledge.

All of this research could have not been completed successfully without the assistance of the staff at the Ferguson Structural Engineering Laboratory. I give my recognition to the technicians: Blake Stasney, Mike Bell, Dennis Phillip and Ray Madonna. Also, the assistance of the office staff has been really important, and I offer my special thanks to Hortensia Peoples, Marie Jo Moore and Regina Forward.

I would like to mention the undergraduates Geoff Mitchell and Ross Sassen for their constant support of this project. My special recognition goes to my friends Jorge Varela, Jaime Argudo and Jennifer Tanner, who continuously supported me in different aspects of this research project and my progress. I would also like to express my recognition to Gelberg Rodriguez, Ivan Ornelas,

Leonardo Guim and Pedro Galvez. For them my best wishes on their own success in their research projects.

Finally, and most importantly, I thank my mother, brother, cousin Hugo, sister-in-law and my three nephews Natalia, Saschita and Anastasia and Karen MacInnes, as they constantly encouraged me to finish this thesis successfully.

December 2003

## **Abstract**

### **Behavior of Autoclaved Aerated Concrete Shear Walls with Low-Strength AAC**

Ulises Max Cancino, M.S.E  
The University of Texas at Austin, 2003

Supervisor: Richard E. Klingner

Three isolated full-scale shear walls of low-strength autoclaved aerated concrete (AAC) were tested at the Structural Engineering Ferguson Laboratory of the University of Texas at Austin. One specimen was constructed with vertical panels, and the other two, with partially grouted reinforced masonry units. The main objective of this study is to validate previously proposed design provisions for low-strength AAC material. The variables considered in these shear wall specimens were the compressive strength of the material, the flexural reinforcement, and the geometry. Test results indicate good agreement between observed and predicted behavior, and validate the previously proposed design provisions. The results support the extension of those design provisions to low-strength AAC shear-wall structures located in seismic zones.

## Table of Contents

CHAPTER 1 INTRODUCTION.....	1
1.1 General .....	1
1.2 Scope of Overall Study .....	1
1.3 Objectives of Overall Study .....	2
1.4 Organization of Overall Study .....	2
1.5 Scope of Thesis .....	3
1.6 Objectives of Thesis .....	4
1.7 Organization of this Thesis .....	5
CHAPTER 2 TEST SPECIMENS, TEST SETUPS, AND TESTING PROCEDURES.....	6
2.1 Introduction .....	6
2.2 Design and Construction of Shear Wall Specimen 17 .....	6
2.2.1 Objectives.....	6
2.2.2 Configuration of Shear Wall Specimen 17 .....	7
2.2.3 Test Setup for Shear Wall Specimen 17.....	9
2.2.3.1 Base Beam.....	9
2.2.3.2 Axial Load System .....	10
2.2.3.3 Lateral Bracing System .....	11
2.2.3.4 Actuators .....	12
2.2.3.5 Instrumentation and Data Acquisition.....	13
2.2.3.5.1 Instrumentation.....	13
2.2.3.5.2 Data Acquisition.....	17
2.2.4 Loading Protocol.....	18

2.2.5	Material Strengths .....	18
2.2.5.1	Compressive Strength .....	18
2.2.5.1.1	Specimen Preparation and Testing Procedure for Compression Tests on AAC Cubes .....	18
2.2.5.1.2	Compression Test Results for AAC Cubes .....	21
2.2.6	Construction of Shear Wall Specimen 17 .....	22
2.3	Design and Construction of Shear Wall Specimens 18 and 19 .....	24
2.3.1	Objectives .....	24
2.3.2	Configurations of Shear Wall Specimen 18 and 19 .....	24
2.3.3	Test Setup for Shear Wall Specimens 18 and 19 .....	27
2.3.3.1	Base Beam .....	27
2.3.3.2	Axial Load System .....	27
2.3.3.3	Lateral Bracing System .....	29
2.3.3.4	Actuators .....	29
2.3.3.5	Instrumentation and Data Acquisition .....	30
2.3.3.5.1	Instrumentation .....	30
2.3.3.5.2	Data Acquisition .....	33
2.3.4	Loading Protocol .....	34
2.3.5	Material Strengths .....	34
2.3.5.1	Compressive Strength .....	34
2.3.5.1.1	Specimen Preparation and Testing Procedure for Compression Tests on AAC Cores .....	34
2.3.5.2	Compression Test Results for AAC Cores .....	36
2.3.5.3	Further Comments on Maximum Useful Strain .....	38
2.3.6	Splitting Tensile Strength .....	41
2.3.6.1	Specimen Preparation and Testing Procedure for Splitting Tensile Tests on AAC Masonry Units .....	41
2.3.6.2	Splitting Tensile Strength for AAC Units .....	43
2.3.6.3	Comparison between observed and predicted splitting tensile strength of AAC .....	44



2.3.7 Construction of Shear Wall Specimens 18 and 19 .....	46
CHAPTER 3 TEST RESULTS FOR AAC SHEAR WALL SPECIMENS.....	50
3.1 Introduction .....	50
3.2 Test Results for Shear Wall Specimen 17 .....	50
3.2.1 Loading History and Major Events for Shear Wall Specimen 17.....	51
3.2.2 Sequence of Crack Formation for Shear Wall Specimen 17.....	54
3.2.2.1 Flexural Cracking in Shear Wall Specimen 17 .....	55
3.2.2.2 Flexure-shear cracking in Shear Wall Specimen 17 .....	56
3.2.2.3 Additional Cracking in Shear Wall Specimen 17 .....	59
3.2.2.4 Final damage in Shear Wall Specimen 17 .....	60
3.2.3 Load-Displacement Behavior of Shear Wall Specimen 17.....	63
3.3 Test Results for Shear Wall Specimen 18.....	64
3.3.1 Loading History and Major Events for Shear Wall Specimen 18.....	65
3.3.2 Sequence of Crack Formation for Shear Wall Specimen 18.....	68
3.3.2.1 Flexural cracking in Shear Wall Specimen 18 .....	69
3.3.2.2 Web-shear cracking in Shear Wall Specimen 18 .....	70
3.3.2.3 Propagation and Additional Web-shear cracking in Shear Wall Specimen 18 .....	72
3.3.2.4 Final damage in Shear Wall Specimen 18 .....	73
3.3.3 Load-Displacement Behavior for Shear Wall Specimen 18 .....	77
3.4 Shear Wall Specimen 19 .....	78
3.4.1 Loading History and Major Events for Shear Wall Specimen 19.....	79
3.4.2 Sequence of Crack Formation for Shear Wall Specimen 19.....	82
3.4.2.1 Flexural cracking in Shear Wall Specimen 19 .....	83
3.4.2.2 Web-shear cracking in Shear Wall Specimen 19 .....	84
3.4.2.3 Propagation and Additional Web-shear cracking in Shear Wall Specimen 19 .....	87
3.4.2.4 Final damage in Shear Wall Specimen 19 .....	88

3.4.3	Load-Displacement Behavior for Shear Wall Specimen 19 .....	91
CHAPTER 4	SIGNIFICANCE OF TEST RESULTS .....	93
4.1	Review of Behavior Modes for AAC Shear Walls .....	93
4.1.1	Flexural Cracking.....	93
4.1.2	Web-shear cracking.....	95
4.1.3	Flexure-shear cracking .....	97
4.1.4	Nominal Flexural Capacity .....	99
4.1.5	Crushing of the Diagonal Strut.....	101
4.1.6	Sliding Shear .....	104
4.2	Hysteretic Behavior of Shear Wall Specimens .....	106
4.2.1	Hysteretic Behavior of Flexure-Dominated Specimens.....	106
4.2.2	Hysteretic Behavior of Shear-Dominated Specimens.....	116
4.2.2.1	Shear Wall Specimen 18 .....	117
4.2.2.2	Shear Wall Specimen 19 .....	122
4.2.2.3	Summary of Results for Shear Wall Specimens 18 and 19 .....	126
CHAPTER 5	SUMMARY, CONCLUSIONS AND RECOMMENDATIONS.....	131
5.1	Summary .....	131
5.2	Conclusions .....	132
5.3	Recommendations for Future Work.....	134
APPENDIX A	DESIGN PROVISIONS FOR REINFORCED AAC SHEAR WALLS ...	136
A.1	Design of AAC Shear Walls .....	136
A.1.1	Web-shear Cracking.....	140
A.1.2	Flexure-Shear Cracking for AAC Shear Walls.....	148
A.1.3	Crushing of the Diagonal Strut.....	155
A.1.4	Sliding Shear Capacity .....	160
A.1.5	Nominal Flexural Capacity .....	169

A.2	Special Provisions for Vertical Panel Construction .....	171
A.2.1	Prediction of Flexural and Shear Capacities for AAC Shear Walls with Vertically Oriented Panels .....	173
A.2.2	Verification of Shear Capacity for Vertical-Panel Shear Walls Tested at UT Austin .....	176
A.2.3	Special Provisions to Avoid Longitudinal Cracking at the Location of Vertical Reinforcement .....	178
A.2.4	Formation of Cracks along Longitudinal Bars in AAC Shear Walls	179
A.2.5	Analysis to Determine if Longitudinal Cracks Formed Prior to Yielding	182
A.2.6	Implications of the Formation of Longitudinal Cracks .....	186
A.2.7	Analysis of Maximum Permissible Area Ratio if Longitudinal Reinforcement Remains Elastic .....	188
A.2.8	Analysis of the Maximum Permissible Area Ratio in a Plastic Hinge Zone .....	193
A.3	Design Examples .....	193
A.3.1	Design of an AAC shear wall .....	193
A.3.1.1	Flexural capacity .....	194
A.3.1.2	Shear capacity .....	196
A.3.2	Design an AAC Shear Wall for Out-of-plane loads .....	198
A.3.2.1	Flexural capacity .....	199
A.3.2.2	Shear capacity .....	202
APPENDIX B ACI 523.5R-XX GUIDE FOR USING AUTOCLAVED AERATED CONCRETE PANELS .....		203
B.1	Introduction .....	203
B.1.1	Definition of Autoclaved Aerated Concrete .....	203
B.1.2	Typical Mechanical and Thermal Characteristics of AAC .....	204
B.1.3	Historical Background of AAC .....	205
B.1.4	Applications of AAC Panels .....	206
B.1.5	Scope and Objectives of this <i>Guide</i> .....	206

B.2	TYPICAL Materials and Manufacture OF AAC .....	208
B.2.1	Materials Used in AAC .....	208
B.2.2	Manufacture of AAC.....	208
B.2.2.1	Preparation, Batching and Mixing of Raw Materials ..	208
B.2.2.2	Casting, Expansion and Initial Hydration.....	209
B.2.2.3	Cutting .....	210
B.2.2.4	Autoclaving .....	211
B.2.2.5	Packaging.....	212
B.2.2.6	AAC Strength Classes .....	213
B.2.3	Typical Dimensions of AAC Units .....	214
B.2.3.1	Plain AAC Wall Units .....	214
B.2.3.2	Reinforced AAC Units .....	215
B.2.4	Dimensional Tolerances .....	216
B.2.5	Identification and Marking of AAC Units .....	216
B.3	Structural Design of Reinforced AAC Elements .....	217
B.3.1	Introductory Remarks regarding Design Provisions .....	217
B.3.2	Proposed Design Provisions for Reinforced AAC Panels .....	218
B.3.2.1	Basic Design Assumptions .....	218
B.3.2.2	Combinations of Flexure and Axial Load .....	219
B.3.2.3	Bond and Development of Reinforcement .....	219
B.3.2.4	Shear .....	220
B.3.2.5	Bearing.....	221
B.4	Handling, Erection and Construction With AAC Units.....	222
B.4.1	Handling of AAC Panels.....	222
B.4.2	Erection of AAC Wall Panels .....	222
B.4.2.1	Erection of AAC Cladding Systems.....	222
B.4.2.2	Erection of Vertical AAC Panels for Bearing-Wall Systems.....	223
B.4.3	Erection of AAC Floor and Roof Panels.....	224

B.4.4	Electrical and Plumbing Installations in AAC .....	224
B.4.5	Exterior Finishes for AAC .....	225
B.4.5.1	Polymer-Modified Stuccos, Paints or Finish Systems .....	225
B.4.5.2	Masonry Veneer .....	225
B.4.5.3	Finishes for Basement Walls .....	225
B.4.6	Interior Finishes for AAC Panels .....	226
B.4.6.1	Interior Plasters .....	226
B.4.6.2	Gypsum Board .....	226
B.4.6.3	High-Durability Finishes for Commercial Applications .....	226
B.4.6.4	Ceramic Tile .....	227
References	.....	228
Vita	.....	230

## List of Tables

Table 2.1	Description of instrumentation used in Shear Wall Specimen 17.....	14
Table 2.2	Dry weights of AAC cubes measured at Babb and at UT Austin.....	20
Table 2.3	Results of compressive strength tests performed at UT Austin.....	22
Table 2.4	Results of compressive strength tests performed at the Babb plant.....	22
Table 2.5	Description of instrumentation used in Shear Wall Specimens 18 and 19.....	31
Table 2.6	Summary of results of moisture content measured in the cores drilled for the compressive test (Babb 3 material).....	35
Table 2.7	Results of compressive strength tests performed at UT Austin.....	37
Table 2.8	Summary of mean maximum useful strains obtained in this study and Tanner (2003).....	38
Table 2.9	Material properties of this study versus those of Tanner (2003).....	40
Table 2.10	Measured moisture contents (Babb 3 material).....	42
Table 2.11	Results of splitting tensile strength tests performed at UT Austin.....	44
Table 3.1	Load Points, maximum load and drift ratios for each cycle for Shear Wall Specimen 17.....	54
Table 3.2	Description of major events for Shear Wall Specimen 17.....	55
Table 3.3	Load Points, maximum load drift ratios for each cycle for Shear Wall Specimen 18.....	68
Table 3.4	Description of major events for Shear Wall Specimen 18.....	69
Table 3.5	Load Points, maximum load and drift ratios for each cycle for Shear Wall Specimen 19.....	82
Table 3.6	Description of major events for Shear Wall Specimen 19.....	83
Table 4.1	Observed versus predicted flexural cracking capacities.....	95
Table 4.2	Observed versus predicted web-shear cracking capacities.....	97
Table 4.3	Observed versus predicted flexure-shear cracking capacities.....	99

Table 4.4 Observed versus predicted values for nominal flexural capacity.....	101
Table 4.5 Observed versus predicted capacities as governed by crushing of the diagonal strut .....	103
Table 4.6 Maximum displacements, ductilities and drift ratios for Shear Wall Specimen 17 .....	112
Table 4.7 Comparison of initial tangent and backbone stiffnesses for flexure- dominated specimens .....	113
Table 4.8 Comparison of secant stiffnesses after flexural cracking for flexure- dominated specimens .....	113
Table 4.9 Comparison of unloading stiffnesses after yield of flexural reinforcement in the south and north direction for flexure-dominated specimens .....	114
Table 4.10 Comparison of stiffnesses after yield of flexural reinforcement for flexure-dominated specimens.....	115
Table 4.11 Maximum useful displacement drift ratios and ductilities for flexure- dominated specimens .....	115
Table 4.12 Observed initial tangent and backbone stiffnesses for shear-dominated specimens .....	127
Table 4.13 Secant stiffnesses after flexural cracking for shear-dominated specimens .....	128
Table 4.14 Unloading stiffnesses after web shear cracking in the south and north direction for shear-dominated specimens.....	129
Table 4.15 Strength ratios after web shear cracking and corresponding displacement ratios for shear-dominated specimens.....	130
Table A.1 Details of shear wall specimens tested at UT Austin .....	138
Table A.2 Details of shear wall specimens tested by Hebel (Germany).....	139
Table A.3 Initial predictions of capacity as governed by web-shear cracking for fully mortared specimens .....	142

Table A.4 Initial predictions of capacity as governed by web-shear cracking for partially mortared specimens .....	143
Table A.5 Prediction of capacity as governed by web-shear cracking for fully mortared specimens (Equation (A.1)) using tested compressive strength ..	146
Table A.6 Prediction of capacity as governed by web-shear cracking for unmortared head joints (Equation (A.2)) using tested compressive strength .....	146
Table A.7 Results for flexure-shear cracking of AAC flexure-dominated shear wall specimens .....	151
Table A.8 Results for flexure-shear cracking of AAC flexure-dominated shear wall specimens using tensile bond strength of material .....	152
Table A.9 Predicted shear wall capacities as governed by crushing of the diagonal strut.....	159
Table A.10 Observed versus predicted nominal shear capacities based on nominal flexural capacity .....	171
Table A.11 Observed versus predicted nominal shear capacities based on nominal flexural capacity with strain hardening included .....	171
Table A.12 Ratio of base shear at formation of vertical cracks to base shear at expected flexural capacity (including overstrength) in the flexure-dominated shear wall specimens.....	179
Table A.13 Ratio of base shear at observed vertical cracking to the nominal flexural capacity (without overstrength) in flexure-dominated AAC shear wall specimens .....	181
Table A.14 Estimation of order of vertical cracking and yielding of longitudinal reinforcement, based on strain gages .....	184
Table A.15 Calculated stresses in tensile reinforcement based on elastic theory for vertical cracks on the south and north sides of the specimen.....	186



Table B.1 Typical mechanical and thermal characteristics of AAC .....	205
Table B.2 Material characteristics of AAC in different strength classes .....	214
Table B.3 Dimensions of plain AAC wall units.....	215
Table B.4 Dimensions of reinforced AAC wall units .....	215
Table B.5 Dimensional tolerances for reinforced AAC units .....	216

## List of Figures

Figure 2.1	Geometry and reinforcement of Shear Wall Specimen 17 .....	8
Figure 2.2	Plan view of Shear Wall Specimen 17 with details of the stainless- steel spiral ties .....	9
Figure 2.3	Typical view of base beam used for Shear Wall Specimen 17.....	10
Figure 2.4	Typical details of the axial load system used for Shear Wall Specimen 17.....	11
Figure 2.5	Different views showing details of the lateral bracing system .....	12
Figure 2.6	Actuator connected to Shear Wall Specimen 17.....	13
Figure 2.7	East face of Shear Wall Specimen 17 showing locations of instrumentation.....	15
Figure 2.8	West face of Shear Wall Specimen 17 showing locations of instrumentation.....	16
Figure 2.9	Typical view of the strain gauge positions in the flexural reinforcement of Shear Wall Specimen 17.....	17
Figure 2.10	Machine used to mill faces of AAC cubes .....	19
Figure 2.11	Typical view of test setup to measure compressive strength.....	21
Figure 2.12	Construction details of Shear Wall Specimen 17 .....	23
Figure 2.13	Geometry and reinforcement of Shear Wall Specimen 18 .....	25
Figure 2.14	Geometry and reinforcement of Shear Wall Specimen 19 .....	26
Figure 2.15	Typical details of modular blocks used in Shear Wall Specimens 18 and 19 .....	26
Figure 2.16	Typical details of the axial load system used for Shear Wall Specimen 18 .....	28
Figure 2.17	Typical details of the axial load system used for Shear Wall Specimen 19 .....	29

Figure 2.18 East face of Shear Wall Specimen 18 showing locations of instrumentation.....	32
Figure 2.19 West face of Shear Wall Specimen 18 showing locations of instrumentation.....	33
Figure 2.20 Typical view of the test setup to measure compressive strength.....	36
Figure 2.21 Compressive stress versus strain (Babb 3 material) .....	37
Figure 2.22 Maximum useful strain versus compressive strength.....	40
Figure 2.23 Test setup to measure splitting tensile strength .....	43
Figure 2.24 Splitting tensile strength versus tested compressive strength.....	46
Figure 2.25 Plan view showing typical details of construction of Shear Wall Specimen 19 .....	47
Figure 2.26 Side view of Shear Wall Specimen 18.....	48
Figure 2.27 Side view of Shear Wall Specimen 19.....	49
Figure 3.1 Prediction of behavior for Shear Wall Specimen 17 .....	51
Figure 3.2 Actual loading history for Shear Wall Specimen 17 .....	52
Figure 3.3 Actual tip displacement history for Shear Wall Specimen 17 .....	53
Figure 3.4 Formation of flexural cracking in Shear Wall Specimen 17.....	56
Figure 3.5 Flexure-shear cracks at north end of Shear Wall Specimen 17 .....	57
Figure 3.6 Formation of flexural-shear cracks in Shear Wall Specimen 17 .....	58
Figure 3.7 Formation of additional flexure-shear cracks, and propagation of cracks from previous events.....	60
Figure 3.8 Cracking in Shear Wall Specimen 17 at end of test .....	61
Figure 3.9 Spalling at the north end of Shear Wall Specimen 17 .....	62
Figure 3.10 Toe crushing north at north end of Shear Wall Specimen 17.....	63
Figure 3.11 Overall hysteretic behavior of Shear Wall Specimen 17 .....	64
Figure 3.12 Prediction of behavior for Shear Wall Specimen 18 .....	65
Figure 3.13 Actual loading history for Shear Wall Specimen 18 .....	66
Figure 3.14 Actual tip displacement history for Shear Wall Specimen 18 .....	67

Figure 3.15 Formation of flexural cracking in Shear Wall Specimen 18.....	70
Figure 3.16 Web-shear cracking at north end of Shear Wall Specimen 18 .....	71
Figure 3.17 Web-shear cracking in Shear Wall Specimen 18.....	72
Figure 3.18 Propagation and formation of additional web-shear cracks in Shear Wall Specimen 18 .....	73
Figure 3.19 Additional web-shear cracking and toe crushing in Shear Wall Specimen 18 .....	75
Figure 3.20 Web-shear cracks in Shear Wall Specimen 18 .....	76
Figure 3.21 Toe crushing at the north end of Shear Wall Specimen 18 .....	77
Figure 3.22 Overall hysteretic behavior of Shear Wall Specimen 18 .....	78
Figure 3.23 Prediction of behavior for Shear Wall Specimen 19 .....	79
Figure 3.24 Actual loading history for Shear Wall Specimen 19 .....	80
Figure 3.25 Actual tip displacement history for Shear Wall Specimen 19 .....	81
Figure 3.26 Flexural cracks in Shear Wall Specimen 19 .....	84
Figure 3.27 Web-shear cracking in Shear Wall Specimen 19.....	85
Figure 3.28 Web-shear cracking in Shear Wall Specimen 19.....	86
Figure 3.29 Propagation and formation of additional web-shear cracks along with some flexure-shear cracks in Shear Wall Specimen 19 .....	88
Figure 3.30 Additional web-shear cracking and toe crushing in Shear Wall Specimen 19 .....	89
Figure 3.31 Web-shear cracking in Shear Wall Specimen 19 at the end of the test .....	90
Figure 3.32 Toe crushing at the north end of Shear Wall Specimen 19 .....	91
Figure 3.33 Overall hysteretic behavior of Shear Wall Specimen 19.....	92
Figure 4.1 Typical flexural cracking.....	94
Figure 4.2 Typical web-shear cracking.....	96
Figure 4.3 Typical flexure-shear cracking .....	98
Figure 4.4 Strain and force distribution in an AAC shear wall.....	100

Figure 4.5 Diagonal cracks and crushing of the diagonal strut .....	102
Figure 4.6 Sliding-shear cracking .....	104
Figure 4.7 Shear friction.....	105
Figure 4.8 Initial tangent and backbone stiffness for Shear Wall Specimen 17	107
Figure 4.9 Stiffness after flexural cracking for Shear Wall Specimen 17.....	108
Figure 4.10 Unloading stiffnesses after yielding of the flexural reinforcement for Shear Wall Specimen 17 .....	109
Figure 4.11 Stiffnesses after yielding of the flexural reinforcement for Shear Wall Specimen 17 .....	110
Figure 4.12 Selected drift ratios for Shear Wall Specimen 17.....	111
Figure 4.13 Initial tangent and backbone stiffnesses for Shear Wall Specimen 18 .....	117
Figure 4.14 Secant stiffnesses after flexural cracking for Shear Wall Specimen 18 .....	118
Figure 4.15 Unloading stiffnesses after web shear cracking for Shear Wall Specimen 18 .....	119
Figure 4.16 Maximum applied load after web shear cracking in the south and north directions for Shear Wall Specimen 18 .....	120
Figure 4.17 Load- displacement response of Shear Wall Specimen 18.....	121
Figure 4.18 Initial tangent and backbone stiffnesses for Shear Wall Specimen 19 .....	122
Figure 4.19 Secant stiffnesses after flexural cracking for Shear Wall Specimen 19 .....	123
Figure 4.20 Unloading stiffnesses after web-shear cracking for Shear Wall Specimen 19 .....	124
Figure 4.21 Maximum applied load after web-shear cracking in the south and north directions for Shear Wall Specimen 19 .....	125
Figure 4.22 Load-displacement response of Shear Wall Specimen 19.....	126

Figure A.1 Test set up for shear wall specimens (UT Austin).....	137
Figure A.2 Test setup for shear wall specimens at Hebel (Germany).....	139
Figure A.3 Ratios of observed to predicted (Equation (A.6)) web-shear cracking capacities for AAC shear-wall specimens with fully mortared head joints	144
Figure A.4 Ratios of observed to predicted (Equation (A.6)) web-shear cracking capacities for AAC shear-wall specimens with partially mortared head joints .....	145
Figure A.5 Observed versus predicted capacities as governed by web-shear cracking (Equation (A.1) and Equation (A.2)) using tested compressive strength .....	147
Figure A.6 Observed versus predicted capacities as governed by web-shear cracking (Equation (A.1)) and Equation (A.2)) using specified compressive strength .....	147
Figure A.7 Flexure-shear cracking.....	148
Figure A.8 Hysteretic behavior of Shear Wall Specimen 13 before and after flexure-shear cracking.....	153
Figure A.9 Hysteretic behavior of Shear Wall Specimen 14b before and after flexure-shear cracking.....	153
Figure A.10 Hysteretic behavior of Shear Wall Specimen 15a before and after flexure-shear cracking.....	154
Figure A.11 Hysteretic behavior of Shear Wall Specimen 15b before and after flexure-shear cracking.....	154
Figure A.12 Hysteretic behavior of Shear Wall Specimen 16 before and after flexure-shear cracking.....	155
Figure A.13 Diagonal compressive strut in an AAC shear wall.....	156
Figure A.14 External forces acting on an AAC shear wall.....	156
Figure A.15 Forces acting on diagonal strut in an AAC shear wall.....	157

Figure A.16 Formation of bed-joint crack in an AAC shear wall with horizontal panels.....	160
Figure A.17 Sliding shear mechanism in an AAC shear wall with horizontal panels.....	161
Figure A.18 Internal lateral forces generated by dowel action along plane of sliding shear mechanism .....	162
Figure A.19 Internal lateral forces generated by friction along plane of sliding for sliding shear mechanism .....	162
Figure A.20 Hysteretic behavior of Two-story Assemblage Specimen.....	164
Figure A.21 Base shear and sliding shear capacity versus Load Point for Two-story Assemblage Specimen.....	164
Figure A.22 Hysteretic behavior of Shear Wall Specimen 4 .....	166
Figure A.23 Base shear and sliding shear capacity versus Load Point for Two-Story AAC Assbemblage Specimen .....	167
Figure A.24 Base shear and reduced sliding shear capacity versus Load Point for Two-story Assemblage Specimen.....	168
Figure A.25 Equilibrium of an AAC shear wall at nominal flexural capacity....	169
Figure A.26 Formation of first diagonal crack in Shear Wall Specimen 2 .....	172
Figure A.27 Formation of additional cracks in Shear Wall Specimen 2.....	173
Figure A.28 Behavior of monolithic AAC shear wall .....	174
Figure A.29 Behavior of individual panel for an AAC shear wall .....	174
Figure A.30 Distribution of axial loads for laterally loaded condition and axially loaded condition .....	175
Figure A.31 Base shear capacity for Shear Wall Specimen 2 considering individual panel behavior and monolithic wall behavior .....	177
Figure A.32 Base shear capacity for Shear Wall Specimen 2 considering individual panel behavior, behavior of panel groups and monolithic wall behavior.....	178

Figure A.33 Ratio of base shear at observed longitudinal crack to base shear at expected flexural capacity ( $f_s=1.25 f_y$ ) .....	180
Figure A.34 Ratio of base shear at observed longitudinal crack to base shear at nominal flexural capacity without overstrength.....	182
Figure A.35 Loss of end block on compression toe in Shear Wall Specimen 16187	
Figure A.36 Loss of end blocks and buckling of compression reinforcement in Shear Wall Specimen 15b .....	187
Figure A.37 Free-body diagram of longitudinal bar with all load transferred through lugs and pressure generated in the surrounding grout .....	189
Figure A.38 Stresses generated perpendicular to a cut along the diameter of a grouted cell.....	191
Figure A.39 Calculation of force corresponding to the splitting tensile stresses across a section of grout .....	192
Figure B.1 Cellular structure of AAC .....	204
Figure B.2 Examples of AAC structural elements .....	207
Figure B.3 Overall steps in manufacture of AAC .....	209
Figure B.4 Fresh AAC after removal of molds.....	210
Figure B.5 Cutting AAC into desired shapes .....	211
Figure B.6 Autoclaving AAC.....	212
Figure B.7 Packaging of finished AAC units.....	213
Figure B.8 Bond mechanism of welded-wire fabric in AAC.....	220



# CHAPTER 1

## Introduction

### 1.1 GENERAL

The continuous advancement of construction technology in creating new materials, design innovations and construction techniques requires the corresponding development of an adequate technical basis for these advances. In particular, it is important to study the mechanical characteristics and behavior of new materials. This is true in particular for autoclaved aerated concrete (AAC), a new material for the United States.

This study forms one part of an extensive research project produced at the Ferguson Structural Engineering Laboratory of the University of Texas at Austin under the sponsorship of the Autoclaved Aerated Concrete Products Association (AACPA). The overall objective of that study is to develop design provisions for AAC (including seismic design), and their underlying technical basis.

### 1.2 SCOPE OF OVERALL STUDY

Research at The University of Texas at Austin has involved the development of design approaches and corresponding design provisions, and the verification of those provisions through extensive testing. It has also involved the development of  $R$  and  $C_d$  factors for seismic design of AAC structural systems.

The experimental study carried out at The University of Texas at Austin has consisted of the testing of 19 AAC shear-wall specimens controlled by different behaviors, and a two-story AAC assemblage specimen. The 19 shear-

wall specimens were tested to develop and validate the design provisions proposed for the AAC shear walls. The assemblage was tested to validate the proposed design and construction provisions on a global level.

### **1.3 OBJECTIVES OF OVERALL STUDY**

Research at The University of Texas at Austin had the following objectives:

- to determine fundamental material properties of the AAC manufactured in the United States;
- to develop and verify the design provisions for AAC shear wall specimens, addressing flexural cracking, web-shear cracking, flexure-shear cracking, sliding shear, crushing of the diagonal strut, and flexural capacity;
- to verify the adequacy of proposed construction details for connections between AAC floor diaphragms and the AAC shear walls;
- to establish the force-reduction factor ( $R$ ) and displacement-amplification factor ( $C_d$ ) for design of AAC structures in seismic zones.

### **1.4 ORGANIZATION OF OVERALL STUDY**

The overall study comprises the following elements:

- the development of the shear-wall test setup and results from pilot specimens, carried out by Matthew Brightman, Jennifer Tanner and Jorge Varela, and described in the MS thesis of Brightman (Brightman 2000);
- the development of design provisions for AAC structural systems, carried out by Jennifer Tanner and Jorge Varela, and additionally by Jaime

Argudo, and described in the PhD dissertation of Tanner (2003) and the MS thesis of Argudo (2003);

- the development of  $R$  and  $C_d$  factors, carried out by Jorge Varela, and described in his PhD dissertation;
- the synthesis of material testing data, carried out by Jennifer Tanner and Jaime Argudo, and described in the PhD dissertation of Tanner (2003) and the MS thesis of Argudo; and
- confirmation of the applicability of previously developed shear-wall provisions to low-strength AAC shear walls, carried out by Ulises Cancino and Jorge Varela, and described in this MS thesis by Cancino (2003).

## **1.5 SCOPE OF THESIS**

The purpose of the study described in this thesis was to conduct and evaluate the results of reversed cyclic load tests on the final 3 of 19 AAC shear wall specimens. The three AAC specimens (SWS17, SWS18 and SWS19) were constructed with vertically oriented, reinforced panels (SWS17) or masonry-type units (SWS18 and SWS19). The tests described here were intended to evaluate the in-plane behavior of those low-strength AAC shear walls, and to validate the applicability to such walls, of previously developed design provisions.

Shear Wall SWS17 was designed to exhibit flexure-dominated behavior. Because the behavior of flexure-dominated walls is well understood, the main purpose of this study was to evaluate improvements in behavior of specimens constructed with spiral ties devices connecting the extreme-fiber elements to the remainder of the wall.

Shear Walls SWS18 and SWS19 were constructed with low-strength AAC material, and were intended to exhibit shear-dominated behavior. They were tested to confirm the applicability to low-strength AAC of previously developed provisions for shear capacity.

## **1.6 OBJECTIVES OF THESIS**

The study described here had the following specific objectives:

- to examine the behavior of the compression toes as influenced by larger grout columns at each end and by the use of stainless steel spiral ties to attach the end blocks to the rest of the wall (SWS17);
- to examine the general hysteretic behavior of the specimens and compare observed story drift and displacement ductility with analytical assumptions (SWS17);
- to validate previously proposed design provisions for AAC shear walls (SWS17);
- to validate the previously proposed design provisions for web-shear cracking, in the case of low-compressive strength AAC (SWS18 and SWS19); and
- to validate the similarity between the overall hysteretic behavior of shear-dominated low-strength AAC shear walls (SWS18 and SWS19), and the shear walls previously tested at UT Austin.
- to validate the similarity between the overall hysteretic behavior of flexure-dominated low-strength AAC shear walls (SWS17), and the shear walls previously tested at UT Austin.

## **1.7 ORGANIZATION OF THIS THESIS**

This thesis is organized as follows: Chapter 2 presents the characteristics of the three AAC shear wall specimens, mechanical properties of the AAC material, instrumentation and planning prior to the tests. Chapter 3 contains information obtained during the tests, including the principal observations and basic behavior of the specimens. Chapter 4 presents an evaluation of the significance of the results obtained from the tests. Finally, Chapter 5 provides the summary, conclusions and recommendations resulting from the study.

Two Appendices are also included:

- Appendix A presents the relevant theory, including the design provisions for reinforced AAC shear walls developed by Tanner (2003) and Varela (2003).
- Appendix B presents the first chapters of the current draft of the ACI 523.5 R-xx Guide for Using Autoclaved Aerated Concrete Panels (Argudo 2003). The purpose of this appendix is to present basic information on AAC, that was not developed by the author.

## **CHAPTER 2**

### **Test Specimens, Test Setups, and Testing Procedures**

#### **2.1 INTRODUCTION**

The testing program included one flexure-dominated specimen (SWS17) and two shear-dominated specimens (SWS18 and SWS19), tested using the same setup and instrumentation used in previous tests by Varela (2003) and Tanner (2003). The setup permitted the application of constant gravity loads and quasi-static, reversed cyclic in-plane shear loads to single-story AAC shear walls. The instrumentation permitted the capture of global behavior (such as displacements and loads), and local behavior (such as stresses in flexural reinforcement).

The results of the AAC material strengths are also presented. The specimens were designed using those strengths, and the wall geometry, reinforcement and axial load were chosen according to the desired mode of behavior.

In this chapter, the objectives, test setup, instrumentation, material strengths, design of specimens, loading protocol and construction of the specimens are presented.

#### **2.2 DESIGN AND CONSTRUCTION OF SHEAR WALL SPECIMEN 17**

##### **2.2.1 Objectives**

Shear Wall Specimen 17 was tested to verify the previously proposed design provisions for the case of a flexure-dominated specimen of low-strength

AAC, and also to evaluate possible improvements in the performance of the wall through the incorporation of stainless-steel spiral ties between the U-blocks and the remainder of the wall. This specimen was intended to fail in flexure. With this intent, the aspect ratio, the axial load and the reinforcement of the specimen were selected.

### **2.2.2 Configuration of Shear Wall Specimen 17**

The wall measured 112 in. (2.84 m) long by 144 in. (3.66 m) high by 8 in. (0.203 m) thick. The height from the bottom of the wall to the line of the load application was 154 in. (3.91 m). The aspect ratio of the wall (height divided by plan length) was 1.34. Figure 2.1 shows the geometry and reinforcement of Shear Wall Specimen 17.

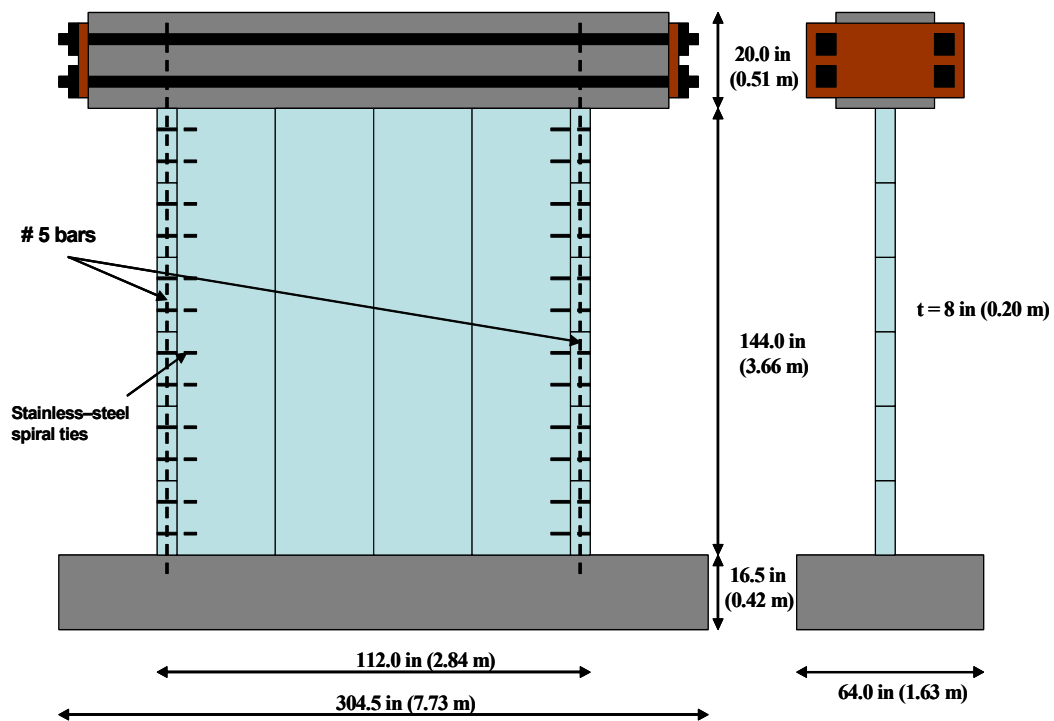


*Figure 2.1: Geometry and reinforcement of Shear Wall Specimen 17*

Figure 2.2 shows a plan view of the masonry-type lintel units (U-blocks) attached to the vertical panels with the stainless-steel spiral ties, and the geometric characteristics of the U-blocks.



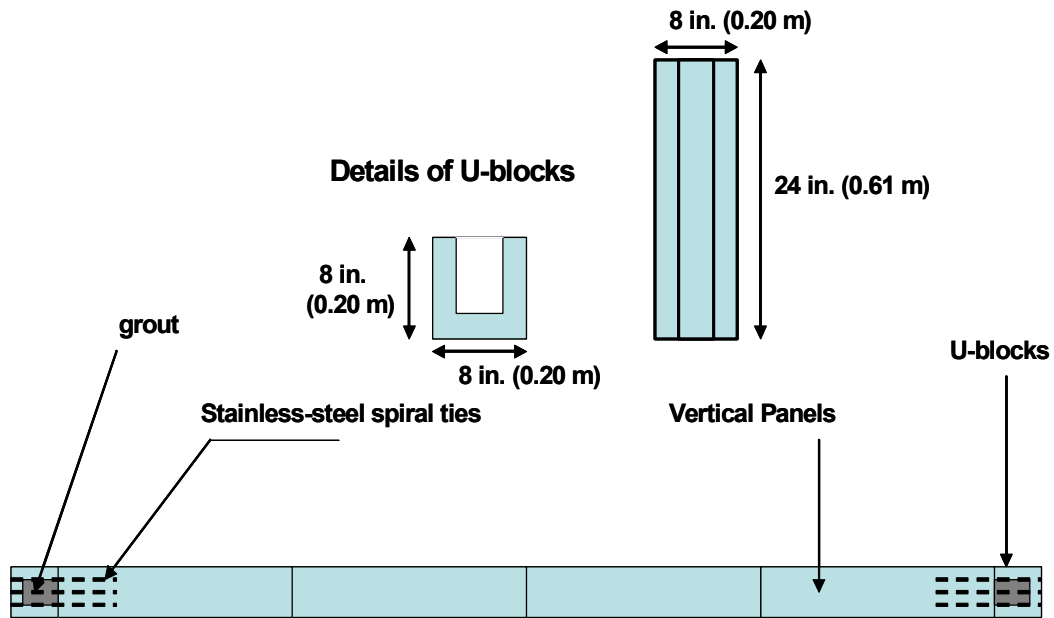


*Figure 2.2: Plan view of Shear Wall Specimen 17 with details of the stainless-steel spiral ties*

## 2.2.3 Test Setup for Shear Wall Specimen 17

### 2.2.3.1 Base Beam

The base beam measured 304.5 in. (7.73 m) long by 64 in. (1.63 m) wide by 16.5 in. (0.42 m) high. To prevent sliding or uplifting, the base beam was tied to the reaction floor of the laboratory through post-tensioned rods. Details of the base beam used for Shear Wall Specimen 17 are shown in Figure 2.3.

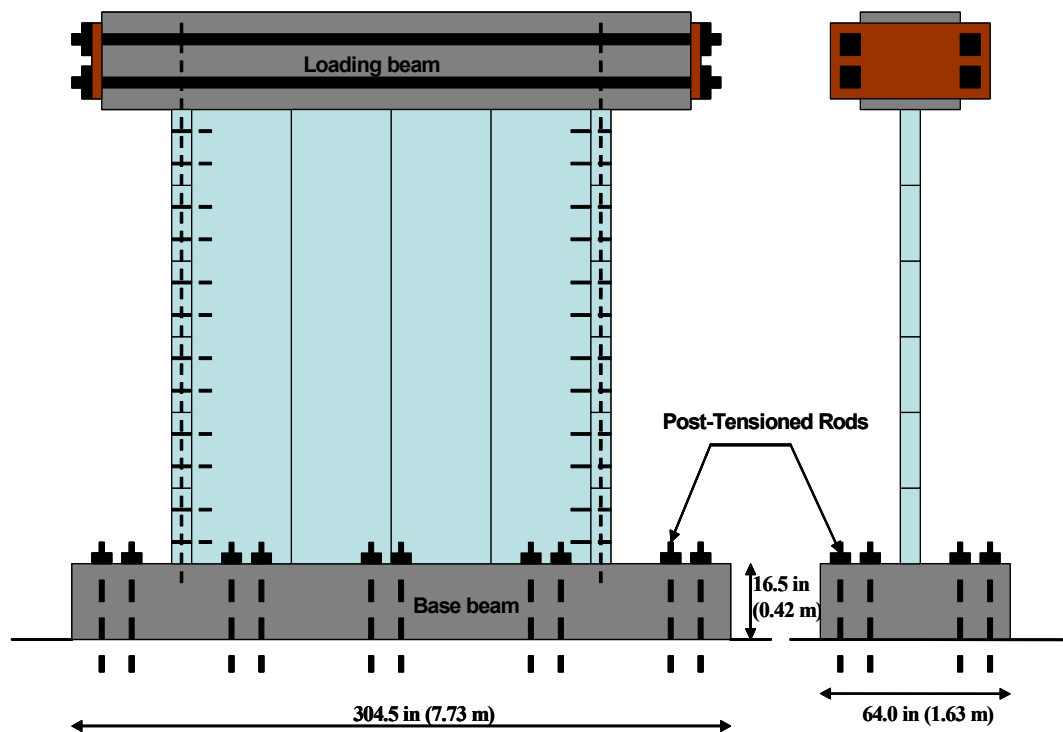


*Figure 2.3: Typical view of base beam used for Shear Wall Specimen 17*

### 2.2.3.2 Axial Load System

The constant axial load of 25 kips (111.2 kN) was applied to the specimen by a loading beam with a weight of 5 kips (22.24 kN), and by hydraulic actuators controlled by a load maintainer that provided 20 kips (89 kN). The axial load from the load maintainer was transmitted through two threaded rods, one at each side of the specimen, and located at the center of the wall. These threaded rods were connected at the top with a steel swivel beam and to the bottom with a swivel steel box which was tied to the base beam with post-tensioned rods. Figure 2.4 shows the axial load system for Shear Wall Specimen 17.

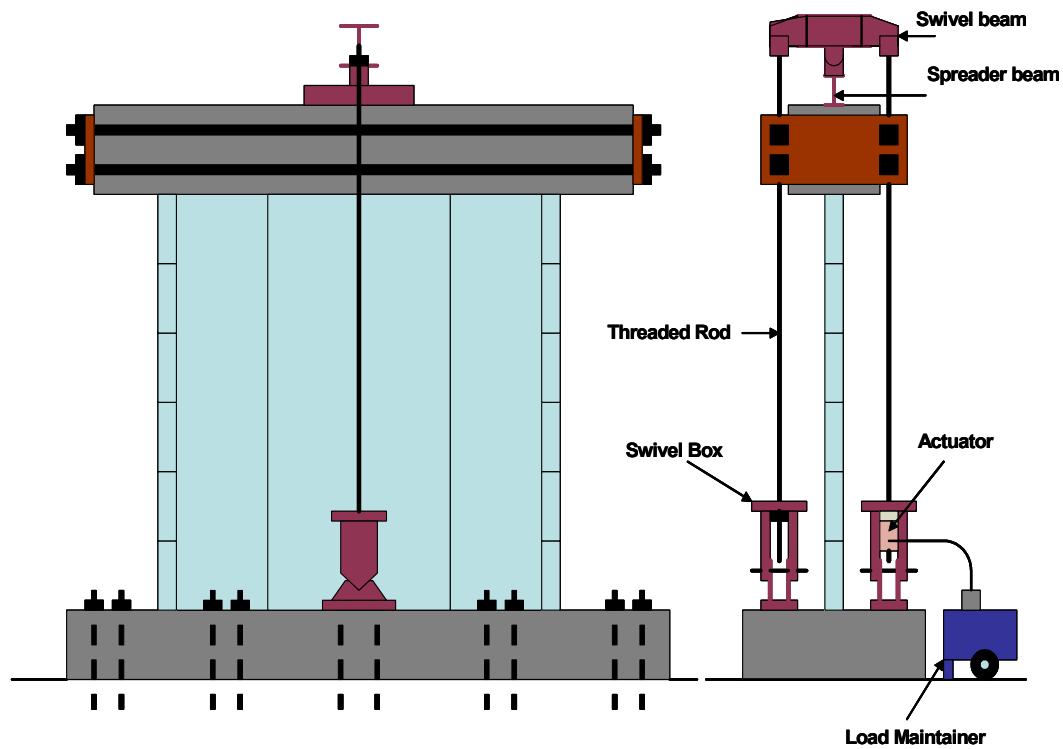


*Figure 2.4: Typical details of the axial load system used for Shear Wall Specimen 17*

### 2.2.3.3 Lateral Bracing System

The lateral bracing system, necessary to provide out-of-plane stability to the specimen, consisted of four steel cables connected to the loading beam of the specimen at four different points. Two of these cables were attached to the reaction wall, and the other two were attached to steel columns (Figure 2.5).

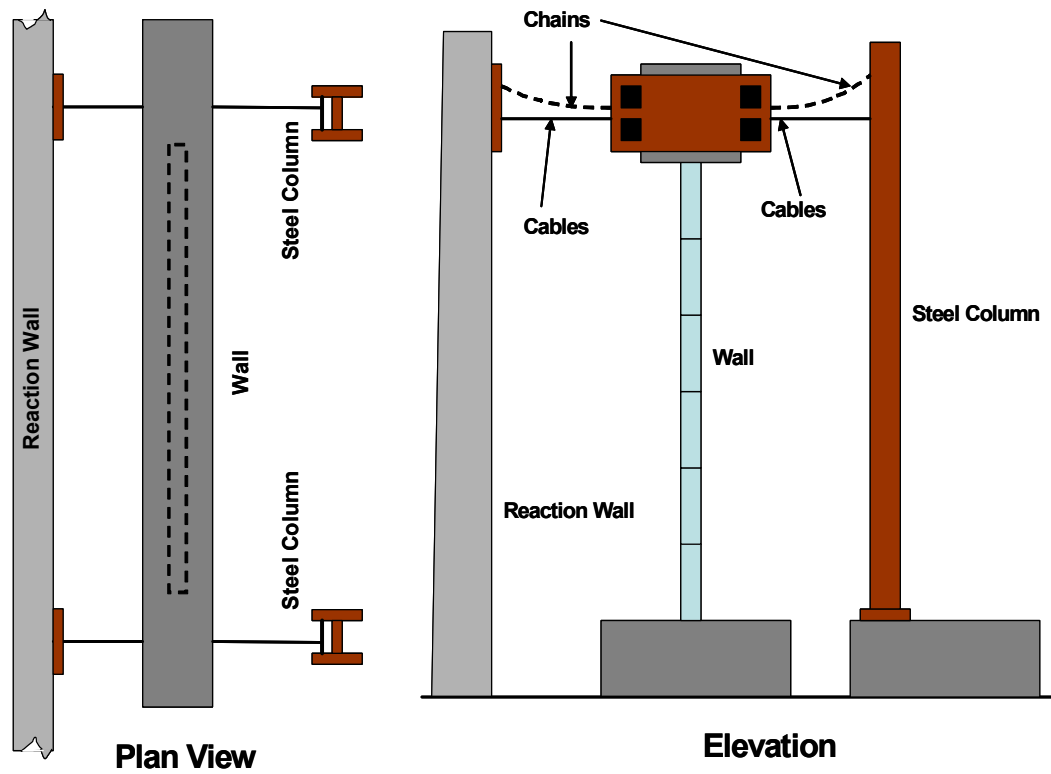


*Figure 2.5: Different views showing details of the lateral bracing system*

#### 2.2.3.4 Actuators

Horizontal load was applied to the specimen with a 60 kips (270 kN) hydraulic actuator, controlled by an air-operated pump. The actuator has a maximum extension of 18.0 in. (0.46 m). Figure 2.6 shows the actuator connected to the loading beam of Shear Wall Specimen 17.

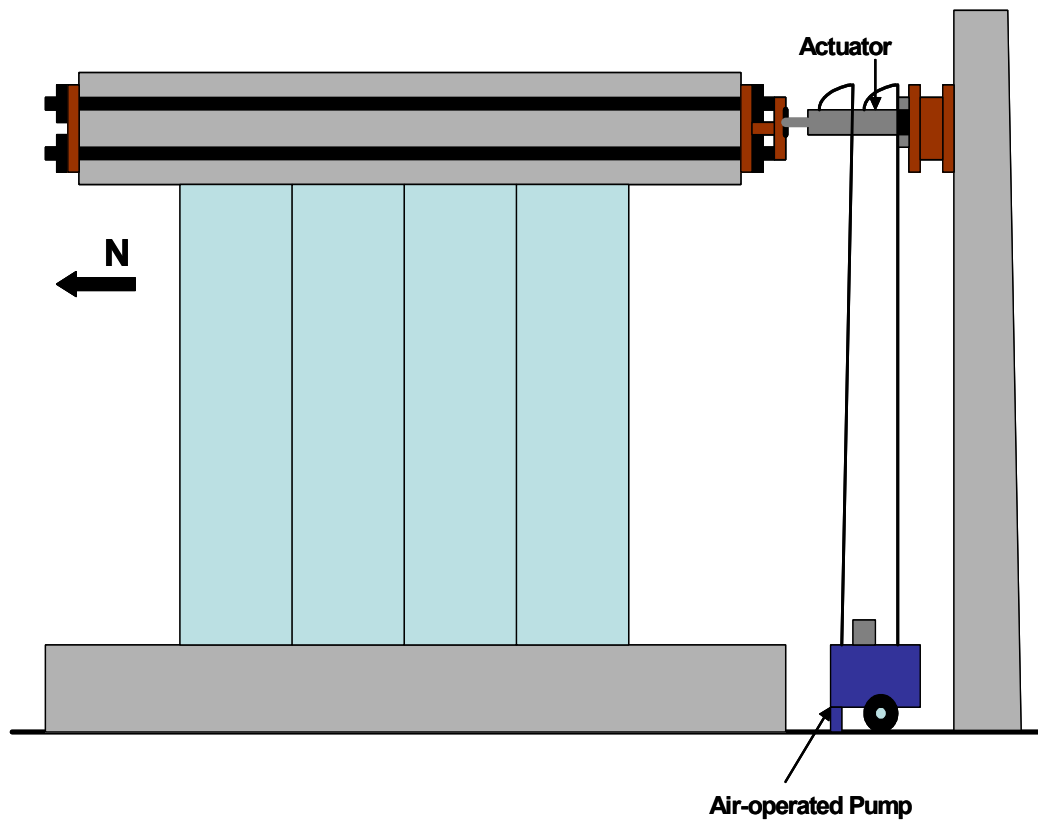


*Figure 2.6: Actuator connected to Shear Wall Specimen 17*

### **2.2.3.5 Instrumentation and Data Acquisition**

#### **2.2.3.5.1 Instrumentation**

The global and local behavior of the specimen was verified through specific instruments to measure pressure, force and displacement. The types of instruments used include: pressure transducers, load cells, force washers, linear potentiometers, and string potentiometers. Table 2.1 describes the instrumentation used in Shear Wall Specimen 17. Figure 2.7 and Figure 2.8 show the location of those instruments on the specimen.

**Table 2.1: Description of instrumentation used in Shear Wall Specimen 17**

<b>Instrument</b>	<b>Label</b>	<b>Kind of Behavior Measurement</b>	<b>Type of Measurement</b>	<b>Output reading on the instrument</b>	<b>Units used in output file</b>
String pot.	SP1	Local Behavior	Vertical displ.	Length	in.
String pot.	SP2	Local Behavior	Vertical displ.	Length	in.
String pot.	SP3	Local Behavior	Vertical displ.	Length	in.
String pot.	SP4	Local Behavior	Vertical displ.	Length	in.
String pot.	SP5	Local Behavior	Vertical displ.	Length	in.
String pot.	SP6	Local Behavior	Vertical displ.	Length	in.
String pot.	SP7	Local Behavior	Diagonal displ.	Length	in.
String pot.	SP8	Local Behavior	Diagonal displ.	Length	in.
String pot.	SP9	Global Behavior	Vertical displ.	Length	in.
String pot.	SP10	Global Behavior	Vertical displ.	Length	in.
String pot.	SP11	Global Behavior	Horizontal displ.	Length	in.
String pot.	SP12	Global Behavior	Horizontal displ.	Length	in.
Linear pot.	LP1	Local Behavior	Found.-floor slip	Length	in.
Linear pot.	LP2	Local Behavior	Wall-L.Beam slip	Length	in.
Linear pot.	LP3	Local Behavior	Wall-L.Beam slip	Length	in.
Linear pot.	LP4	Local Behavior	Wall-Found. slip	Length	in.
Load Cell	LC	Global Behavior	Force in ram	Force	kips
Force Washer	FW	Local Behavior	Force in rods	Force	kips
Pressure Trans	PT1	Global Behavior	Pressure in ram	Pressure	ksi
Pressure Trans	PT2	Global Behavior	Pressure in ram	Pressure	ksi

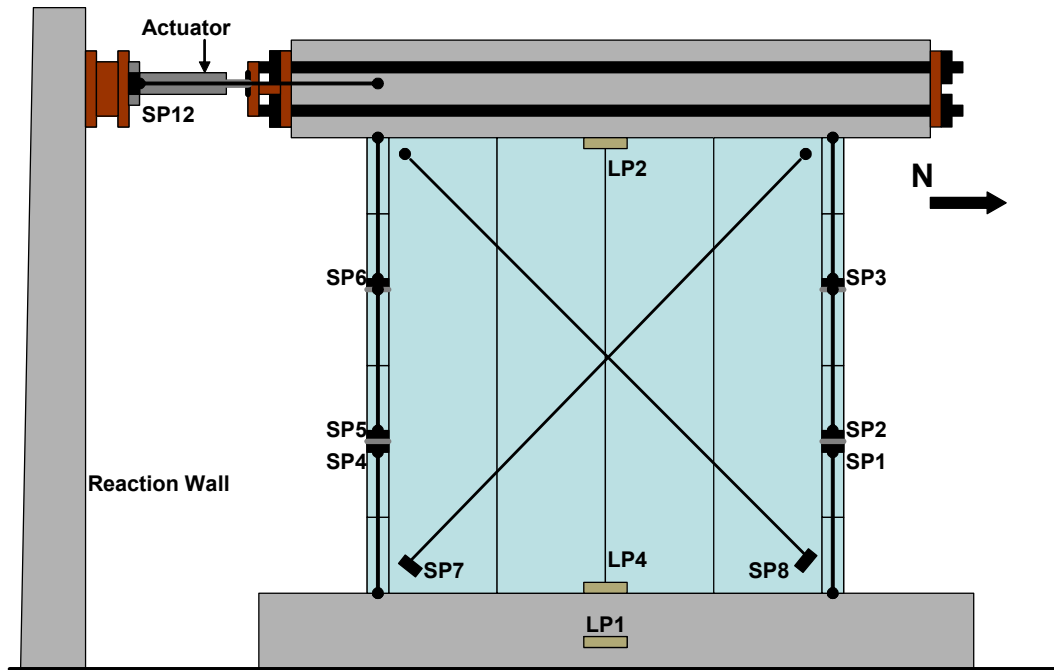


*Figure 2.7: East face of Shear Wall Specimen 17 showing locations of instrumentation*

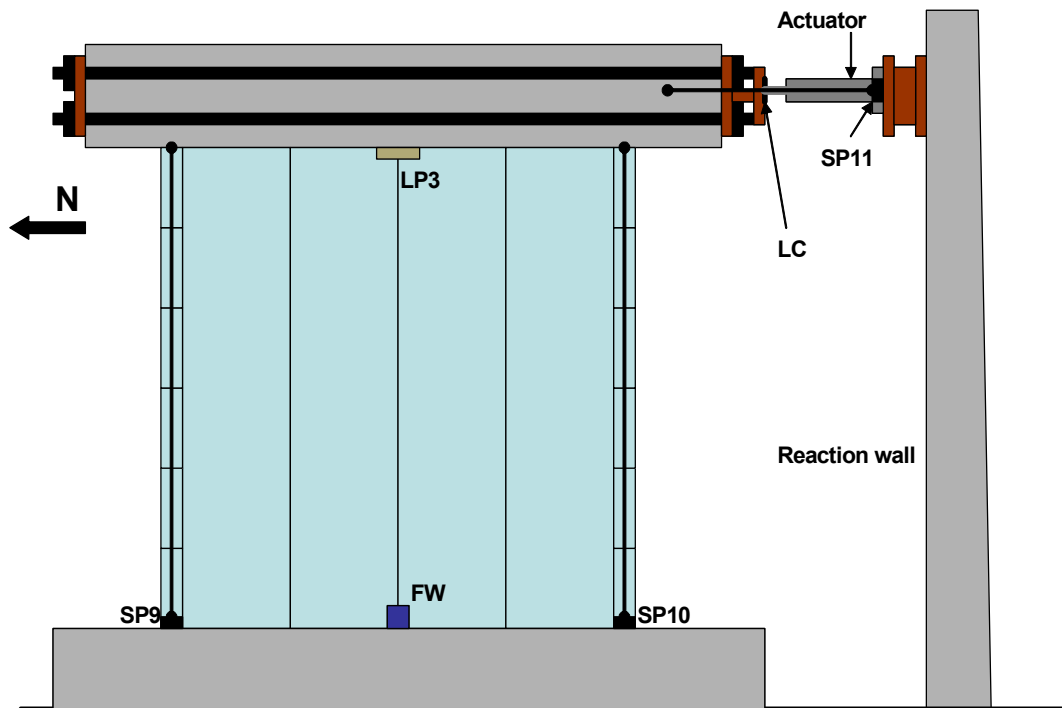


*Figure 2.8: West face of Shear Wall Specimen 17 showing locations of instrumentation*

Additionally, three strain gauges were attached to each flexural reinforcing bar at three different levels within the bottom 8 in. (200 mm). These strain gauges measured the stress induced in the flexural reinforcement during the application of the horizontal force (Figure 2.9).



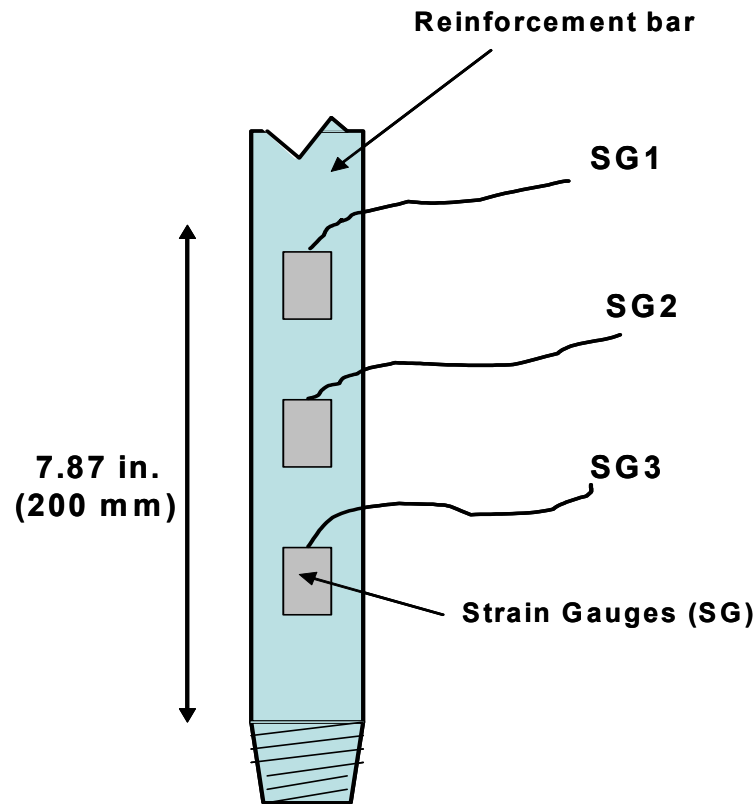


*Figure 2.9: Typical view of the strain gauge positions in the flexural reinforcement of Shear Wall Specimen 17*

#### **2.2.3.5.2 Data Acquisition**

The instruments were connected to a full-bridge, and the strain gauges, to a quarter-bridge box. The full-bridge box was excited with 10 volts and the quarter-bridge box with 2 volts, both were provided by a precision power supply. These bridge boxes were connected to a HP3852A scanner. Analog-to-digital conversion was carried out by a National Instruments card in a Windows-based microcomputer running MS Excel 7.0.

## **2.2.4 Loading Protocol**

The lateral loading program consisted of reversed cycles to a monotonically increasing maximum load or displacement. Prior to starting the tests, an initial cycle of low-lateral load, normally 5 kips (22.5 kN), was applied to every specimen to check the complete setup (loading equipment, lateral bracing, instruments and data acquisition). Initial loading cycles were applied under load control to load levels predicted to produce major events in the shear-wall specimens tested. Subsequent loading cycles were applied under displacement control. For Shear Wall Specimen 17, the loading history was switched from load to displacement control after yield of flexural reinforcement.

## **2.2.5 Material Strengths**

### ***2.2.5.1 Compressive Strength***

Shear Wall Specimen 17 was constructed using AAC material corresponding to Class PAAC4, which has a specified compressive strength of 4 MPa (580 psi). The compressive strength of the AAC material in that specimen was tested for compliance with that specified strength.

#### ***2.2.5.1.1 Specimen Preparation and Testing Procedure for Compression Tests on AAC Cubes***

Cubes for the compressive tests were prepared from the AAC material used to construct Shear Wall Specimen 17. This material had been shipped to UT from Babb International, Inc. (Adel, GA). In this thesis, it is designated “Babb 4.”

Nine cubes were prepared at the Babb plant for testing according to ASTM C1386. The cubes were removed from AAC blocks using a dry circular saw to extract roughly cubical blocks of AAC. These blocks were then cut into 4-

in. (100 mm) cubes using a water-cooled circular saw. All cubes were oriented so that they would be tested perpendicular to the direction of rise.

All faces of the AAC cubes were milled using a machine with two grinding wheels that allowed milling two parallel faces of the cubes at the same time (Figure 2.10).



*Figure 2.10: Machine used to mill faces of AAC cubes*

After the cubes were milled, their moisture content was measured by weighing. Because that moisture content exceeded the maximum value specified in ASTM C1386, the cube specimens were placed in an oven for 24 hours at a constant temperature of 140 degrees Fahrenheit. After that time, the cubes were again weighed. The weights of AAC cubes measured at Babb Plant and at UT Austin are presented in Table 2.2.

*Table 2.2: Dry weights of AAC cubes measured at Babb and at UT Austin*

<b>Material</b>	<b>Block Number</b>	<b>Weight (after oven) at Babb lb (kg)</b>	<b>Weight (after oven) at UT Austin lb (kg)</b>	<b>Ratio of the Weight at Babb to Weight at UT Austin</b>
<b>Babb 4</b>	<b>1-1</b>	<b>1.51 (0.6873)</b>	<b>1.48 (0.6707)</b>	<b>1.02</b>
<b>Babb 4</b>	<b>1-2</b>	<b>1.45 (0.6594)</b>	<b>1.43 (0.6478)</b>	<b>1.01</b>
<b>Babb 4</b>	<b>1-3</b>	<b>1.44 (0.6565)</b>	<b>1.42 (0.6440)</b>	<b>1.01</b>
<b>Babb 4</b>	<b>1-4</b>	<b>1.42 (0.6470)</b>	<b>1.42 (0.6450)</b>	<b>1.00</b>
<b>Babb 4</b>	<b>1-5</b>	<b>1.39 (0.6300)</b>	<b>1.38 (0.6294)</b>	<b>1.00</b>
<b>Babb 4</b>	<b>1-6</b>	<b>1.38 (0.6280)</b>	<b>1.38 (0.6256)</b>	<b>1.00</b>

Three cubes were tested at the Babb plant laboratory, and the rest were sent to UT Austin for confirmatory compressive strength tests (Varela 2003). Compression testing was performed in a universal machine, which includes a load cell and a spherical seat to apply uniform load. Data were recorded using data-acquisition software of the Ferguson Structural Engineering Laboratory of UT Austin. Figure 2.11 shows the test setup used in the compressive tests.



*Figure 2.11: Typical view of test setup to measure compressive strength*

#### ***2.2.5.1.2 Compression Test Results for AAC Cubes***

Compressive-strength results for the six specimens tested at UT Austin, summarized in Table 2.3, ranged from 737 psi (5.08 MPa) to 944 psi (6.51 MPa), with a final average of 811 psi (5.59 MPa), and a COV of 9.33 %. Compressive-strength results for the three specimens tested at the Babb plant laboratory are summarized in Table 2.4. The moisture content of the cubes complied with the range of 5 % to 15 % specified by ASTM C1386.

**Table 2.3: Results of compressive strength tests performed at UT Austin**

Material	Cube	$f_{AAC}$ psi (MPa)	Duration of Test (seconds)	Average psi (MPa)	COV (%)	Average psi (MPa)	COV (%)
Babb 4	1-1	811 (5.59)	110	774 (5.30)	4.78	811 (5.59)	9.33
Babb 4	1-2	775 (5.34)	110				
Babb 4	1-3	737 (5.08)	150				
Babb 4	1-4	944 (6.51)	120	877 (6.0)	7.10		
Babb 4	1-5	821 (5.66)	120				
Babb 4	1-6	866 (5.97)	150				

**Table 2.4: Results of compressive strength tests performed at the Babb plant**

Material	Cube	$f_{AAC}$ psi (MPa)	Duration of Test (seconds)	Average psi (MPa)	COV (%)
Babb 4	1-7	870 (6.00)	60	793 (5.50)	8.61
Babb 4	1-8	769 (5.30)	110		
Babb 4	1-9	740 (5.10)	53		

### 2.2.6 Construction of Shear Wall Specimen 17

The surface of the base beam was roughened and pre-wetted. A leveling bed was applied, using conventional Portland cement-lime masonry mortar conforming to ASTM C270, Type S by proportion. The vertical panels were set up and joined with thin-bed mortar, and were clamped together to apply pressure

to the face of the joints. The plumbness of the panels was checked frequently during construction. The U-blocks were placed at each end of the wall, and were joined to the vertical panels using thin-bed mortar and stainless-steel spiral ties. The cores created by these U-blocks and the vertical panels were filled with coarse grout conforming to ASTM C476 by proportion and consolidated by vibrator. Figure 2.12 shows a partial view of Shear Wall Specimen 17 after construction.

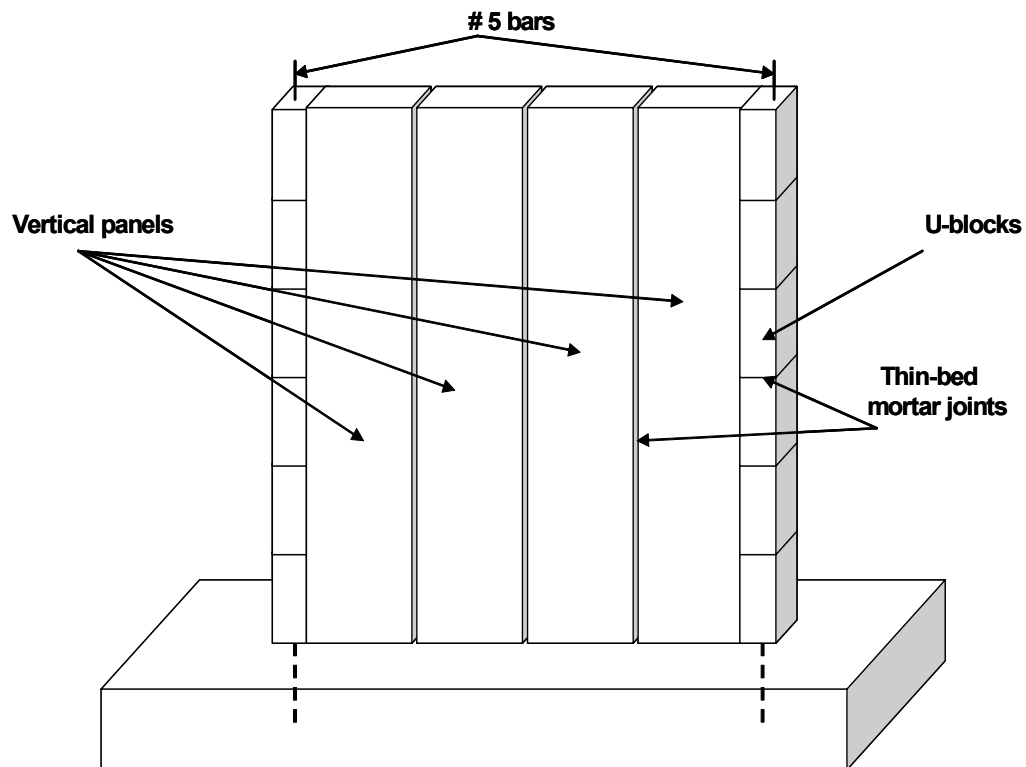


*Figure 2.12: Construction details of Shear Wall Specimen 17*

## **2.3 DESIGN AND CONSTRUCTION OF SHEAR WALL SPECIMENS 18 AND 19**

### **2.3.1 Objectives**

Shear Wall Specimens 18 and 19 were tested to verify the previously proposed design provisions for the case of a shear-dominated specimen of low-strength AAC, and also to examine the overall hysteretic behavior of the walls. These specimens were intended to fail in web-shear cracking. With this intent, their aspect ratio, axial load and flexural reinforcement were selected.

### **2.3.2 Configurations of Shear Wall Specimen 18 and 19**

Shear Wall Specimen 18 was constructed with AAC masonry units placed in running bond. The wall measured 144 in. (3.66 m) long by 144 in. (3.66 m) high by 8 in. (0.203 m) thick. The height from the bottom of the wall to the line of the load application was 154 in. (3.91 m). The aspect ratio of the wall (height divided by plan length) was 1.07. The threaded rods used as external flexural reinforcement corresponded to ASTM A193-B7 bars 1 in. (25.4 mm) in diameter. Figure 2.13 shows the geometry and reinforcement of Shear Wall Specimen 18.

Shear Wall Specimen 19 was constructed with AAC masonry units placed in running bond. The wall measured 216 in. (5.49 m) long by 144 in. (3.66 m) high by 8 in. (0.203 m) thick. The height from the bottom of the wall to the line of the load application was 154 in. (3.91 m). The aspect ratio of the wall (height divided by plan length) was 0.71. The threaded rods used as external flexural reinforcement corresponded to ASTM A193-B7 bars 1 in. (25.4 mm) in diameter. Figure 2.14 shows the geometry and reinforcement of Shear Wall Specimen 19.



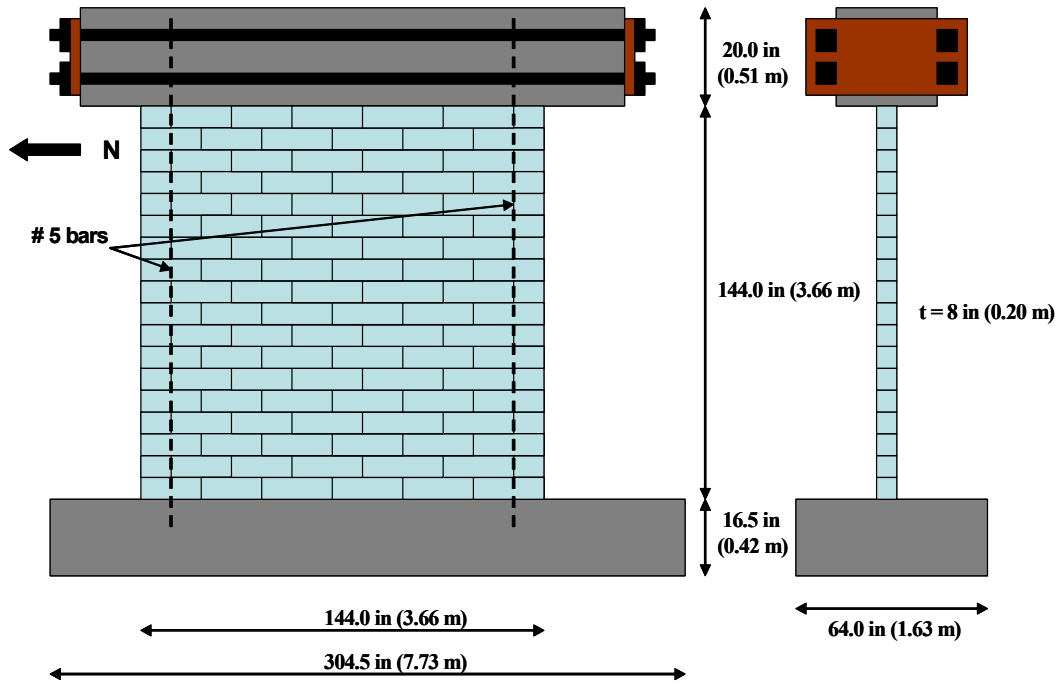


*Figure 2.13: Geometry and reinforcement of Shear Wall Specimen 18*

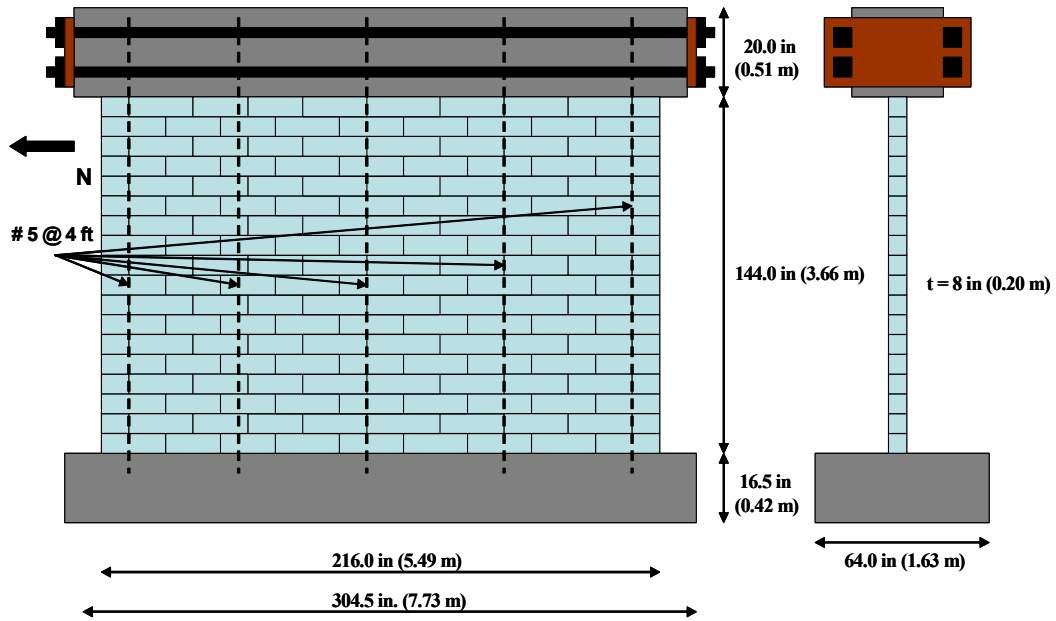


**Figure 2.14: Geometry and reinforcement of Shear Wall Specimen 19**

Figure 2.15 shows the geometric characteristics of the modular blocks used in Shear Wall Specimens 18 and 19.

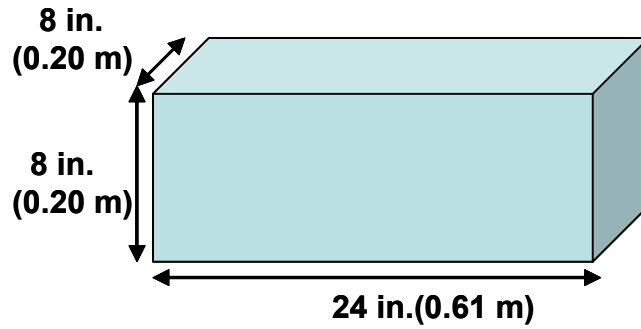


**Figure 2.15: Typical details of modular blocks used in Shear Wall Specimens 18 and 19**

### **2.3.3 Test Setup for Shear Wall Specimens 18 and 19**

#### **2.3.3.1 Base Beam**

The foundation used for Shear Wall Specimens 18 and 19 was a base beam with identical geometric characteristics to that of the base used for Shear Wall Specimen 17.

#### **2.3.3.2 Axial Load System**

An axial load of 45 kips (200.12 kN) was applied to Shear Wall Specimen 18 by a loading beam with a weight of 5 kips (22.24 kN) and four threaded rods post-tensioned manually which provided 40 kips (177.88 kN) in total. These threaded rods, two at each end of the specimen, were connected at the top with transverse steel beams and to the bottom with steel boxes which were tied to the base beam with bolts (post-tensioned rods). Figure 2.16 shows the axial load system used for Shear Wall Specimen 18.

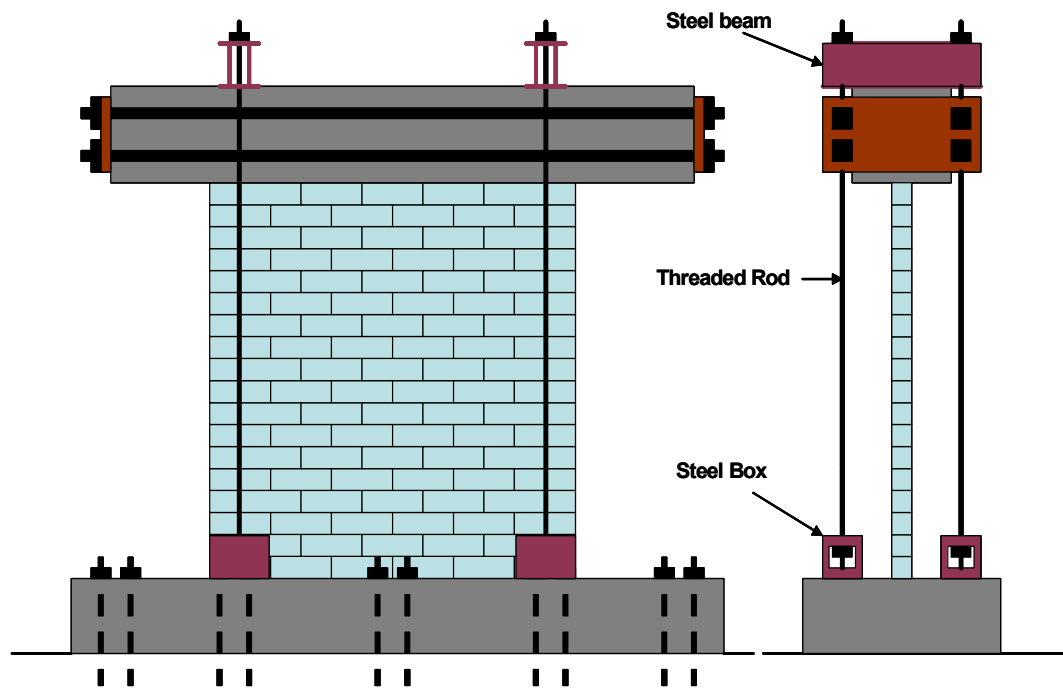


*Figure 2.16: Typical details of the axial load system used for Shear Wall Specimen 18*

An axial load of 58 kips (258 kN) was applied to Shear Wall Specimen 19 by a loading beam with a weight of 8 kips (35.58 kN) and four threaded rods post-tensioned manually to provide 50 kips (222.40 kN) in total. The setup of these threaded rods was the same as for Shear Wall Specimen 18. Figure 2.17 shows the axial load system used for Shear Wall Specimen 19.

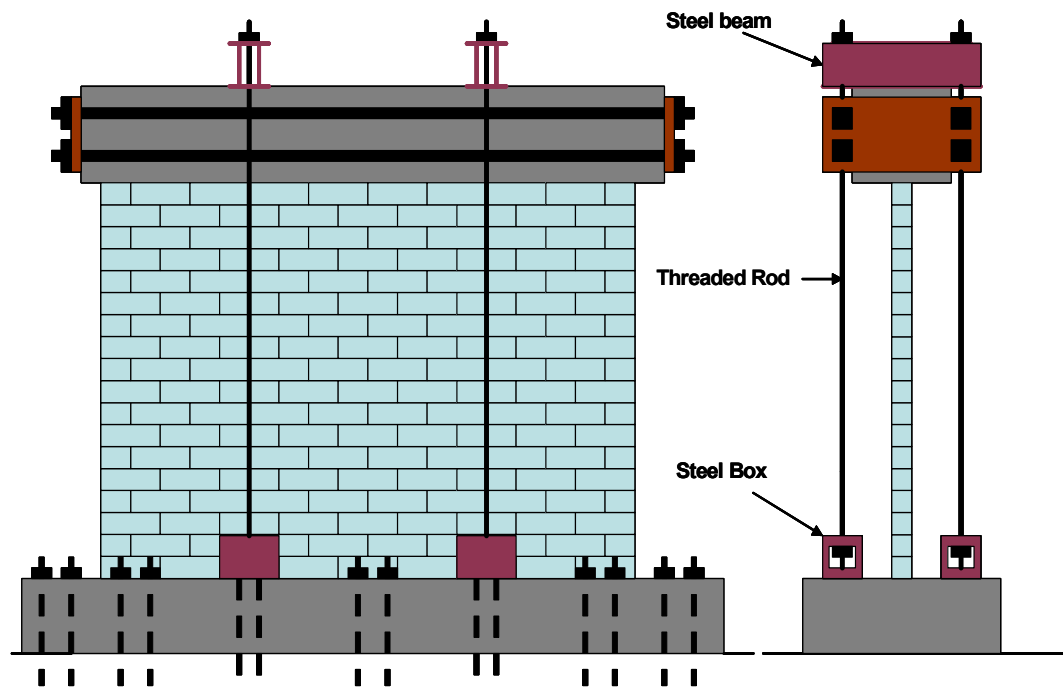


*Figure 2.17: Typical details of the axial load system used for Shear Wall Specimen 19*

### **2.3.3.3 Lateral Bracing System**

The lateral bracing system was necessary to provide out-of-plane stability to the specimens. The system was identical to that used for Shear Wall Specimen 17.

### **2.3.3.4 Actuators**

The actuator was identical to that used for Shear Wall Specimen 17.

### ***2.3.3.5 Instrumentation and Data Acquisition***

#### ***2.3.3.5.1 Instrumentation***

The global and local behavior of both specimens was verified through specific instruments to measure pressure, force and displacement. The types of instruments used include: pressure transducers, load cells, force washers, linear potentiometers, and string potentiometers. Table 2.5 describes the instrumentation used in Shear Wall Specimens 18 and 19. Figure 2.18 and Figure 2.19 show the location of that instrumentation in Shear Wall Specimen 18. The same configuration of instrumentation was used in Shear Wall Specimen 19.

**Table 2.5: Description of instrumentation used in Shear Wall Specimens 18 and**

**19**

<b>Instrument</b>	<b>Label</b>	<b>Kind of Behavior Measurement</b>	<b>Type of Measurement</b>	<b>Output reading on the instrument</b>	<b>Units used in output file</b>
String pot.	SP1	Local Behavior	Vertical displ.	Length	in.
String pot.	SP2	Local Behavior	Vertical displ.	Length	in.
String pot.	SP3	Local Behavior	Vertical displ.	Length	in.
String pot.	SP4	Local Behavior	Vertical displ.	Length	in.
String pot.	SP5	Local Behavior	Vertical displ.	Length	in.
String pot.	SP6	Local Behavior	Vertical displ.	Length	in.
String pot.	SP7	Local Behavior	Diagonal displ.	Length	in.
String pot.	SP8	Local Behavior	Diagonal displ.	Length	in.
String pot.	SP9	Global Behavior	Vertical displ.	Length	in.
String pot.	SP10	Global Behavior	Vertical displ.	Length	in.
String pot.	SP11	Global Behavior	Horizontal displ.	Length	in.
String pot.	SP12	Global Behavior	Horizontal displ.	Length	in.
Linear pot.	LP1	Local Behavior	Found.-floor slip	Length	in.
Linear pot.	LP2	Local Behavior	Wall-L.Beam slip	Length	in.
Linear pot.	LP3	Local Behavior	Wall-L.Beam slip	Length	in.
Linear pot.	LP4	Local Behavior	Wall-Found. slip	Length	in.
Load Cell	LC	Global Behavior	Force in ram	Force	kips
Force Washer	FW1	Local Behavior	Force in rods	Force	kips
Force Washer	FW2	Local Behavior	Force in rods	Force	kips
Force Washer	FW3	Local Behavior	Force in rods	Force	kips
Force Washer	FW4	Local Behavior	Force in rods	Force	kips
Pressure Trans	PT1	Global Behavior	Pressure in ram	Pressure	ksi
Pressure Trans	PT2	Global Behavior	Pressure in ram	Pressure	ksi

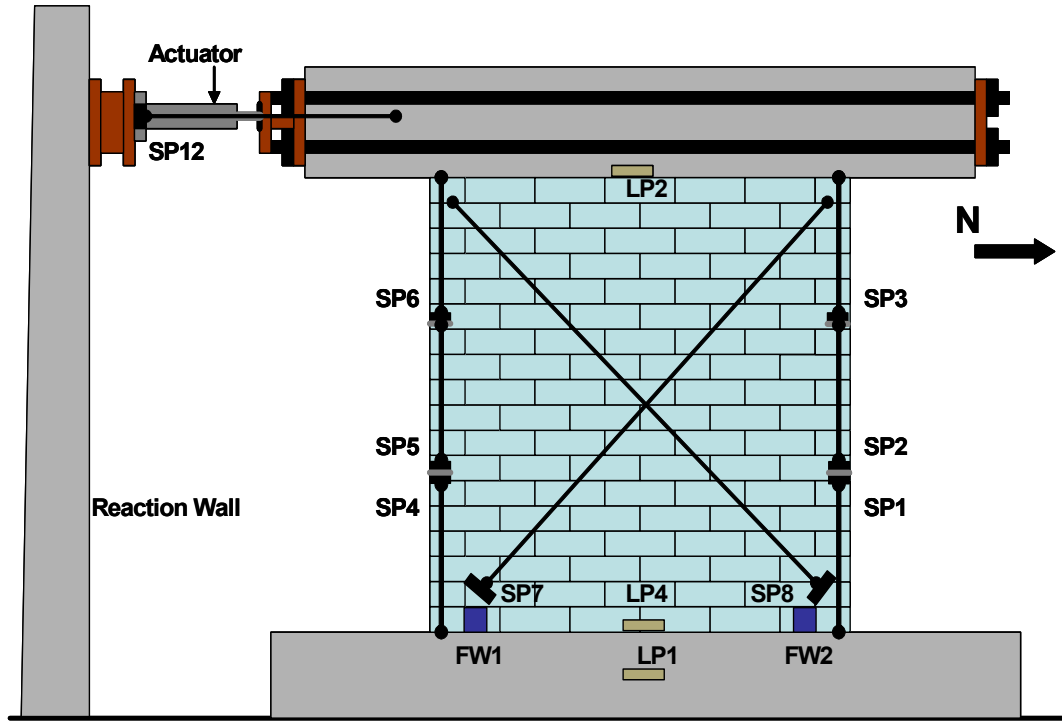


*Figure 2.18: East face of Shear Wall Specimen 18 showing locations of instrumentation*



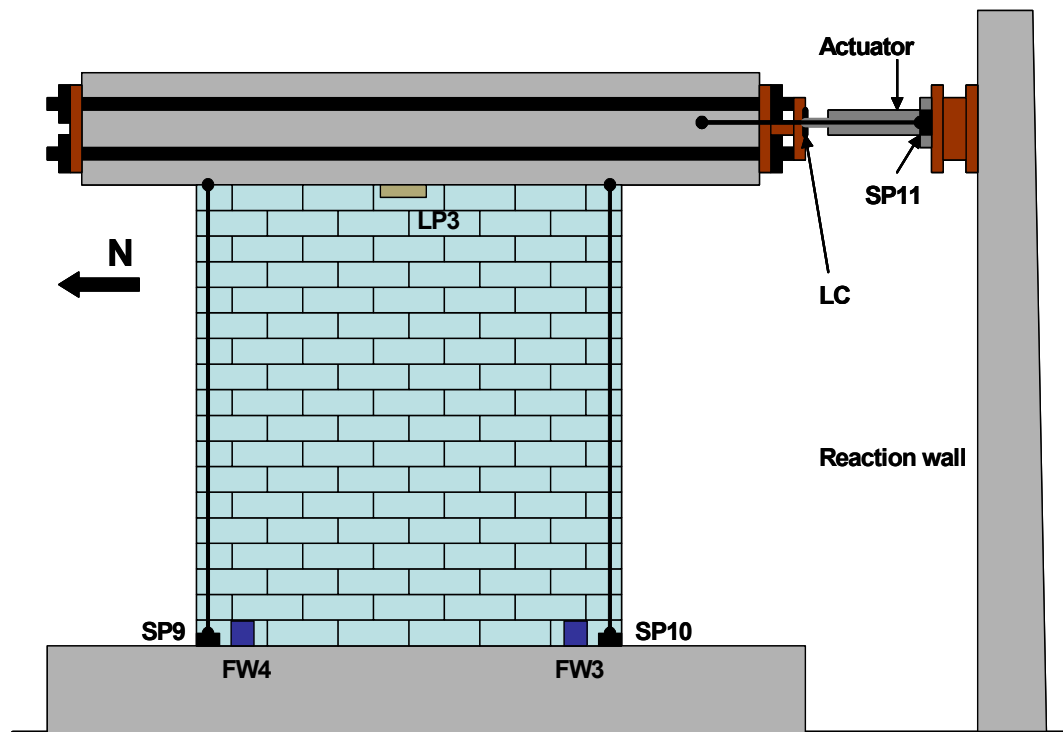


*Figure 2.19: West face of Shear Wall Specimen 18 showing locations of instrumentation*

Additionally, two strain gauges were attached to each extreme flexural reinforcing bar at two different levels within the bottom 4 in. (100 mm). These strain gauges measured the stress induced in the flexural reinforcement during the application of the horizontal force. The strain-gauge positions in Shear Wall Specimens 18 and 19 were similar to those used in Shear Wall Specimen 17.

### ***2.3.3.5.2 Data Acquisition***

The data acquisition system and connection of the instrumentation used in Shear Wall Specimens 18 and 19 were the same as those used for Shear Wall Specimen 17.

### **2.3.4 Loading Protocol**

The lateral loading program used for Shear Wall Specimens 18 and 19 was similar to that used for Shear Wall Specimen 17. For the shear-dominated specimens, the loading history was switched from load to displacement control after web-shear cracking.

### **2.3.5 Material Strengths**

#### ***2.3.5.1 Compressive Strength***

Shear Wall Specimens 18 and 19 were constructed using AAC material corresponding to Class PAAC2, which has a specified compressive strength of 2 MPa (290 psi). The compressive strength of the AAC material in those specimens was tested for compliance with that specified strength, using cubes prepared at the Babb plant and cores taken from masonry type units at UT Austin.

#### ***2.3.5.1.1 Specimen Preparation and Testing Procedure for Compression Tests on AAC Cores***

Cores for the compressive tests were prepared from the AAC material used to construct Shear Wall Specimen 18 and 19. This material had been shipped to UT from Babb International, Inc. (Adel, GA). In this thesis, that material is designated “Babb 3.”

Nine cores were prepared at UT for testing according to the same protocol prescribed for testing cubes in ASTM C1386. The cores were removed from the center and the outer third of AAC units, and measured  $7\frac{13}{16}$  in. (198 mm) long by  $3\frac{11}{16}$  in. (94 mm) in diameter. Their aspect ratio (length divided by diameter) was 2.

After the cores were extracted, their weight, density and moisture contents were measured. The moisture content of the cores must be between 5 % and 15 % according to ASTM C1386. The moisture content (MC) was measured three times: at the time of the compressive test; at the end of the test; and five days after the end of the test as a confirmation of the dry density. Table 2.6 shows the moisture content recorded from the cores.

**Table 2.6: Summary of results of moisture content measured in the cores drilled for the compressive test (Babb 3 material)**

Core	Immediately before the Test			Immediately after the Test			5 days after the Test		
	Measured Density (pcf)	Dry Density (pcf)	MC (%)	Measured Density (pcf)	Dry Density (pcf)	MC (%)	Measured Density (pcf)	Dry Density (pcf)	MC (%)
1-1	34.10	30.09	13.33	34.10	30.09	13.33	31.61	30.09	5.05
1-2	33.27	30.09	10.57	32.86	30.09	9.21	30.57	30.09	1.60
1-3	32.86	30.09	9.21	32.44	30.09	7.81	30.57	30.09	1.60
2-1	33.69	30.09	11.96	34.50	30.09	14.66	31.82	30.09	5.75
2-2	32.02	30.09	6.41	N.A	30.09	N.A	N.A	30.09	N.A
2-3	32.02	30.09	6.41	32.02	30.09	6.41	30.15	30.09	0.2
3-1	31.61	30.09	5.05	31.61	30.09	5.05	30.15	30.09	0.2
3-2	33.27	30.09	10.57	32.86	30.09	9.21	30.78	30.09	2.29
3-3	33.69	30.09	11.96	33.27	30.09	10.57	30.78	30.09	2.29

The compressive test setup included an extensometer attached to a linear potentiometer with a 2-inch range of measuring the axial deformation during the test. The test was performed in a universal testing machine, which includes a load cell and a spherical head to apply uniform load to cores. Data were recorded using

data-acquisition software of the Ferguson Structural Engineering Laboratory of UT Austin. Figure 2.20 shows the test setup used in the compressive tests.



*Figure 2.20: Typical view of the test setup to measure compressive strength*

### **2.3.5.2 Compression Test Results for AAC Cores**

Compressive strengths for the six cores, summarized in Table 2.7, ranged from 287 psi (1.99 MPa) to 370 psi (2.57 MPa), with a mean of 344 psi (2.39 MPa) and a COV of 8.13 %. Figure 2.21 shows the stress-strain curves obtained for the six cores.

**Table 2.7: Results of compressive strength tests performed at UT Austin**

Material	Core	$f_{AAC}$ psi (MPa)	Moisture Content (%)	Average psi (MPa)	COV (%)	Average psi (MPa)	COV (%)
Babb 3	1	350 (2.43)	13.33	347 (2.41)	2.45	344 (2.39)	8.13
Babb 3	2	335 (2.32)	10.57				
Babb 3	3	355 (2.46)	9.21				
Babb 3	4	370 (2.57)	11.96	341 (2.37)	11.27		
Babb 3	5	367 (2.55)	10.57				
Babb 3	6	287 (1.99)	6.41				

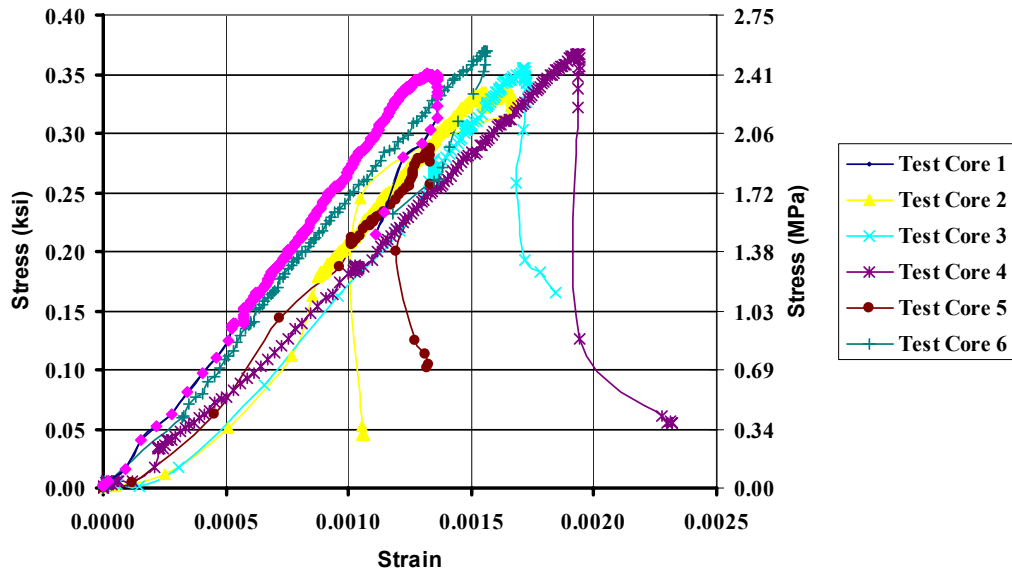


**Figure 2.21: Compressive stress versus strain (Babb 3 material)**

The range of maximum strains was less than 0.003, and was also less than the values reported by Tanner (2003). To investigate this apparent discrepancy,

the maximum strain values of this study and those of previous studies were investigated further, and are discussed immediately below.

### 2.3.5.3 Further Comments on Maximum Useful Strain

Table 2.8 summarizes for each lot of material, the mean maximum useful strain ( $\epsilon_{AAC \text{ max}}$ ) reported in this study and the values reported by Tanner (2003). Figure 2.22 is a graph of those maximum strain values as a function of tested compressive strength.

**Table 2.8: Summary of mean maximum useful strains obtained in this study and Tanner (2003)**

Shipment	Study	$f_{AAC}$ psi (MPa)	$\epsilon_{AAC \text{ max}}$
Babb 3	Cancino (2003)	0.34 (2.34)	0.0015
Contec 1	Tanner (2003)	0.75 (5.16)	0.0025
Contec 2	Tanner (2003)	0.95 (6.53)	0.0027
Babb 1	Tanner (2003)	1.10 (7.56)	0.0027
Hebel 2	Tanner (2003)	1.30 (8.94)	0.0030
Ytong 2	Tanner (2003)	0.63 (4.33)	0.0026
Babb 2	Tanner (2003)	0.48 (3.3)	0.0020

Figure 2.22 shows a clear tendency for the maximum useful strain of AAC to decrease with decreasing compressive strength. Results reported in this thesis for low-strength AAC are consistent with those reported previously by Tanner (2003).

In previous work by Tanner (2003), Varela (2003) and Argudo (2003), the value of  $\varepsilon_{AAC \text{ max}}$  was reported as a constant 0.003, independent of compressive strength. Though not used directly in design provisions,  $\varepsilon_{AAC \text{ max}}$  is indirectly related to vital behavioral characteristics such as nominal flexural capacity, and the available ductility and drift capacities used to establish appropriate values of  $R$  and  $C_d$ .

Because ( $\varepsilon_{AAC \text{ max}}$ ) is apparently lower for low-strength AAC, the behavior of structural elements of low-strength AAC must be carefully reviewed to ensure that previously developed expressions for nominal flexural capacity and ductility and drift capacity are applicable to low-strength AAC as well. Parenthetically, one would expect the nominal flexural capacity of AAC elements to be governed by the mechanical characteristics of the reinforcement in all practical cases, and therefore not sensitive to  $\varepsilon_{AAC \text{ max}}$ . One would also expect ductility and drift capacity to be directly verifiable from wall tests. In subsequent chapters of this thesis, those comparisons are made.

It is also necessary to examine the internal consistency of stress-strain data reported here for low-strength AAC, with that reported by Tanner (2003). That comparison is presented in Table 2.9, in terms of tested versus specified compressive strengths and observed versus predicted values of  $E_{AAC}$ . In that table, the relationship between observed and specified compressive strength for low-strength AAC is seen to be consistent with those for higher-strength AAC. Additionally, the relationship between observed  $E_{AAC}$  and that predicted by Equation 2.1 is seen to be consistent with that reported previously for higher-strength AAC.

$$E_{AAC} = 6500 f_{AAC}^{0.6} \quad \text{Equation 2.1}$$

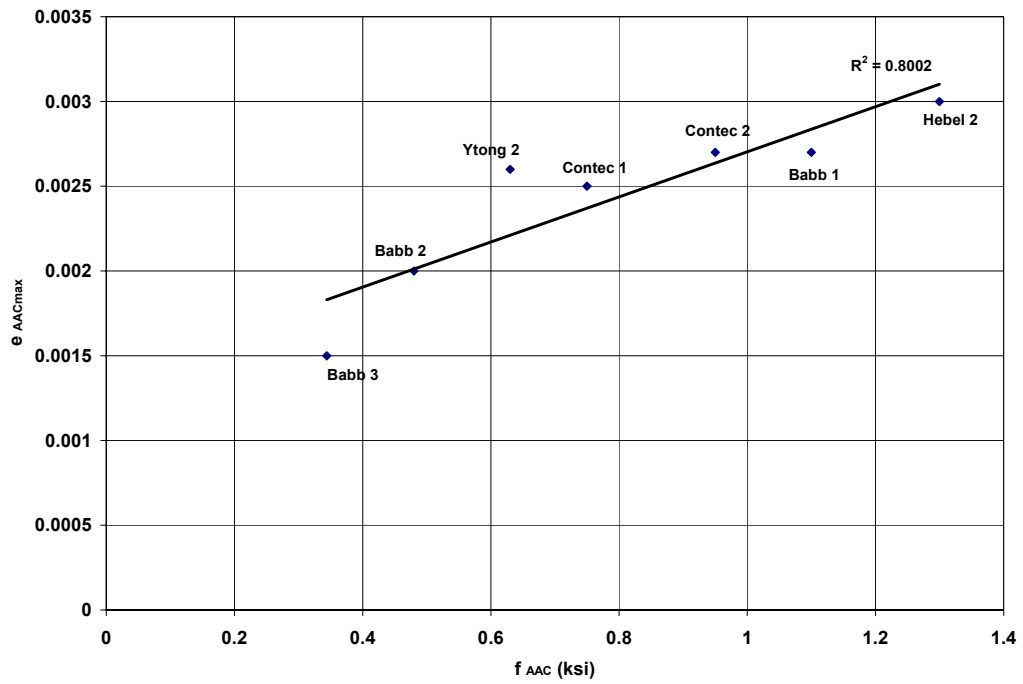


*Figure 2.22: Maximum useful strain versus compressive strength*

*Table 2.9: Material properties of this study versus those of Tanner (2003)*

Study	$f_{AAC}$ psi (MPa)	$f'_{AAC}$ psi (MPa)	$\frac{f_{AAC}}{f'_{AAC}}$	Observed $E_{AAC}$ ksi (GPa)	Predicted $E_{AAC}$ ksi (GPa)	Observed / Predicted $E_{AAC}$
This study	344 (2.39)	290 (2.0)	1.18	223 (1.50)	195 (1.31)	1.14
Tanner (2003)	715 (4.9)	580 (4.0)	1.23	296 (1.99)	295 (1.98)	1.00
Tanner (2003)	1170 (8.0)	870 (6.0)	1.34	466 (3.13)	377 (2.54)	1.23



### **2.3.6 Splitting Tensile Strength**

Shear Wall Specimens 18 and 19 were constructed using AAC material corresponding to Class PAAC2, which has a specified compressive strength of 2 MPa (290 psi). The tensile strength of the AAC material in those specimens was tested.

#### ***2.3.6.1 Specimen Preparation and Testing Procedure for Splitting Tensile Tests on AAC Masonry Units***

Units for the splitting tensile tests were prepared from the AAC material used to construct Shear Wall Specimens 18 and 19. This material had been shipped to UT from Babb International, Inc. (Adel, GA). In this thesis, it is designated as “Babb 3.”

Six units were prepared at UT for testing according to ASTM C1006. The measurements of these units were  $7\frac{13}{16}$  in. (198 mm) high by  $7\frac{13}{16}$  in. (198 mm) wide by 24 in. (610 mm) long.

After the units were prepared, their weight, density and moisture contents were measured. The moisture content of the units must be between 5 % and 15 % according to ASTM C1386. The moisture content (MC) was measured three times; at the time of the tensile test, at the end of the test, and five days after the end of the test. Table 2.10 shows the moisture content recorded from the units.

**Table 2.10: Measured moisture contents (Babb 3 material)**

Unit	Immediately before the Test			Immediately after the Test			5 days after the Test		
	Measured Density (pcf)	Dry Density (pcf)	MC (%)	Measured Density (pcf)	Dry Density (pcf)	MC (%)	Measured Density (pcf)	Dry Density (pcf)	MC (%)
<b>1</b>	33.64	30.09	11.80	33.62	30.09	11.73	31.71	30.09	5.38
<b>2</b>	32.87	30.09	9.24	32.85	30.09	9.17	31.59	30.09	4.99
<b>3</b>	33.57	30.09	11.57	33.53	30.09	11.43	31.90	30.09	6.02
<b>4</b>	32.58	30.09	8.28	32.51	30.09	8.04	31.14	30.09	3.49
<b>5</b>	32.58	30.09	8.28	32.56	30.09	8.21	30.72	30.09	2.09
<b>6</b>	33.29	30.09	10.63	33.29	30.09	10.63	31.61	30.09	5.05

The test was performed in a universal machine, where the masonry units were placed between two rods, one at the bottom face and the other at the top face. Data were recorded using the readings of the universal machine. Figure 2.23 shows the test setup used in the splitting tensile tests.

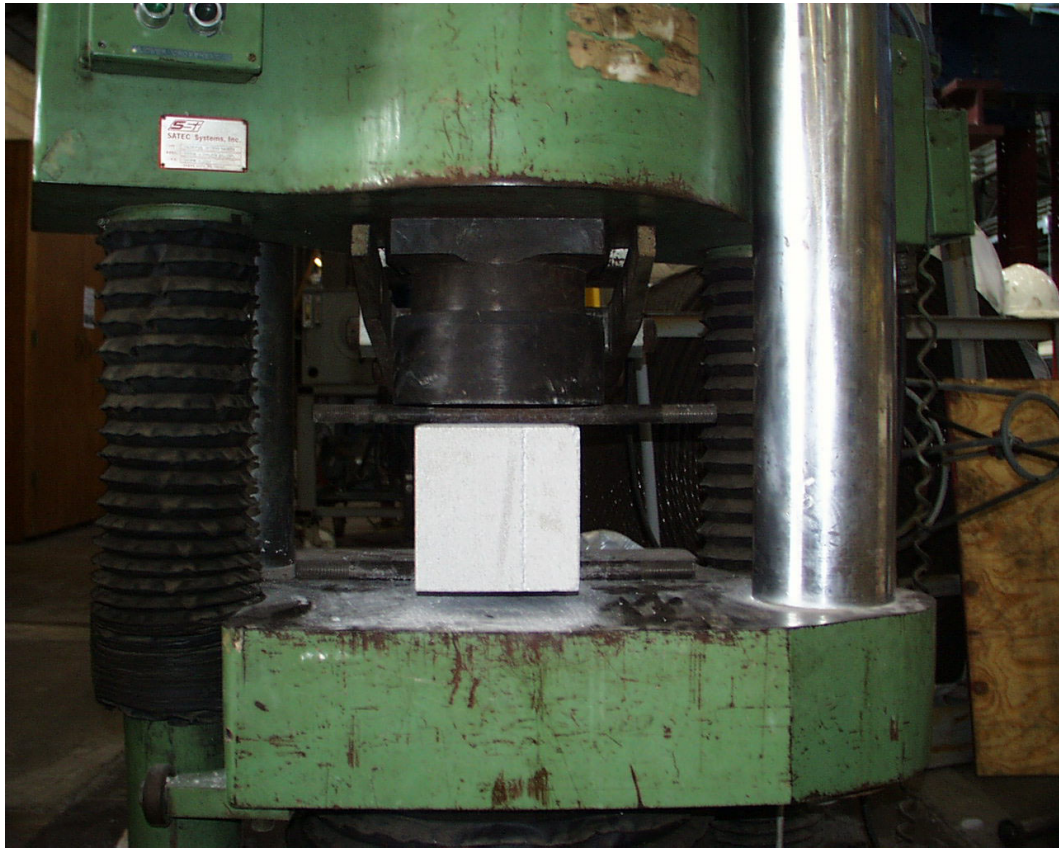


*Figure 2.23: Test setup to measure splitting tensile strength*

### ***2.3.6.2 Splitting Tensile Strength for AAC Units***

Splitting tensile strength for the six units, summarized in Table 2.11, ranged from 49.02 psi (0.34 MPa) to 58.41 psi (0.40 MPa), with a mean of 52.85 psi (0.37 MPa) and a COV of 6.99 %.

**Table 2.11: Results of splitting tensile strength tests performed at UT Austin**

Material	Unit	Moisture Content (%)	Load (Kips)	$f_t$ psi (MPa)	Average psi (MPa)	COV (%)	Average psi (MPa)	COV (%)
Babb 3	1	11.80	4.80	50.07 (0.35)	52.50 (0.36)	6.55	52.85 (0.37)	6.99
Babb 3	2	9.24	5.50	57.37 (0.40)				
Babb 3	3	11.57	4.80	50.07 (0.35)				
Babb 3	4	8.28	4.70	49.02 (0.34)	53.19 (0.37)	7.34		
Babb 3	5	8.28	5.60	58.41 (0.40)				
Babb 3	6	10.63	5.00	52.15 (0.36)				

The results obtained for the tensile strength ranged from 16 % and 21 % of the specified compressive strength of 290 psi (2 MPa), and from 14 % to 17 % of the mean tested compressive strength of 344 psi (2.37 MPa).

### **2.3.6.3 Comparison between observed and predicted splitting tensile strength of AAC**

Through tensile strength tests performed at the University of Texas at Austin and elsewhere, an equation (Equation 2.2) to predict the tensile strength of AAC has been proposed (Argudo 2003).

$$f_t = 2.4\sqrt{f'_{AAC}}$$

Equation 2.2

The predicted tensile strength obtained using a specified compressive strength of 290 psi (2 MPa) into Equation 2.2 was 40.87 psi (0.28 MPa). This value corresponds to the 77% of the average tensile value obtained from the tests which represents a conservative estimation of the real value. On the other hand, after the evaluation of Equation 2.2 with the average compressive strength of 344 psi (2.37 MPa) obtained from the test a tensile strength of 44.51 psi (0.31 MPa) was obtained which corresponds to 84.22 %, of the average tensile value. Figure 2.24 shows this last result (UT). Clearly, the relation between splitting tensile strength and tested compressive strength for low-strength AAC, is consistent with that obtained previously for higher-strength AAC.

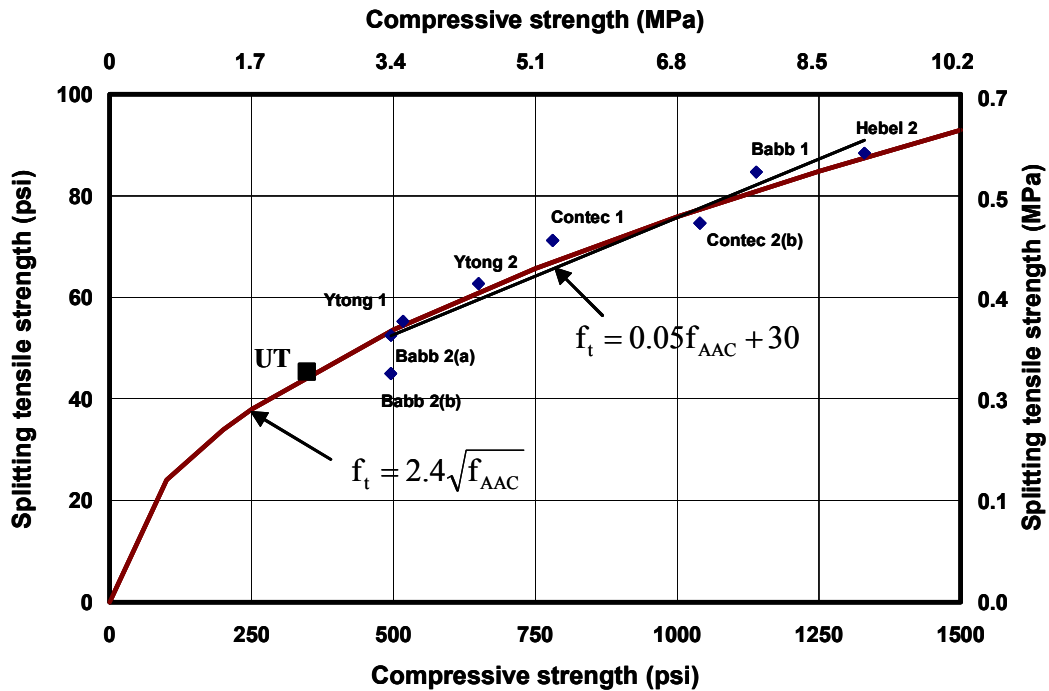
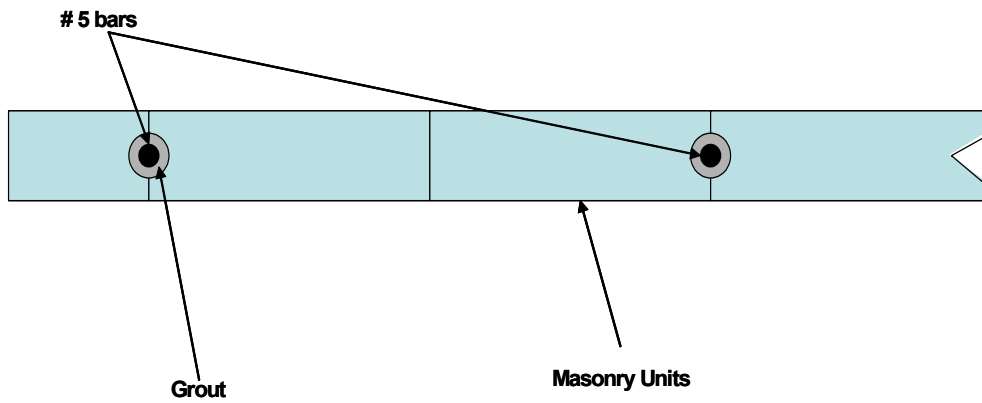


Figure 2.24: Splitting tensile strength versus tested compressive strength

### 2.3.7 Construction of Shear Wall Specimens 18 and 19

The surface of the base beam was roughened and pre-wetted. A leveling bed was applied, using conventional Portland cement-lime masonry mortar conforming to ASTM C270, Type S by proportion. The masonry units were set up in running bond and joined with thin-bed mortar. To prevent horizontal misalignment, a guide string was connected to two guide poles located at each end of the walls. The plumb was also checked every three courses during the construction. Figure 2.25 shows construction details of Shear Wall Specimen 19.



*Figure 2.25: Plan view showing typical details of construction of Shear Wall Specimen 19*

Figure 2.26 and Figure 2.27 show the views of Shear Wall Specimens 18 and 19 respectively, after construction.



*Figure 2.26: Side view of Shear Wall Specimen 18*





*Figure 2.27: Side view of Shear Wall Specimen 19*

## **CHAPTER 3**

### **Test Results for AAC Shear Wall Specimens**

#### **3.1 INTRODUCTION**

The objective of this chapter is to describe the results obtained from the flexure-dominated wall (SWS17) and the shear-dominated walls (SWS18 and SWS19). The results obtained for each specimen are accompanied by the objectives, loading history, description of the major events observed during the test, and hysteretic behavior of the walls. Design of each shear wall specimen comprised the following steps: selection of plan length, which, in combination with a constant specimen height, defined the specimen's aspect ratio; selection of the amount and distribution of flexural reinforcement, to encourage the desired behavior; prediction of each limit state, based on that aspect ratio and flexural reinforcement, using interaction diagrams of base shear capacity as a function of axial load; and iteration of aspect ratio, flexural reinforcement and axial load to produce a specimen with the intended behavior. When each specimen was tested, its observed capacity in relevant limit states was compared with the corresponding predicted capacity.

#### **3.2 TEST RESULTS FOR SHEAR WALL SPECIMEN 17**

The behavior of Shear Wall Specimen 17 is predicted using the interaction diagram of Figure 3.1. In that interaction diagram, relevant behavior modes of the specimen are represented, including flexural cracking, flexure-shear cracking, sliding shear, web-shear cracking, and nominal flexural capacity. The applied

axial load for Shear Wall Specimen 17 was selected as 25 kips (111.2 kN). At this axial load, the major events in order of occurrence were flexural cracking, flexure-shear cracking, and nominal flexural capacity. Web-shear cracking, sliding shear, and crushing of the diagonal strut are not expected to occur because the curves corresponding to them lie to the right of the curve representing nominal flexural capacity.

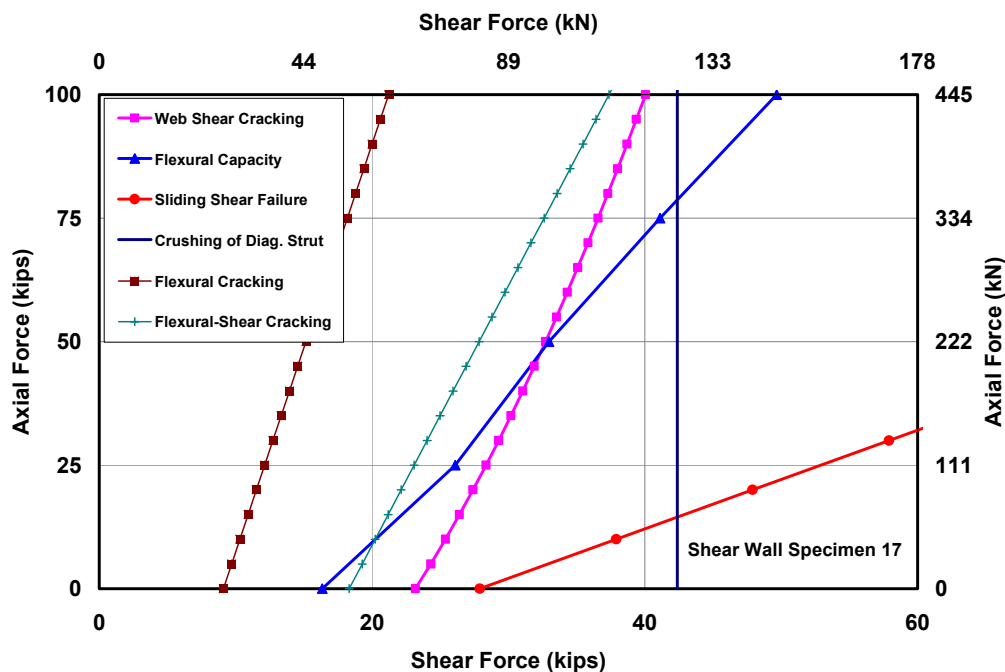


*Figure 3.1: Prediction of behavior for Shear Wall Specimen 17*

### 3.2.1 Loading History and Major Events for Shear Wall Specimen 17

The actual loading and displacement histories for Shear Wall Specimen 17 are presented in Figure 3.2 and Figure 3.3 respectively. The numbers on the graphs refer to load points (each point during the test when data were recorded). Positive values of the base shear force correspond to loading to the south, and

negative values, to loading to the north. Each cycle is subdivided into an “a” portion (positive displacements) followed by a “b” portion (negative displacements). For each cycle of loading, the maximum loads and drift ratios are shown in Table 3.1.

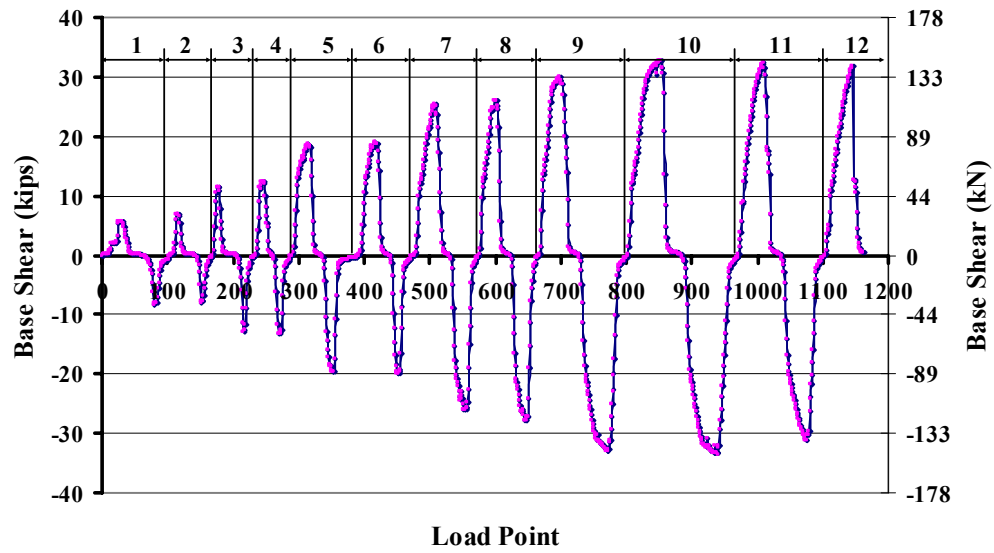


*Figure 3.2: Actual loading history for Shear Wall Specimen 17*

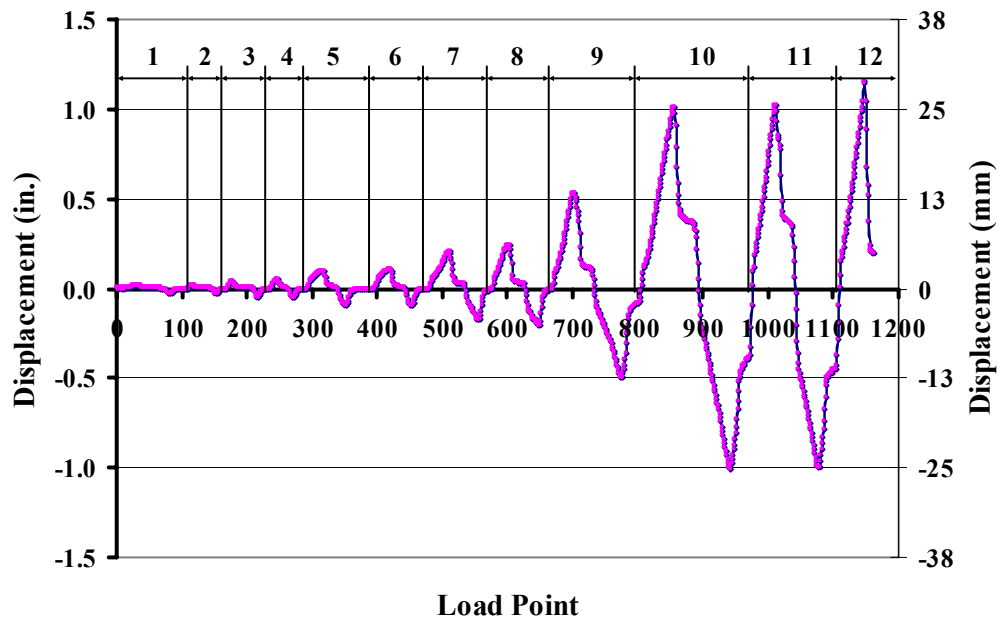


*Figure 3.3: Actual tip displacement history for Shear Wall Specimen 17*

**Table 3.1: Load Points, maximum load and drift ratios for each cycle for Shear Wall Specimen 17**

<b>Cycle</b>	<b>Load Points</b>	<b>Max. Applied Load (kips)</b>	<b>Max. Applied Load (kN)</b>	<b>Max. Drift Ratio (%)</b>	<b>Cycle</b>	<b>Load Points</b>	<b>Min. Applied Load (kips)</b>	<b>Min. Applied Load (kN)</b>	<b>Min. Drift Ratio (%)</b>
<b>1a</b>	1-60	5.71	25.42	0.010	<b>1b</b>	61-105	-8.29	-36.88	0.018
<b>2a</b>	106-141	6.95	30.92	0.012	<b>2b</b>	142-168	-7.92	-35.23	0.016
<b>3a</b>	169-204	11.41	50.80	0.027	<b>3b</b>	205-234	-13.01	-57.91	0.030
<b>4a</b>	235-259	12.32	54.83	0.030	<b>4b</b>	260-290	-13.25	-58.97	0.032
<b>5a</b>	291-334	18.56	82.57	0.062	<b>5b</b>	335-392	-19.70	-87.67	0.059
<b>6a</b>	393-437	18.87	83.95	0.067	<b>6b</b>	438-476	-19.88	-88.45	0.060
<b>7a</b>	477-530	25.31	112.63	0.134	<b>7b</b>	531-575	-24.34	-108.30	0.111
<b>8a</b>	576-622	26.03	115.83	0.156	<b>8b</b>	623-667	-27.86	-123.97	0.131
<b>9a</b>	668-727	30.01	133.53	0.344	<b>9b</b>	728-802	-32.99	-146.82	0.326
<b>10a</b>	803-884	32.73	145.63	0.653	<b>10b</b>	885-971	-33.46	-148.89	0.657
<b>11a</b>	972-1035	32.47	144.50	0.661	<b>11b</b>	1036-1103	-31.31	-139.33	0.649
<b>12a</b>	1104-1162	31.77	141.40	0.748					

### **3.2.2 Sequence of Crack Formation for Shear Wall Specimen 17**

The behavior of Shear Wall Specimen 17 is described through major events observed during the test. These major events refer to significant changes in the condition of the specimen. In Table 3.2, each major event is matched with its respective load point and the corresponding changes in the specimen. In the remainder of this section, each major event is discussed further.

**Table 3.2: Description of major events for Shear Wall Specimen 17**

<b>Major Event</b>	<b>Load Point</b>	<b>Physical Description</b>
1	176	Flexural cracking, loading south
2	348	Flexural cracking, loading north
3	306	Propagation of flexural cracks, loading south
4	351	Propagation of flexural cracks, loading north
5	508	Flexure-shear crack, loading south
6	547	Flexure-shear crack, loading north
7	600-699	Propagation and additional flexure-shear cracks, loading south
8	645-772	Propagation and additional flexure-shear cracks, loading north
9	845, 854	Vertical crack formed between panels, loading south
10	935	Vertical crack formed between panel and U-block, loading north
11	940	Propagation of flexure-shear cracks, loading north
12	978	Propagation of flexure-shear cracks, loading south
13	1121	Crushing at north toe and fracture of the flexural reinforcement at north end

### **3.2.2.1 Flexural Cracking in Shear Wall Specimen 17**

According to Table 3.2, Major Events 1 and 2 correspond to flexural cracking at the north end and the south ends of the specimen respectively. At the north end of the specimen (loading to the south), flexural cracking occurred at a load of 11.41 kips (50.8 kN) and a drift ratio of 0.026 % (Load Point 176). At the south end of the specimen (loading to the north) flexural cracking occurred at a load of 18.81 kips (83.72 kN) and a drift ratio of 0.053 % (Load Point 348). Flexural cracking was predicted at a base shear of 12.1 kips (53.82 kN). The

ratios of observed to predicted cracking strength were 0.94 (loading to the south) and 1.55 (loading to the north).

As the test progressed, these flexural cracks propagated toward the center of the specimen from both ends. These observations correspond to Major Events 3 and 4, which were recorded at Load Point 306 (loading to the south) and Load Point 351 (loading to the north). This cracking pattern is shown in Figure 3.4.

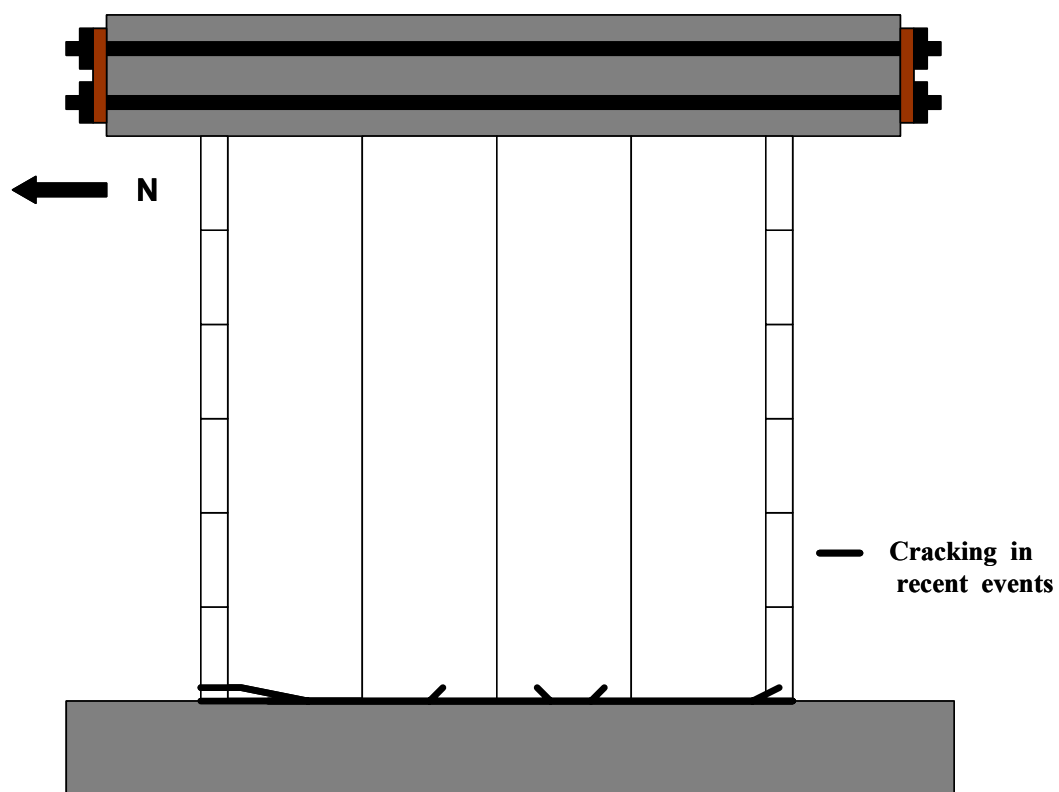


*Figure 3.4: Formation of flexural cracking in Shear Wall Specimen 17*

### *3.2.2.2 Flexure-shear cracking in Shear Wall Specimen 17*

Major Events 5 and 6 denote the formation of flexure-shear cracks while loading south and north respectively. At the north end (loading to the south), these



cracks formed at a base shear of 25.31 kips (112.63 kN) and a drift ratio of 0.13 % (Load Point 508). This flexure-shear crack formed at the first and second U-blocks at the bottom of Shear Wall Specimen 17, and continued to the middle of the first panel at the north end of the specimen. These cracks are shown in detail in Figure 3.5.

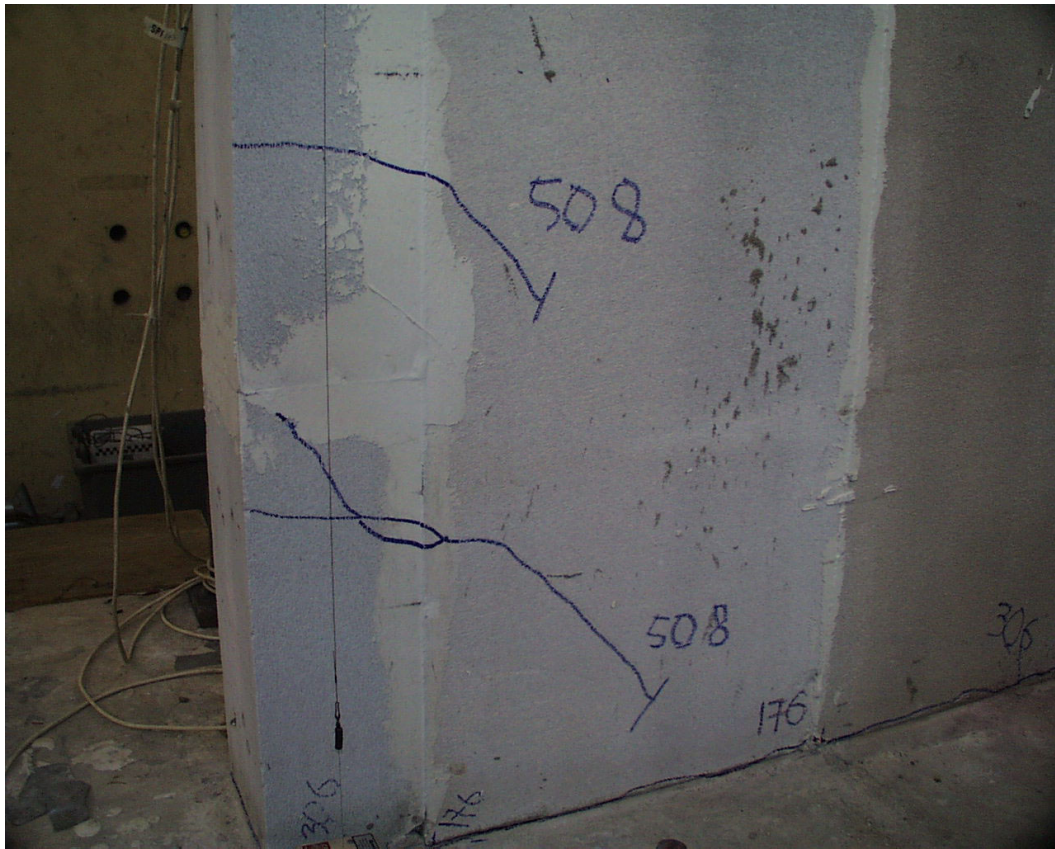


***Figure 3.5: Flexure-shear cracks at north end of Shear Wall Specimen 17***

At the south end (loading to the north), these cracks formed at a base shear of 24.34 kips (108.30 kN) and a drift ratio of 0.082 % (Load Point 547). Flexural-shear cracking was predicted at a base shear of 23.09 kips (102.70 kN). The ratios of observed to predicted flexure-shear cracking strength were 1.09 (loading to the south) and 1.05 (loading to the north).

Yielding of the flexural reinforcement was observed at a base shear of 25.0 kips (111.2 kN) (loading to the south). This observation corresponds to Major Event 7.

As the test progressed, existing flexure-shear cracks propagated at both ends of the specimen. Additional flexure-shear cracks formed at approximately 12 in. (0.30m) and 24 in. (0.61m) from the bottom of the wall as the applied load increased to 26.03 kips (115.83 kN) loading to the south, and to 27.86 kips (123.97 kN) loading to the north. These observations also correspond to Major Event 7 (Load Point 600) and Major Event 8 (Load Point 645). This cracking pattern is shown in Figure 3.6.

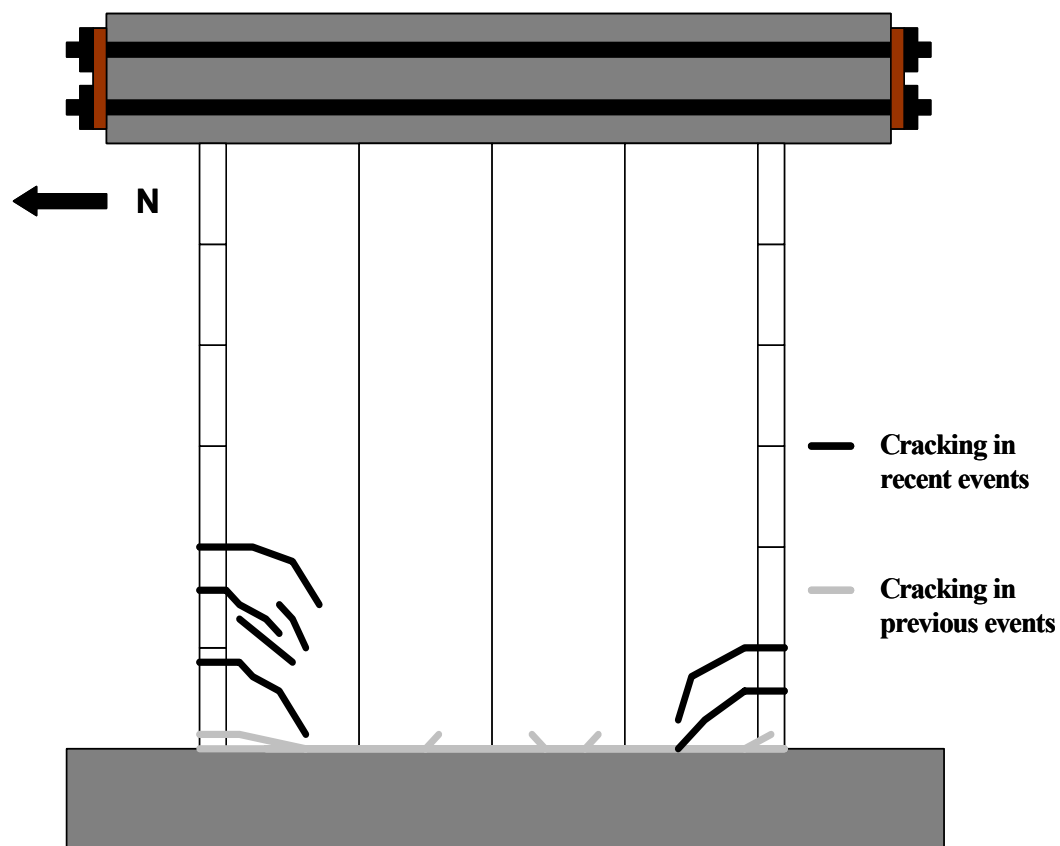


*Figure 3.6: Formation of flexure-shear cracks in Shear Wall Specimen 17*

### ***3.2.2.3 Additional Cracking in Shear Wall Specimen 17***

Major Events 9 and 10 correspond to the formation of additional flexure-shear cracks and the development of vertical cracks in Shear Wall Specimen 17. At the north end, additional flexure-shear cracks formed at Load Point 845, which corresponded to a base shear of 32.11 kips (142.89 kN). These cracks were located approximately 5 ft. (1.52m) from the base of the specimen, and propagated from its north extreme fiber to the middle of the first panel. At Load Point 935, similar crack propagation occurred at the south end, at a base shear of 33.28 kips (148.12 kN). Vertical cracks formed between the first and second vertical panels at the north end of the specimen and between the fourth vertical panel and the U-block at the south end of the specimen, approximately 6 ft. (1.83m) from the bottom of the wall.

Major Events 11 and 12 correspond to propagation of previously formed flexure-shear cracks. These observations correspond to Load Point 940 and Load Point 978, loading to the north and south respectively. Figure 3.7 shows the pattern of cracks at this stage of the test.

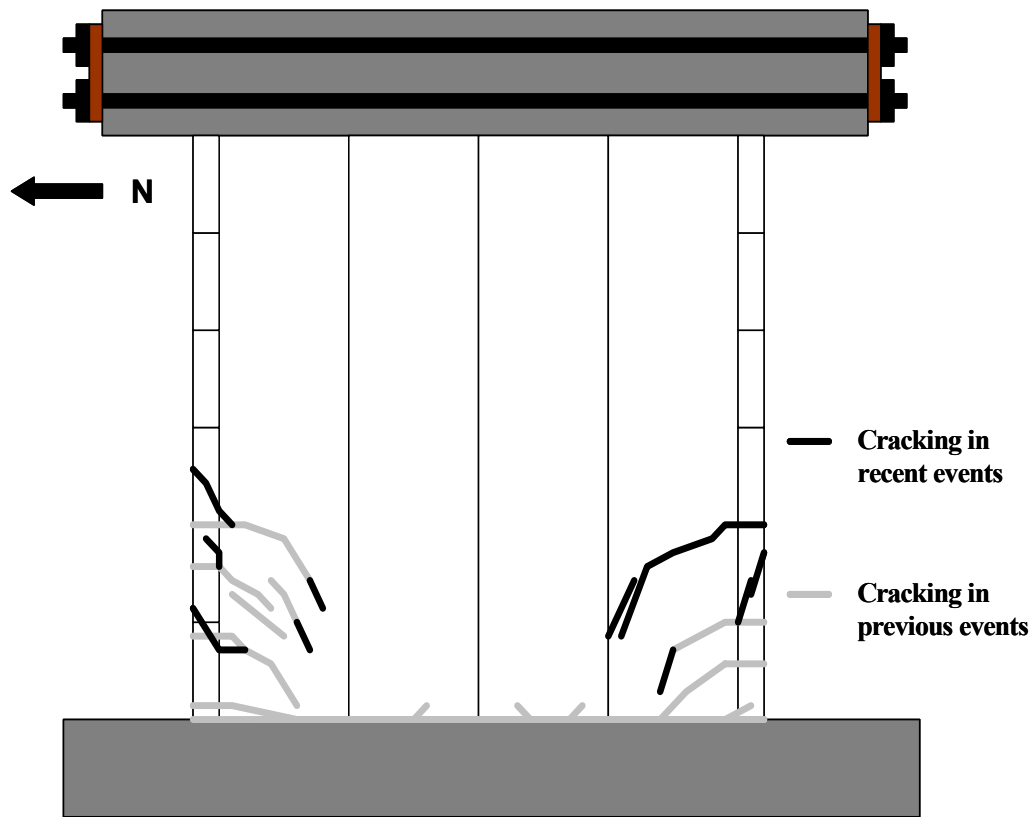


*Figure 3.7: Formation of additional flexure-shear cracks, and propagation of cracks from previous events*

#### **3.2.2.4 Final damage in Shear Wall Specimen 17**

The final stage of testing of Shear Wall Specimen 17 was Major Event 13, which denoted progressive damage at both ends of the specimen, as the previously formed flexure-shear cracks propagated toward the center and the mid-height of the wall. At Load Point 1121, which corresponded to a base shear of 17.81 kips (79.25 kN), toe spalling and crushing started at the north end. This damage, along with yield of the flexural reinforcement, resulted in a gradual and continuous drop in the in-plane lateral stiffness of the specimen. Capacity was limited by fracture of flexural reinforcement at the north end of the specimen

(while loading to the south), and was later confirmed as brittle fracture by the absence of necking of the affected bar.

Figure 3.8 shows the damage in Shear Wall Specimen 17 at the end of the test. The significant spalling at the bottom of the north end of the specimen during the final increments of load is shown in Figure 3.9 and Figure 3.10.

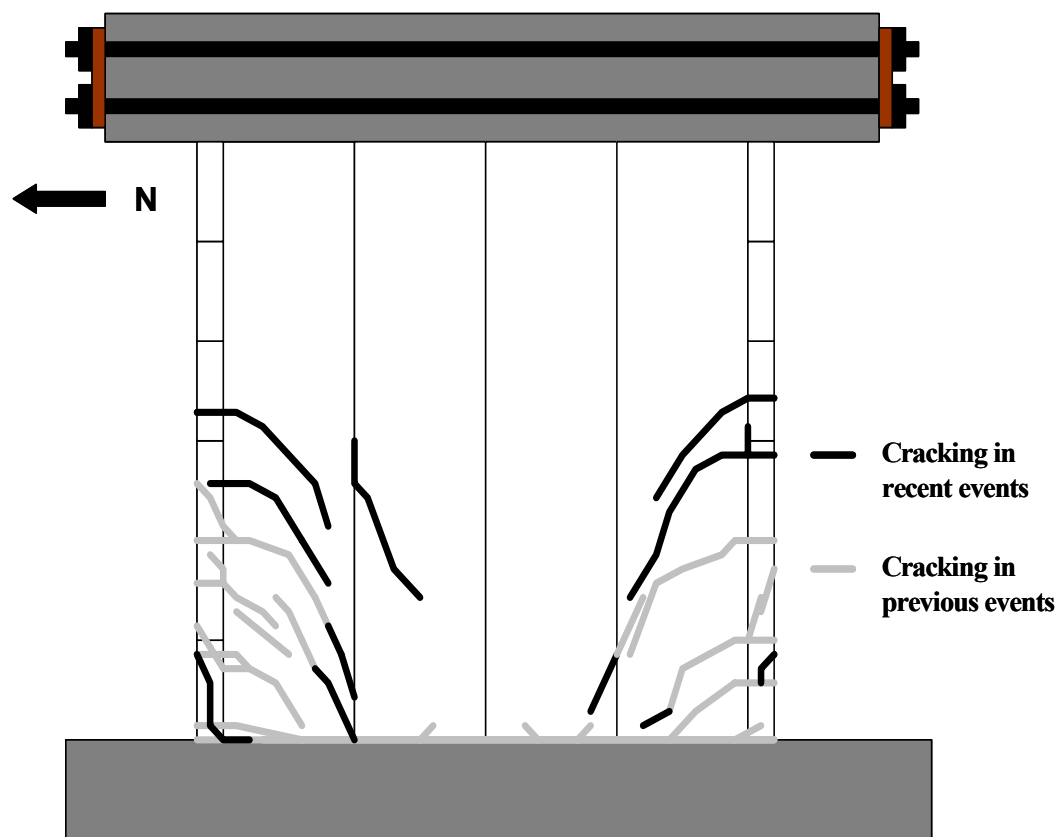


*Figure 3.8: Cracking in Shear Wall Specimen 17 at end of test*



*Figure 3.9: Spalling at the north end of Shear Wall Specimen 17*





*Figure 3.10: Toe crushing north at north end of Shear Wall Specimen 17*

### **3.2.3 Load-Displacement Behavior of Shear Wall Specimen 17**

The overall hysteretic behavior of Shear Wall Specimen 17 is shown in Figure 3.11. The initial stiffness of the load-displacement curve was 111 kip/in. (16 kN/mm). Flexural reinforcement yielded at a base shear of 25 kips (111.2 kN) and a corresponding displacement of 0.18 in. (0.45 mm). The test was stopped at a tip displacement of 1 in. (25 mm) because the flexural reinforcement fractured at the north end of the specimen.

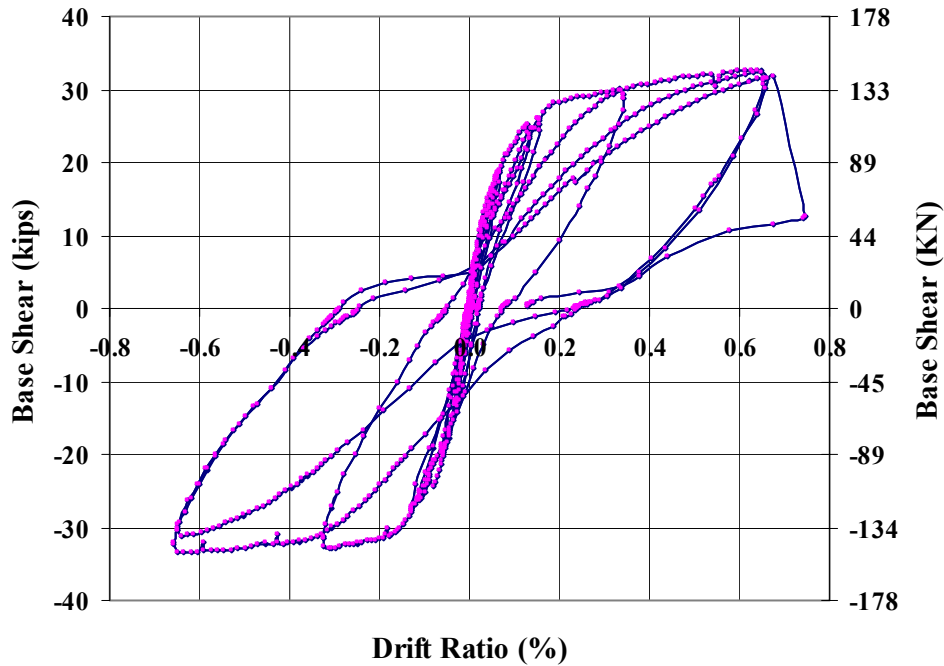


*Figure 3.11: Overall hysteretic behavior of Shear Wall Specimen 17*

### 3.3 TEST RESULTS FOR SHEAR WALL SPECIMEN 18

The behavior of Shear Wall Specimen 18 is predicted using the interaction diagram of Figure 3.12. In that interaction diagram, relevant behavior modes of the specimen are represented, including flexural cracking, sliding shear, web-shear cracking, crushing of the diagonal strut and nominal flexural capacity. The applied axial load for Shear Wall Specimen 18 was selected as 45 kips (200.5 kN). At this axial load, the major events in order of occurrence were flexural cracking, web-shear cracking, crushing of diagonal strut, sliding shear failure, flexure-shear cracking and yielding of flexural reinforcement. Sliding shear cracking, flexure-shear cracking and yielding of flexural reinforcement were not



expected to occur, because the curves corresponding to them lie to the right of the curve representing web-shear cracking failure.

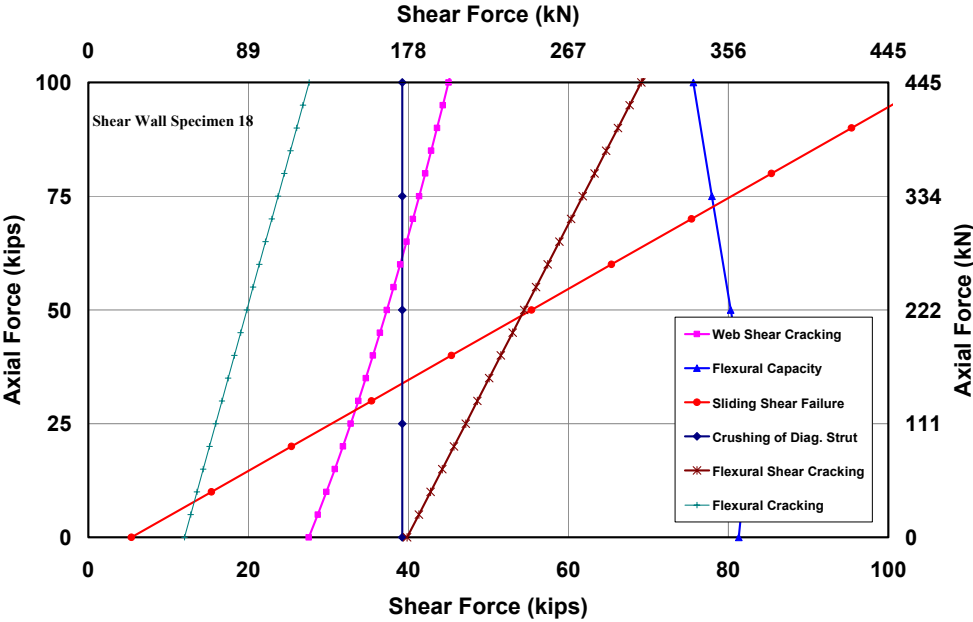


*Figure 3.12: Prediction of behavior for Shear Wall Specimen 18*

**3.3.1 Loading History and Major Events for Shear Wall Specimen 18**

The actual loading and displacement histories for Shear Wall Specimen 18 are presented in Figure 3.13 and Figure 3.14 respectively. The numbers on the graphs refer to load points (each point during the test when data were recorded). Positive values of the base shear force correspond to loading to the south, and negative values, to loading to the north. Each cycle is subdivided into an “a” portion (positive displacements) followed by a “b” portion (negative displacements). The procedure of loading the specimen was started by loading toward the south. For each cycle of loading, the maximum loads and drift ratios are shown in Table 3.3.

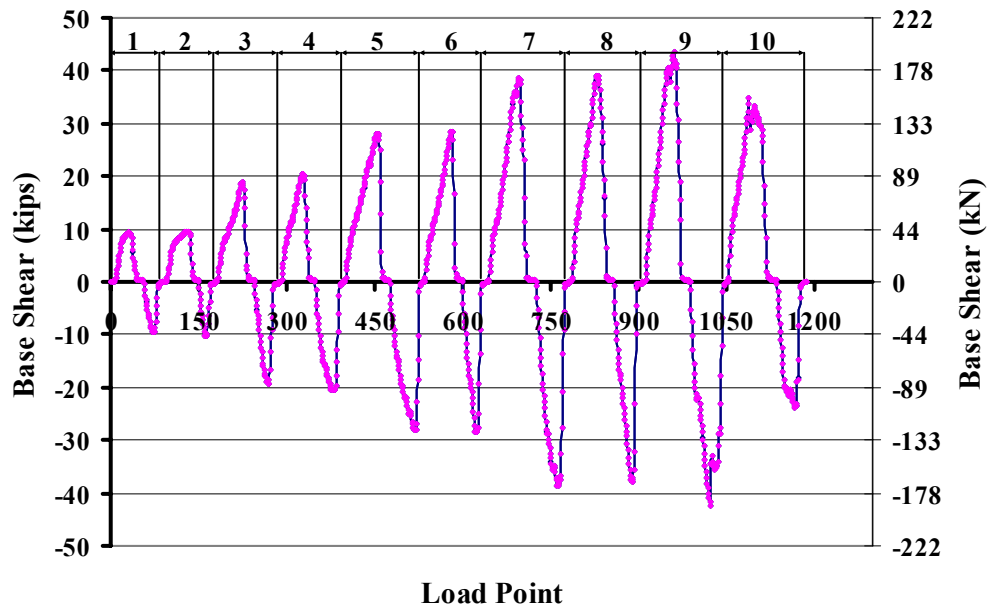


*Figure 3.13: Actual loading history for Shear Wall Specimen 18*

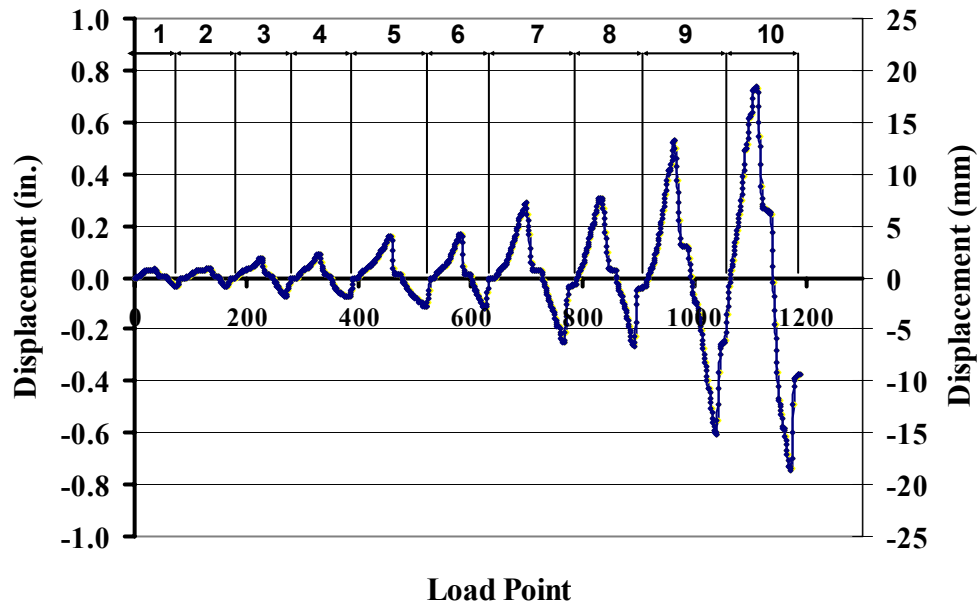


*Figure 3.14: Actual tip displacement history for Shear Wall Specimen 18*

**Table 3.3: Load Points, maximum load drift ratios for each cycle for Shear  
Wall Specimen 18**

<b>Cycle</b>	<b>Load Points</b>	<b>Max. Applied Load (kips)</b>	<b>Max. Applied Load (kN)</b>	<b>Max. Drift Ratio (%)</b>	<b>Cycle</b>	<b>Load Points</b>	<b>Min. Applied Load (kips)</b>	<b>Min. Applied Load (kN)</b>	<b>Min. Drift Ratio (%)</b>
<b>1a</b>	1-56	9.30	41.38	0.020	<b>1b</b>	57-92	-9.45	-42.03	0.022
<b>2a</b>	93-149	9.53	42.43	0.020	<b>2b</b>	150-180	-10.16	-45.19	0.023
<b>3a</b>	181-245	18.77	83.51	0.048	<b>3b</b>	246-290	-19.31	-85.93	0.045
<b>4a</b>	291-348	20.31	90.39	0.056	<b>4b</b>	349-398	-20.36	-90.60	0.048
<b>5a</b>	399-475	27.87	124.04	0.102	<b>5b</b>	476-534	-28.09	-124.98	0.074
<b>6a</b>	535-599	28.32	126.02	0.107	<b>6b</b>	600-644	-28.29	-125.90	0.075
<b>7a</b>	645-726	38.59	171.71	0.186	<b>7b</b>	727-785	-38.63	-171.92	0.162
<b>8a</b>	786-858	39.01	173.62	0.200	<b>8b</b>	859-911	-37.99	-169.04	0.171
<b>9a</b>	912-987	43.61	194.06	0.343	<b>9b</b>	988-1052	-42.46	-188.96	0.392
<b>10a</b>	1053-1136	33.17	147.59	0.477	<b>10b</b>	1137-1188	-23.81	-105.97	0.482

### **3.3.2 Sequence of Crack Formation for Shear Wall Specimen 18**

The behavior of Shear Wall Specimen 18 is described through major events observed during the test. These major events refer to significant changes in the condition of the specimen. Each major event is matched with its respective load point and the corresponding changes in the specimen, in Table 3.4. In the remainder of this section, each major event is discussed further.

**Table 3.4: Description of major events for Shear Wall Specimen 18**

<b>Major Event</b>	<b>Load Point</b>	<b>Physical Description</b>
<b>1</b>	441	Flexural cracking, loading south
<b>2</b>	509	Flexural cracking, loading north
<b>3</b>	456	Propagation of flexural cracks, loading south
<b>4</b>	517	Propagation of flexural cracks, loading north
<b>5</b>	689	Web-shear cracking, loading south
<b>6</b>	754, 763	Web-shear cracking, loading north
<b>7</b>	696, 829	Additional Web-shear cracking, loading south
<b>8</b>	763, 889	Additional Web-shear cracking, loading north
<b>9</b>	952, 961	Diagonal cracks formed, loading south
<b>10</b>	1001, 1023	Diagonal cracks formed, loading north
<b>11</b>	1034	Additional diagonal cracks formed with toe crushing, loading north
<b>12</b>	1089, 1103	Additional diagonal cracks formed with toe crushing, loading south

### **3.3.2.1 Flexural cracking in Shear Wall Specimen 18**

According to Table 3.4, Major Events 1 and 2 correspond to flexural cracking at the north and south ends of the specimen respectively. At the north end of the specimen (loading to the south), flexural cracking occurred at a load of 22.63 kips (100.69 kN) and a drift ratio of 0.068 % (Load Point 441). At the south end of the specimen (loading to the north) flexural cracking occurred at a load of 24.99 kips (111.23 kN) and a drift ratio of 0.062 % (Load Point 509). Flexural cracking was predicted at a base shear of 19.0 kips (84.51 kN). The ratios of observed to predicted cracking strength were 1.19 (loading to the south) and 1.32 (loading to the north).

As the test progressed, these flexural cracks propagated toward the center of the specimen from both ends. These observations correspond to Major Events 3 and 4, which were recorded at Load Point 456 (loading to the south) and Load Point 517 (loading to the north). This cracking pattern is shown in Figure 3.15.

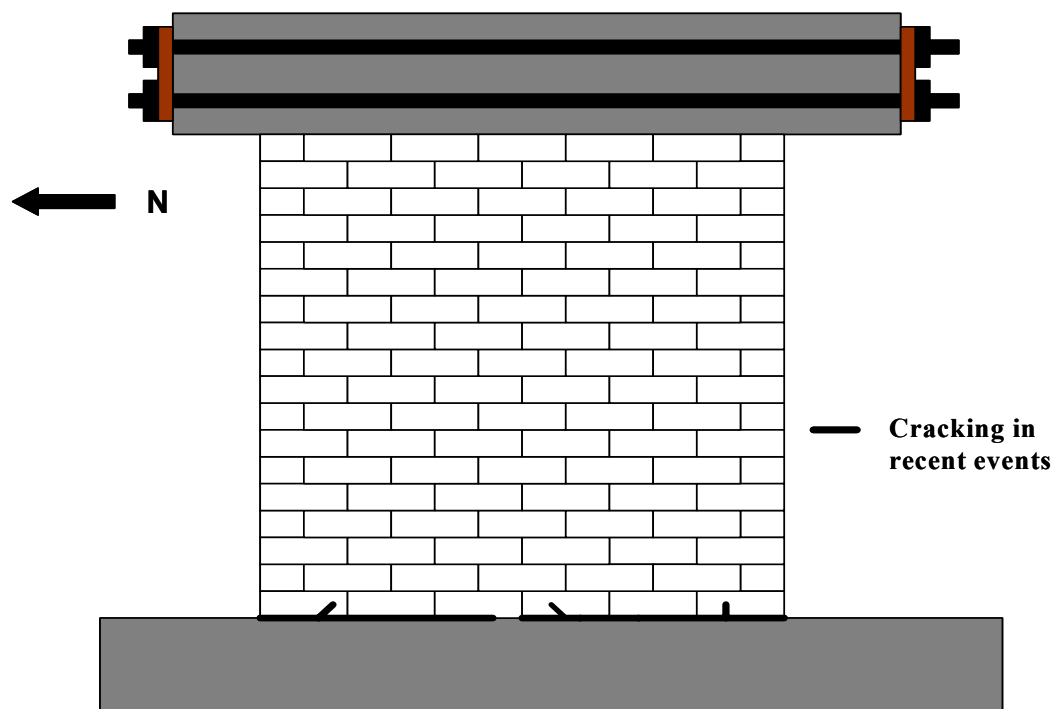


*Figure 3.15: Formation of flexural cracking in Shear Wall Specimen 18*

### **3.3.2.2 Web-shear cracking in Shear Wall Specimen 18**

Major Events 5 and 6 denote the formation of web-shear cracking while loading south and north respectively. At the north end (loading to the south), these cracks formed at a base shear of 36.07 kips (160.50 kN) and a drift ratio of 0.16 % (Load Point 689). This web-shear crack formed at the third and fifth course of blocks approximately 24 in. (0.61 m) and 40 in. (1.02 m) from the bottom of Shear Wall Specimen 18. These cracks are shown in detail in Figure 3.16.

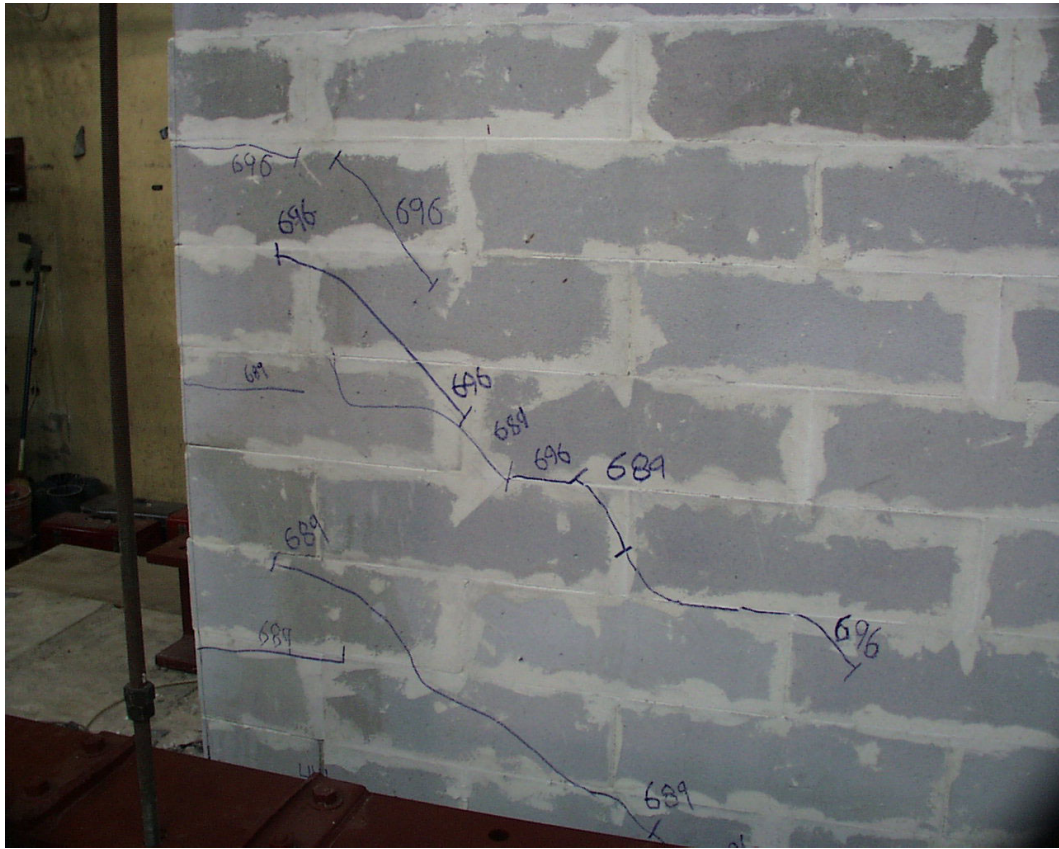


**Figure 3.16: Web-shear cracking at north end of Shear Wall Specimen 18**

At the south end (loading to the north), these cracks formed at a base shear of 35.66 kips (158.70 kN) and a drift ratio of 0.120 % (Load Point 754). Web-shear cracking was predicted at a base shear of 37.0 kips (164.58 kN). The ratios of observed to predicted web-shear cracking strength were 0.97 (loading to the south) and 0.96 (loading to the north).

As the test progressed, existing web-shear cracks propagated at both ends of the specimen. Additional web-shear cracks formed in the fifth course of units, approximately 40 in. (1.02 m) from the bottom of the wall as the applied load increased to 38.59 kips (171.71 kN), loading to the south and 38.63 kips (171.92

kN), loading to the north. These observations correspond to Major Event 7 (Load Point 696) and Major Event 8 (Load Point 763). The corresponding cracking pattern is shown in Figure 3.17.

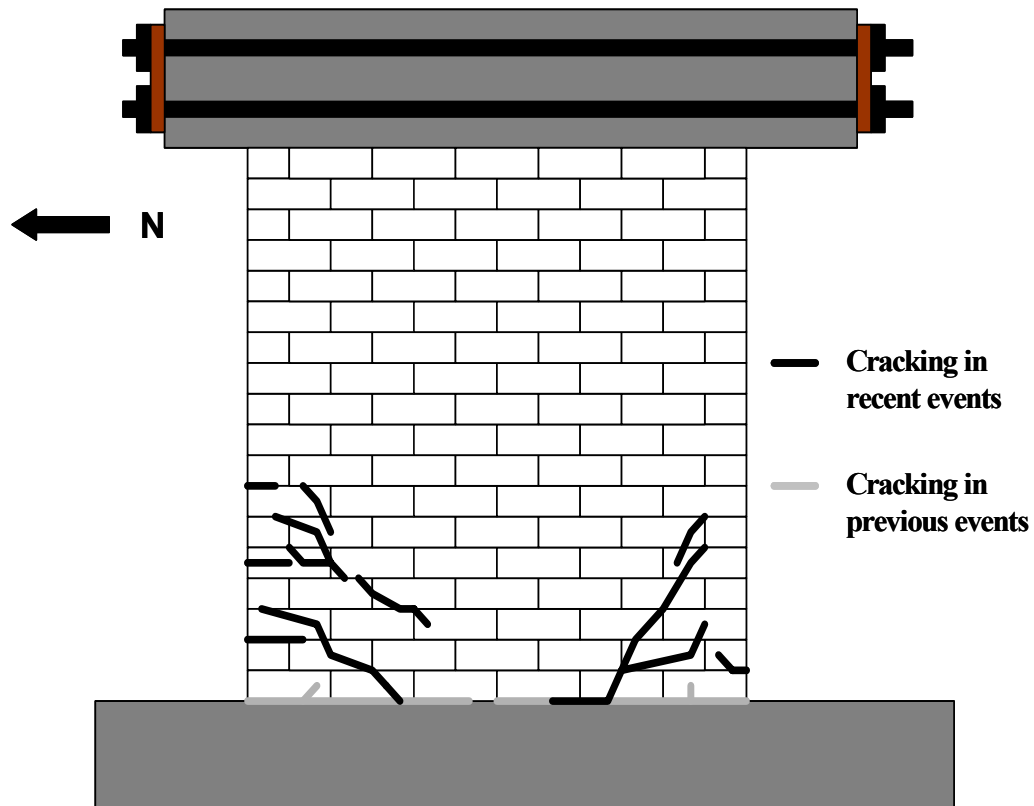


*Figure 3.17: Web-shear cracking in Shear Wall Specimen 18*

### *3.3.2.3 Propagation and Additional Web-shear cracking in Shear Wall Specimen 18*

Major Events 9 and 10 correspond to the propagation of existing web-shear cracks and the development of new web-shear cracks in Shear Wall Specimen 18. At the north end, additional web-shear cracks formed at Load Point 952 which corresponded to a base shear force of 40.69 kips (181.07 kN). These cracks were located along the height of the wall and spread from the north end of



the wall toward the center of it. At Load Point 1023, similar cracks occurred at the south end, at a base shear of 42.46 kips (188.96 kN). Diagonal cracks formed close to the south end of the wall. At this stage of the test, the north end of the specimen showed a major level of damage, with a large amount of cracking developing toward the center of the wall. This cracking pattern showed that the specimen was close to toe crushing. The cracking pattern associated with Major Events 9 and 10 is shown in Figure 3.18.

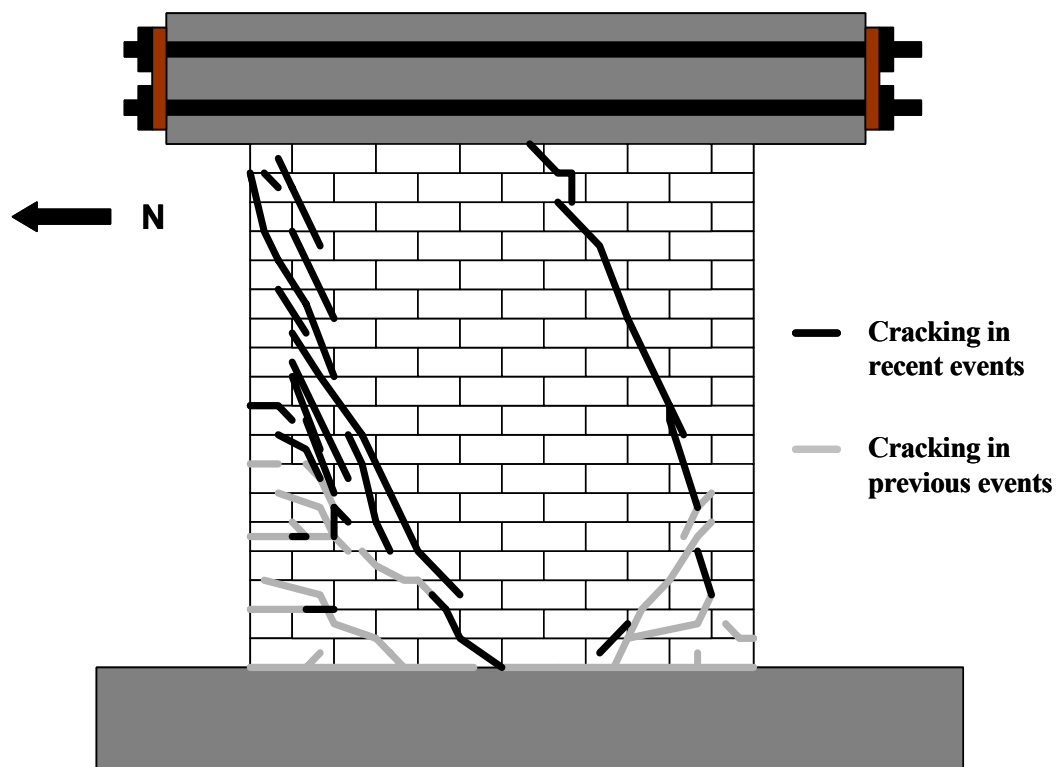


***Figure 3.18: Propagation and formation of additional web-shear cracks in Shear Wall Specimen 18***

#### ***3.3.2.4 Final damage in Shear Wall Specimen 18***

Major Events 11 and 12 denoted the final stage in the test of Shear Wall Specimen 18, and were associated with progressive damage at both ends of the

specimen. This damage consisted of the propagation and formation of additional web-shear cracks extended through the units and the mortar joints. At Load Point 1034, corresponding to a base shear of 35.03 kips (155.87 kN), toe crushing was observed at the south end of the specimen. An analogous situation occurred at the north end at Load Point 1089, which corresponded to a base shear of 34.73 kips (154.54 kN). At this stage, the specimen showed toe crushing at both ends, and significant reductions in in-plane stiffness (about 21 % of the initial stiffness) and shear capacity. This observation is based on the reduction in slope showed by the hysteretic curve. The test was ended in Loading Cycle 10, at a maximum base shear of 31.82 kips (141.59 kN).

Figure 3.19 shows the damage in Shear Wall Specimen 18 at the end of the test. The significant extent and width of web-shear cracks are shown in Figure 3.20 and Figure 3.21.

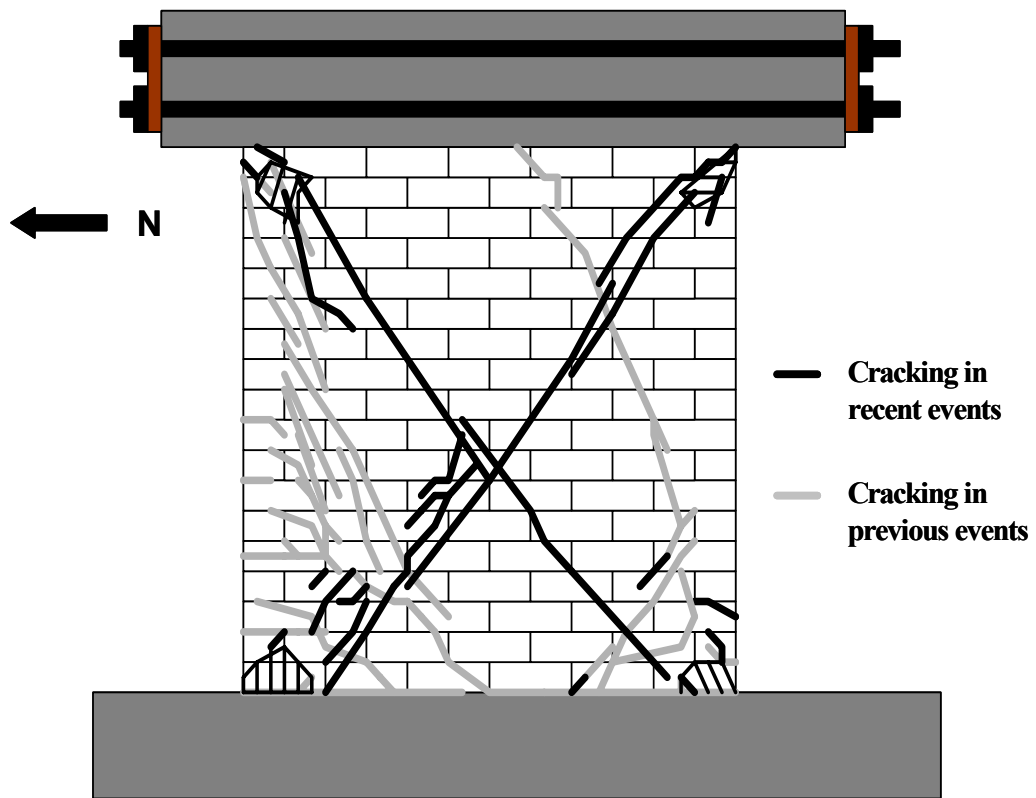


*Figure 3.19: Additional web-shear cracking and toe crushing in Shear Wall Specimen 18*



**Figure 3.20: Web-shear cracks in Shear Wall Specimen 18**

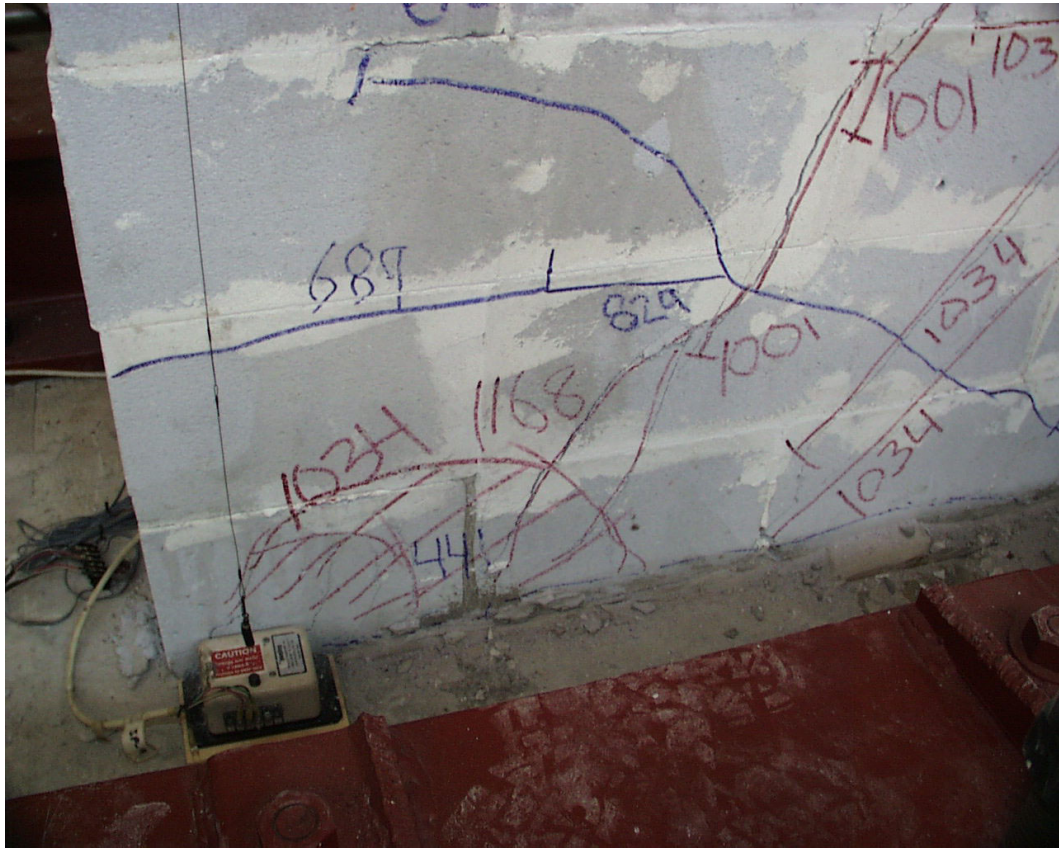


*Figure 3.21: Toe crushing at the north end of Shear Wall Specimen 18*

### **3.3.3 Load-Displacement Behavior for Shear Wall Specimen 18**

The overall hysteretic behavior of Shear Wall Specimen 18 is shown in Figure 3.22. The maximum drift ratio for this specimen was about 0.48 % in both directions. The test was stopped at in-plane displacements of 0.73 in. (18.54 mm).

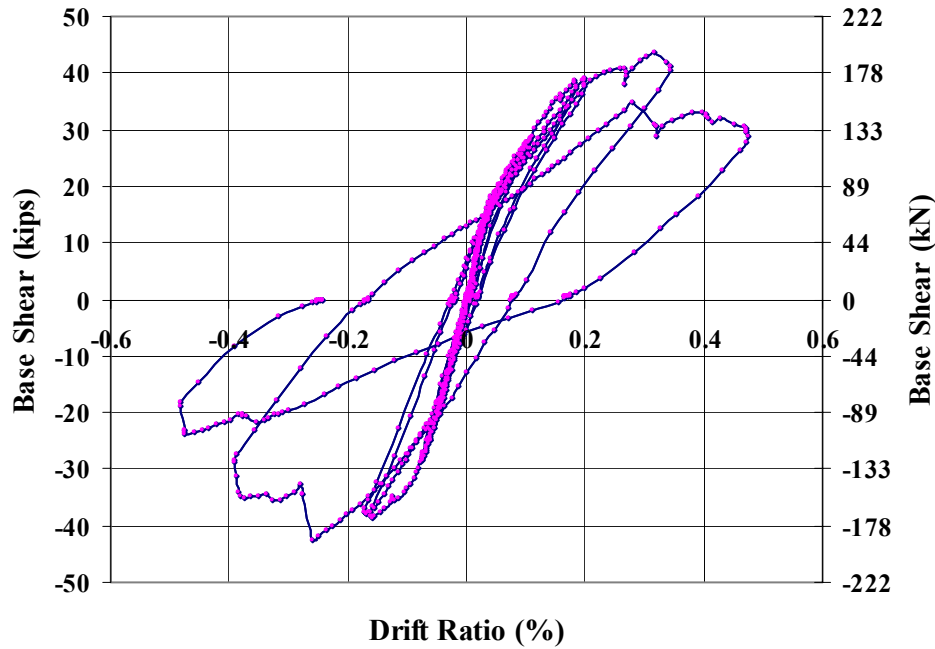


*Figure 3.22: Overall hysteretic behavior of Shear Wall Specimen 18*

### 3.4 SHEAR WALL SPECIMEN 19

The behavior of Shear Wall Specimen 19 was predicted using the interaction diagram of Figure 3.23. In that interaction diagram, relevant behavior modes of the specimen are represented, including flexural cracking, sliding shear, web-shear cracking, crushing of the diagonal strut and nominal flexural capacity. The applied axial load for Shear Wall Specimen 19 was selected as 58 kips (258.0 kN). At this axial load, the major events in order of occurrence were flexural cracking, web-shear cracking, crushing of diagonal strut, sliding shear failure, and yielding of flexural reinforcement. Sliding shear cracking and yielding of flexural reinforcement are not expected to occur because the curves corresponding to them lie to the right of the curve representing web-shear cracking failure.

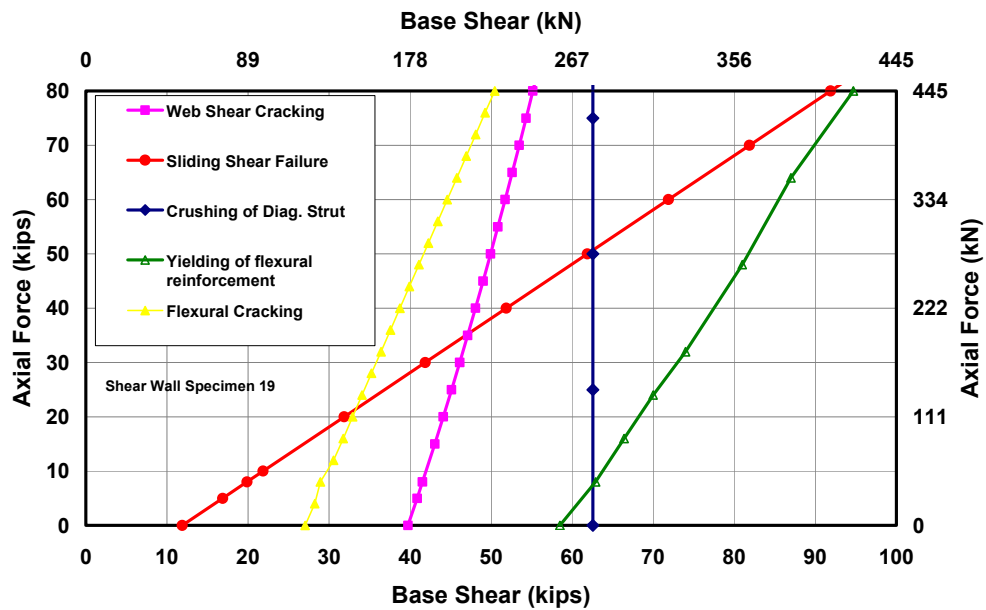


*Figure 3.23: Prediction of behavior for Shear Wall Specimen 19*

### 3.4.1 Loading History and Major Events for Shear Wall Specimen 19

The actual loading and displacement histories for Shear Wall Specimen 19 are presented in Figure 3.24 and Figure 3.25 respectively. The numbers on the graphs refer to load points (each point during the test when data were recorded). Positive values of the base shear force correspond to loading to the south, and negative values, to loading to the north. Each cycle is subdivided into an “a” portion (positive displacements) followed by a “b” portion (negative displacements). The procedure of loading the specimen was started by loading toward the south. For each cycle of loading, the maximum loads and drift ratios are shown in Table 3.5.

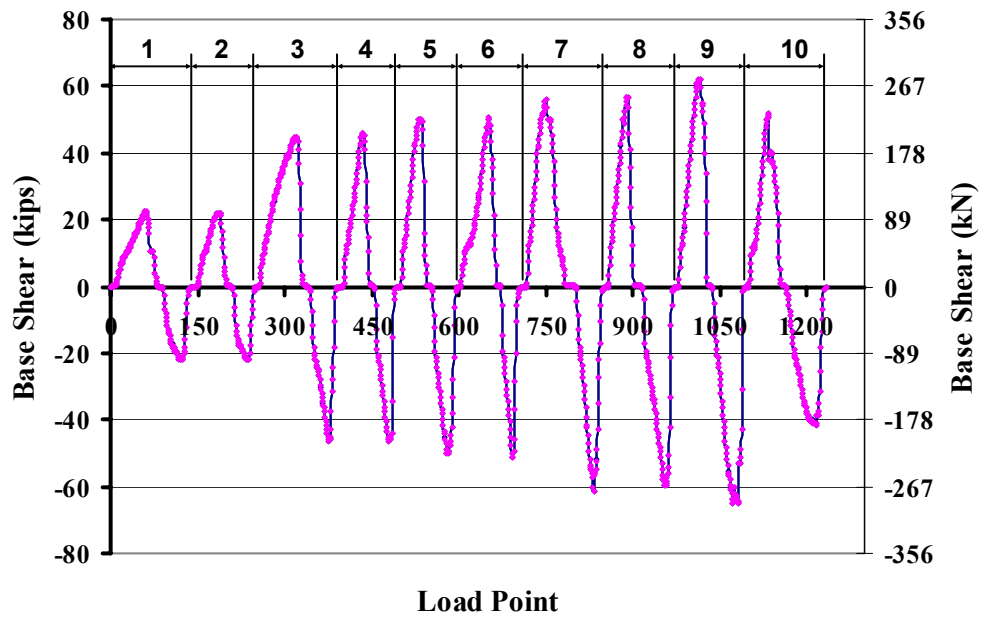


*Figure 3.24: Actual loading history for Shear Wall Specimen 19*



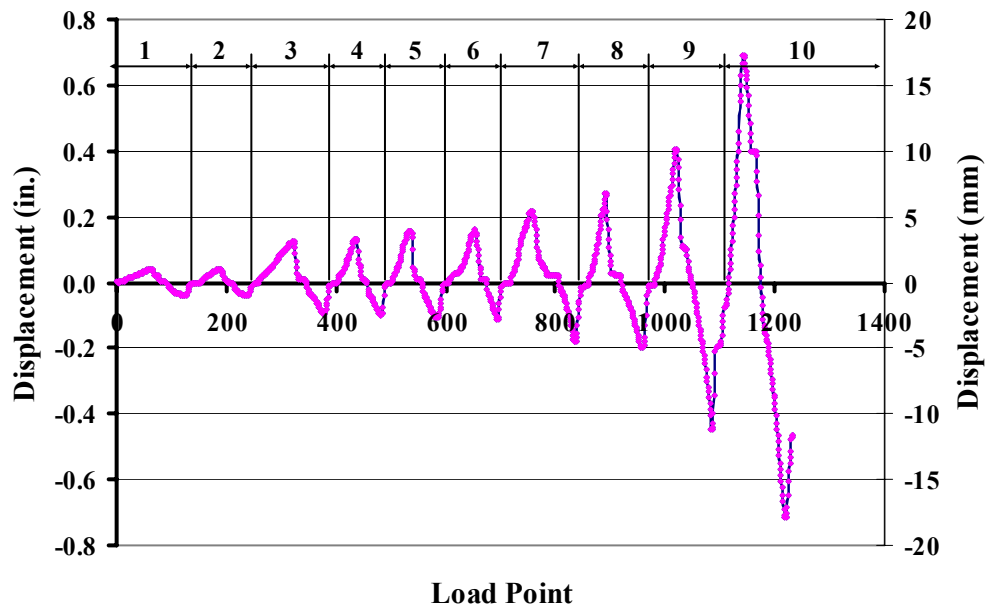


*Figure 3.25: Actual tip displacement history for Shear Wall Specimen 19*

**Table 3.5: Load Points, maximum load and drift ratios for each cycle for Shear Wall Specimen 19**

<b>Cycle</b>	<b>Load Points</b>	<b>Max. Applied Load (kips)</b>	<b>Max. Applied Load (kN)</b>	<b>Max. Drift Ratio (%)</b>	<b>Cycle</b>	<b>Load Points</b>	<b>Min. Applied Load (kips)</b>	<b>Min. Applied Load (kN)</b>	<b>Min. Drift Ratio (%)</b>
<b>1a</b>	1-81	22.26	99.04	0.027	<b>1b</b>	82-148	-21.94	-97.62	0.026
<b>2a</b>	149-206	21.95	97.67	0.026	<b>2b</b>	207-255	-22.11	-98.37	0.026
<b>3a</b>	256-338	44.72	198.99	0.079	<b>3b</b>	339-400	-46.41	-206.53	0.063
<b>4a</b>	401-453	46.02	204.79	0.086	<b>4b</b>	454-500	-46.35	-206.26	0.063
<b>5a</b>	501-550	50.21	223.44	0.100	<b>5b</b>	551-602	-50.00	-222.50	0.070
<b>6a</b>	603-672	50.48	224.66	0.103	<b>6b</b>	673-717	-51.09	-227.37	0.074
<b>7a</b>	718-800	56.00	249.21	0.142	<b>7b</b>	801-857	-61.38	-273.12	0.118
<b>8a</b>	858-915	56.78	252.66	0.174	<b>8b</b>	916-979	-59.55	-265.00	0.130
<b>9a</b>	980-1037	62.21	276.85	0.263	<b>9b</b>	1038-1100	-65.02	-289.33	0.290
<b>10a</b>	1101-1163	51.58	229.52	0.449	<b>10b</b>	1164-1234	-41.52	-184.78	0.464

### **3.4.2 Sequence of Crack Formation for Shear Wall Specimen 19**

The behavior of Shear Wall Specimen 19 is described through major events observed during the test. These major events refer to significant changes in the condition of the specimen. Each major event is matched with its respective load point and the corresponding changes in the specimen, in Table 3.6. In the remainder of this section, each major event is discussed further.

**Table 3.6: Description of major events for Shear Wall Specimen 19**

<b>Major Event</b>	<b>Load Point</b>	<b>Physical Description</b>
<b>1</b>	304	Flexural cracking, loading south
<b>2</b>	357	Flexural cracking, loading north
<b>3</b>	317	Propagation of flexural cracks, loading south
<b>4</b>	376	Propagation of flexural cracks, loading north
<b>5</b>	751	Web-shear cracking, loading south
<b>6</b>	828,833	Web-shear cracking, loading north
<b>7</b>	884	Flexure-shear cracks, loading south
<b>8</b>	890	Additional Web-shear cracking, loading south
<b>9</b>	955	Additional Web-shear cracking and flexure-shear cracking, loading north
<b>10</b>	1016	Diagonal cracks formed, loading south
<b>11</b>	1073	Diagonal cracks formed, loading north
<b>12</b>	1083	Additional diagonal cracks formed with toe crushing, loading north
<b>13</b>	1134	Additional diagonal cracks formed with toe crushing, loading south

#### **3.4.2.1 Flexural cracking in Shear Wall Specimen 19**

According to Table 3.6, Major Events 1 and 2 correspond to flexural cracking at the north end and the south end of the specimen respectively. At the north end of the specimen (loading to the south), flexural cracking occurred at a load of 39.06 kips (173.82 kN) and a drift ratio of 0.062 % (Load Point 304). At the south end of the specimen (loading to the north) flexural cracking occurred at a load of 25.07 kips (111.58 kN) and a drift ratio of 0.028 % (Load Point 357). Flexural cracking was predicted at a base shear of 43.0 kips (191.26 kN). The

ratios of observed to predicted cracking strength were 0.91 (loading to the south) and 0.58 (loading to the north).

As the test progressed, these flexural cracks propagated toward the center of the specimen from both ends. These observations correspond to Major Events 3 and 4, which were recorded at Load Point 317 (loading to the south) and Load Point 376 (loading to the north). This cracking pattern is shown in Figure 3.26.

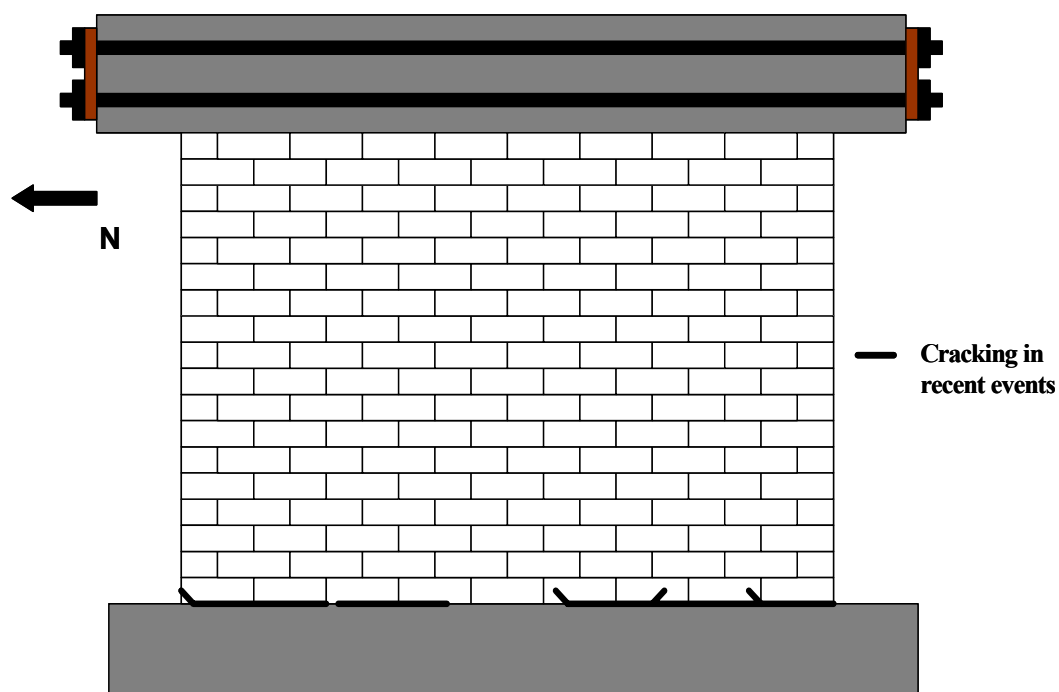


*Figure 3.26: Flexural cracks in Shear Wall Specimen 19*

#### **3.4.2.2 Web-shear cracking in Shear Wall Specimen 19**

Major Events 5 and 6 denote the formation of web-shear cracking while loading south and north respectively. At the north end (loading to the south), these cracks formed at a base shear of 56.00 kips (249.21 kN) and a drift ratio of 0.126 % (Load Point 751). This web-shear crack formed approximately in the central

portion of the specimen and covered Shear Wall Specimen 19 from top to bottom. These cracks are shown in detail in Figure 3.27.



***Figure 3.27: Web-shear cracking in Shear Wall Specimen 19***

At the south end (loading to the north), these cracks formed at a base shear force of 54.84 kips (244.04 kN) and a drift ratio of 0.083 % (Load Point 828). Web-shear cracking was predicted at a base shear of 52.0 kips (231.30 kN). The ratios of observed to predicted web-shear cracking strength were 1.07 (loading to the south) and 1.05 (loading to the north).

As the test progressed, flexure-shear cracking was observed at Load Point 884, which corresponded to Major Event 7. This cracking was located at the north end of the specimen, approximately 30 in. (0.76 m) from the bottom of Shear Wall Specimen 19. Major Event 8, which corresponded to Load Point 890 and a base shear force of 56.78 kips (252.66 kN), was characterized by the propagation of the existing web-shear cracks from the middle height of the specimen toward the bottom of the specimen. Major Event 9 is characterized by the formation of additional flexure-shear cracks and the propagation of those cracks toward the bottom of the specimen. This was observed as the applied load was 59.55 kips (265.00 kN), loading to the north. Cracking associated with Major Events 7, 8 and 9 is shown in Figure 3.28.

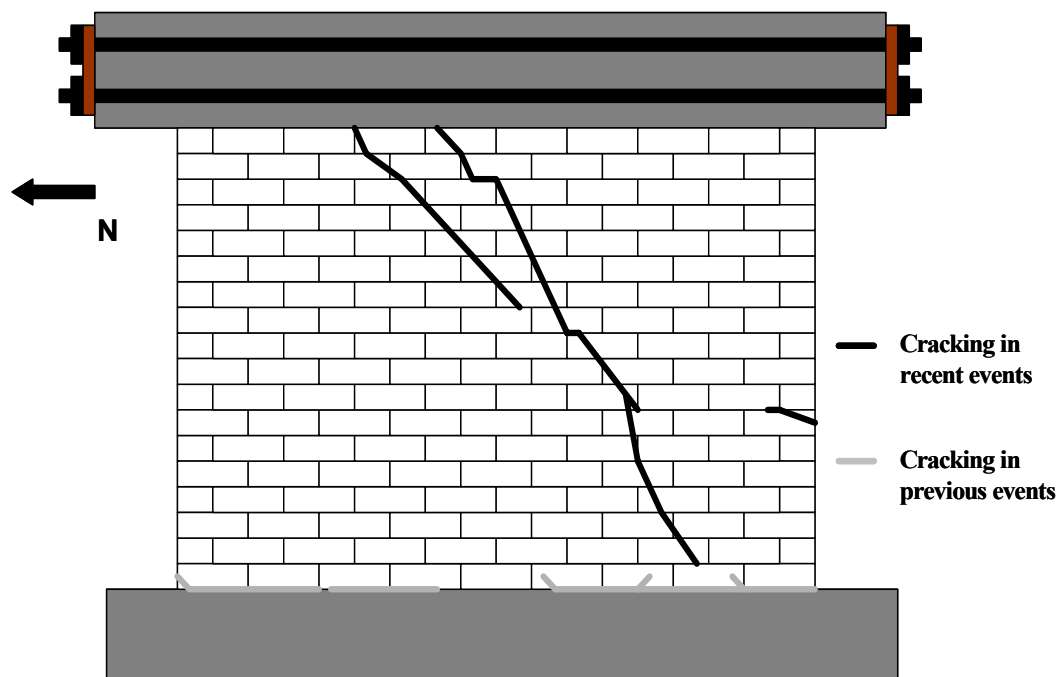


*Figure 3.28: Web-shear cracking in Shear Wall Specimen 19*

### ***3.4.2.3 Propagation and Additional Web-shear cracking in Shear Wall Specimen 19***

Major Events 10 and 11 correspond to the propagation of existing web-shear cracks and the development of new web-shear cracks in Shear Wall Specimen 19. At the north end, additional web-shear cracks formed at Load Point 1016, which corresponded to a base shear of 62.21 kips (276.85 kN). These cracks were extended through the wall and covering the center portion of the specimen almost to the base of the south end. A similar situation was observed at the south end of Shear Wall Specimen 19, specifically at Load Point 1073, corresponding to a base shear of 65.02 kips (289.33 kN). These diagonal cracks formed from the top to the bottom of the specimen and extended from the center portion of the specimen toward its north base. At this stage of the test, the south end of the specimen showed major damage, with cracking developing from the mid-height of the south end toward the bottom of it. The cracking pattern associated with Major Events 10 and 11 is shown in Figure 3.29.

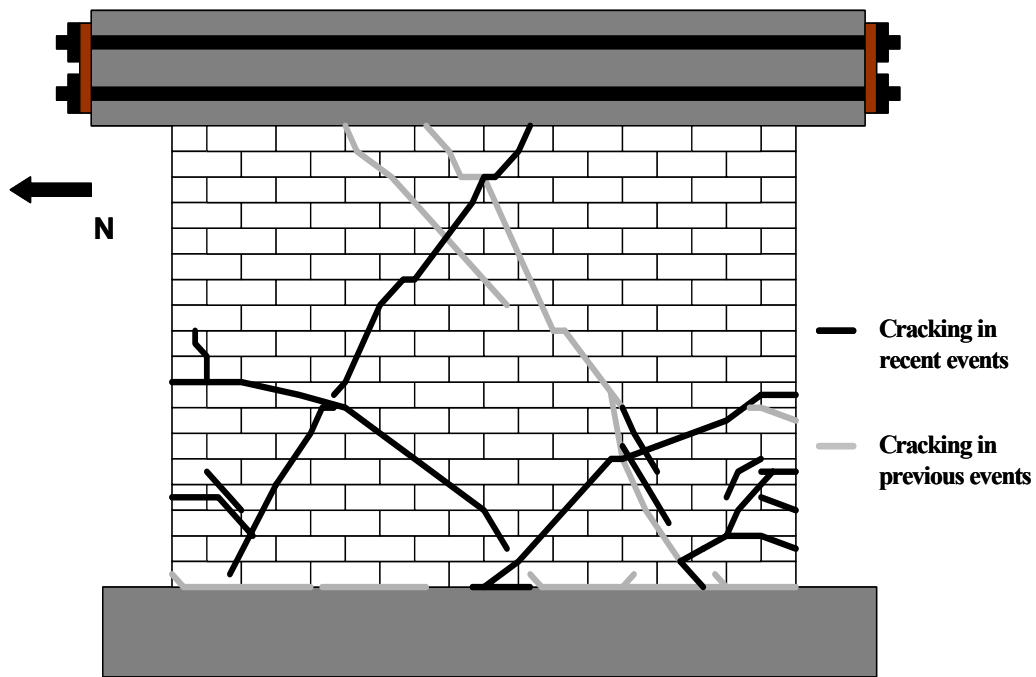


***Figure 3.29: Propagation and formation of additional web-shear cracks along with some flexure-shear cracks in Shear Wall Specimen 19***

#### ***3.4.2.4 Final damage in Shear Wall Specimen 19***

Major Events 12 and 13 denote the final stage in the test of Shear Wall Specimen 19, and are associated with progressive damage at both ends of the specimen. This damage consisted of the propagation and formation of additional web-shear cracks in the specimen from the top to the bottom. At Load Point 1083, which corresponded to a base shear of 64.83 kips (288.47 kN), toe crushing was observed at the north end of the specimen. A similar situation occurred at the south end of the specimen at Load Point 1134, which corresponded to a base shear of 51.58 kips (229.52 kN). At this stage, the specimen showed major damage with crushing of both compressive toes, along with a significant drop in in-plane stiffness (about 14 % of the initial stiffness) and strength. This



observation is based on the reduction in slope of the hysteretic curve. The test was ended in Loading Cycle 10.

Figure 3.30 shows the damage in Shear Wall Specimen 19 at the end of the test. The significant amount and opening of the web-shear cracks and crushing of the diagonal strut is shown in Figure 3.31 and Figure 3.32 respectively.

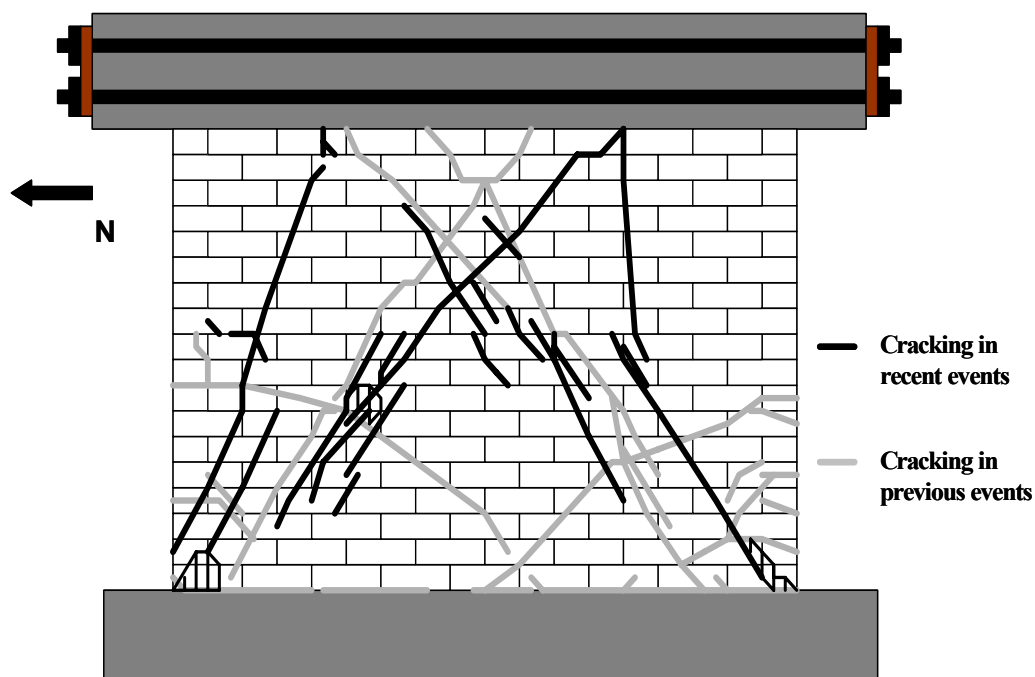


*Figure 3.30: Additional web-shear cracking and toe crushing in Shear Wall Specimen 19*

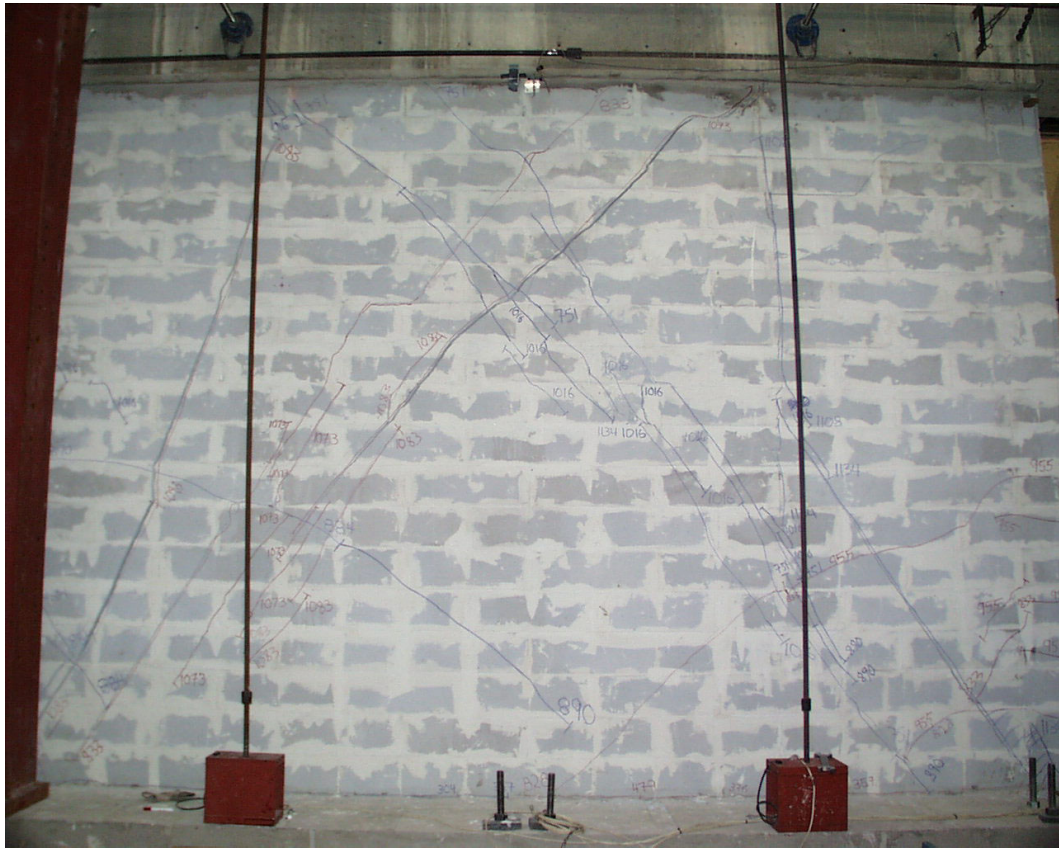


*Figure 3.31: Web-shear cracking in Shear Wall Specimen 19 at the end of the test*



*Figure 3.32: Toe crushing at the north end of Shear Wall Specimen 19*

### **3.4.3 Load-Displacement Behavior for Shear Wall Specimen 19**

The overall hysteretic behavior of Shear Wall Specimen 19 is shown in Figure 3.33. The maximum drift ratio for this specimen was about 0.49 % in both directions. The test was stopped at in-plane displacements of 0.71 in (18.00 mm).

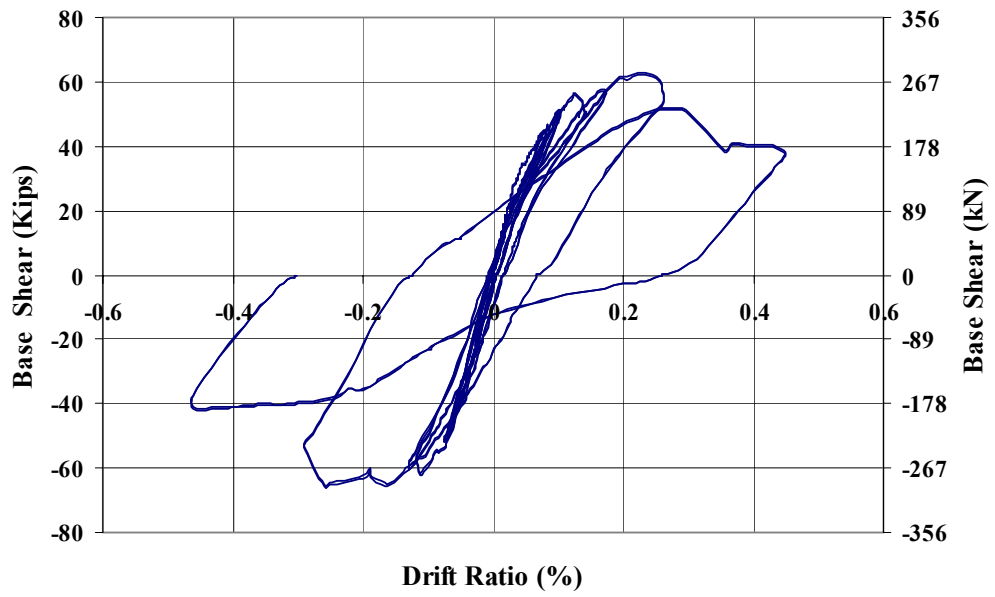


*Figure 3.33: Overall hysteretic behavior of Shear Wall Specimen 19*

## **CHAPTER 4**

### **Significance of Test Results**

In this chapter, the overall hysteretic behavior of each specimen is evaluated and compared with predicted behavior. Each observed behavior mode is confirmed, and the validity of previously proposed design provisions is assessed for flexure- as well as shear-dominated behavior.

#### **4.1 REVIEW OF BEHAVIOR MODES FOR AAC SHEAR WALLS**

For the specimens tested at UT, the relevant design-related behavior modes are: flexural cracking, web-shear cracking, flexure-shear cracking, yielding of the flexural reinforcement, crushing of the diagonal strut, and sliding shear. In this section, the previously developed design provisions for each behavior mode are reviewed (Tanner 2003, Argudo 2003). In subsequent sections, the capacities predicted by those design provisions are compared with the observed capacities for each specimen.

##### **4.1.1 Flexural Cracking**

Flexural cracking occurs when the flexural tensile strength of the material, which is represented by the modulus of rupture, is exceeded by the flexural tensile stress. For design purposes, the modulus of rupture is given by Equation 4.1 , and is capped at 50 psi (0.34 MPa). The general form of the proposed equation for flexural cracking is based on principal tensile stresses (Equation 4.2) (Tanner 2003 and Appendix A of this thesis). Flexural cracking occurs at the base of a

cantilever wall because the moment is greatest there (Figure 4.1). If the element has flexural reinforcement, flexural cracking does not constitute failure.

$$f_r = 2 \times 2.4 \sqrt{f_{AAC}} \quad \text{Equation 4.1}$$

$$V_{cr} = \frac{tl_w^2}{6h} \times \left( f_r + \frac{N_u}{tl_w} \right) \quad \text{Equation 4.2}$$

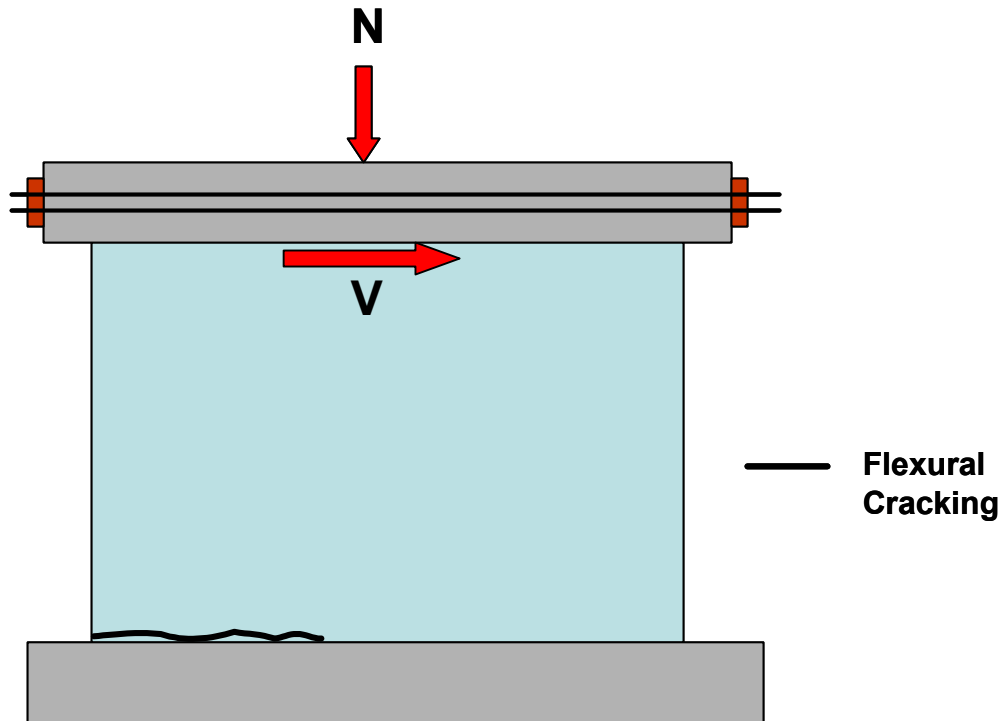


**Figure 4.1: Typical flexural cracking**

Shear Wall Specimens 17, 18 and 19 exhibited flexural cracking. Table 4.1 shows the ratios of observed to predicted flexural cracking capacities for these specimens (SWS17, SWS18, and SWS19) and the corresponding mean value for the specimens tested at The University of Texas at Austin by Tanner (2003).

**Table 4.1 Observed versus predicted flexural cracking capacities**

<b>Specimen Number</b>	<b>Observed Base Shear Capacity, kips (kN)</b>	<b>Predicted Base Shear Capacity kips (kN)</b>	<b>Observed / Predicted Capacity</b>
17	15.11 (67.2)	12.10 (53.82)	1.25
18	23.81 (105.9)	19.00 (84.51)	1.25
19	32.07 (142.6)	43.00 (191.26)	0.75
Specimens of Tanner (2003)	27.83 (123.8) COV (99 %)	25.11 (111.70) COV (95 %)	1.10

Table 4.1 shows a good agreement between the observed and predicted flexural cracking capacities of the three specimens tested in this study, and good consistency between the specimens of this study and those reported by Tanner (2003).

#### **4.1.2 Web-shear cracking**

Web-shear cracking occurs when principal tensile stresses exceed the diagonal tensile strength of the AAC material (Figure 4.2). This type of cracking was observed in Shear Wall Specimens 17 and 18.

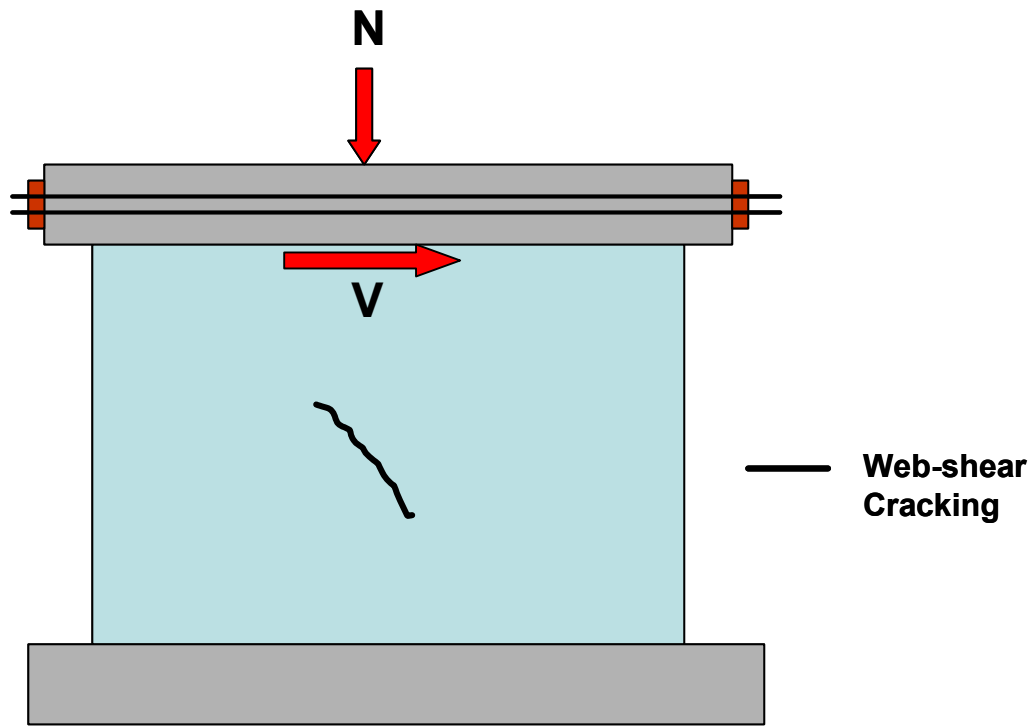


**Figure 4.2: Typical web-shear cracking**

The design equation for web-shear cracking capacity of fully mortared AAC shear walls is given in Equation 4.3 (Tanner 2003 and Appendix A of this thesis).

$$V_{AAC} = 0.9l_w t \sqrt{f'_{AAC}} \sqrt{1 + \frac{N_u}{2.4\sqrt{f'_{AAC}}l_w t}} \quad \text{Equation 4.3}$$

Shear Wall Specimens 18 and 19 exhibited web-shear cracking. Table 4.2 shows observed versus predicted web-shear cracking capacities for these specimens, along with the corresponding mean value for the specimens tested at The University of Texas at Austin by Tanner (2003). The table shows good



agreement between the observed and predicted web-shear cracking capacities of the shear-dominated specimens tested in this study, and reasonable consistency between the specimens of this study and those reported by Tanner (2003).

*Table 4.2 Observed versus predicted web-shear cracking capacities*

<b>Specimen Number</b>	<b>Observed Base Shear Capacity, kips (kN)</b>	<b>Predicted Base Shear Capacity, kips (kN)</b>	<b>Observed / Predicted Capacity</b>
18	35.87 (159.5)	37.0 (164.5)	0.97
19	55.42 (246.5)	52.0 (231.3)	1.06
Specimens of Tanner (2003)	72.3 (321.5) COV (64 %)	58.0 (257.5) COV (58 %)	1.24

#### **4.1.3 Flexure-shear cracking**

Flexure-shear cracking occurs when principal tensile stresses are sufficient to cause a flexural crack to propagate diagonally into the web of the element (Figure 4.3).

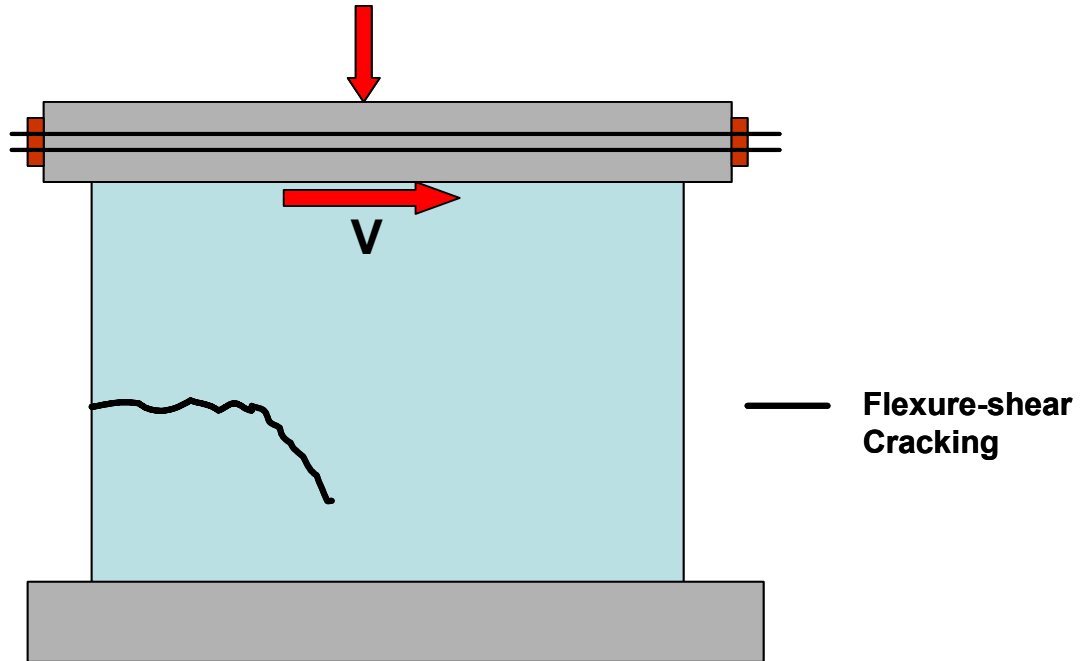


**Figure 4.3: Typical flexure-shear cracking**

The design formula used for flexure-shear cracking capacity is given in Equation 4.4, and includes the previously developed expression for the diagonal tensile strength of AAC material as discussed in Chapter 2 of this thesis (Tanner 2003, Argudo 2003).

$$V_c = \left[ 0.6\sqrt{f'_{AAC}} + \frac{l_w \left( 1.25\sqrt{f'_{AAC}} + 0.21 \frac{N}{l_w t} \right)}{\frac{M}{V} - \frac{l_w}{2}} \right] td \quad \text{Equation 4.4}$$

As discussed in Tanner (2003) and in Appendix A of this thesis, flexure-shear cracking does not constitute a limit state in the specimens tested at the

University of Texas at Austin, because it is not associated with a significant change in capacity or stiffness.

Shear Wall Specimen 17 exhibited flexure-shear cracking. Table 4.3 shows the results of observed versus predicted flexure-shear cracking capacity for this specimen and the corresponding mean value for the specimens tested at The University of Texas at Austin by Tanner (2003). The values for SWS 17 are consistent with values reported by Tanner.

**Table 4.3 Observed versus predicted flexure-shear cracking capacities**

<b>Specimen Number</b>	<b>Observed Base Shear Capacity, kips (kN)</b>	<b>Predicted Base Shear Capacity, kips (kN)</b>	<b>Observed / Predicted Capacity</b>
17	24.83 (110.4)	23.09 (102.7)	1.08
Specimens of Tanner (2003)	13.63 (60.6) COV (66 %)	12.24 (54.44) COV (63 %)	1.11

#### **4.1.4 Nominal Flexural Capacity**

The nominal flexural capacity of the flexure-dominated AAC shear-wall specimens tested at The University of Texas at Austin was determined using conventional flexural theory (Figure 4.4), using a maximum compressive strain in the AAC material of 0.003, and an equivalent rectangular stress block with a height of  $0.85f_{AAC}$  and a depth  $\beta_1 = 0.67$  (Argudo 2003). The design formula used for nominal flexural capacity is given in Equation 4.5.

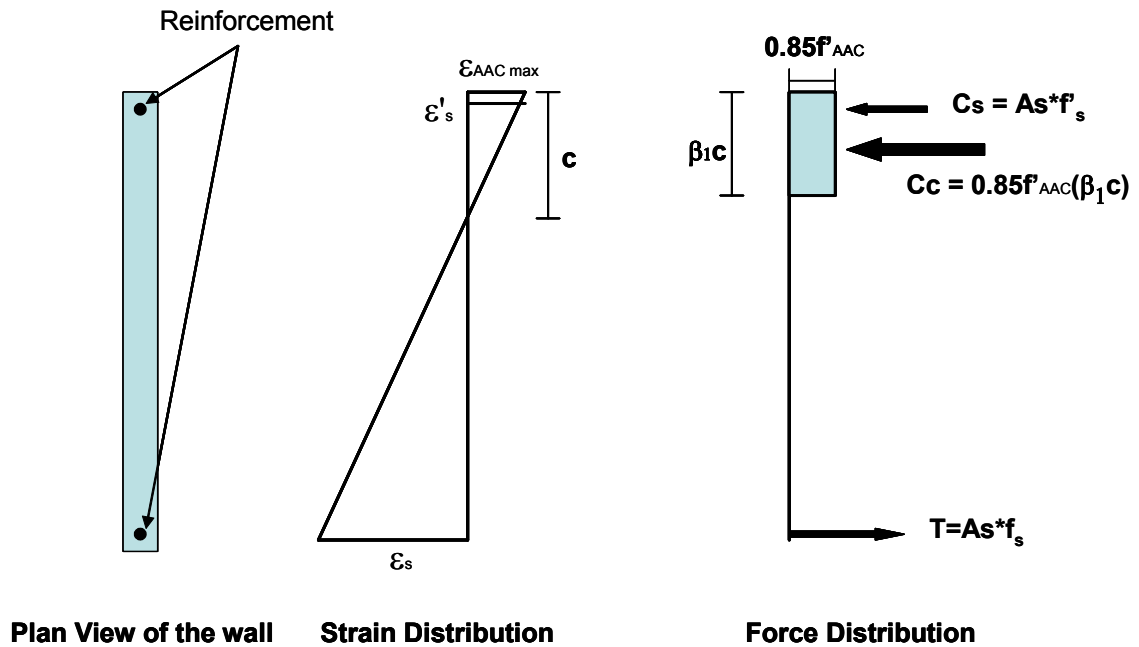


Figure 4.4: Strain and force distribution in an AAC shear wall

$$V_n = \left[ \frac{A_s f_s}{h} \times \left( \frac{l_w}{2} - x_i \right) \right] \quad \text{Equation 4.5}$$

Because the behavior of Shear Wall Specimens 18 and 19 was governed (as intended) by web-shear cracking rather than flexure, they did not reach their nominal flexural capacity. Shear Wall Specimen 17, whose behavior was governed (as intended) by flexure, did reach its nominal flexural capacity. Table 4.4 shows that the ratios of observed versus predicted nominal flexural capacities for this specimen are very consistent with the corresponding mean flexural capacities of the specimens tested at The University of Texas at Austin (Tanner 2003). Although  $\epsilon_{AAC \max}$  decreases below 0.003 for low-strength AAC, nominal

flexural capacities are still well predicted, because they are governed by the reinforcement.

*Table 4.4 Observed versus predicted values for nominal flexural capacity*

<b>Specimen Number</b>	<b>Observed Base Shear Capacity, kips (kN)</b>	<b>Predicted Base Shear Capacity, kips (kN)</b>	<b>Observed / Predicted Capacity</b>
17	25.0 (111.2)	25.8 (114.8)	0.97
Specimens Tanner (2003)	19.4 (86.2) COV (58 %)	18.65 (83.0) COV (54 %)	1.04 COV (6 %)

#### **4.1.5 Crushing of the Diagonal Strut**

Crushing of the diagonal strut occurs when high overturning moments and high base shears combine to produce a localized compression failure at the toe of an AAC shear wall (Figure 4.5).

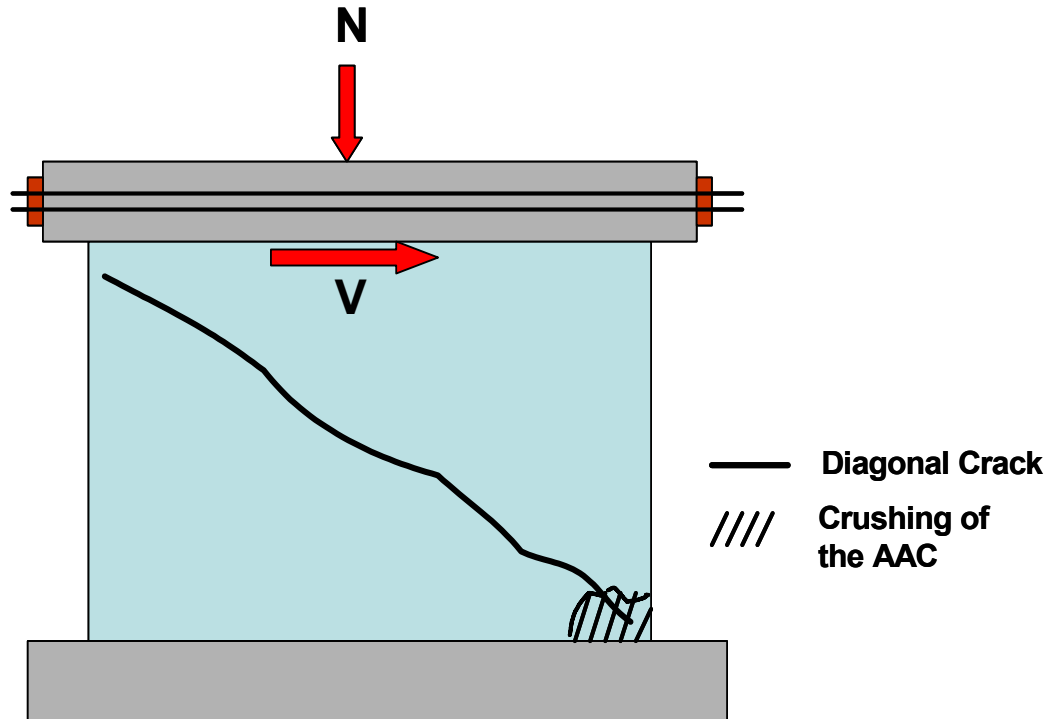


***Figure 4.5: Diagonal cracks and crushing of the diagonal strut***

The design provisions previously proposed by Tanner (2003) for crushing of the diagonal strut are based on the results of tests conducted at The University of Texas at Austin (Tanner 2003, Varela 2003). In that development, a horizontal width of the diagonal strut of  $0.25l_w$  was used. The equation (Equation 4.6) must be checked only for walls with  $M/Vd < 1.5$ , because this failure mode does not occur for walls with  $M/Vd \geq 1.5$  (Tanner 2003).

$$V_{AAC} = 0.17 f'_{AAC} t \times \left[ \frac{h l_w^2}{h^2 + \left( \frac{3}{4} l_w \right)^2} \right] \quad \text{Equation 4.6}$$

Shear Wall Specimens 18 and 19 exhibited crushing of the diagonal strut. Table 4.5 shows ratios of observed versus predicted capacities as governed by crushing of the diagonal strut for these specimens, and the corresponding mean value of those ratios for the specimens tested at The University of Texas at Austin by Tanner (2003).

***Table 4.5 Observed versus predicted capacities as governed by crushing of the diagonal strut***

<b>Specimen Number</b>	<b>Observed Base Shear Capacity, kips (kN)</b>	<b>Predicted Base Shear Capacity, kips (kN)</b>	<b>Observed / Predicted Capacity</b>
18	34.88 (155.15)	39.26 (174.63)	0.89
19	58.21 (258.92)	62.56 (278.27)	0.93
Specimens Tanner (2003)	108.5 (482.6) COV (73 %)	120.5 (536.0) COV (73 %)	0.90

Table 4.5 shows a good agreement of ratios between the observed and predicted crushing of the diagonal strut for the shear-dominated specimens tested in this study, and good consistency between the specimens of this study and those reported by Tanner (2003).

#### 4.1.6 Sliding Shear

Sliding shear occurs along a bed joint when the shear there exceeds the combined capacity from adhesion and shear friction (Figure 4.6, Figure 4.7).

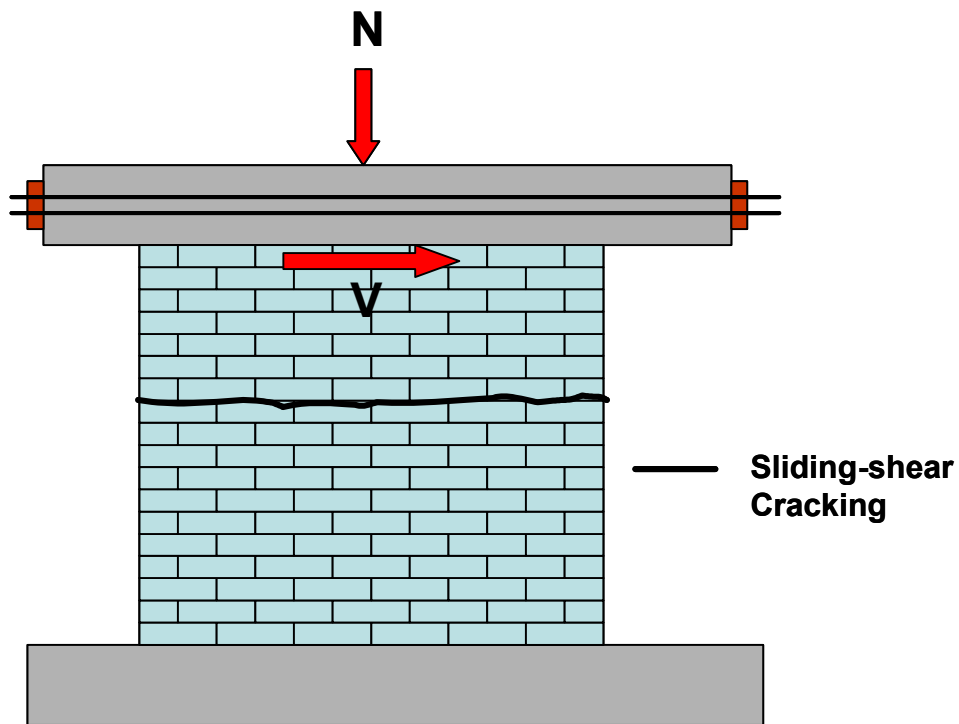


*Figure 4.6 Sliding-shear cracking*



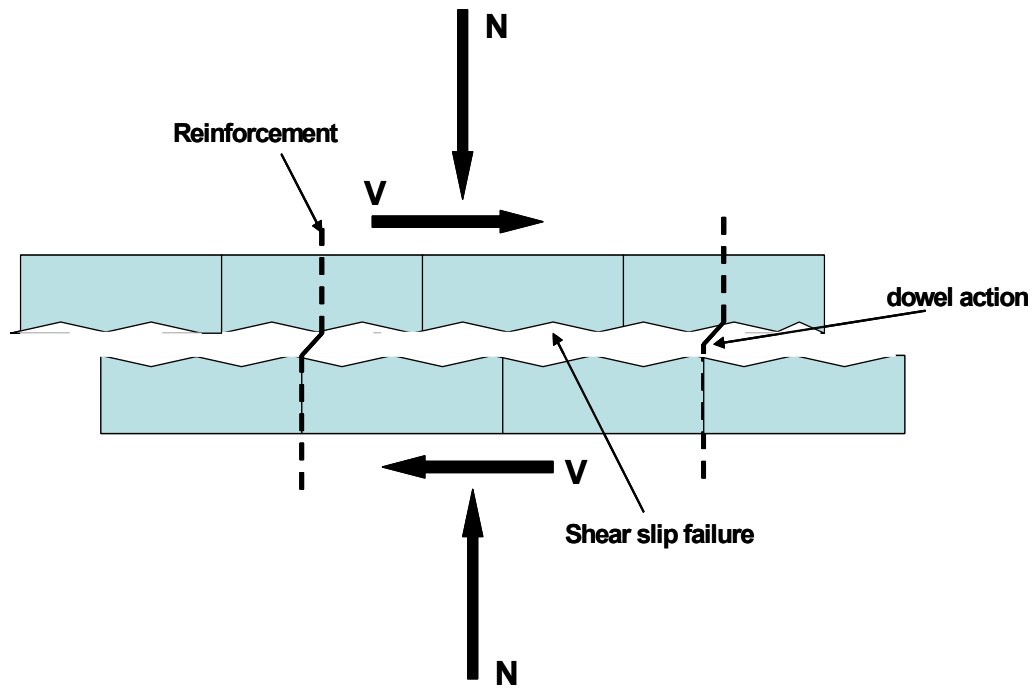


**Figure 4.7: Shear friction**

As previously developed by Tanner (2003), sliding-shear capacity is given by Equation 4.7.

$$V_{sliding} = N + A_{vf} f_s \quad \text{Equation 4.7}$$

For design purposes, the contribution of reinforcement is conservatively neglected (Tanner 2003), leading to Equation 4.8. Because sliding shear was not observed in Shear Wall Specimens 17, 18 and 19, comparison with the results of Tanner is not possible.

$$V_{sliding} = \mu N_u \quad \text{Equation 4.8}$$

## **4.2 HYSTERETIC BEHAVIOR OF SHEAR WALL SPECIMENS**

In this section, the hysteretic behavior of Shear Wall Specimens 17, 18 and 19 is presented and compared with that obtained in the specimens tested by Tanner (2003) and Varela (2003). The behavior of the flexure-dominated specimen (SWS17) is described first, followed by the behavior of the shear-dominated specimens (SWS 18 and SWS 19).

### **4.2.1 Hysteretic Behavior of Flexure-Dominated Specimens**

The hysteretic load-displacement response of flexure-dominated AAC shear-wall specimens can be described in terms of the following:

- initial stiffness;
- stiffness after flexural cracking;
- stiffness after yielding of the flexural reinforcement;
- unloading stiffness after yielding of the flexural reinforcement;
- capacity;
- degradation of stiffness with cycling;

- degradation of strength with cycling; and
- displacement ductility.

For flexure-dominated Shear Wall Specimen 17, initial tangent stiffness ( $K_{ot-o}$ ) was calculated as the slope of the first half-cycle of the load-displacement curve. The initial backbone stiffness ( $K_{ob-o}$ ) was calculated as the slope of the straight line between the origin and the last point in that first half-cycle (Figure 4.8).

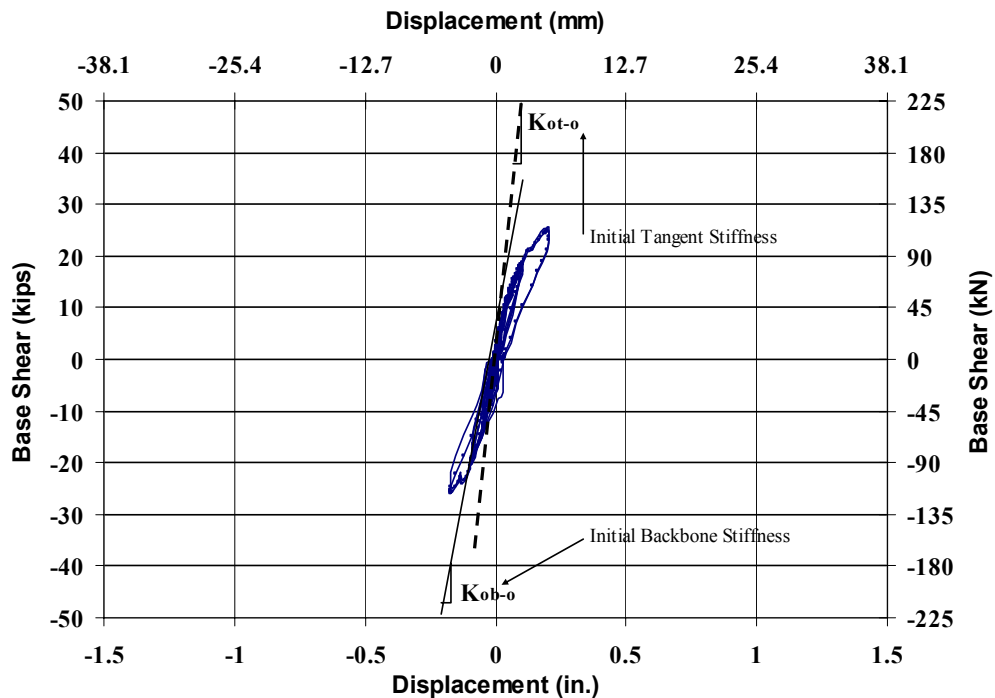


**Figure 4.8: Initial tangent and backbone stiffness for Shear Wall Specimen 17**

The secant stiffness after flexural cracking was calculated as the applied load at which yielding of the flexural reinforcement was observed, divided by the corresponding horizontal displacement (Figure 4.9). Yielding of the flexural

reinforcement was detected using strain gages on the flexural reinforcement.  $D_{ys}$  and  $D_{yn}$  are the displacements at yielding of the flexural reinforcement in the south and north directions respectively, and  $K_{cr-os}$  and  $K_{cr-on}$  are the corresponding stiffnesses.

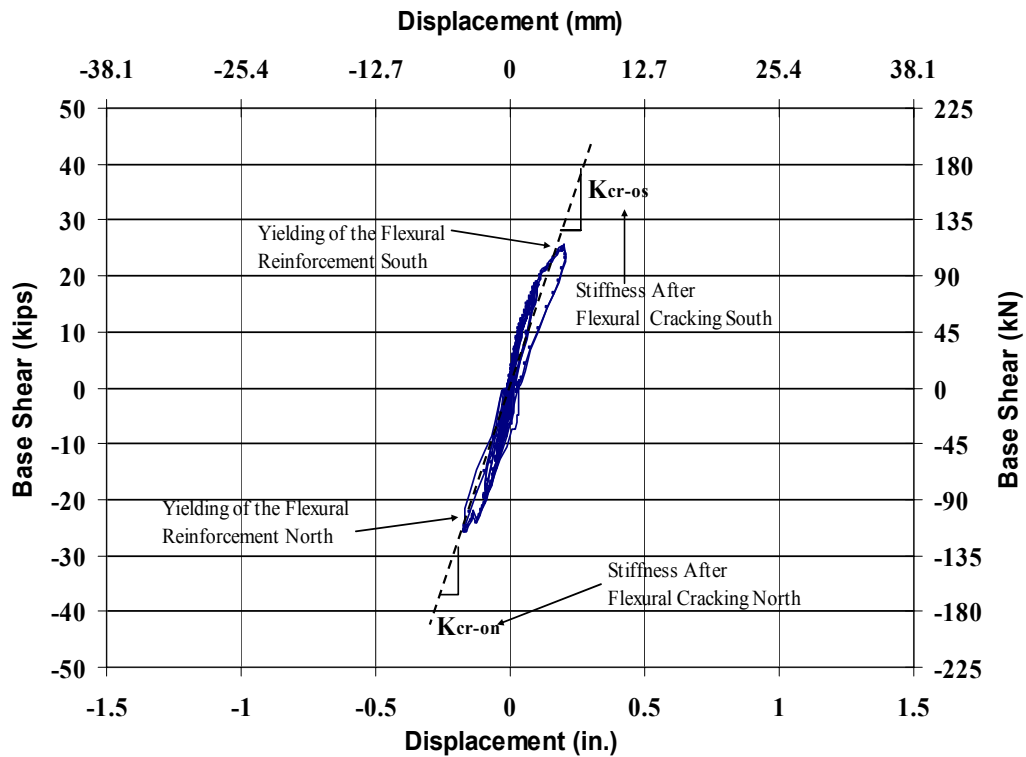


**Figure 4.9: Stiffness after flexural cracking for Shear Wall Specimen 17**

The unloading stiffness after yielding of the flexural reinforcement was calculated using the tangent to the load-displacement curve on first unloading after observed yield of flexural reinforcement (Figure 4.10). Two unloading stiffnesses were calculated for the specimen, one corresponding to displacements

in the south direction ( $K_{u-os}$ ) and the other to displacements in the north direction ( $K_{u-on}$ ).

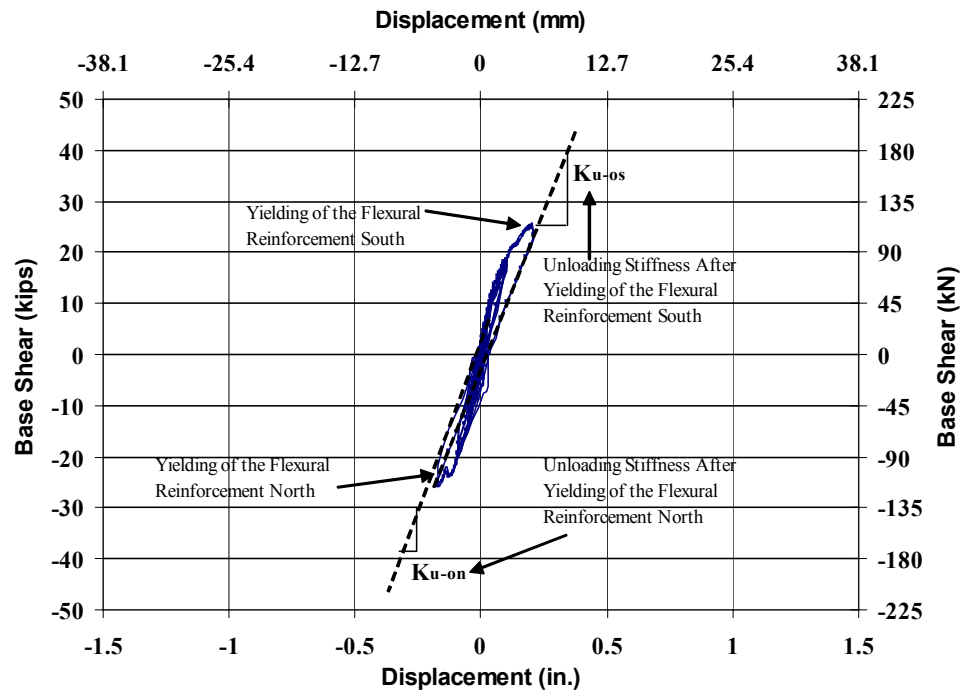


**Figure 4.10: Unloading stiffnesses after yielding of the flexural reinforcement for Shear Wall Specimen 17**

The stiffness after yielding of the flexural reinforcement was calculated as the slope of the tangent to the load-displacement curve after observed yield of flexural reinforcement (Figure 4.11). Two stiffnesses after yielding of the flexural reinforcement were calculated for this flexure-dominated specimen, one corresponding to loading the specimen in the south direction ( $K_{y-os}$ ), and the other in the north direction ( $K_{y-on}$ ).

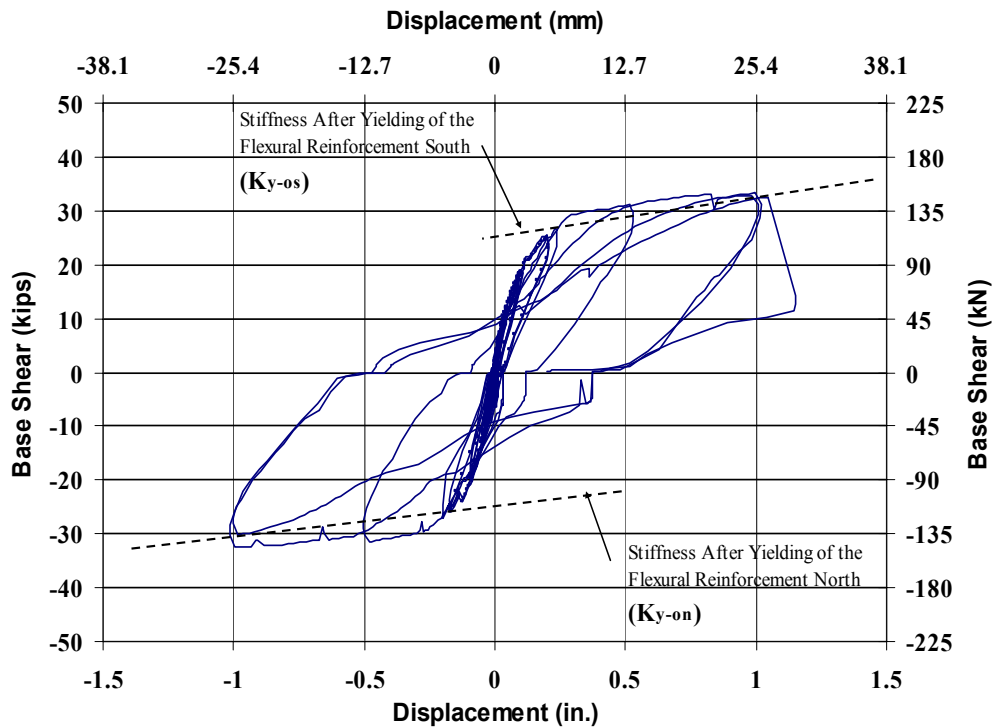


**Figure 4.11: Stiffnesses after yielding of the flexural reinforcement for Shear Wall Specimen 17**

The maximum useful horizontal displacement was taken as that corresponding to the smaller of the following displacements:

- the displacement corresponding to a reduction of more than 10 % in the maximum capacity of the specimen in a given load cycle, compared to the maximum capacity in the same direction in the previous load cycle; and
- the displacement corresponding to a significant change in the shape of the hysteretic loop from the corresponding previous load cycle.

Using this maximum useful displacement, maximum global drift ratios were calculated for this flexure-dominated specimen, one corresponding to loading the

specimen in the south direction ( $\delta_{os}$ ) and the other in the north direction ( $\delta_{on}$ ). Corresponding displacement ductilities were also calculated for loading to the south ( $\mu_{\Delta-os}$ ) and to the north ( $\mu_{\Delta-on}$ ).

The maximum useful displacements in the south and north directions for this specimen were both 1.01 in. (25.6 mm). The corresponding drift ratios were both 0.65 %, and the displacement ductilities were both 5.61. Figure 4.12 shows how the maximum drift ratios in the south and north directions were determined for Shear Wall Specimen 17.

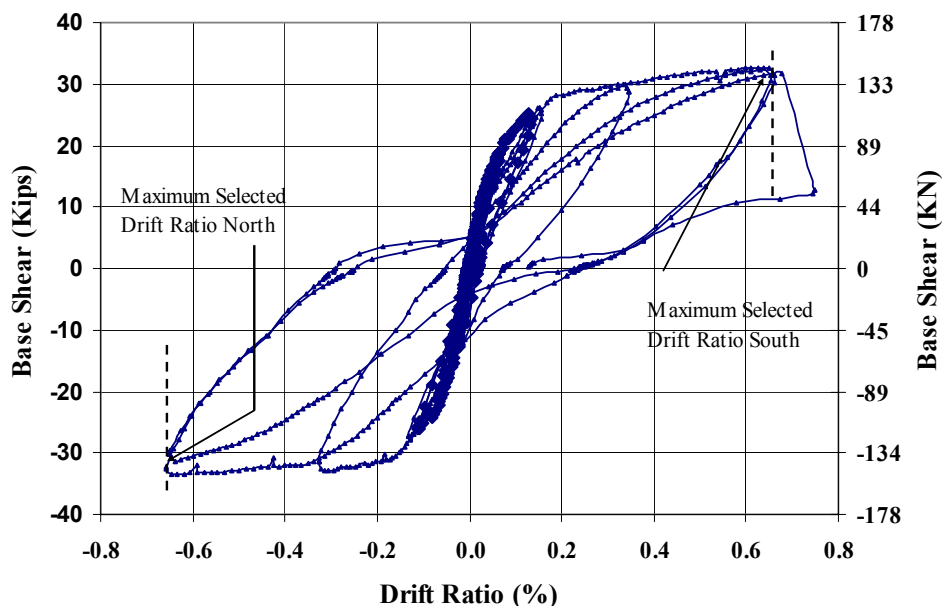


**Figure 4.12: Selected drift ratios for Shear Wall Specimen 17**

For Shear Wall Specimen 17, the response quantities discussed above are given in Table 4.6.

**Table 4.6 Maximum displacements, ductilities and drift ratios for Shear Wall Specimen 17**

$\Delta_n$ (in.) (mm)	$\Delta_s$ (in.) (mm)	$\mu_{\Delta-os}$	$\mu_{\Delta-on}$	$\delta_{os}$ (%)	$\delta_{on}$ (%)
1.01 (25.6)	1.01 (25.6)	5.61	5.61	0.65	0.65

In the remainder of this section, the hysteretic behavior of Shear Wall Specimen 17 as described above is summarized and compared with the corresponding results for the flexure-dominated specimens discussed in Varela (2003).

For initial tangent stiffness ( $K_{ot-o}$ ), initial backbone stiffness ( $K_{ob-o}$ ), and for the ratio of initial backbone stiffness to initial tangent stiffness, values are presented in Table 4.7. The results show that ratio of backbone stiffness versus initial tangent stiffness for this specimen is consistent with the corresponding mean value of those ratios for the specimens tested by Varela (2003). Differences between the absolute stiffnesses obtained in this study and those obtained by Varela (2003) are due to differences in material ( $f_{AAC}$ ), geometry, and reinforcement among specimens.



**Table 4.7 Comparison of initial tangent and backbone stiffnesses for flexure-dominated specimens**

Specimen Number	$K_{ot-o}$ Kips/in. (kN/mm)	$K_{ob-o}$ Kips/in. (kN/mm)	$K_{ob-o}/K_{ot-o}$
17	359.3 (63.0)	346.5 (60.7)	0.96
Specimens of Varela (2003)	116.0 (20.3) COV (75 %)	118.1 (20.7) COV (56 %)	1.01

For secant stiffnesses after flexural cracking in the south ( $K_{cr-os}$ ) and north ( $K_{cr-on}$ ) directions, and for the ratio of those observed secant stiffness after flexural cracking to initial tangent stiffness, results are presented in Table 4.8. The results show that ratio of secant stiffness versus initial tangent stiffness in both directions for this specimen is consistent with the corresponding mean value of those ratios for the specimens tested by Varela (2003).

**Table 4.8 Comparison of secant stiffnesses after flexural cracking for flexure-dominated specimens**

Specimen Number	$K_{cr-os}$ Kips/in. (kN/mm)	$K_{cr-os}/K_{ot-o}$	$K_{cr-on}$ Kips/in. (kN/mm)	$K_{cr-on}/K_{ot-o}$
17	138.8 (24.3)	0.39	138.8 (24.3)	0.39
Specimens of Varela (2003)	50.2 (8.8) COV (76 %)	0.45 COV (31 %)	59.2 (13.0) COV (62 %)	0.42 COV (18 %)

For unloading stiffnesses after yielding of the flexural reinforcement in the south ( $K_{u-os}$ ) and north ( $K_{u-on}$ ) directions, and for the ratio of those unloading

stiffnesses to the initial tangent stiffness, values are presented in Table 4.9. The ratios in both directions are consistent with the corresponding mean value of those ratios for the specimens tested by Varela (2003).

**Table 4.9 Comparison of unloading stiffnesses after yield of flexural reinforcement in the south and north direction for flexure-dominated specimens**

Specimen Number	$K_{u-os}$ Kips/in. (kN/mm)	$K_{u-os}/K_{ot-o}$	$D_{u-os}/D_{ys}$	$K_{u-on}$ Kips/in. (kN/mm)	$K_{u-on}/K_{ot-o}$	$D_{u-on}/D_{yn}$
17	109.8 (19.45)	0.31	1.17	130.1 (23.0)	0.36	1.11
Specimens of Varela (2003)	37.0 (6.5) COV (71 %)	0.35 COV (33 %)	1.58 COV (34 %)	35.1 (6.15) COV (56 %)	0.27 COV (28 %)	1.66 COV (33 %)

For the stiffnesses after yield of flexural reinforcement in the south ( $K_{y-os}$ ) and north ( $K_{y-on}$ ) directions, and for the ratio of those stiffnesses to initial tangent stiffness, values are presented in Table 4.10. The ratios in both directions are consistent with the corresponding mean values of those ratios for the specimens tested by Varela (2003).

**Table 4.10 Comparison of stiffnesses after yield of flexural reinforcement for flexure-dominated specimens**

<b>Specimen Number</b>	<b><math>K_{y-os}</math> Kips/in. (kN/mm)</b>	<b><math>K_{y-os}/K_{ot-o}</math></b>	<b><math>K_{y-on}</math> Kips/in. (kN/mm)</b>	<b><math>K_{y-on}/K_{ot-o}</math></b>
17	9.0 (1.59)	0.025	7.0 (1.24)	0.019
Specimens of Varela (2003)	1.88 (0.33) COV (59 %)	0.021 COV (47 %)	2.08 (0.67) COV (74 %)	0.018 COV (52 %)

Maximum useful global drift ratios and corresponding displacement ductilities are presented in Table 4.11. Shear Wall Specimen 17 had a higher ductility in both directions than the other flexure-dominated specimens, probably due to the helical ties used to connect the end units with the rest of the wall.

**Table 4.11 Maximum useful displacement drift ratios and ductilities for flexure-dominated specimens**

<b>Specimen Number</b>	<b><math>\delta_{os}</math> (%)</b>	<b><math>\delta_{on}</math> (%)</b>	<b><math>\mu_{\Delta-os}</math></b>	<b><math>\mu_{\Delta-on}</math></b>
17	0.65	0.65	5.6	5.6
Specimens of Varela (2003)	1.37 COV (32 %)	0.9 COV (31 %)	5.2 COV (9 %)	3.78 COV (43 %)

The capacity of Shear Wall Specimen 17 was governed by its nominal flexural capacity. The hysteretic loops showed a similar pattern for loading and unloading. The pinching was due to flexure-shear cracks.

Comparison of hysteretic behavior observed for Shear Wall Specimen 17 with that previously observed by Varela (2003) shows that the behaviors are generally consistent, so that the values of  $R$  and  $C_d$  previously proposed by Varela

can be safely used with flexure-dominated specimens of low-strength AAC. This is true even though  $\varepsilon_{AAC \text{ max}}$  is slightly lower than 0.003 for low-strength AAC.

#### 4.2.2 Hysteretic Behavior of Shear-Dominated Specimens

The hysteretic load-displacement response of shear-dominated specimens can be described in terms of the following:

- initial stiffness;
- stiffness after flexural cracking;
- unloading stiffness after web-shear cracking; and
- strength degradation after web-shear cracking.

Initial tangent and backbone stiffnesses were calculated for each shear-dominated wall specimen, as for the flexure-dominated specimens (Figure 4.13). The secant stiffness after flexural cracking was calculated as the applied load at which web-shear cracking was first observed, divided by the corresponding horizontal displacement.  $F_{ws1}$  and  $D_{ws1}$  are the load and displacement at which web-shear cracking was first observed in the south direction, and  $F_{wn1}$  and  $D_{wn1}$  are the corresponding values in the north direction. Two secant stiffnesses were calculated for each shear-dominated specimen; one in the south direction ( $K_{cr-os}$ ) and the other in the north direction ( $K_{cr-on}$ ) (Figure 4.14). The unloading stiffness after web shear cracking was calculated using the tangent to the load-displacement curve on first unloading after observed web-shear cracking (Figure 4.15). Two unloading stiffnesses were calculated for each shear-dominated specimen, one corresponding to displacements in the south direction ( $K_{u-os}$ ) and the other to displacements in the north direction ( $K_{u-on}$ ).  $D_{u-os}$  and  $D_{u-on}$  are the maximum observed displacements in the load cycles at which those unloading stiffnesses were calculated in the south and north directions respectively. The strength ratio after web shear cracking was calculated as the maximum applied

load in the corresponding next cycle after web shear cracking divided by the applied load at which web shear cracking was first observed during the test.  $F_{ws2}$  and  $F_{wn2}$  are the maximum loads in the following cycle after web shear cracking was first observed in the south and north directions respectively, and  $D_{ws2}$  and  $D_{wn2}$  are the displacements corresponding to those loads. Two strength ratios were calculated for each shear-dominated specimen, one for loading to the south, and the other to the north.

#### 4.2.2.1 Shear Wall Specimen 18

The initial tangent stiffness and the initial backbone stiffness of Shear Wall Specimen 18 were 300.7 kips/in. (52.7 kN/mm) and 299.5 kips/in. (52.5 kN/mm) respectively (Figure 4.13).

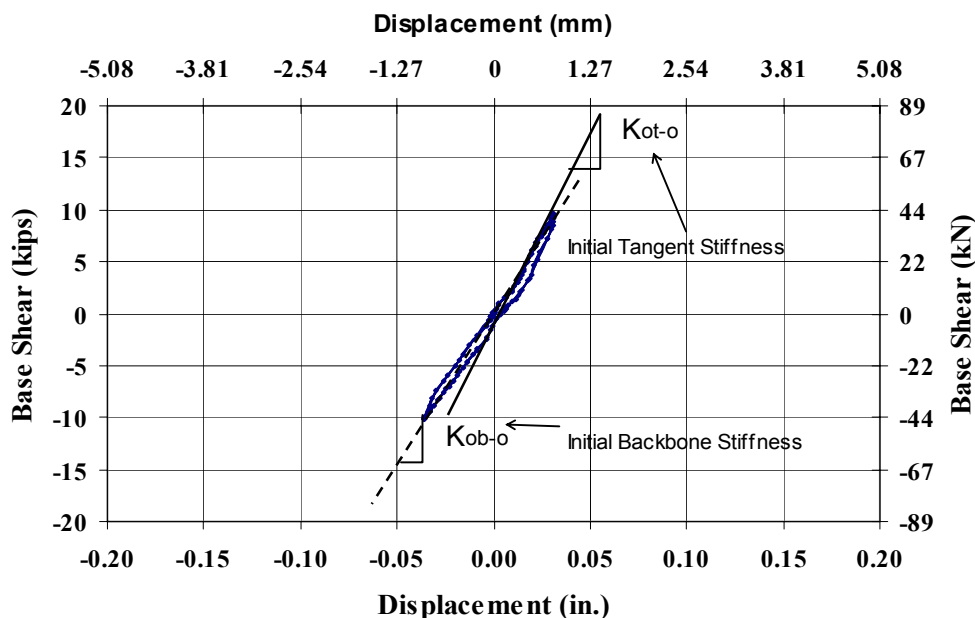
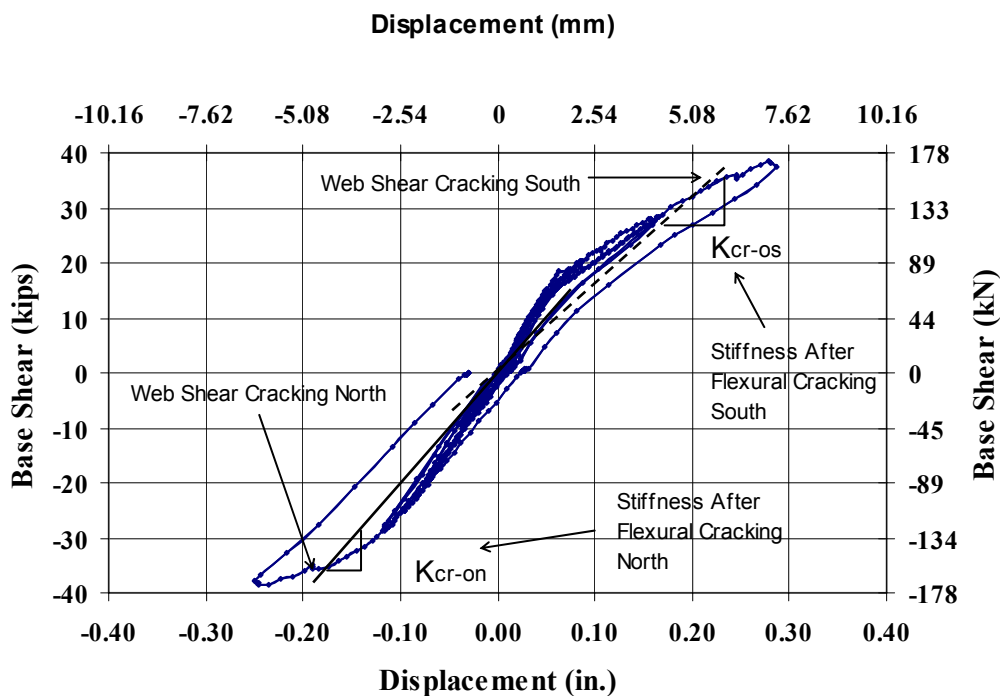


Figure 4.13: Initial tangent and backbone stiffnesses for Shear Wall Specimen

The web-shear cracking load in the north direction was 35.66 kips (158.7 kN); the horizontal displacement was 0.18 in. (4.6 mm); and the corresponding stiffness after flexural cracking was 198.1 kips/in. (34.7 kN/mm). In the south direction, the corresponding values were 36.07 kips (164.58 kN), 0.24 in. (6.1 mm), and 150.3 kips/in.(26.4 kN/mm). Figure 4.14 shows secant stiffnesses after flexural cracking for Shear Wall Specimen 18.



**Figure 4.14: Secant stiffnesses after flexural cracking for Shear Wall Specimen**

**18**

The unloading stiffnesses after web-shear cracking in the south and north directions were 138.6 kips/in. (24.3 kN/mm) and 140.0 kips/in. (24.55 kN/mm) respectively (Figure 4.15).

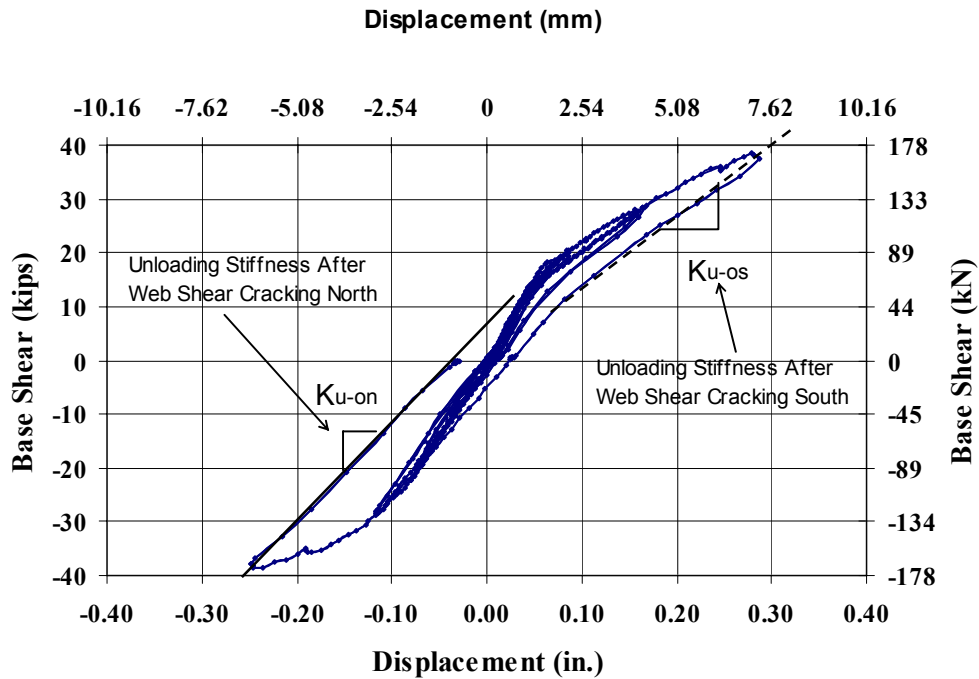


**Figure 4.15: Unloading stiffnesses after web shear cracking for Shear Wall Specimen 18**

The maximum capacity in the next cycle in the south direction after web-shear cracking was first observed in that same direction was 39 kips (173 kN), at a horizontal displacement of 0.31 in. (7.8 mm), and the corresponding strength ratio between the observed web-shear cracking load and the maximum observed load at the next cycle was 1.08. The corresponding values for the north direction were 37.9 kips (168.9 kN), 0.26 in. (6.6 mm), and 1.06. Both sets of values are shown in Figure 4.16 for Shear Wall Specimen 18. The complete hysteretic load-displacement response of Shear Wall Specimen 18 at the end of the test is presented in Figure 4.17.

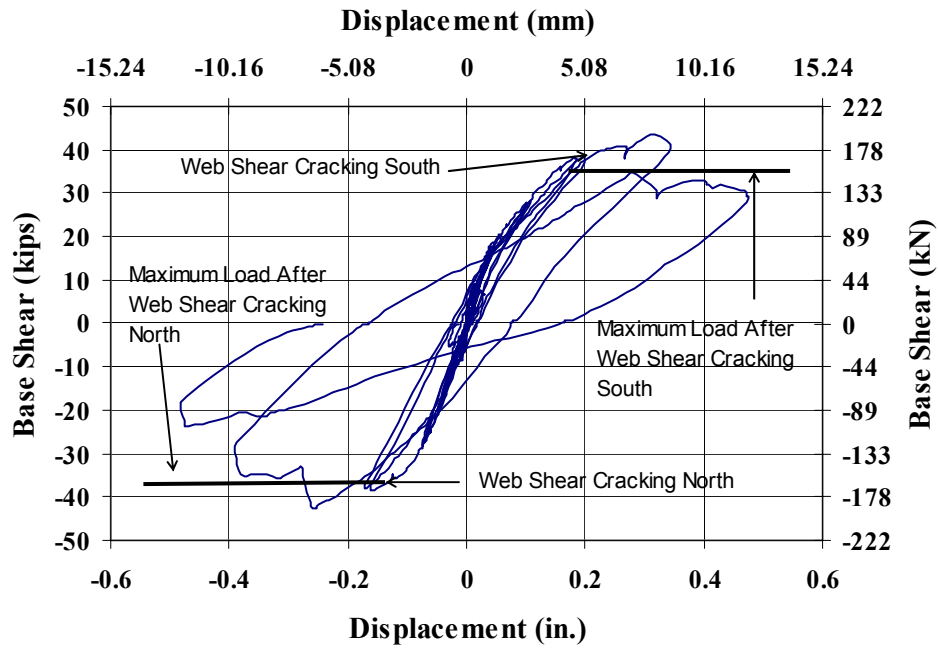


*Figure 4.16: Maximum applied load after web shear cracking in the south and north directions for Shear Wall Specimen 18*



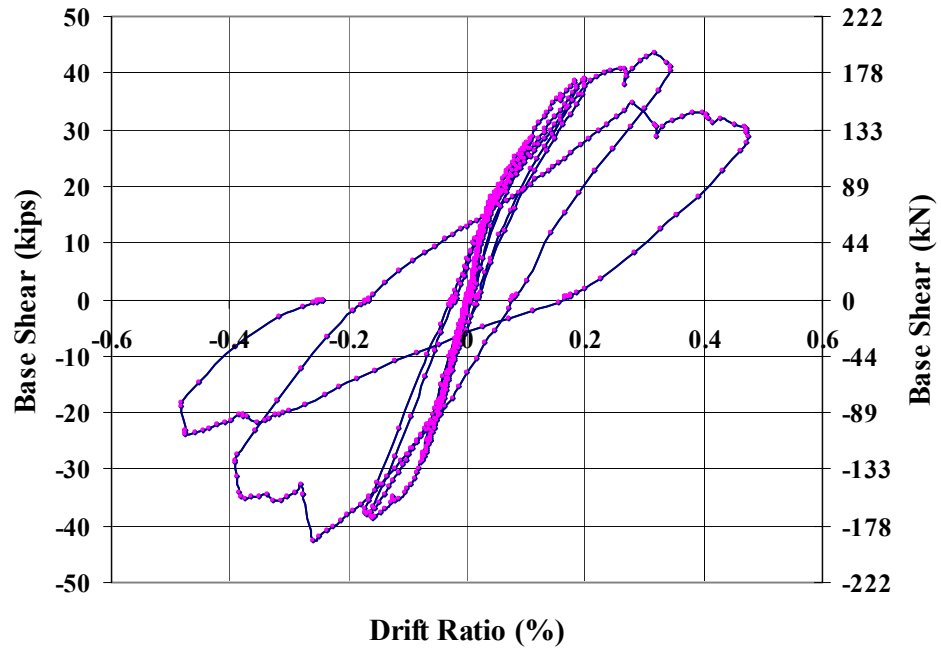


*Figure 4.17 Load- displacement response of Shear Wall Specimen 18*

#### 4.2.2.2 Shear Wall Specimen 19

The initial tangent stiffness and the initial backbone stiffness of Shear Wall Specimen 19 were 586.1 kips/in. (102.8 kN/mm) and 548.3 kips/in. (96.1 kN/mm) respectively (Figure 4.18).

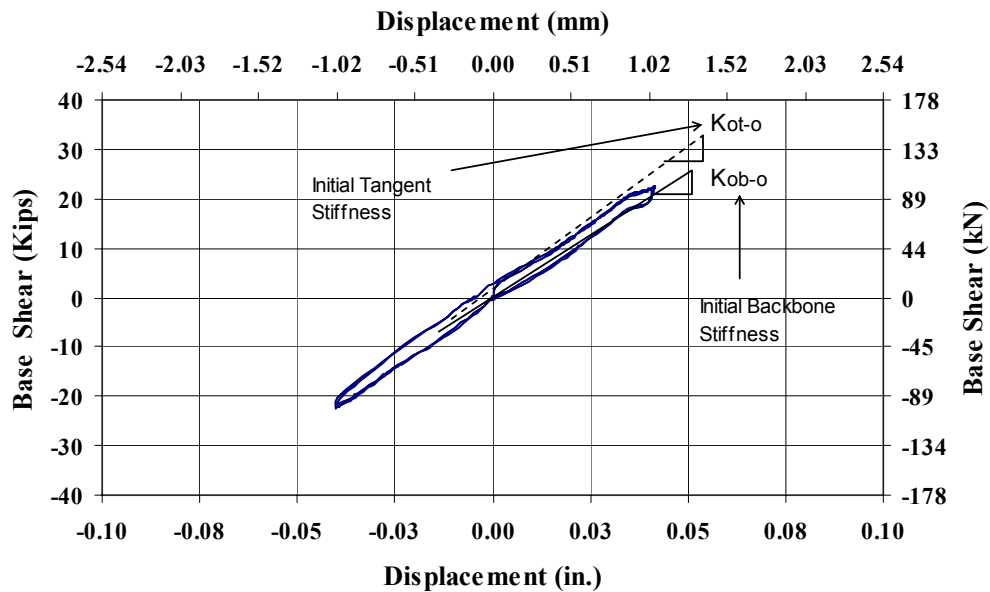


**Figure 4.18: Initial tangent and backbone stiffnesses for Shear Wall Specimen 19**

The web-shear cracking load in the north direction was 54.84 kips (243.9 kN), at a horizontal displacement of 0.13 in. (3.3 mm). The corresponding stiffness after flexural cracking was 421.8 kips/in. (73.9 kN/mm). In the south direction, the corresponding values were 56.00 kips (249.1 kN), 0.19 in. (4.8 mm), and 294.7 kips/in. (51.7 kN/mm). Figure 4.19 shows both secant stiffnesses after flexural cracking for Shear Wall Specimen 19.

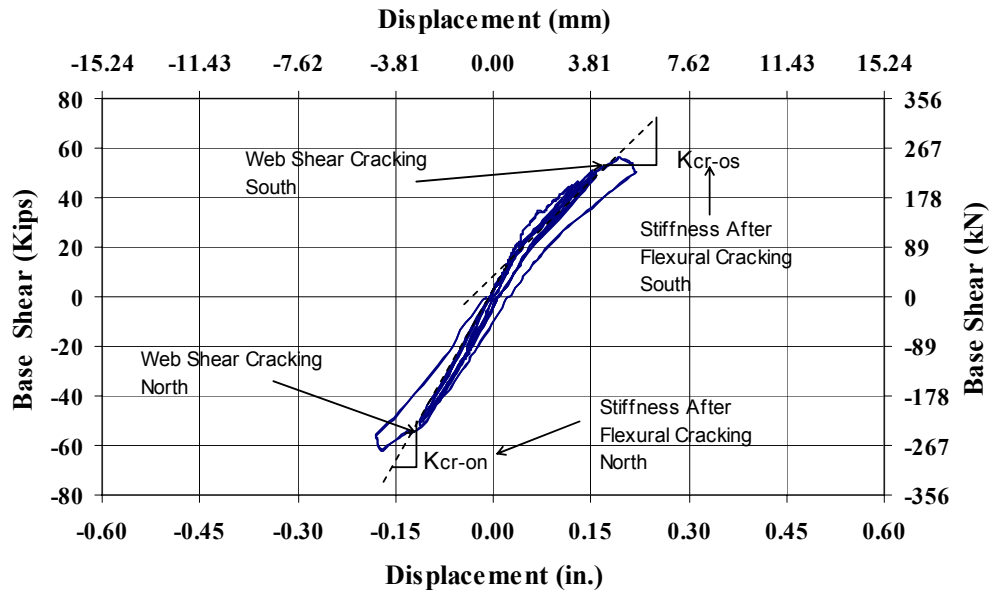


**Figure 4.19: Secant stiffnesses after flexural cracking for Shear Wall Specimen**

19

The unloading stiffnesses after web-shear cracking in the south and north directions were 227.6 kips/in. (39.9 kN/mm) and 320.7 kips/in. (56.25 kN/mm) respectively (Figure 4.20).

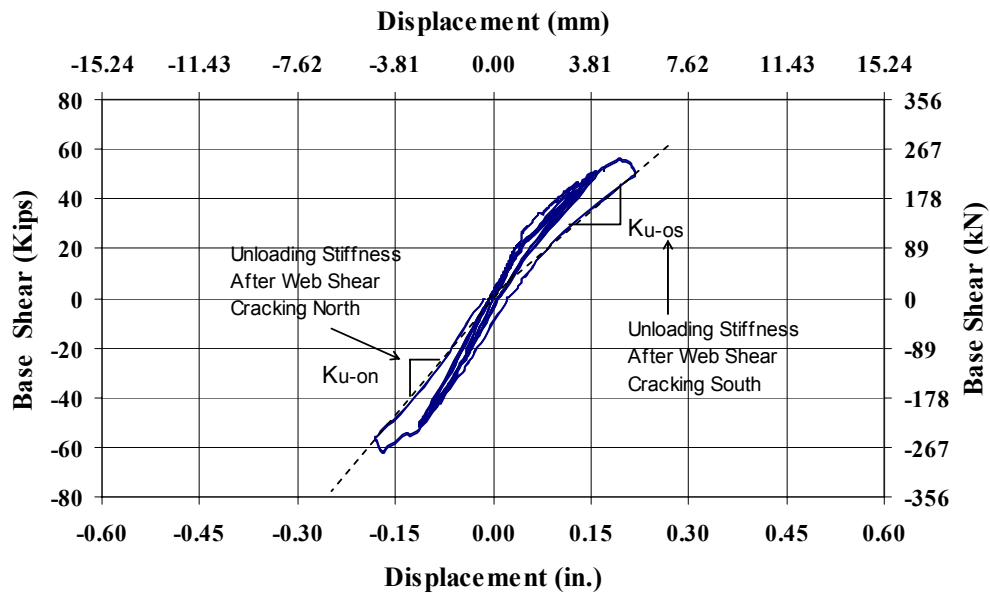


**Figure 4.20: Unloading stiffnesses after web-shear cracking for Shear Wall Specimen 19**

The maximum capacity in the south direction in the next cycle after web shear-cracking was first observed in that direction was 56.78 kips (255 kN), at a displacement of 0.25 in. (6.4 mm), and the corresponding strength ratio between the observed web-shear cracking load and the maximum observed load at the next cycle was 1.01. In the north direction, the corresponding values were 59.5 kips (267.9 kN), 0.20 in. (5.1 mm), and 1.08. Both maximum applied loads in the next corresponding cycles after web-shear cracking are shown in Figure 4.21 for Shear Wall Specimen 19. The complete hysteretic load-displacement response of Shear Wall Specimen 19 at the end of the test is presented in Figure 4.22.

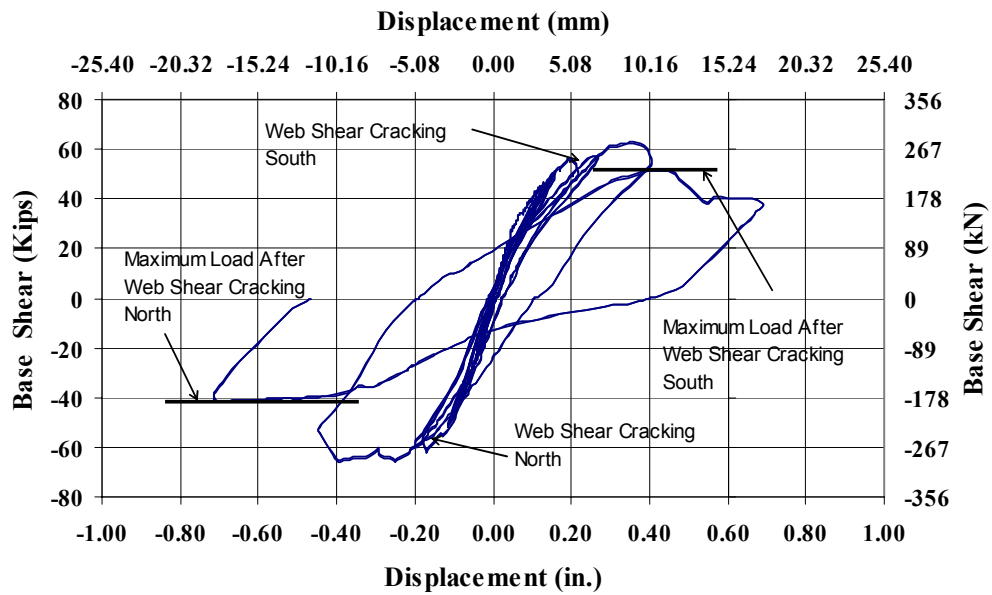


*Figure 4.21: Maximum applied load after web-shear cracking in the south and north directions for Shear Wall Specimen 19*

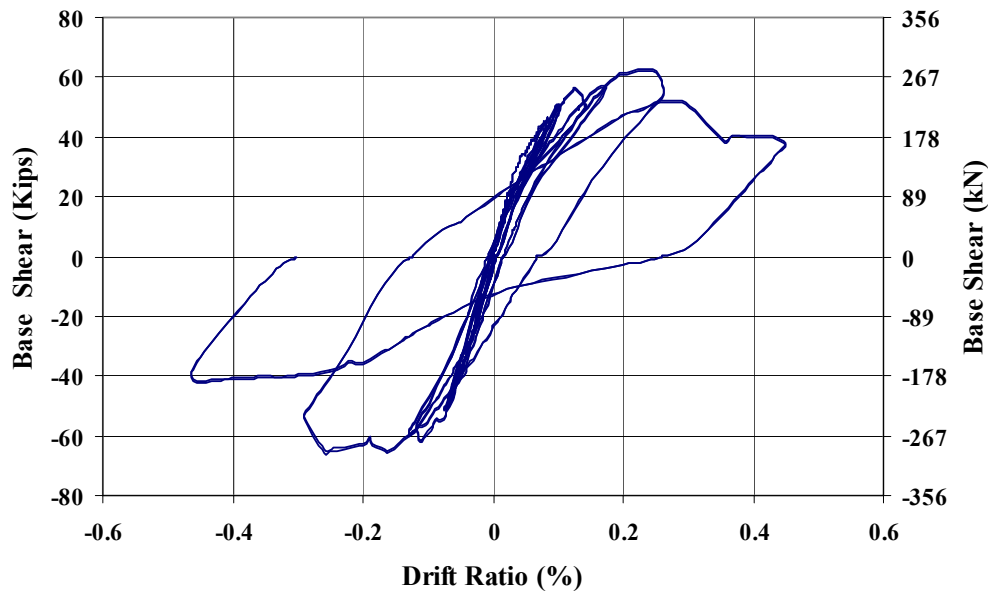


**Figure 4.22 Load-displacement response of Shear Wall Specimen 19**

#### **4.2.2.3 Summary of Results for Shear Wall Specimens 18 and 19**

In this section, the hysteretic behavior of Shear Wall Specimens 18 and 19 is compared with that of the shear-dominated specimens of Varela (2003).

The observed initial tangent stiffness ( $K_{ot-o}$ ), initial backbone stiffness ( $K_{ob-o}$ ), and the ratio of the initial backbone stiffness to initial tangent stiffness for Shear Wall Specimens 18 and 19, are compared in Table 4.12 with the corresponding mean value of the shear-dominated specimens tested by Varela (2003). The ratio of observed backbone stiffness to initial tangent stiffness of the Shear Wall Specimens 18 and 19 is consistent with the corresponding mean value of the specimens tested by Varela (2003). The difference between the absolute stiffnesses obtained in this study and the corresponding to those of the specimens tested by Varela (2003) are due to differences in material ( $f_{AAC}$ ), geometry, and reinforcement.

**Table 4.12 Observed initial tangent and backbone stiffnesses for shear-dominated specimens**

<b>Specimen Number</b>	<b><math>K_{ot-o}</math> Kips/in. (kN/mm)</b>	<b><math>K_{ob-o}</math> Kips/in. (kN/mm)</b>	<b><math>K_{ob-o}/K_{ot-o}</math></b>
18	300.7 (52.7)	299.5 (52.5)	0.99
19	586.1 (102.8)	548.3 (96.1)	0.94
Specimens of Varela (2003)	464.6 (81.5) COV (65 %)	459.4 (80.6) COV (65 %)	0.98

The observed secant stiffnesses after flexural cracking in the south ( $K_{cr-os}$ ) and north ( $K_{cr-on}$ ) directions, and the ratio of those observed secant stiffness after flexural cracking to initial tangent stiffness for Shear Wall Specimens 18 and 19 and the corresponding mean value of the shear-dominated specimens tested by Varela (2003), are presented in Table 4.13. The ratios are consistent with the corresponding mean values of the specimens tested by Varela (2003).

**Table 4.13 Secant stiffnesses after flexural cracking for shear-dominated specimens**

<b>Specimen Number</b>	<b><math>K_{cr-os}</math> Kips/in. (kN/mm)</b>	<b><math>K_{cr-os} / K_{ot-o}</math></b>	<b><math>K_{cr-on}</math> Kips/in. (kN/mm)</b>	<b><math>K_{cr-on} / K_{ot-o}</math></b>
18	150.3 (26.4)	0.50	198.1 (34.7)	0.66
19	294.7 (51.7)	0.50	421.8 (73.9)	0.72
Specimens of Varela (2003)	263.1 (46.1) COV (88 %)	0.56	347.1 (60.8) COV (74 %)	0.75

The unloading stiffnesses after web shear cracking in the south ( $K_{u-os}$ ), and north ( $K_{u-on}$ ) directions, and the ratio of those unloading stiffnesses to the initial tangent stiffness for Shear Wall Specimen 18 and 19 and the corresponding mean value of the shear-dominated specimens tested by Varela are presented in Table 4.14. The ratios are consistent with the corresponding mean values of the specimens tested by Varela (2003).



**Table 4.14 Unloading stiffnesses after web shear cracking in the south and north direction for shear-dominated specimens**

<b>Specimen Number</b>	<b><math>K_{u-os}</math> Kips/in. (kN/mm)</b>	<b><math>K_{u-os}/K_{ot-o}</math></b>	<b><math>D_{u-os}/D_{ws1}</math></b>	<b><math>K_{u-on}</math> Kips/in. (kN/mm)</b>	<b><math>K_{u-on}/K_{ot-o}</math></b>	<b><math>D_{u-on}/D_{wn1}</math></b>
18	138.6 (24.3)	0.46	1.17	140.0 (24.5)	0.47	1.38
19	227.6 (39.9)	0.39	1.15	320.7 (56.3)	0.54	1.39
Specimens of Varela (2003)	280.1 (49.1) COV (73 %)	0.60	1.15 COV (15 %)	298.1 (52.2) COV (75 %)	0.64	1.19 COV (17 %)

The strength ratio after web shear cracking and the ratio of the horizontal displacement at the maximum applied load in the corresponding next cycle after web shear cracking, to the horizontal displacement at web shear cracking in the south and north directions for Shear Wall Specimens 18 and 19, are compared in Table 4.15 with the corresponding mean value of the shear-dominated specimens tested by Varela (2003). The strength ratios after web shear cracking in both south and north directions of Shear Wall Specimens 18 and 19 are similar. The strength ratios after web shear cracking in both south and north directions for Shear Wall Specimens 18 and 19 are consistent with the corresponding mean values of the specimens tested by Varela (2003).

***Table 4.15 Strength ratios after web shear cracking and corresponding displacement ratios for shear-dominated specimens***

<b>Specimen Number</b>	<b><math>F_{ws2} / F_{ws1}</math></b>	<b><math>D_{ws2} / D_{ws1}</math></b>	<b><math>F_{wn2} / F_{wn1}</math></b>	<b><math>D_{wn2} / D_{wn1}</math></b>
18	1.08	1.29	1.06	1.44
19	1.01	1.32	1.08	1.54
Specimens of Varela (2003)	0.94 COV (26 %)	1.51 COV (28 %)	0.91 COV (34 %)	1.66 COV (22 %)

The shear capacity of Shear Wall Specimens 18 and 19 was governed by crushing of the diagonal strut. The overall hysteretic behavior of these two specimens was characterized by a sudden degradation in stiffness after web-shear cracking, and showed a behavior consistent with that of the shear-dominated specimens tested by Varela (2003).

The main conclusion obtained from the comparison between the test results and the predicted results is that the proposed design provisions for shear capacity accurately predicted the capacities of shear-dominated Shear Wall Specimens 18 and 19. This permits one to conclude that these design provisions, originally developed for shear walls using higher-strength AAC specimens, are valid for low-strength AAC specimens as well.

## CHAPTER 5

### Summary, Conclusions and Recommendations

#### 5.1 SUMMARY

The purpose of this study was to evaluate the results of reversed cyclic load tests on 3 shear-wall specimens constructed with low-strength AAC (autoclaved aerated concrete). One shear wall specimen (SWS17) was designed to exhibit flexure-dominated behavior; the other two (SWS18 and SWS19) were designed to exhibit shear-dominated behavior.

The flexure-dominated specimen was constructed with vertically oriented, reinforced panels of low-strength AAC material. The objectives of this test were to examine the specimen's general hysteretic behavior, and to evaluate possible improvements in that behavior due to stainless steel spiral ties connecting the extreme-fiber elements to the remainder of the specimen.

The shear-dominated specimens were constructed with masonry-type units of low-strength AAC material. The specimens, with aspect ratios (height to plan length) of 0.71 and 1.34, had different arrangements of flexural reinforcement. The objectives of these tests were to examine the specimens' overall hysteretic behavior and to validate the applicability to low-strength AAC shear walls, of proposed design provisions previously developed based on shear-wall and assemblage tests with higher-strength AAC material. The overall hysteretic behavior of the specimens tested in this study was compared with the corresponding behavior of those specimens tested by Varela (2003). The results obtained with the proposed design provisions for the different capacities of the

specimens tested in this study were compared with the corresponding mean values of those specimens tested by Tanner (2003).

In each test, quasi-static reversed cyclic loads were applied to each specimen, and the major events and overall hysteretic behavior were evaluated. After each test, overall damage was summarized; major events and hysteretic behavior were compared with predicted responses; and maximum drift ratios and displacement ductilities were assessed.

This study is the final facet of an extensive research project performed at the Ferguson Structural Engineering Laboratory of The University of Texas at Austin, using results from that and other testing laboratories (Tanner 2003, Varela 2003, Argudo 2003).

## **5.2 CONCLUSIONS**

- 1) Previously proposed design provisions for nominal flexural capacity accurately predicted the capacity of flexure-dominated Shear Wall Specimen 17, and therefore are valid for low-strength AAC specimens as well as the higher-strength AAC specimens originally used to develop those provisions.
  
- 2) The maximum useful strain obtained in this study for low-strength AAC was less than the value of 0.003 reported by Tanner (2003). In fact, the maximum useful strain decreases with decreasing compressive strength, and was between 0.0015 and 0.002 for low-strength AAC. Because that capacity is governed by the mechanical characteristics of the reinforcement in all practical cases, regardless of the value of  $\epsilon_{AAC \max}$ , previously proposed expressions for nominal flexural capacity are still

valid. Previously proposed expressions for AAC modulus as a function of specified compressive strength are also valid.

- 3) Stainless steel spiral ties, used to connect the end U-blocks of Shear Wall Specimen 17 to the vertical panels comprising the rest of the wall, significantly reduced deterioration of the compression toes of that specimen under cycles of reversed cyclic load. The specimen achieved in-plane lateral drift ratios of 0.65 % and lateral ductilities of 5 in both directions.
- 5) Previously proposed design provisions for web-shear capacity accurately predicted the capacity of shear-dominated Shear Wall Specimens 18 and 19, and therefore are valid for low-strength AAC specimens as well as the higher-strength AAC specimens originally used to develop those provisions.
- 6) The shear capacity of Shear Wall Specimens 18 and 19 was governed by crushing of the diagonal strut, at a drift ratio of 0.37 % (loading to the north) for Shear Wall Specimen 18 and 0.26 % (loading to the north) for Shear Wall Specimen 19.
- 7) The overall hysteretic behavior of the shear-dominated specimens (SWS18 and SWS19) was characterized by a sudden degradation in stiffness after web-shear cracking and showed a behavior consistent with that of the shear-dominated specimens tested by Varela (2003). The maximum drift ratios obtained for Shear Wall Specimens 18 and 19 were 0.48 % and 0.49 % in both directions respectively.

- 8) The ductilities and drifts obtained in this study are consistent with those obtained by Varela (2003) for flexure-dominated shear walls of higher-strength AAC material, in spite of the lower maximum useable strain of the low-strength AAC. Therefore, the  $R$  and  $C_d$  values proposed by Varela (2003) are valid for low-strength AAC material as well.
- 9) Based on the close agreement obtained between observed and predicted values for capacities and stiffnesses, the analytical models used to represent the behavior of shear-dominated and flexure-dominated specimens, constructed with AAC material of medium and high compressive strength, are also applicable to specimens constructed with AAC material of low compressive strength.

### **5.3 RECOMMENDATIONS FOR FUTURE WORK**

- 1) Additional testing should be performed on AAC shear walls with openings. Such testing would provide information about the behavior (limit states) of AAC walls with openings compared to the capacity predictions of current design provisions.
- 2) Additional work should be performed to develop strut-and-tie models for AAC walls. These models would offer the possibility of simplified design approaches by combining web-shear cracking, flexure-shear cracking and crushing of the diagonal strut, in a single design model.
- 3) Additional research should be performed on ways to use grouted regions within AAC shear walls to increase their resistance to flexural

compression, to crushing of the diagonal strut, and perhaps to sliding. Possible failure at the interface between the AAC material and the grout can be avoided using spiral ties. The purpose of this research would be to improve the strength and ductility of AAC shear walls.

- 4) Additional research should be conducted on the behavior and design of AAC infill panels in frames of structural steel or reinforced concrete. Such infills could increase the strength, stiffness and energy dissipation capacity of framed structures, in retrofit as well as new construction.
- 5) Additional research should be conducted on increasing the sliding-shear capacity of AAC shear walls. This would result in AAC structures with higher factors of safety against sliding in zones with large spectral ordinates.

# **APPENDIX A**

## **Design Provisions for Reinforced AAC Shear Walls**

### **A.1 DESIGN OF AAC SHEAR WALLS**

Appendix A was originally developed as part of the PhD dissertation of Tanner (2003). It is included here so that the reader will be able to see the context in which the design provisions discussed in this thesis were originally proposed.

A suite of 14 AAC shear wall specimens, with aspect ratios (height of the point of load application divided by the plan length) from 0.6 to 3, has been tested at the University of Texas at Austin. The behavior of each shear wall may be shear- or flexure-dominated. The shear-dominated specimens were heavily reinforced in flexure using external reinforcement. The flexure-dominated specimens were lightly reinforced in flexure. The test setup is shown in Figure A.1.



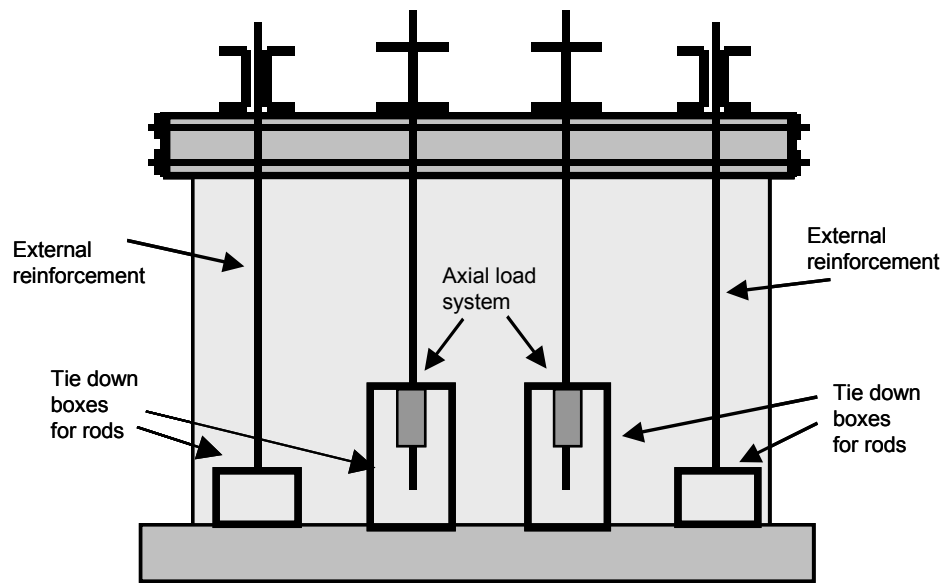


*Figure A.1 Test set up for shear wall specimens (UT Austin)*

Physical details for each specimen are presented in Table A.1. The number after the supplier's name identifies in which shipment the AAC material arrived.

**Table A.1 Details of shear wall specimens tested at UT Austin**

Specimen	Failure Mode	AAC units	Material supplier	Length in. (m)	Height in. (m)	Thickness in. (m)	Aspect Ratio	Interior Vertical Reinforcement
1	Shear	Horiz. Panels	Contec 1	240 (6.1)	154 (3.9)	8 (0.2)	0.64	No
2	Shear	Vert. Panels	Ytong 1	240 (6.1)	154 (3.9)	8 (0.2)	0.64	No
3	Shear	Blocks	Ytong 2	240 (6.1)	151 (3.8)	8 (0.2)	0.63	No
4	Shear	Horiz. Panels	Matrix 1	240 (6.1)	154 (3.9)	8 (0.2)	0.64	#5 (16 mm) at 48 in. (1.2 m)
5	Shear	Blocks	Contec 2	240 (6.1)	151 (3.8)	8 (0.2)	0.63	No
7	Shear	Blocks	Ytong 2	144 (3.7)	151 (3.8)	8 (0.2)	1.05	No
9	Shear	Horiz. Panels	Matrix 1	96 (2.4)	154 (3.9)	8 (0.2)	1.60	No
11	Shear	Blocks	Contec 2	48 (1.2)	151 (3.8)	8 (0.2)	3.15	No
13	Flexure	Horizontal Panels	Ytong 1	72 (2.1)	154 (3.9)	8 (0.2)	2.13	# 5 (16 mm) 12 in. (0.6 m) from ends
14a	Flexure	Horizontal Panels	Babb 1	56 (1.4)	154 (3.9)	10 (0.3)	3.2	# 5 (16 mm) 4 in. (0.1 m) from ends
14b	Flexure	Horizontal Panels	Babb 1	56 (1.4)	154 (3.9)	10 (0.3)	3.2	# 5 (16 mm) 4 in. (0.1 m) from ends
15a	Flexure	Vertical Panels with End Blocks	Babb 1	112 (2.8)	154 (3.9)	10 (0.3)	1.4	# 5 (16 mm) 8 in. (0.2 m) from ends
15b	Flexure	Vertical Panels with End Blocks	Babb 1	112 (2.8)	154 (3.9)	10 (0.3)	1.4	# 5 (16 mm) 8 in. (0.2 m) from ends
16	Flexure	Vertical Panels with U End Blocks	Babb 1	112 (2.8)	154 (3.9)	10 (0.3)	1.4	# 5 (16 mm) 8 in. (0.2 m) from ends
17	Flexure	Vertical Panels with U End Blocks	Babb 2	112 (2.8)	154 (3.9)	10 (0.3)	1.4	# 5 (16 mm) 8 in. (0.2 m) from ends

Results from a suite of 12 shear-wall tests performed by Hebel (Germany) provide additional information<sup>1</sup>. Each of those walls measured 8.2 ft (2.5 m) long, 8.2 ft (2.5 m) tall and 9.5 in. (0.24 m) thick. The aspect ratio of each specimen is 1.0. The test set up is shown in Figure A.2. Additional physical details for each Hebel specimen are presented in Table A.2.

<sup>1</sup> Personal communication, Violandi Vratsanou, Hebel AG, Germany, November 2000

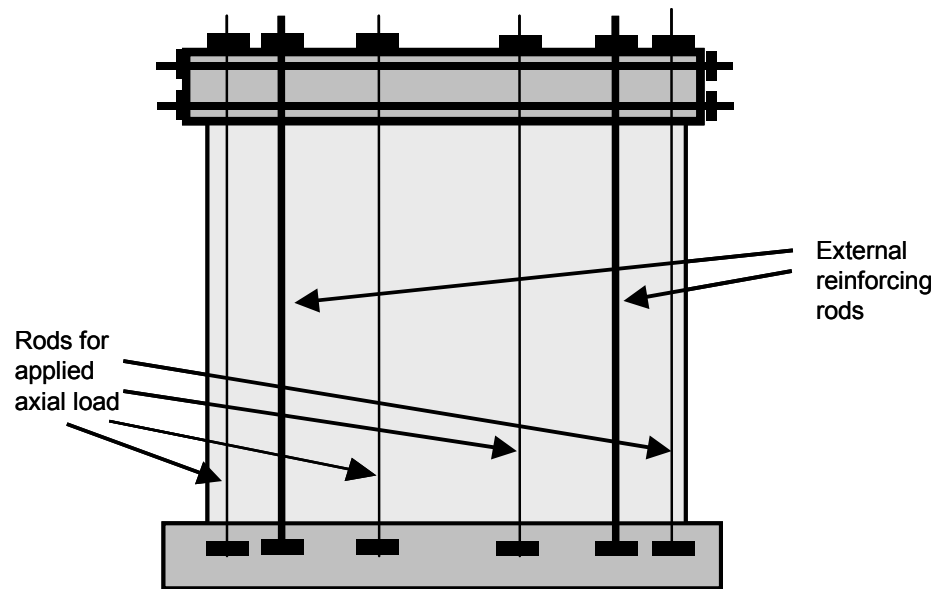


*Figure A.2 Test setup for shear wall specimens at Hebel (Germany)*

*Table A.2 Details of shear wall specimens tested by Hebel (Germany)*

Specimen	AAC Units	Mortared Head Joints	Type of Running Bond
3.3	Blocks	No	one-half
3.2	Blocks	No	one-half
3.4	Blocks	No	one-half
3.5	Blocks	No	one-fifth
3.6	Blocks	Yes	one-fifth
4.3	Blocks	No	one-half
4.4	Blocks	No	one-half
4.1	Blocks	No	one-half
4.5	Blocks	No	one-fifth
4.6	Blocks	No	one-fifth
4.7	Blocks	Yes	one-fifth
4.8	Blocks	Yes	one-fifth

In the Hebel tests, axial load was applied using uniformly spaced, external post-tensioning rods. This axial load was monitored and was kept constant. Two additional 1 in. (25 mm) diameter rods on each side of the wall, with initial pre-tension less than 0.5 kip (2 kN), were used as external reinforcement. As the wall

displaces laterally in its own plane, tensile forces increase in the external reinforcement on the tension side. The rods on the compressive side of the wall are not initially post-tensioned, so the force in them does not decrease as the force in the tension rods increases. Increasing the force in the tension rods without decreasing the force in the compression rods is equivalent to applying an additional compressive axial load to the wall. Therefore, the axial load in the Hebel specimens changed as the lateral load changed. The axial load used to evaluate the behavior of the Hebel specimens at each state is the initial axial load (including weight of loading equipment) plus the summation of tensile forces in the rods at that state.

### A.1.1 Web-shear Cracking

Using additional data points determined at UT Austin between November 2001 and August 2002, the relationship between splitting tensile strength and “1386 density” presented in Equation (A.1) has been replaced by  $f_t = 2.4 \sqrt{f'_{AAC}}$ . As discussed in this section, that difference in splitting tensile strength is less a few percent, and the actual change in computed values of  $V_{AAC}$  is quite small.

This section is dedicated to explaining the changes. The form of the equation for  $V_{AAC}$  will stay the same, with only slight changes in the external coefficients. In the following section, the derivation of the equation for web-shear cracking is reviewed.

$$V_{AAC} = 0.9 \ell_w t \sqrt{f'_{AAC}} \sqrt{1 + \frac{P_u}{2.4 \sqrt{f'_{AAC}} \ell_w t}} \quad \text{Equation (A.1)}$$

$$V_{AAC} = 0.6 \ell_w t \sqrt{f'_{AAC}} \sqrt{1 + \frac{P_u}{2.4 \sqrt{f'_{AAC}} \ell_w t}} \quad \text{Equation (A.2)}$$

$$V_{AAC} = 0.37 \ell_w t f_t \sqrt{1 + \frac{P_u}{f_t \ell_w t}} \quad \text{Equation (A.3)}$$

$$V_{AAC} = 0.25 \ell_w t f_t \sqrt{1 + \frac{P_u}{f_t \ell_w t}} \quad \text{Equation (A.4)}$$

This inclined crack forms when the principal tensile stress in the web exceeds the tensile strength of the AAC. That principal stress is given by Equation (A.5), in which the normal stress in the wall is  $n$  and the maximum shear stress in the center of the web is  $v$ .

$$f_t = \sqrt{\left[\left(\frac{n}{2}\right)^2 + (v^2)\right]} - \frac{n}{2} \quad \text{where} \quad v = \frac{3V}{2l_w t} \quad \text{and} \quad n = \frac{P}{l_w t} \quad \text{Equation (A.5)}$$

Substituting the equations for shear stress and axial stress into the above equation, and solving for the shear, the corresponding shear capacity is given by Equation (A.6):

$$V_{AAC} = \frac{2l_w t}{3} f_t \cdot \left[1 + \left(\frac{P}{f_t l_w t}\right)\right]^{0.5} \quad \text{Equation (A.6)}$$

For reinforced concrete shear walls, ACI 318-02 uses a conservative (low) diagonal tensile capacity of  $4\sqrt{f'_c}$  (US customary units) to develop a

conservative, semi-empirical equation for shear capacity as governed by web-shear cracking (ACI 318-02).

Web-shear cracking was observed in all AAC shear-wall specimens tested at The University of Texas at Austin except Shear Wall Specimen 2 (constructed of vertical panels). In addition, the tests performed by Hebel (Germany) provide corroborating data on shear strength as controlled by web-shear cracking. The observed and predicted web-shear cracking capacities based on Equation (A.6) are presented in Table A.3 and Table A.4 for fully and partially mortared specimens respectively.

***Table A.3 Initial predictions of capacity as governed by web-shear cracking for fully mortared specimens***

<b>Specimen</b>	<b>Axial load, P kips (kN)</b>	<b>Observed <math>V_{AAC}</math> kips (kN)</b>	<b>Predicted <math>V_{AAC}</math> kips (kN)</b>	<b>Observed <math>V_{AAC}</math> / Predicted <math>V_{AAC}</math></b>
1 (UT)	156.0 (694)	164.2 (730)	127.7 (568)	1.29
3 (UT)	120.0 (534)	81.3 (362)	111.4 (495)	0.73
4 (UT)	120.0 (534)	110.5 (492)	132.5 (589)	0.83
5 (UT)	60.0 (267)	62.2 (277)	117.4 (522)	0.53
7 (UT)	80.0 (356)	57.4 (255)	68.7 (305)	0.84
9 (UT)	30.0 (267)	37.7 (168)	55.9 (249)	0.67
11 (UT)	25.0 (111)	15.6 (69)	26.9 (120)	0.58
Assemblage (UT)	25.0 (111)	52.0 (231)	96.7 (430)	0.54
3.6 (Hebel)	36.8 (164)	27.7 (123)	39.3 (175)	0.71
4.7 (Hebel)	62.4 (277)	46.7 (208)	57.7 (256)	0.81
4.8 (Hebel)	178.2 (792)	61.5 (273)	80.3 (357)	0.77
			Mean	0.70
			COV (%)	16.8

**Table A.4 Initial predictions of capacity as governed by web-shear cracking for partially mortared specimens**

Specimen	Axial load, P kips (kN)	Observed $V_{AAC}$ kips (kN)	Predicted $V_{AAC}$ kips (kN)	Observed $V_{AAC}$ / Predicted $V_{AAC}$
3.3 (Hebel)	60.0 (267)	18.3 (81)	36.2 (161)	0.50
3.2 (Hebel)	26.2 (116)	20.6 (92)	42.0 (187)	0.49
3.4 (Hebel)	49.7 (221)	24.4 (109)	52.2 (232)	0.47
3.5 (Hebel)	89.8 (399)	18.2 (81)	36.7 (163)	0.49
4.3 (Hebel)	30.3 (135)	23.7 (105)	49.4 (220)	0.48
4.4 (Hebel)	30.3 (135)	32.1 (143)	62.7 (279)	0.51
4.1 (Hebel)	85.5 (380)	25.1 (112)	76.7 (341)	0.33
4.5 (Hebel)	153.9 (685)	21.3 (95)	48.5 (216)	0.44
4.6 (Hebel)	33.5 (149)	29.9 (133)	74.5 (331)	0.40
			Mean	0.46
			COV (%)	13.1

The shear strength of the AAC shear-wall specimens was initially predicted using Equation (A.6). The ratios of observed to predicted capacities, shown in Table A.3, indicate that the ratio of observed strength to predicted strength of Shear Wall Specimen 1 (UT Austin) is significantly greater than for the other specimens, and can be considered an anomaly with respect to the rest of the tests. The remaining specimens show lower observed than predicted strengths, indicating that Equation (A.6) is unconservative.

To further evaluate the effects of mortared head joints, the AAC shear-walls tested at UT Austin and by Hebel (Germany) are divided into two groups: those with fully mortared head joints, and those with unmortared head joints. The range of ratios of observed  $V_{AAC}$  to predicted  $V_{AAC}$  is 0.54 to 0.1.29 for the fully mortared specimens, and 0.33 to 0.51 for the partially mortared specimens. For the specimens with fully mortared head joints, the mean ratio of observed to predicted  $V_{AAC}$  is 0.70, with a coefficient of variation of 17%. For the specimens with unmortared head joints, corresponding values are 0.46 and 13%.

These data can be plotted in Figure A.3 and Figure A.4. In each figure, the mean ratio of observed capacity to that predicted using the theoretical Equation (A.6) is represented by a solid horizontal line. Also plotted on each figure is the normal distribution with the same mean and COV as the test data. The lower 10% fractile of that distribution, shown by a dashed horizontal line, has a value of 0.55 for the fully mortared specimens and 0.38 for the partially mortared ones.

Equation (A.6) was therefore reduced so that it would correspond to the lower 10% fractiles of the ratios of observed to predicted capacities. In carrying out that reduction, fully mortared and partially mortared specimens were considered separately. Equation (A.6) was multiplied by 0.55 to obtain proposed Equation (A.1) for fully mortared specimens. In the same way, Equation (A.6) was multiplied by 0.38 to obtain proposed Equation (A.2) for partially mortared specimens.

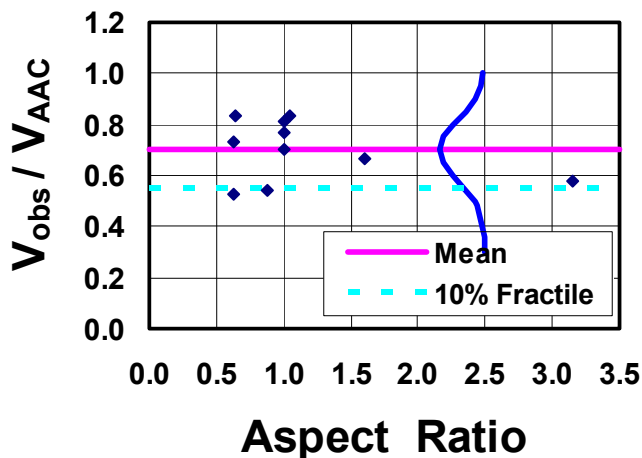


**Figure A.3 Ratios of observed to predicted (Equation (A.6)) web-shear cracking capacities for AAC shear-wall specimens with fully mortared head joints**



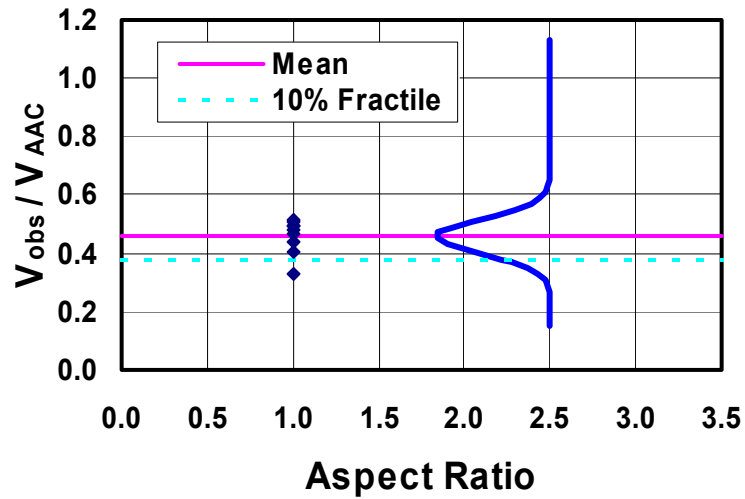


**Figure A.4 Ratios of observed to predicted (Equation (A.6)) web-shear cracking capacities for AAC shear-wall specimens with partially mortared head joints**

The predicted  $V_{AAC}$  using Equation (A.1) and Equation (A.2) are presented in Table A.5 and Table A.6.

Table A.6 shows the prediction of capacity for all specimens that exhibited web-shear cracking. Ratios of observed  $V_{AAC}$  versus predicted  $V_{AAC}$  using Equation (A.1) and Equation (A.2) based on the tested compressive strength are presented in Figure A.5. In that figure, a solid diagonal line represents perfect agreement between observed and predicted shear capacities. The proposed equations are very close, or have slight errors in the direction of conservatism, for the specimens tested. If the ACI 318-02 equation for web shear cracking is used directly for AAC (substituting  $f_{AAC}$  for  $f_c$ ), the predicted capacity is greater than that observed, and hence unconservative. This is also true if the ACI 318-02 equation for web shear cracking is used with equivalent expressions for the tensile strength of concrete and for AAC. The web-shear cracking capacity will be further reduced by using the specified compressive strength rather than the tested

compressive strength. These results for the specimens tested at UT Austin are presented in Figure A.6. The one data point where the observed  $V_{AAC}$  falls below the predicted  $V_{AAC}$  is the Two-story Assemblage Specimen where the tested compressive strength fell below the specified compressive strength.

**Table A.5 Prediction of capacity as governed by web-shear cracking for fully mortared specimens (Equation (A.1)) using tested compressive strength**

Specimen	Axial load, P kips (kN)	Observed $V_{AAC}$ kips (kN)	Predicted $V_{AAC}$ kips (kN)	Observed $V_{AAC}$ / Predicted $V_{AAC}$
1 (UT)	156.0 (694)	164.2 (730)	70 (312)	2.34
3 (UT)	120.0 (534)	81.3 (362)	61 (273)	1.33
4 (UT)	120.0 (534)	110.5 (492)	73 (324)	1.52
5 (UT)	60.0 (267)	62.2 (277)	65 (287)	0.96
7 (UT)	80.0 (356)	57.4 (255)	38 (168)	1.52
9 (UT)	30.0 (267)	37.7 (168)	31 (137)	1.22
11 (UT)	25.0 (111)	15.6 (69)	15 (66)	1.05
Assemblage (UT)	26.0 (116)	52.0 (231)	53 (237)	0.98
3.6 (Hebel)	36.8 (164)	27.7 (123)	22 (96)	1.28
4.7 (Hebel)	62.4 (277)	46.7 (208)	32 (141)	1.47
4.8 (Hebel)	178.2 (792)	61.5 (273)	44 (197)	1.39
			Mean	1.27
			COV (%)	16.8

**Table A.6 Prediction of capacity as governed by web-shear cracking for unmortared head joints (Equation (A.2)) using tested compressive strength**

Specimen	Axial load, P kips (kN)	Observed $V_{AAC}$ kips (kN)	Predicted $V_{AAC}$ kips (kN)	Observed $V_{AAC}$ / Predicted $V_{AAC}$
3.3 (Hebel)	26.2 (116)	18.3 (81)	14 (61)	1.33
3.2 (Hebel)	49.7 (221)	20.6 (92)	16 (71)	1.29
3.4 (Hebel)	89.8 (399)	24.4 (109)	20 (88)	1.23
3.5 (Hebel)	26.6 (118)	18.2 (81)	14 (62)	1.30
4.3 (Hebel)	30.3 (135)	23.7 (105)	19 (84)	1.26
4.4 (Hebel)	85.5 (380)	32.1 (143)	24 (106)	1.35
4.1 (Hebel)	153.9 (685)	25.1 (112)	29 (130)	0.86
4.5 (Hebel)	33.5 (149)	21.3 (95)	18 (82)	1.15
4.6 (Hebel)	158.1 (703)	29.9 (133)	28 (126)	1.06
			Mean	1.21
			COV (%)	13.1

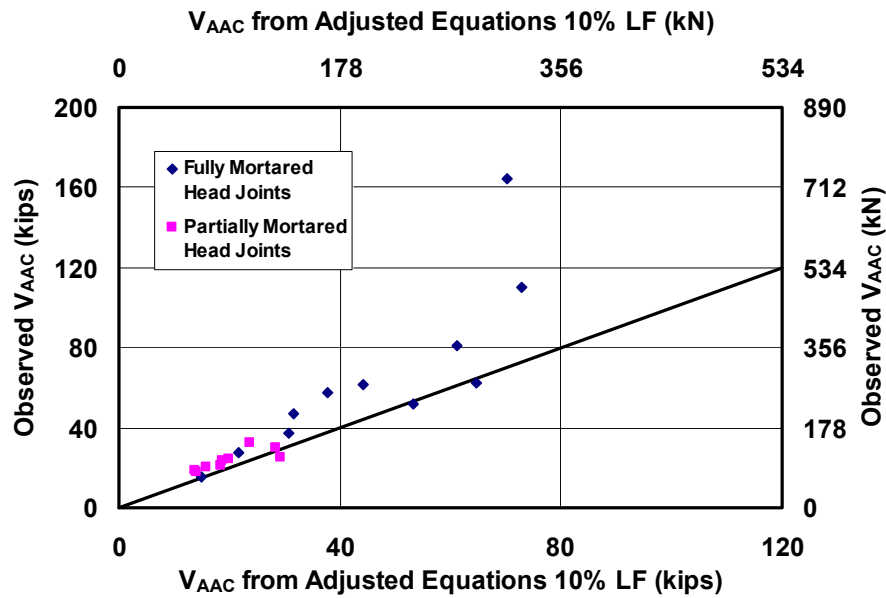


*Figure A.5 Observed versus predicted capacities as governed by web-shear cracking (Equation (A.1) and Equation (A.2)) using tested compressive strength*

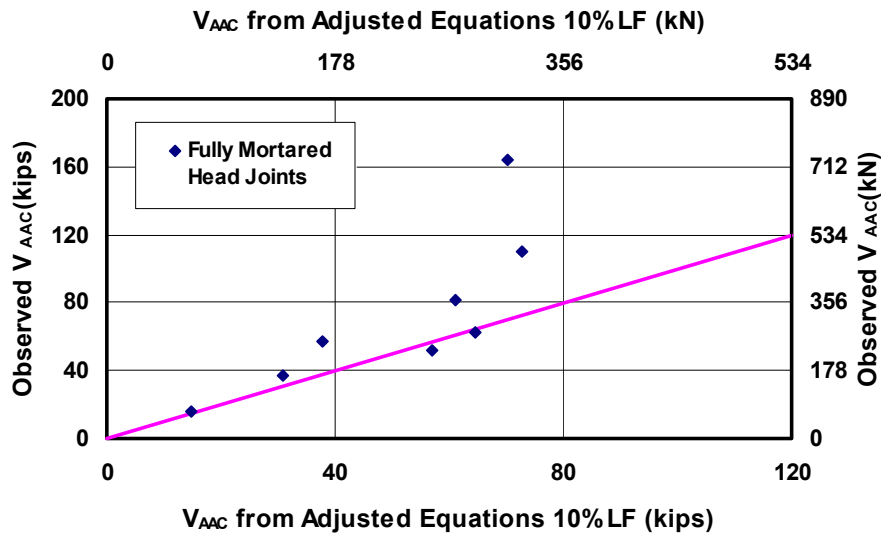


*Figure A.6 Observed versus predicted capacities as governed by web-shear cracking (Equation (A.1) and Equation (A.2)) using specified compressive strength*

### A.1.2 Flexure-Shear Cracking for AAC Shear Walls

A flexure-shear crack begins as a horizontal crack at a height of about one-half the plan length of the wall ( $l_w$ ) above the base of the wall, and then propagates diagonally through the center of the wall, as shown in Figure A.7.

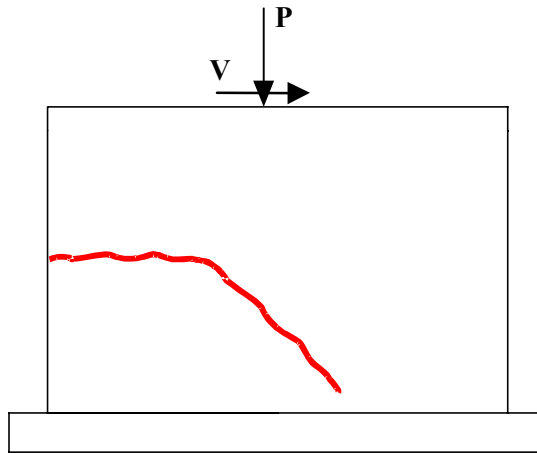


*Figure A.7 Flexure-shear cracking*

The formation of this crack is governed by the flexural tensile stress in the wall (Equation (A.7)).

$$\sigma = \frac{M}{S_x} \pm \frac{N}{A_n} \quad \text{Equation (A.7)}$$

Based on experiments with reinforced concrete shear walls, the controlling horizontal crack develops at a height of about  $l_w/2$ . Therefore, the moment at the crack,  $M_{\text{flcr}}$  is:

$$M_{flcr} = M - \frac{Vl_w}{2} \quad \text{Equation (A.8)}$$

where M is the moment at the base. Equation (A.9) presents the base shear at the formation of the flexural portion of the flexure-shear crack:

$$V_{flcr} = \frac{S_x \left( f_r + \frac{N}{l_w t} \right)}{\frac{M}{V} - \frac{l_w}{2}} \quad \text{Equation (A.9)}$$

ACI 318-02 uses a conservative (low) flexural tensile strength of  $6\sqrt{f'_c}$  (US customary units) substituted into Equation (A.9); experiments have shown an additional force of  $0.6\sqrt{f'_c} \cdot td$  is required to develop the crack. Therefore, ACI 318-02 uses Equation (A.10) for the flexure-shear cracking capacity.

$$V_c = \left[ 0.6\sqrt{f'_c} + \frac{l_w \left( 1.25\sqrt{f'_c} + 0.21 \frac{N}{l_w t} \right)}{\frac{M}{V} - \frac{l_w}{2}} \right] \cdot td \quad \text{Equation (A.10)}$$

Flexure-shear cracking was not observed in the 8 shear-dominated shear wall specimens tested at UT Austin because the exterior unbonded reinforcement (threaded rods) prevents vertical tensile stresses from forming at the base of the wall after flexural cracking (see Figure A.1). Flexure-shear cracking was

observed in the 6 flexure-dominated shear wall specimens. In every case the flexural portion of the flexure-shear crack formed first in the horizontal joint.

Based on the location of the flexural crack, the predicted load can be determined based on Equation (A.9) (see Table A.7). For AAC the modulus of rupture was calculated using  $f_r = 2 \cdot f_t$ , and the tested splitting tensile strength. This value was used in Equation (A.9). For flexure-dominated shear wall specimens, with the exception of Shear Wall Specimen 14a, the ratio of observed load versus predicted load ranges from 0.6 to 1.3. The mean ratio is 0.86 with a COV of 36%.

The observed load is lower than the predicted load because the failure occurred in the joint between the AAC and the thin-bed mortar rather than in the AAC material itself. A relationship for the tensile bond strength  $f_{\text{bond}}$  between AAC and thin-bed mortar was determined based on tests performed at UAB was presented in Section 3.6.2. Equation (A.11) presents the tensile bond strength for AAC densities greater than 32 pcf ( $2 \text{ kg/m}^3$ ). This indicates that for mid- to high-density AAC the tensile bond strength,  $f_{\text{bond}}$ , will be lower than the modulus of rupture. The tensile bond strength of the material in the flexure-dominated specimens except Shear Wall Specimen 13, is 94 psi (0.7 MPa) based on a density of 39.9 pcf ( $2.5 \text{ kg/m}^3$ ). Shear Wall Specimen 13 had a density below the limit of 32 pcf; therefore the modulus of rupture will govern the formation of a flexure-shear crack. The results of using the tensile bond strength rather than the modulus of rupture in Equation (A.9) for the remaining specimens are presented in Table A.8. With the exception of Shear Wall Specimen 14a, the ratios of observed to predicted strength range from 1.0 to 1.3 with a mean of 1.15 and a COV of 6.5%.

Shear Wall Specimen 14a exhibited flexural cracks at the base of the wall prior to testing. These cracks are presumed to have occurred while moving the top of the wall (out-of-plane) approximately 1 in. (25 mm) to the east to align the rams and loading beam. This would be expected to cause premature out-of-plane flexural cracks on the west side of the wall, which is where the first flexure-shear cracks did in fact occur.

$$f_{bond} = 1.5 \cdot \rho + 34$$

Equation (A.11)

$\rho$  in lb/ft<sup>3</sup>, and  $f_{bond}$  in lb/in.<sup>2</sup>

$$f_{bond} = 0.04 \cdot f_{AAC} + 66$$

Equation (A.12)

$f_{AAC}$  and  $f_{bond}$  in lb/in.<sup>2</sup>

**Table A.7 Results for flexure-shear cracking of AAC flexure-dominated shear wall specimens**

Specimen	$f_r$	N kips (kN)	Tested $V_{flcr}$ North kips (kN)	Predicted $V_{flcr}$ North Kips (kN)	Tested $V_{flcr}$ South kips (kN)	Predicted $V_{flcr}$ South kips (kN)	Observed $V_{flcr}$ /Predicted $V_{flcr}$ North Kips (kN)	Observed $V_{flcr}$ /Predicted $V_{flcr}$ North kips (kN)
13	110 (0.8)	25 (111)	9.6 (43)	8.2 (36)	10.1 (45)	8.0 (36)	1.18	1.26
14a	178 (1.2)	5 (22)	N/A	N/A	2.8 (12)	7.4 (33)	N/A	0.38
14b	178 (1.2)	5 (22)	4.9 (22)	7.4 (33)	4.6 (20)	7.4 (33)	0.66	0.62
15a	178 (1.2)	25 (111)	21.5 (96)	31.9 (142)	24.0 (107)	39.1 (174)	0.71	0.61
15b	178 (1.2)	25 (111)	20.0 (89)	-17.9 (-80)	17.5 (78)	17.1 (76)	0.66	0.60
16	178 (1.2)	25 (111)	-24.0 (-107)	31.9 (142)	21.8 (97)	32.4 (144)	0.75	0.67
							Mean	0.86
							COV (%)	36.1

**Table A.8 Results for flexure-shear cracking of AAC flexure-dominated shear wall specimens using tensile bond strength of material**

Specimen	$f_{bond}$	P kips (kN)	Tested $V_{flcr}$ North kips (kN)	Predicted $V_{flcr}$ North Kips (kN)	Tested $V_{flcr}$ South kips (kN)	Predicted $V_{flcr}$ South kips (kN)	Observed $V_{flcr}$ /Predicted $V_{flcr}$ North Kips (kN)	Observed $V_{flcr}$ /Predicted $V_{flcr}$ North kips (kN)
13	110 (0.8)	25 (111)	9.6 (43)	8.2 (36)	10.1 (45)	8.0 (36)	1.18	1.26
14a	94 (0.7)	5 (22)	N/A	N/A	2.8 (12)	4.1 (18)	N/A	0.68
14b	94 (0.7)	5 (22)	4.9 (22)	4.1 (18)	4.6 (20)	4.1 (18)	1.19	1.11
15a	94 (0.7)	25 (111)	21.5 (96)	18.7 (83)	24.0 (107)	22.9 (102)	1.15	1.05
15b	94 (0.7)	25 (111)	20.0 (89)	-17.9 (-80)	17.5 (78)	17.1 (76)	1.12	1.02
16	94 (0.7)	25 (111)	24.0 (107)	18.7 (83)	21.8 (97)	19.0 (84)	1.28	1.15
							Mean	1.15
							COV (%)	6.5

The predictions of Table A.8 can be repeated with the equivalent equation in terms of compressive strength using Equation (A.12). The resulting average ratio of observed  $V_{flcr}$  to predicted  $V_{flcr}$  is 1.1, with a COV of 14%.

The formation of flexural cracks did not cause a decrease in strength or stiffness of the specimens. Examples of the hysteretic behavior are shown in Figure A.8 through Figure A.12. In each case at least one load cycle was completed before a significant loss of stiffness was observed. Furthermore, the vertical reinforcement was sufficient to carry the load after flexure-shear cracking occurred. Based on these conclusions, no limiting design equations are proposed for flexure-shear cracking.



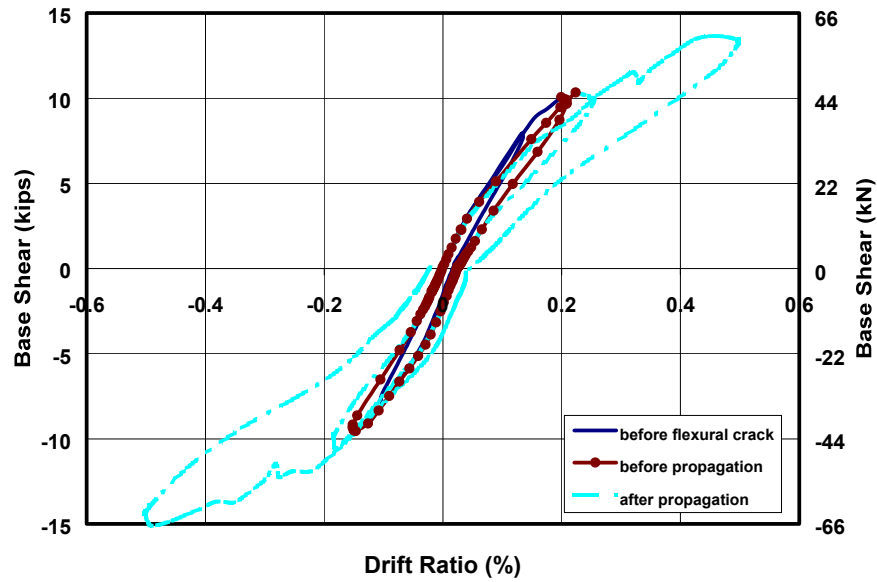


*Figure A.8 Hysteretic behavior of Shear Wall Specimen 13 before and after flexure-shear cracking*

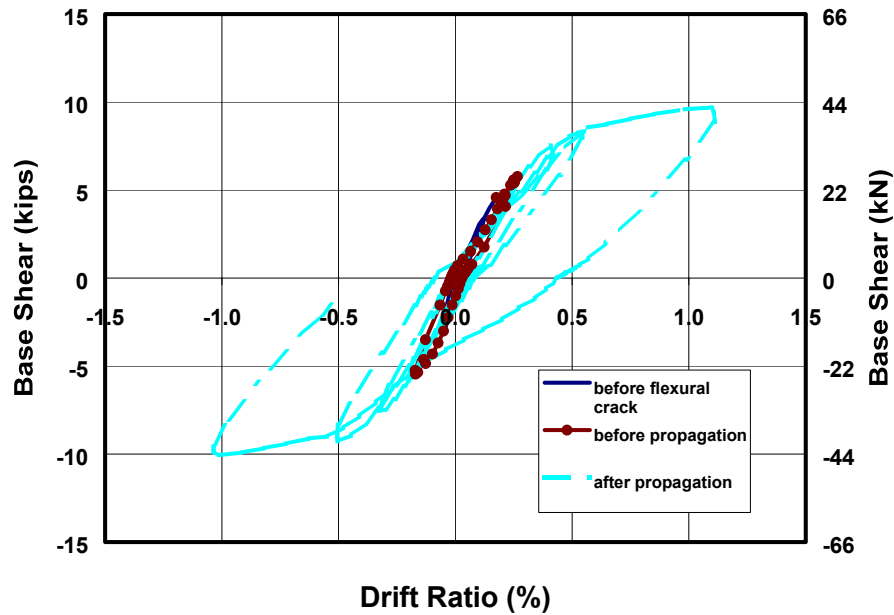


*Figure A.9 Hysteretic behavior of Shear Wall Specimen 14b before and after flexure-shear cracking*

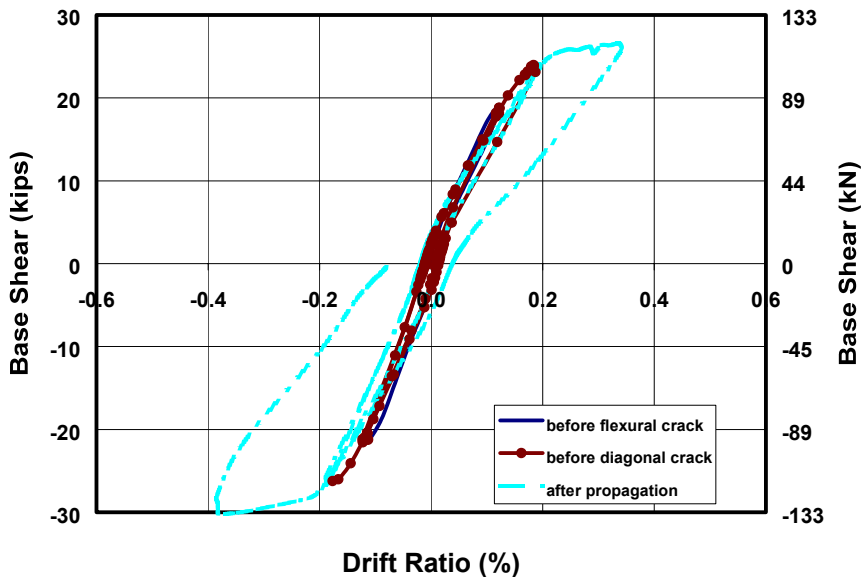


*Figure A.10 Hysteretic behavior of Shear Wall Specimen 15a before and after flexure-shear cracking*

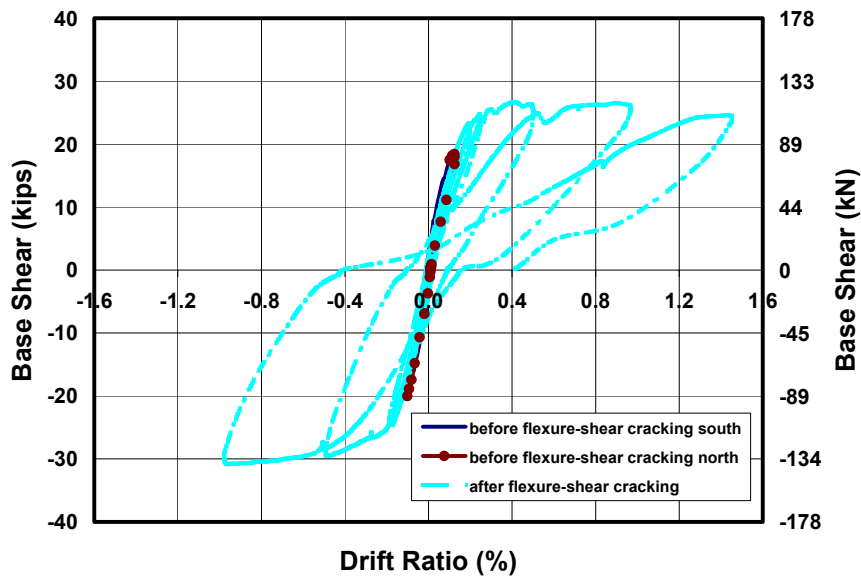


*Figure A.11 Hysteretic behavior of Shear Wall Specimen 15b before and after flexure-shear cracking*

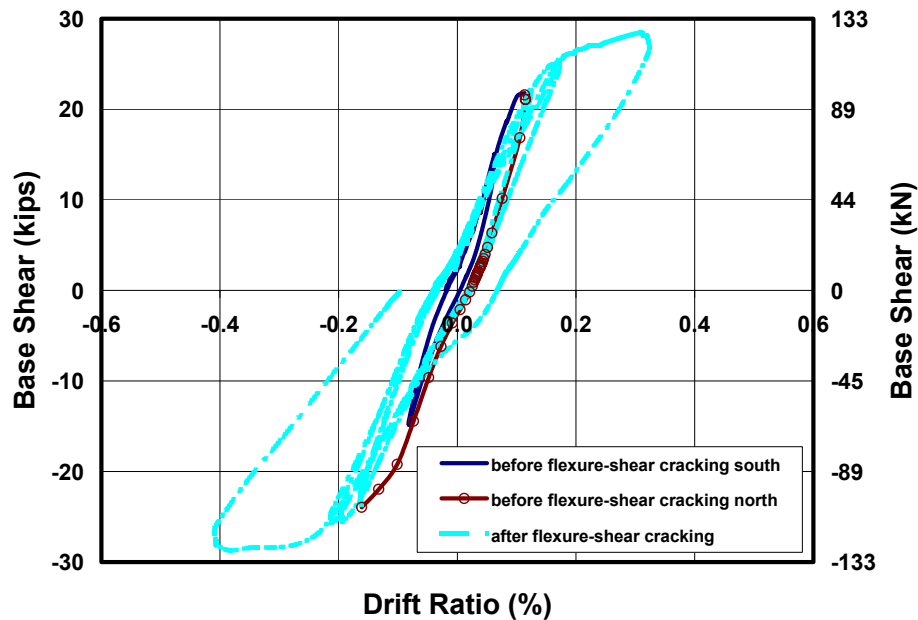


*Figure A.12 Hysteretic behavior of Shear Wall Specimen 16 before and after flexure-shear cracking*

### A.1.3 Crushing of the Diagonal Strut

An AAC shear wall can transfer load through the formation of a diagonal strut. The resultant of the applied lateral load and vertical forces acting on a wall is transferred along a diagonal strip in the wall (Figure A.13). The compressive force transferred along the diagonal strut is equilibrated at the base of the wall by the frictional resistance and by the vertical component of the compressive force in the diagonal strut. AAC shear walls with high axial loads can fail by crushing of this diagonal strut.

Crushing of the diagonal strut will occur in an AAC shear wall when the compressive stress in the strut exceeds the compressive strength of the AAC. Figure A.14 shows the external forces acting on an AAC shear wall due to in-plane shear and axial load.

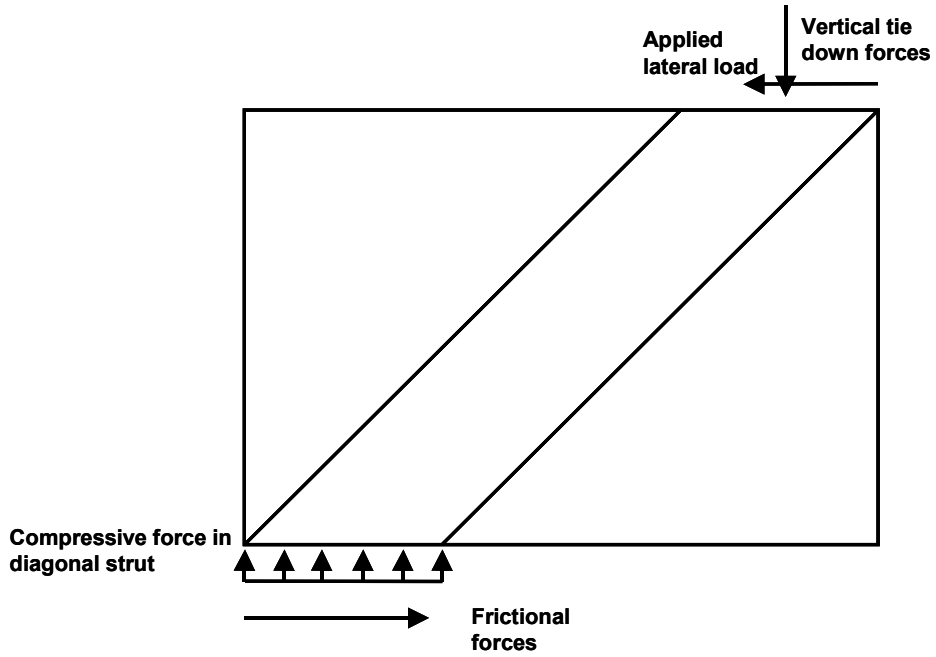


*Figure A.13 Diagonal compressive strut in an AAC shear wall*

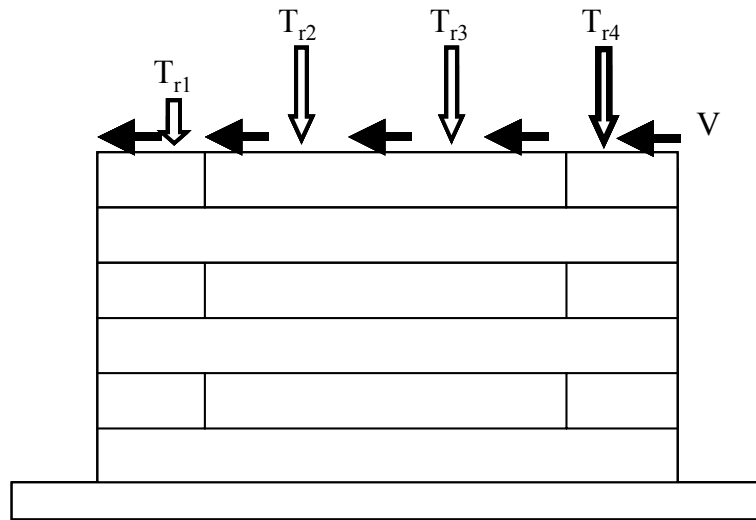


*Figure A.14 External forces acting on an AAC shear wall*

Diagonal crushing can be predicted using a strut-and-tie model consisting of two elements: a diagonal compression strut ( $F_{\text{strut}}$ ); and a tension tie-down force ( $T$ ). The compressive force in the diagonal strut is the resultant of the vertical tie-down forces and the applied horizontal load. Because the system is statically determinate, the vertical component is the summation of the force in the tie-down rods, and the horizontal component is the applied lateral load ( $V$ ).

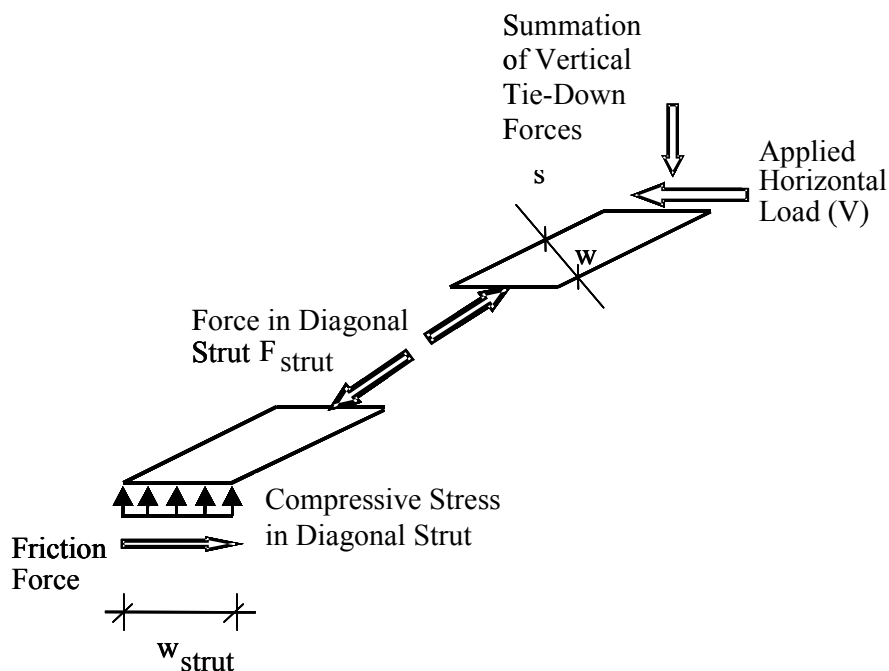


**Figure A.15 Forces acting on diagonal strut in an AAC shear wall**

Equation (A.19) represents the horizontal force ( $V$ ) at crushing based on equilibrium of horizontal forces at the base of the diagonal strut. The derivation can be shown in Equation (A.13) to Equation (A.18). The limiting force in the diagonal strut is based on an uniform compressive stress acting over the smallest area of the strut, as shown in Equation (A.13). The maximum applied lateral load is related by geometry to the force in the strut. Likewise, the minimum width of

the strut can be related to the horizontal width of the diagonal strut. By substitution, the lateral load of Equation (A.19) can be expressed in terms of the wall geometry and horizontal width of the strut (see Equation (A.16) and Equation (A.17)).

$$F_{strut} = w t f_{AAC} \quad \text{Equation (A.13)}$$

$$V_{ds} = F_{strut} \cos(\theta) \quad \text{Equation (A.14)}$$

$$w = \sin(\theta) w_{strut} \quad \text{Equation (A.15)}$$

$$\quad \text{Equation (A.16)}$$

$$\cos(\theta) = \frac{l_w - w_{strut}}{\left[ h^2 + (l_w - w_{strut})^2 \right]^{0.5}}, \sin(\theta) = \frac{h}{\left[ h^2 + (l_w - w_{strut})^2 \right]^{0.5}} \quad \text{Equation (A.17)}$$

$$V_{ds} = w_{strut} \cdot t \cdot f_{AAC} \cos(\theta) \sin(\theta) \quad \text{Equation (A.18)}$$

$$V_{ds} = f_{AAC} \cdot t \cdot w_{strut} \left[ \frac{h \cdot (l_w - w_{strut})}{\left[ h^2 + (l_w - w_{strut})^2 \right]} \right] \quad \text{Equation (A.19)}$$

Shear Wall Specimen 1 (UT Austin) confirmed this proposed model for crushing of the diagonal strut. Minor spalling occurred at the toe at a load of 152 kips (676 kN), and major spalling, at a load of 167.6 kips (745 kN). The observed horizontal width of the diagonal strut was approximately one-quarter of the plan length. Using Equation (A.19), crushing of the diagonal strut for Shear Wall Specimen 1 was predicted at a lateral load of 185.1 kips (823 kN). The ultimate load was 90% of the load predicted by the model for crushing of the diagonal

strut. Since, the model for crushing of the diagonal strut was unconservative in this case, it is multiplied by a factor of 0.9. Equation (A.20) incorporates this factor and a width of the compression strut of  $0.25l_w$ . The results of the predicted lateral load at crushing of the diagonal strut, for an assumed strut width of one-quarter of the plan length, are presented along with the ultimate lateral load in Table A.9.

$$V_{AAC} = 0.17 \frac{f_{AAC} \cdot h \cdot l_w^2}{h^2 + \left(\frac{3}{4}l_w\right)^2} \quad \text{Equation (A.20)}$$

**Table A.9 Predicted shear wall capacities as governed by crushing of the diagonal strut**

Specimen	$V_{ds}$ kips (kN)	$0.9V_{ds}$ kips (kN)	Maximum V kips (kN)	$0.9 V_{ds} -$ Maximum V	Maximum V / $0.9 V_{ds}$
1	185 (824)	167 (741)	168 (745)	-1 (-4)	1.01
3	154 (683)	138 (615)	118 (526)	20 (89)	0.86
4	315 (1403)	284 (1262)	126 (561)	158 (701)	0.44
5	246 (1093)	221 (984)	85 (377)	136 (607)	0.38
7	89 (394)	80 (355)	59 (263)	21 (91)	0.74
9	98 (436)	88 (392)	42 (189)	46 (204)	0.48
11	23 (100)	20 (90)	17 (74)	4 (16)	0.82
13	21 (93)	19 (84)	22.5 (100)	-4 (-16)	1.19
14a	36 (162)	33 (146)	9.9 (44)	23 (102)	0.30
14b	36 (162)	33 (146)	10.1 (45)	23 (101)	0.31
15a	121 (537)	109 (483)	30.1 (134)	79 (350)	0.28
15b	121 (537)	109 (483)	30.9 (137)	78 (346)	0.28
16	121 (537)	109 (483)	35.2 (157)	73 (327)	0.32

In the remaining shear wall specimens crushing of the diagonal strut was avoided by limiting the axial load. The validity of Equation (A.20) was indirectly determined by avoiding crushing. In Shear Wall Specimen 13, the maximum lateral load was higher than the proposed equation for the design provisions

without observing crushing of a diagonal strut. One reason for the discrepancy is that the assumed width of the diagonal strut of one-quarter of the plan length of the wall is no longer valid. The aspect ratio of Shear Wall Specimen 13 is 2. Since the model was adequate for walls with aspect ratios less than 2, that aspect ratio is used as an upper limit to the proposed Code equation.

#### **A.1.4 Sliding Shear Capacity**

An AAC shear wall of horizontal panels or masonry-type blocks exhibits a bed-joint crack when the shear stress on the bed joints exceeds the interface shear capacity,  $v$  (Figure A.18 ). An AAC shear wall subject to sliding shear across a horizontal bed joint is presented in (Figure A.16). After the crack forms the shear is resisted by the vertical reinforcement and frictional forces due to the axial load.

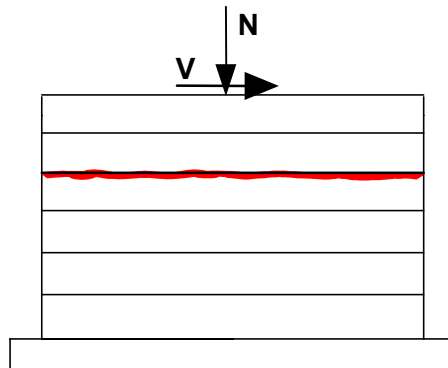


***Figure A.16 Formation of bed-joint crack in an AAC shear wall with horizontal panels***



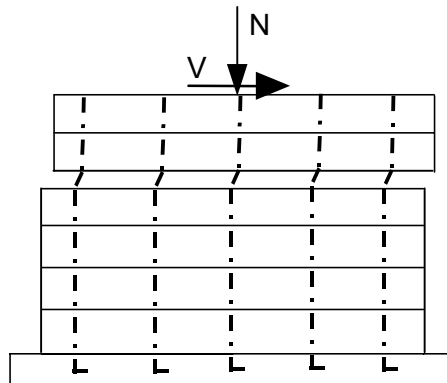


***Figure A.17 Sliding shear mechanism in an AAC shear wall with horizontal panels***

After the crack forms, some resistance will be provided by shear friction across the bed joints:

$$V_{ss} = \mu(A_v f_s + N) \quad \text{Equation (A.21)}$$

Sliding shear resistance is the product of the coefficient of friction across an interface, and the force acting perpendicular to that interface. This mechanism is referred to in ACI 318 as “shear friction.” This resistance can come from reinforcement crossing the interface and applied axial load.

In the traditional “shear friction” mechanism, sliding over a rough joint causes one section of the crack to lift upwards; this result in yielding of the vertical reinforcement, which provides additional clamping force. Under reversed cyclic loading of AAC, the roughness of the bed joints can decrease, and resistance to sliding shear is provided by dowel action of reinforcement crossing the bed joints. This contribution to  $V_{ss}$  is the area of the reinforcement

perpendicular to the crack and the shear resistance of the bars,  $0.6f_y$ . This contribution to the sliding shear mechanism is shown in Figure A.18.

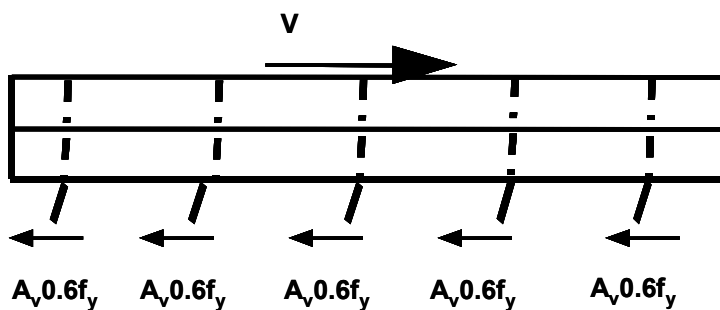


*Figure A.18 Internal lateral forces generated by dowel action along plane of sliding shear mechanism*

Frictional resistance is the second component of resistance due to sliding shear. Figure A.19 is a free-body diagram showing the horizontal equilibrium due to frictional forces.

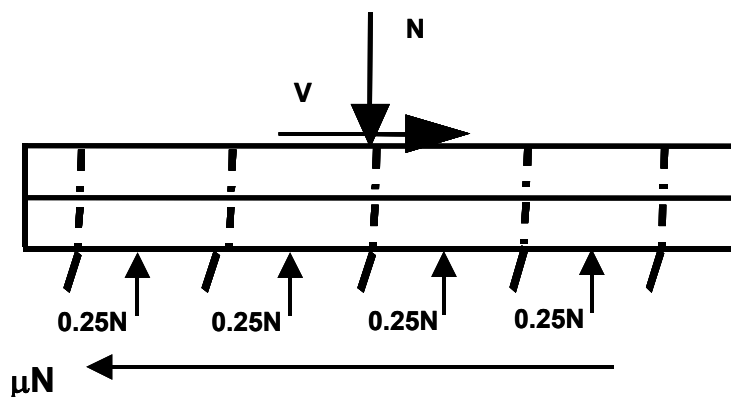


*Figure A.19 Internal lateral forces generated by friction along plane of sliding for sliding shear mechanism*

$$V_{ss} = \mu N + 0.6A_s f_y \quad \text{Equation (A.22)}$$

In subsequent specimens, the clamping force  $N$  was determined such that the shear capacity will be limited by web-shear cracking or flexure-shear cracking, rather than bed-joint sliding. Sliding shear was avoided in 12 out of the remaining 14 specimens; it was observed in Shear Wall Specimen 4 and the Two-story Assemblage Specimen. Since the specimens were designed to avoid sliding shear, sufficient dowels were placed to ensure that  $V_{ss}$  was significantly greater than  $V_{AAC}$ . In four specimens,  $V_{max}$  was greater than  $V_{AAC}$ . Shear Wall Specimen 3 and Shear Wall Specimen 5 were both overdesigned in sliding shear. The load did not reach the sliding shear capacity because the specimen capacities were limited by distributed web-shear cracking. Shear Wall Specimen 4 and the Two-story Assemblage Specimen can be used to determine the effectiveness of Equation (A.22).

The hysteretic behavior for the Two-story Assemblage Specimen is shown in Figure A.20. The total base shear and sliding shear capacity for the specimen versus Load Point is presented in Figure A.21. The design sliding shear capacity is presented for the contribution of axial load and dowels (Equation (A.22)) and the contribution of axial load only. A coefficient of friction of 1.0 was used since the sliding plane occurred between the vertical panels and the leveling bed mortar. The entire axial load was applied through gravity, therefore, the axial load remained constant throughout the test. In this specimen the longitudinal steel and dowels contribute significantly to the capacity for several cycles. Damage around the dowels began at Load Point 677 and continued throughout the test. Each loading cycle was accompanied by increasing damage. The cumulative damage at each cycle is accompanied by a continually decreasing base shear, as shown in load points above 800 in Figure A.21.

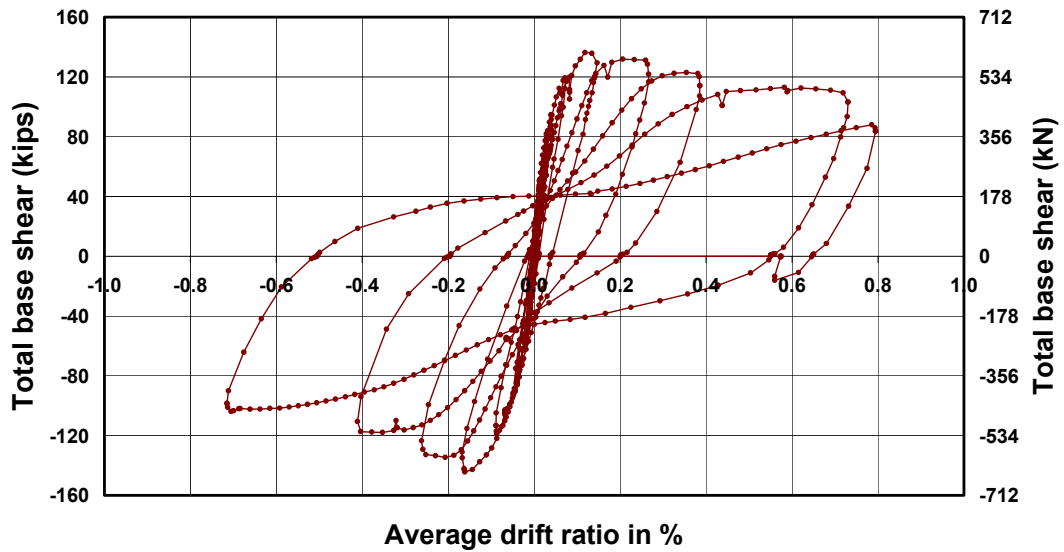


Figure A.20 Hysteretic behavior of Two-story Assemblage Specimen

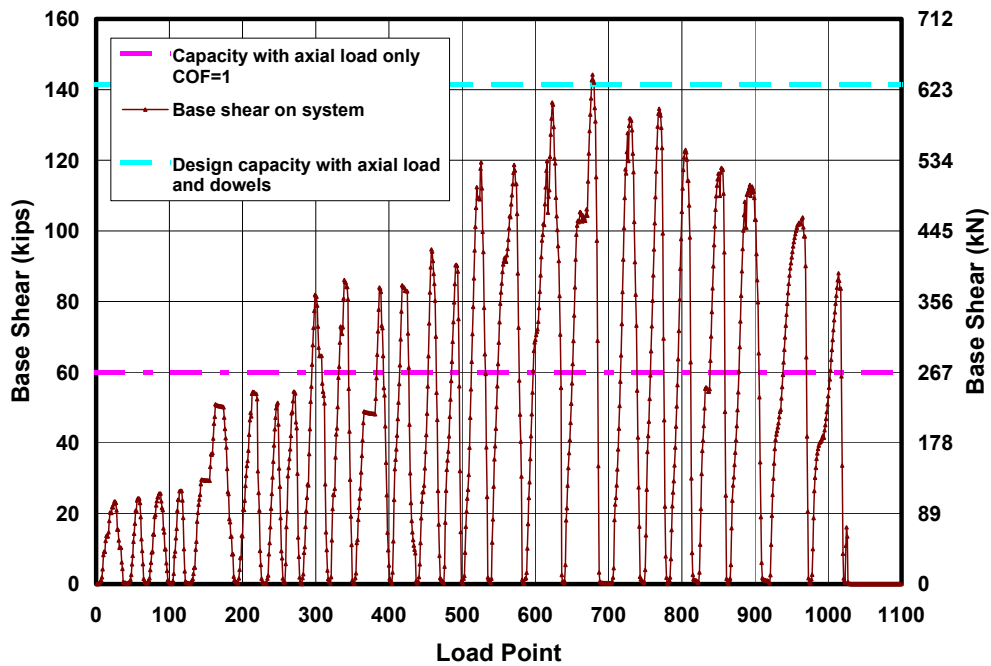


Figure A.21 Base shear and sliding shear capacity versus Load Point for Two-story Assemblage Specimen

Sliding was observed in two adjacent panels in Shear Wall Specimen 4. A horizontal crack formed along the bed joint between the second and third courses. This crack formed in three stages, corresponding to Load Points 634, 717 and 764. The final crack propagation occurred after the maximum base shear was reached. A graph of base shear versus Load Point for Shear Wall Specimen 4 is shown in Figure A.22. Since the sliding occurred between panels, a coefficient of friction of 0.8 was used to predict the capacity. The applied base shear increased beyond the sliding shear resistance for the level of axial load that was applied to the specimen. Several diagonal cracks formed at the compression toes of the walls. Spalling between these cracks occurred at Load Point 871.

The axial load consisted of three portions: gravity load from loading equipment; load applied through the load maintainer; and post-tensioning force in the rods. The pressure in the load maintainer system was checked during testing. It did not change, nor did the contribution of axial load due to gravity. Any decrease in axial load would therefore have to have occurred due to a loss of post-tensioning. This was observed in the spalling of the compression toe that occurred at Load Point 871. The loss of post-tensioning decreased the applied axial load and thus decreased the sliding shear capacity.

The measured axial load capacity of Figure A.23 includes the unchanged axial load and the measured force in the external rods. As the base shear increases, a slight increase is also observed in the axial load (see Load Point 1080 through 1110). This is the increase in load in the axial rods caused by the in-plane rotation of the wall about its compression toe. At later load points, at points of zero base shear the force in the rods decreases due to toe crushing. This can be observed in the difference between measured axial loads at two points where the

base shear is zero. For example, at Load Point 830 the measured axial load is 91 kips (405 kN); at Load Point 890 it decreases to 87 kips (387 kN); and at Load Point 960 it further decreases to 82 kips (365 kN).

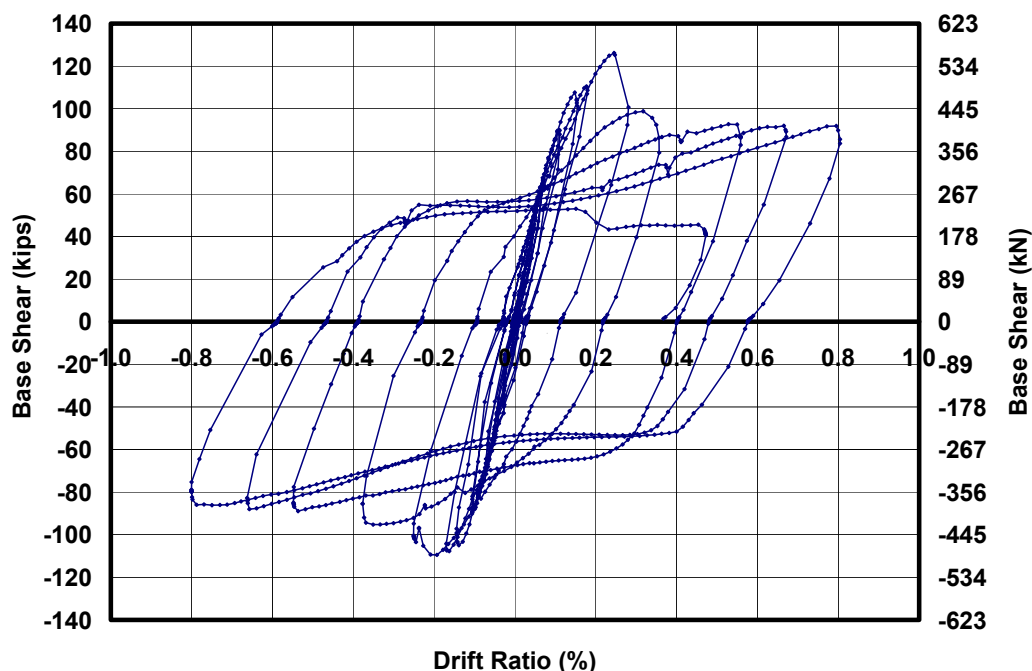


**Figure A.22 Hysteretic behavior of Shear Wall Specimen 4**

For load points beyond 700 the base shear capacity decreases. This was also observed in the Two-story Assemblage Specimen. This is a further indication that as damage increases the effectiveness of the dowel action decreases. As the damage increases, the resistance provided by bearing on the dowel is reduced. For this reason, the proposed code language conservatively neglects the contribution of the dowels as shown in Equation (A.23).

$$V_{ss} = \mu N \quad \text{Equation (A.23)}$$

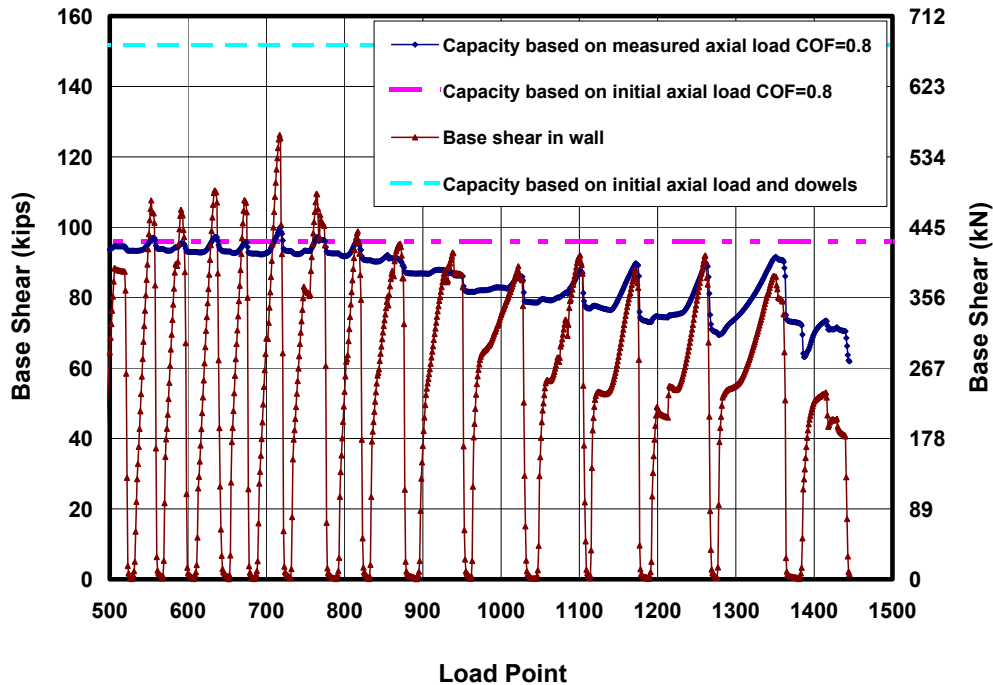


***Figure A.23 Base shear and sliding shear capacity versus Load Point for Two-Story AAC Asssemblage Specimen***

Structures with small axial load may have low sliding shear capacity. In these cases the interface shear strength between AAC and thin-bed mortar may be used. Based on the direct shear tests performed at UT Austin, the average interface shear strength between AAC and thin-bed mortar was 64 psi (441 kPa), with a COV of 44%. A lower 5 % fractile is proposed, for design, reducing the interface shear strength to 17 psi (117 kPa). This value is conservative compared to test results of 45 psi (310 kPa) to 82 psi (565 kPa).

The measured axial load in Figure A.23 does not include the tensile forces in the internal reinforcement. Although those forces were not measured, they can

be estimated based on flexural calculations. The wall instrumentation indicates that the longitudinal reinforcement in the wall had yielded at the bed joint where sliding occurred. When the lateral load is removed and the bed-joint gap closes, the bars will be subject to compression. Based on an assumed debonded bar length, the compressive forces can be estimated. The solid blue line in Figure A.24 shows the revised axial load considering compressive stresses in longitudinal reinforcement.

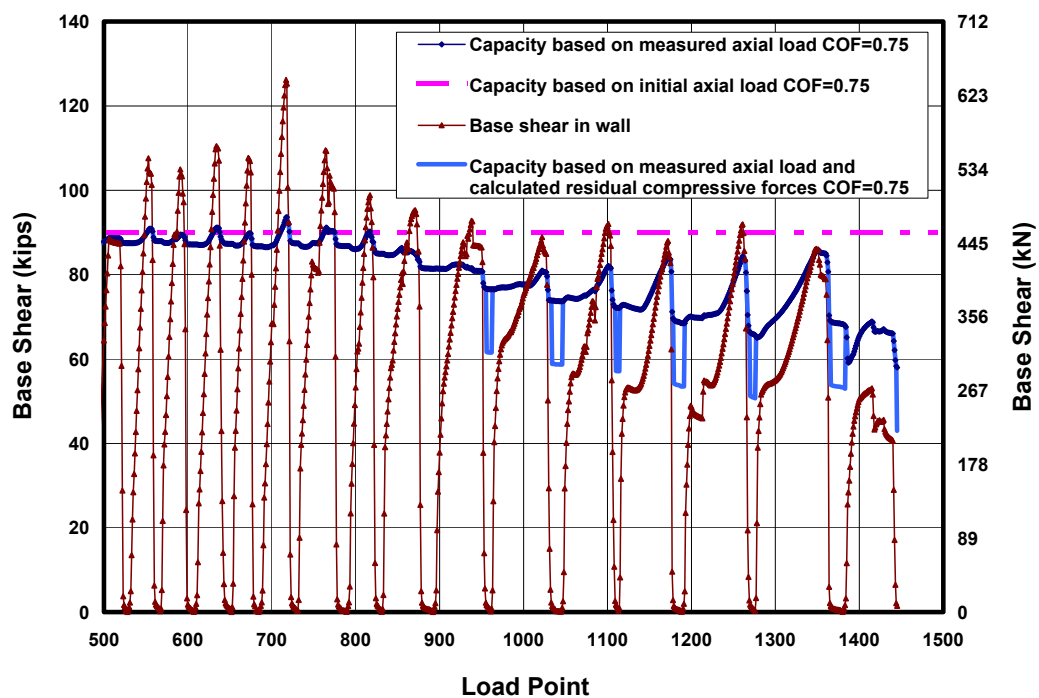


*Figure A.24 Base shear and reduced sliding shear capacity versus Load Point for Two-story Assemblage Specimen*



### A.1.5 Nominal Flexural Capacity

The nominal flexural capacity of AAC shear walls can be determined based on equilibrium of a cross section. Using the proposed design provisions, the nominal flexural capacity of AAC shear walls can be predicted using conventional flexural theory. The compressive zone is determined based on a linear strain relationship, using a maximum useful compressive strain in the AAC of 0.003 (RILEM 1993 and Section 4.3.1), and an equivalent rectangular stress block whose height is  $0.85f'_{AAC}$  (or  $0.85f'_m$ ), and whose depth is  $\beta_1c$ , where  $\beta_1 = 0.67$  (Figure A.25). The value of  $\beta_1$  is selected to maintain equilibrium between the equivalent stress block and a triangular compressive stress distribution based on tested stress-strain results of Section 3.6.1.

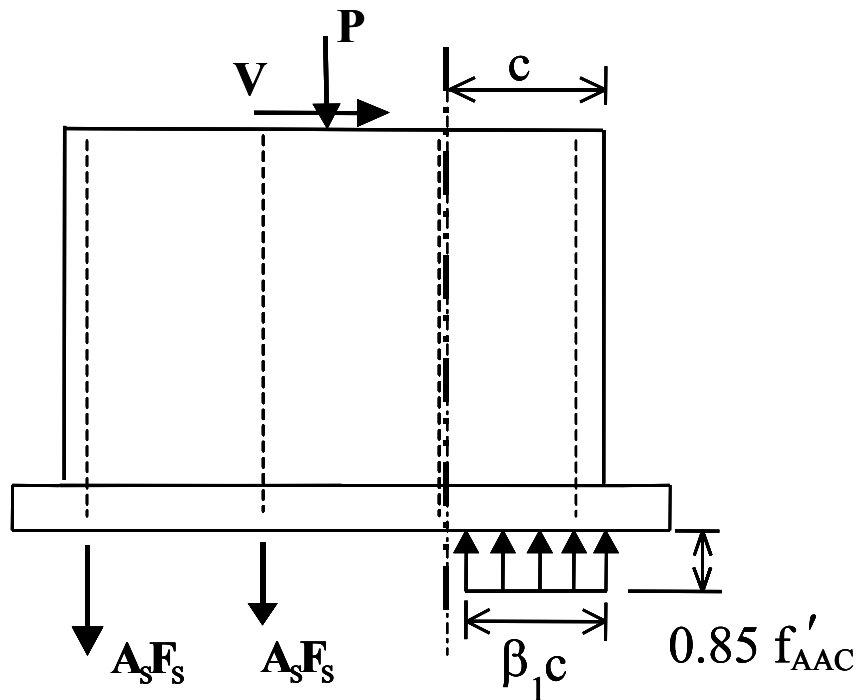


*Figure A.25 Equilibrium of an AAC shear wall at nominal flexural capacity*

Observed versus predicted nominal flexural capacities can be compared for flexure-dominated Shear Wall Specimen 14a, 14b, 15a and 15b. During the test of Shear Wall Specimen 13 and Shear Wall Specimen 16, the actuators used to apply the constant axial load inadvertently reached the end of their travel. As increasing lateral drifts were applied, axial load on the wall inadvertently increased. To successfully interpret those test results, the probable axial load applied to the walls was back-calculated from the predicted flexural capacity, removing those two tests from consideration for verifying observed versus predicted flexural capacity.

The nominal flexural capacity was calculated using a steel yield strength of 75 ksi (490 MPa), based on mill reports, along with the assumptions of 8.8.2. The ratios of observed to predicted strength range from 1.11 to 1.29, with an average of 1.19 and a COV of 5.8%. A refined analysis was performed considering strain hardening using RCCOLA (RCCOLA). The effect of strain hardening will increase the nominal flexural capacity as shown in the results of Table A.11. With this refinement the range of observed to predicted nominal flexural capacity ranges from 0.95 to 1.13. The average is 1.03 with a COV of 6.2%.

**Table A.10 Observed versus predicted nominal shear capacities based on nominal flexural capacity**

Specimen	Predicted $V_{Mn}$ kips (kN)	Observed $V_{Mn}$ South kips (kN)	Observed $V_{Mn}$ North kips (kN)	Observed / Predicted $V_{Mn}$ South	Observed / Predicted $V_{Mn}$ North
14a	8.5 (38)	9.4 (42)	NA	1.11	NA
14b	8.5 (38)	9.9 (44)	10.1 (45)	1.16	1.19
15a	23.9 (106)	28.8 (128)	30.1 (134)	1.21	1.26
15b	23.9 (106)	26.7 (119)	30.9 (137)	1.12	1.29
Average					1.19
COV (%)					5.8

**Table A.11 Observed versus predicted nominal shear capacities based on nominal flexural capacity with strain hardening included**

Specimen	Predicted $V_{Mn}$ kips (kN)	Observed $V_{Mn}$ South kips (kN)	Observed $V_{Mn}$ North kips (kN)	Observed / Predicted $V_{Mn}$ South	Observed / Predicted $V_{Mn}$ North
14a	9.9 (44)	9.4 (42)	NA	0.95	NA
14b	9.9 (44)	9.9 (44)	10.1 (45)	1.00	1.02
15a	27.4 (122)	28.8 (128)	30.1 (134)	1.05	1.10
15b	27.4 (122)	26.7 (119)	30.9 (137)	0.97	1.13
Average					1.03
COV (%)					6.2

## A.2 SPECIAL PROVISIONS FOR VERTICAL PANEL CONSTRUCTION

AAC panels oriented vertically have potential planes of failure along continuous head joints. These cracks may be attributed to shrinkage or weak joints, where the thin-bed mortar is not in contact with both panel faces. The presence of vertical cracks can change the behavior of a shear wall specimen. The observance of this behavior in Shear Wall Specimen 2 will be discussed then

theoretical and design methodologies will be presented in Sections A.2.1 and A.2.2.

In Shear Wall Specimen 2, two vertical cracks formed prior to testing. Shortly after flexural cracks formed another two vertical cracks formed and separated the wall into smaller sections. The initial cracks are indicated by gray lines and the cracks formed during testing are indicated by black lines in Figure A.26. The first diagonal crack formed at a load of 55.6 kips (247 kN). As the load increased, additional vertical and diagonal cracks formed in the specimen (Figure A.27).

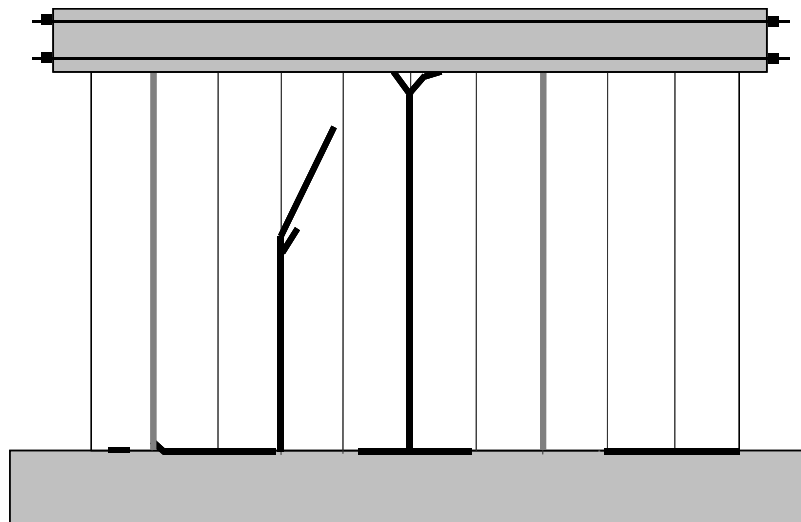


*Figure A.26 Formation of first diagonal crack in Shear Wall Specimen 2*

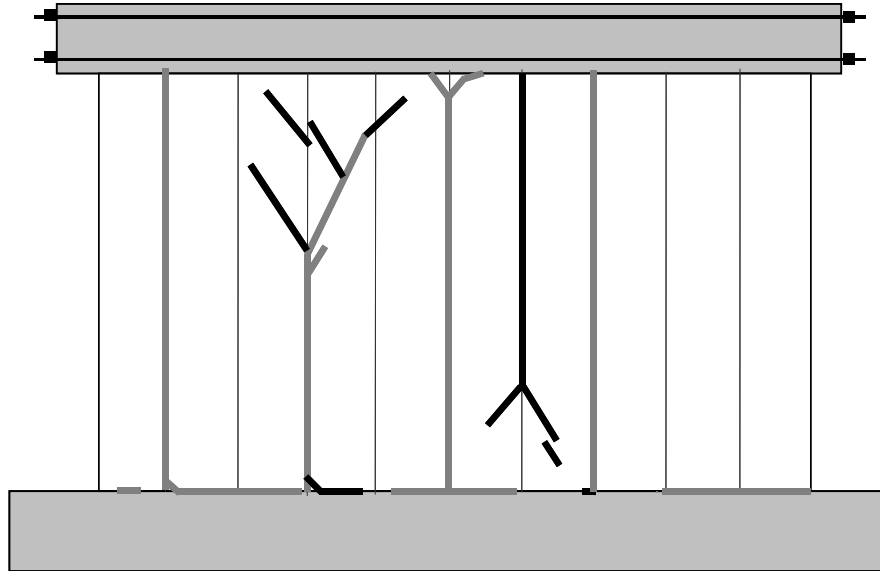


*Figure A.27 Formation of additional cracks in Shear Wall Specimen 2*

### **A.2.1 Prediction of Flexural and Shear Capacities for AAC Shear Walls with Vertically Oriented Panels**

In the case of monolithic behavior, the wall behaves as a cantilever (see Figure A.28). In the case of individual panels, the stiffness of the loading beam is large compared to a single panel, and the loading beam restrains the wall at the top (Figure A.29). If the wall behaves monolithically, the shear capacity will remain the same as presented in Section A.1, and the flexural design will be conventional. If the panels are separated by vertical cracks at the head joints, however, the behavior will change. That is the subject of this section.

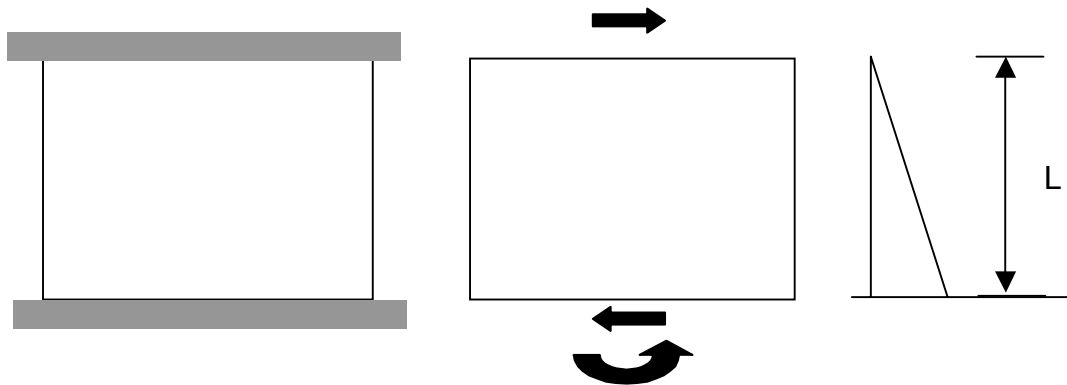


**Figure A.28 Behavior of monolithic AAC shear wall**

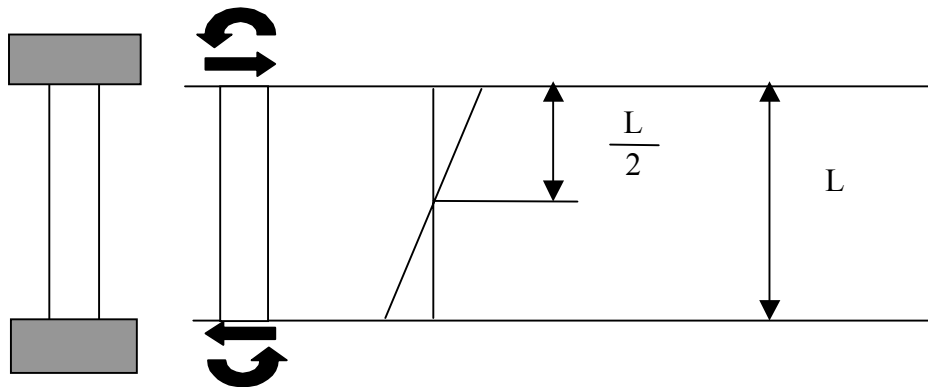


**Figure A.29 Behavior of individual panel for an AAC shear wall**

The most critical case would be panels with vertical cracks at every section. The flexural capacity can be predicted based on the sum of the capacity of the individual panels. An interaction diagram for a single panel can be calculated and the flexural capacity of each panel can be determined based on the axial load in the respective panel; a value that depends on the forces acting on the wall. The lateral load will produce a series of axial loads in each panel that vary linearly based on the wall geometry. The applied axial load per panel will be the total axial load divided by the number of panels (see Figure A.30).

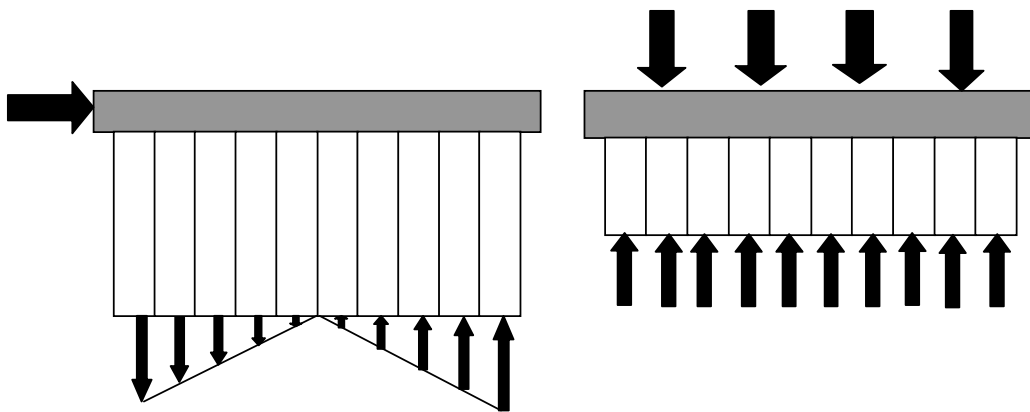


**Figure A.30** *Distribution of axial loads for laterally loaded condition and axially loaded condition*

If the net axial load applied to each panel is within the straight-line portion of the interaction diagram for a single panel, the total wall capacity will be the capacity at the axial load in a single panel, multiplied by the number of panels:

$$V_{wall} = \Sigma V_{panels} \quad \text{Equation (A.24)}$$

$$M_{wall} = \Sigma M_{panels} \quad \text{Equation (A.25)}$$

If the wall behaves as individual panels, the aspect ratio of piece becomes large; each panel behaves as a beam subject to compressive and lateral loads. The shear capacity in this condition can be predicted using the shear equations for beams presented in Section 4.5.

### **A.2.2 Verification of Shear Capacity for Vertical-Panel Shear Walls Tested at UT Austin**

The application of the individual panel design equations and the monolithic wall equations for Shear Wall Specimen 2 is presented in Figure A.31. The base shear at which cracking occurred was 55 kips (245 kN), and the maximum base shear was 92 kips (410 kN). The design equations are much more conservative than the wall behavior.

Several conditions can increase the performance of a head joint between vertical panels:

- a) Cleaning and wetting the panel face prior to application of the thin-bed mortar improves the adhesion.
- b) Applying mortar to both faces of the vertical joint improves the mortar coverage at the joint.
- c) Clamping adjacent panels applies pressure and improves the joint quality.

In Shear Wall Specimen 2 the panel faces were prepared and pressure was applied perpendicular to the joint, parallel to the plane of the wall. Initially, the joints were not mortared on both faces. After a lack of coverage was observed in several joints, the panel was removed, cleaned and re-installed with mortar applied to both faces of the joint. This procedure was applied thereafter. The joint was clamped at the base (using one clamp on each wall face) and at the top (using one clamp at the centerline of the wall).



In the remaining specimens constructed of vertical panels (Shear Wall Specimens 15, 16 and the Two-story Assemblage Specimen), vertical cracks were not observed. In each case the three previous construction recommendations were used. Pressure was applied to the joint using 4 clamps, one clamp on each wall face, both at the bottom and top of the wall.

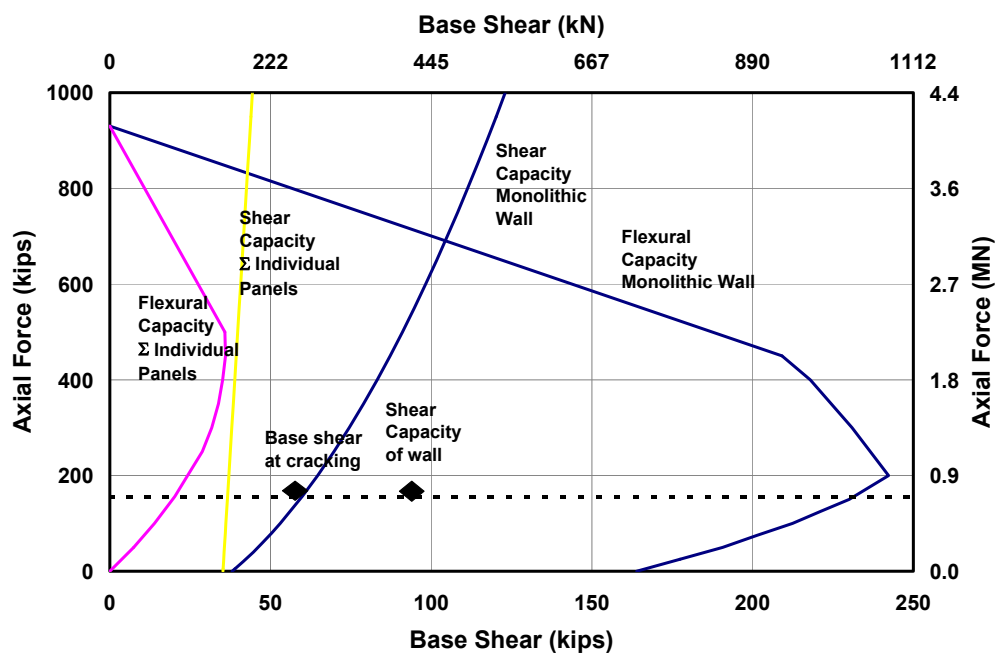


*Figure A.31 Base shear capacity for Shear Wall Specimen 2 considering individual panel behavior and monolithic wall behavior*

In these specimens, vertical cracks at the joints were not observed until the end of the test when the wall stiffness was reduced due to prior cracks. Furthermore, the cracks left at least three panels joined together. For this construction type, the proposed design recommendation is to relax the individual panel requirements to groups of three panels connected together. The changes to the flexure and shear design capacities are presented in Figure A.32. Equation

(A.3) to predict web-shear cracking was used for panel groups with an aspect ratio less than 2.

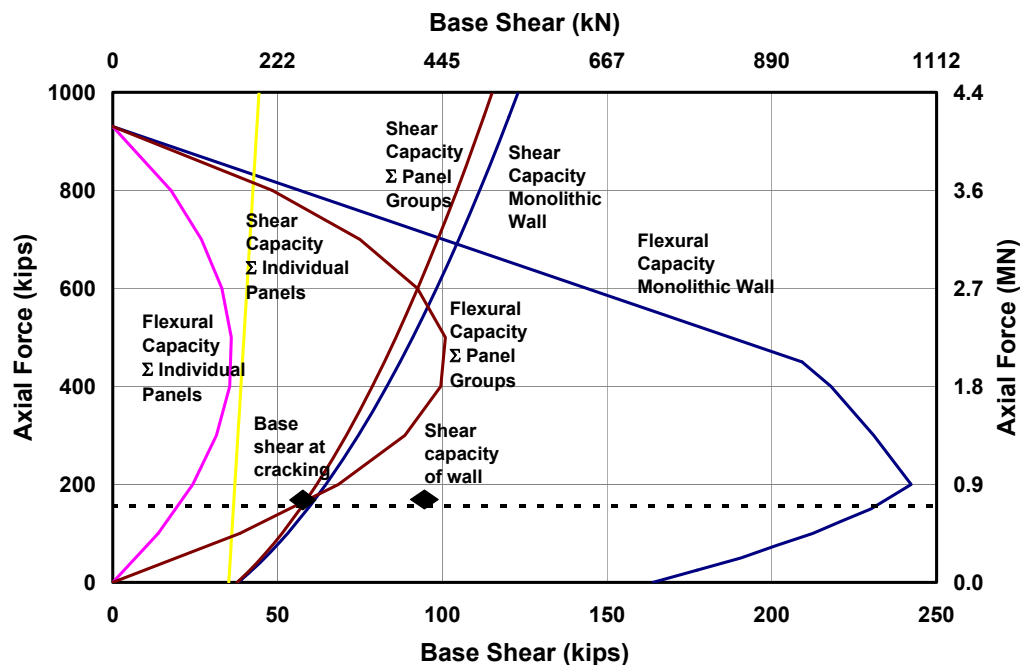


*Figure A.32 Base shear capacity for Shear Wall Specimen 2 considering individual panel behavior, behavior of panel groups and monolithic wall behavior*

### A.2.3 Special Provisions to Avoid Longitudinal Cracking at the Location of Vertical Reinforcement

In each of the flexure-dominated specimens vertical (longitudinal) cracks formed along the grouted cores and the surrounding AAC. In the following sections the observed load at which these cracks formed is presented, along with two analyses to determine if the cracks occurred before yielding of the flexural reinforcement. The effect of these longitudinal cracks is presented, followed by design recommendations intended to prevent their formation.

#### A.2.4 Formation of Cracks along Longitudinal Bars in AAC Shear Walls

The base shears at which cracks formed along longitudinal reinforcement formed are presented in Table A.12. The base shear at which the first and second cracks formed along the vertical reinforcement is presented in Column 2 of that table. No second observed vertical crack data are presented for Shear Wall Specimen 14a, because that wall was tested in one direction only. The base shear at the expected flexural capacity (nominal capacity increased by steel overstrength) is presented in Column 3.

**Table A.12 Ratio of base shear at formation of vertical cracks to base shear at expected flexural capacity (including overstrength) in the flexure-dominated shear wall specimens**

AAC Shear Wall Specimen	Base shear at first and second observed vertical crack, kips (kN)	Base shear at expected flexural capacity ( $f_s=1.25f_y$ ) $V_{max}$ kips (kN)	Ratio of base shear at observed crack to $V_{max}$ ( $f_s=1.25f_y$ )
13	13.6 (60) – first 15.6 (69) - second	13.0 (58)	1.05 – first 1.20 – second
14a	6.9 (31) – first NA – second	8.3 (37)	0.83 – first NA – second
14b	7.0 (31) – first 9.8 (44) - second	8.3 (37)	0.84 – first 1.18 – second
15a	26.5 (118) – first 27.3 (128) - second	23.8 (106)	1.11 – first 1.15 – second
15b	17.5 (78) – first 24.5 (109) - second	23.8 (106)	0.74 – first 1.03 – second
16	24.0 (107)– first 28.0 (125) - second	25.5 (113)	0.94 – first 1.10 – second

The ratios of base shear at the observed crack to the base shear at the expected flexural capacity range from 0.74 to 1.20, with an average of 1.02 and a COV of 16%. Longitudinal cracks were observed in three specimens at 74% to 84% of the expected flexural capacity. The ratios of base shear at cracking to expected flexural capacity, along with a corresponding normal distribution, are

shown in Figure A.33. As shown in that figure, it is highly probable that an AAC shear wall will reach between 74% and 84% of its expected flexural capacity in a moderate to strong earthquake, and therefore highly probable that such longitudinal cracks would form.

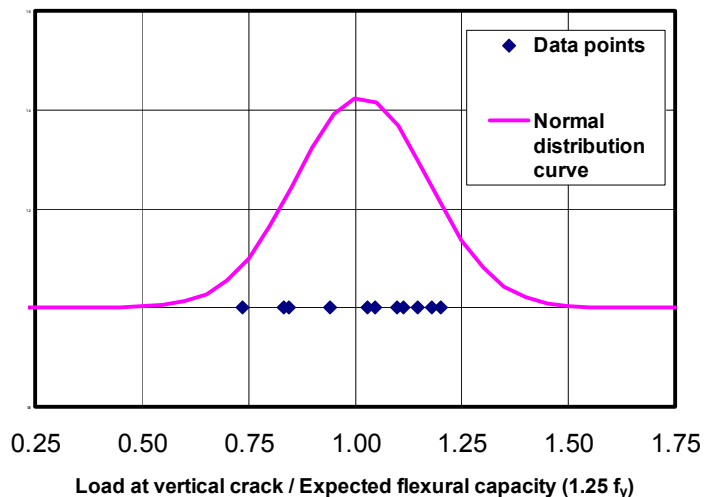


**Figure A.33 Ratio of base shear at observed longitudinal crack to base shear at expected flexural capacity ( $f_s=1.25 f_y$ )**

For lower base shears, a similar analysis can be performed. The results of Table A.12 are reproduced based on nominal moment capacity (rather than expected), and are presented in Table A.13. In this case the ratios of base shear at longitudinal cracking to base shear at nominal capacity range from 0.84 to 1.42, with an average of 1.2 and a COV of 15.5%. These data are illustrated graphically in Figure A.34. The ratio of 1.0 between base shear at longitudinal cracking to base shear at nominal flexural capacity, corresponds to a 16% lower fractile. A 5% lower fractile corresponds to a ratio of 0.88. Based on these results, 5% of shear walls would exhibit longitudinal cracking at the factored nominal flexural capacity. To further determine if vertical cracks would occur at

service loads, analyses were performed to determine if the cracks formed prior to yielding, and are presented in the following section.

***Table A.13 Ratio of base shear at observed vertical cracking to the nominal flexural capacity (without overstrength) in flexure-dominated AAC shear wall specimens***

<b>Specimen</b>	<b>Base shear at first and second observed vertical crack kips (kN)</b>	<b>Base shear at design flexural capacity <math>V_{Mn}</math> kips (kN)</b>	<b>Ratio of base shear at first observed crack to <math>V_{Mn}</math></b>
13	13.6 (60) – first 15.6 (69) - second	11.4 (51)	1.19 – first 1.37 – second
14a	6.9 (31) – first NA – second	6.9 (31)	1.00 – first NA – second
14b	7.0 (31) – first 9.8 (44) - second	6.9 (31)	1.01 – first 1.41 – second
15a	26.5 (118) – first 27.3 (128) - second	20.9 (93)	1.27 – first 1.31 – second
15b	17.5 (78) – first 24.5 (109) - second	20.9 (93)	0.84 – first 1.17 – second
16	24.0 (107) – first 28.0 (125) - second	22.2 (99)	1.08 – first 1.26 – second

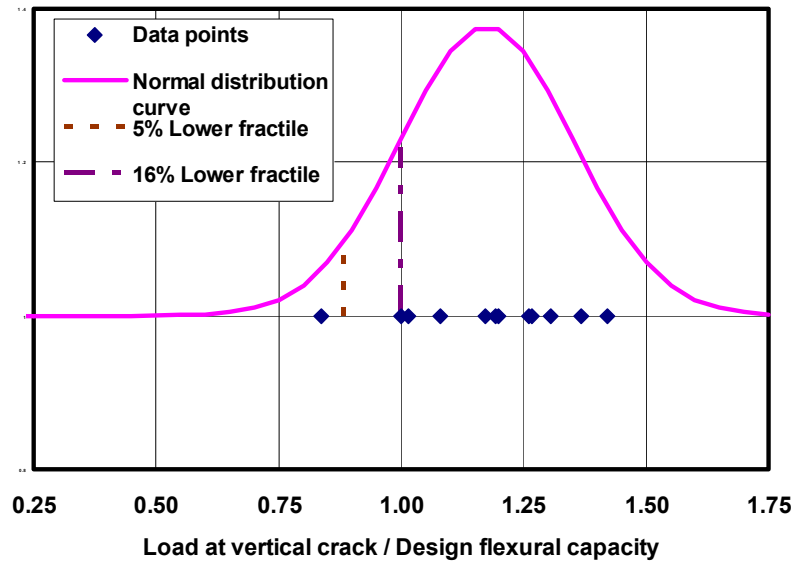


*Figure A.34 Ratio of base shear at observed longitudinal crack to base shear at nominal flexural capacity without overstrength*

### **A.2.5 Analysis to Determine if Longitudinal Cracks Formed Prior to Yielding**

Additional analysis was performed to determine if longitudinal cracks formed before or after the vertical reinforcement yielded. If the vertical cracks formed prior to yielding, then those cracks might also be present in walls at factored design loads. If the vertical cracks formed after yielding, it can be assumed that they would occur only during overloading beyond the nominal capacity.

Strain was measured by three strain gages on the longitudinal reinforcement at each end of the wall. If one strain gage indicated strains beyond yield and another strain gage indicated strains near but not exceeding yield, this was assumed to denote yielding. The base shear and load points at the formation

of longitudinal cracks in each specimen, while loading to the south and to the north, are recorded in Column 2 of Table A.14. In Shear Wall Specimen 13, strain gage data were not available; for this reason, in Column 2 both the South and North loading directions are labeled “NA.” The base shear and load points at the yielding of the flexural reinforcement are presented in Column 3. Since load points are assigned in ascending order, the first event (either longitudinal cracking or yielding of longitudinal reinforcement) has the lowest-numbered load point. The event that occurred first for each loading direction is presented in Column 4. If the load-point numbers did not vary by more than 5, it was assumed that longitudinal cracking occurred simultaneously with yielding of flexural reinforcement, and was therefore associated with that yielding. For example, in Shear Wall Specimen 14a while loading to the south, longitudinal cracking was observed at Load Point 542, and the longitudinal reinforcement was determined to have yielded at Load Point 539. Since these load points do not vary by more than 5, it was concluded that the longitudinal cracking and yielding of the reinforcement occurred simultaneously, as indicated in Column 4. Finally, the ratio of base shear at longitudinal cracking to base shear at yielding is presented in Column 5.

**Table A.14 Estimation of order of vertical cracking and yielding of longitudinal reinforcement, based on strain gages**

Specimen	Base shear at observed vertical crack, loading south and loading north, Kips (kN) Load point	Base shear at yielding of flexural reinforcement, loading south and loading north, kips (kN) Load point	Estimated order of yielding of reinforcement and longitudinal cracking	Ratio of base shear at formation of longitudinal crack of base shear at yielding of flexural reinforcement
13	13.6 (60) LP 1023 - S 15.6 (69) LP 1232 - N	NA - S NA - N	NA - S NA - N	NA - S NA - N
14a	6.9 (31) LP 542 - S NA - N	6.2 (27.6) LP 539 - S NA - N	Together - S NA - N	1.1 - S NA - N
14b	7.0 (31) LP 326 - S 9.8 (25) LP 487 - N	7.5 (33) LP 327 - S 8.9 (40) LP 410 - N	Together - S Yielding - N	0.9 - S 1.1 - N
15a	28.8 (128) LP 437 - S 27.3 (121) LP 528 - N	22.1 (98) LP 299 - S 26.0 (116) LP 333 - N	Yielding - S Yielding - N	1.3 - S 1.1 - N
15b	17.5 (78) LP 202 - S 24.5 (109) LP 338 - N	23.7 (102) LP 363 - S 24.5 (109) LP 340 - N	Cracking - S Together - N	0.7 - S 1.0 - N
16	28.0 (125) LP 716 - S 24.0 (107) LP 426 - N	27.0 (120) LP 704 - S 26.8 (119) LP 754 - N	Yielding - S Cracking - N	1.0 - S 0.9 - N

In four cases, yielding occurred before longitudinal cracking; and in two cases, it occurred afterwards. In the remaining cases these events probably occurred simultaneously. In both cases where the flexural reinforcement yielded after longitudinal cracks were observed, the ratio of base shear at formation of longitudinal cracking to base shear at yielding was also less than 1. This further supports the conclusion that if #5 bars are used in 3-in. grouted cores, longitudinal cracks may form prior to yielding of the flexural reinforcement. The ratio of base shear at longitudinal cracking to base shear at yielding is less than 1.25 for all of the specimens, which indicates that longitudinal cracks will probably form prior to reaching the nominal flexural capacity considering a strain hardening factor of 1.25. This analysis does not consider the height at which the vertical crack formed. If the crack formed at a height of 48 in. (1.2 m) the stress in the reinforcement could be significantly below yield. The impact of crack height is considered in a separate analysis.



An additional analysis was performed to estimate the stress in the flexural reinforcement at longitudinal cracking, using elastic flexural stresses calculated based on a cracked transformed section (Table A.15). The applied base shear was converted to an applied moment at the location of the crack by multiplying by the height of the wall minus the crack height. The stress in the longitudinal tensile reinforcement was computed using Equation (A.26). The contributions from the axial load are not presented in Table A.15 because they were less than 2 ksi (14 MPa). The distance from the neutral axis to the centroid of the tensile reinforcement is denoted by  $y_{As}$ ; the modular ratio between steel and AAC is denoted by  $n$ ; and the cracked transformed moment of inertia is denoted by  $I_{ctr}$ . The results indicate that in 6 of the 11 cases, calculated stresses at longitudinal cracking exceeded the expected yield strength of 75 ksi (10.9 GPa). This indicates that approximately half of the vertical cracks occurred prior to or simultaneously with yielding of the flexural reinforcement.

$$\sigma_{As} = \frac{My_{As}n}{I_{ctr}} - \frac{Pn}{A_r} \quad \text{Equation (A.26)}$$

**Table A.15 Calculated stresses in tensile reinforcement based on elastic theory for vertical cracks on the south and north sides of the specimen**

Specimen	Base shear at observed vertical crack, loading south and loading north kips (kN)	Height of the vertical crack in. (m)	Cracked transformed moment of inertia in. <sup>4</sup> (m <sup>4</sup> )	yAs, distance from the area of tensile steel to the neutral axis in. (m)	Calculated stress in tensile reinforcement for first observed vertical crack ksi (GPa)
13	13.6 (60) – S 15.6 (69) – N	24 (0.6) – S 24 (0.6) – N	64900 (0.027)	45 (1.1)	96 (0.67) – S 111 (0.79) – N
14a	6.9 (31) – S NA – N	48 (1.2) – S NA – N	46100 (0.019)	39 (1.0)	49 (0.35) – S NA – N
14b	7.0 (31) – S 9.8 (44) – N	24 (0.6) – S 48 (1.2) – N	46100 (0.019)	39 (1.0)	61 (0.44) – S 70 (0.50) – N
15a	28.8 (128) – S 27.3 (121) – N	48 (1.2) – S 0 (0) – N	226800 (0.094)	86 (2.2)	91 (0.65) – S 127 (0.90) – N
15b	17.5 (78) – S 24.5 (109) – N	12 (0.3) – S 24 (0.6) – N	226800 (0.094)	86 (2.2)	74 (0.53) – S 95 (0.68) – N
16	28.0 (125) – S 24.0 (107) – N	0 (0) – S 24 (0.6) – N	309100 (0.129)	94 (2.4)	104 (0.73) – S 75 (0.54) – N

### A.2.6 Implications of the Formation of Longitudinal Cracks

The above evaluations show that longitudinal cracks are highly probable in real AAC shear walls subject to lateral loads. This section is devoted to explaining the probable consequences of those cracks and providing design recommendations for preventing them.

Cracks along reinforcement in a grouted core are inherently undesirable, because they provide an opportunity for air and water to enter the core, and thereby increase the probability of corrosion of that reinforcement. Longitudinal cracks along the height of the wall, combined with horizontal cracks, can cause the end blocks to spall and crush sooner than in otherwise identical walls without longitudinal cracks (Figure A.35). Longitudinal cracks can also lead to buckling of the longitudinal reinforcement in the compression toe (Figure A.36).



**Figure A.35** Loss of end block on compression toe in Shear Wall Specimen 16

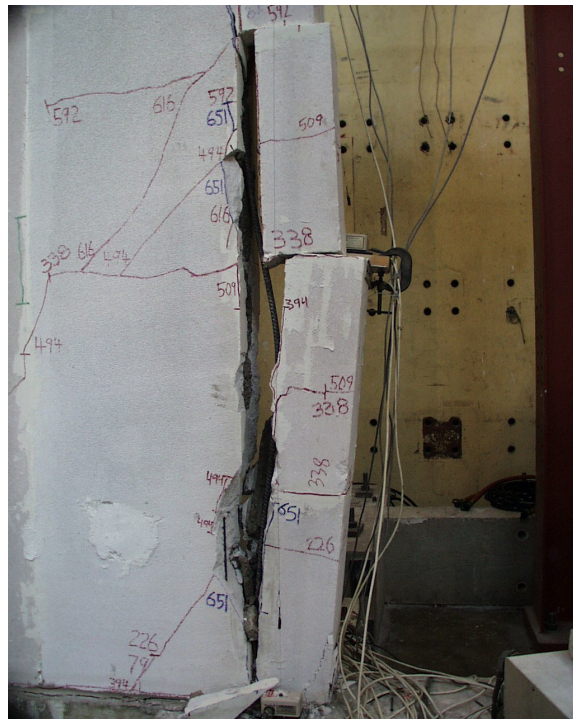


**Figure A.36** Loss of end blocks and buckling of compression reinforcement in Shear Wall Specimen 15b

As the load is reversed, the previously buckled longitudinal reinforcement may fracture, effectively reducing the wall's flexural capacity to zero. Examples of the undesirable consequences of loss of the compression toe are shown by Shear Wall Specimen 15b and Shear Wall Specimen 16.

Resistance to cracks along longitudinal reinforcement could be increased. Longitudinal splitting cracks could be prevented by increasing the size of grouted core or decreasing the bar diameter. This is equivalent to limiting the ratio of area of the longitudinal reinforcement to area of core (area ratio).

The area ratio of a #5 (17 mm) bar in a 3-in. (76 mm) diameter grouted core (4.4%) was observed to produce splitting along longitudinal bars in plastic hinge zones. This is inherently undesirable for AAC shear walls. Such cracking not been observed with #4 bars in 3-in. grouted cores, even at splices. A #4 (12 mm) bar in a 3 in. (76 mm) core corresponds to an area ratio of 2.8%. For that reason, the proposed design provisions for AAC masonry and reinforced AAC panels limit the maximum ratio of the area of reinforcement to the area of the grouted core containing that reinforcement, to 3% in plastic hinge zones.

#### **A.2.7 Analysis of Maximum Permissible Area Ratio if Longitudinal Reinforcement Remains Elastic**

Area ratios of reinforcement up to 4.5% are permitted, provided that radial (splitting) stresses can be limited by limiting the bond stress, which in turn means limiting the shear. The formation of radial stresses is explained in Section 8.8 of this dissertation, and briefly reviewed here.

After the initial adhesion between the reinforcement and concrete is broken, load is transferred from deformed reinforcement to the surrounding concrete or grout by the deformations (lugs). The axial component of the force transferred by the lugs to a vertical core is the difference in force ( $\Delta T$ ) in a section of vertical reinforcement (Figure A.37). The associated radial component of that force also acts on the surrounding grout (Figure A.37). The resultant forces generally act at about 45 degrees to the axis of the reinforcement, so that the resultants of the radial and axial component of the forces are equal. The radial forces generated per length of the bar equal the change in force in the bar over that same length. The pressure generated by the radial forces in the longitudinal bar can be determined by dividing the radial forces by the product of the circumference of the deformed bar and the length of the section of the bar,  $\Delta x$ , as shown in Figure A.37. The diameter of the longitudinal bar is denoted by  $d_{\text{bar}}$ .

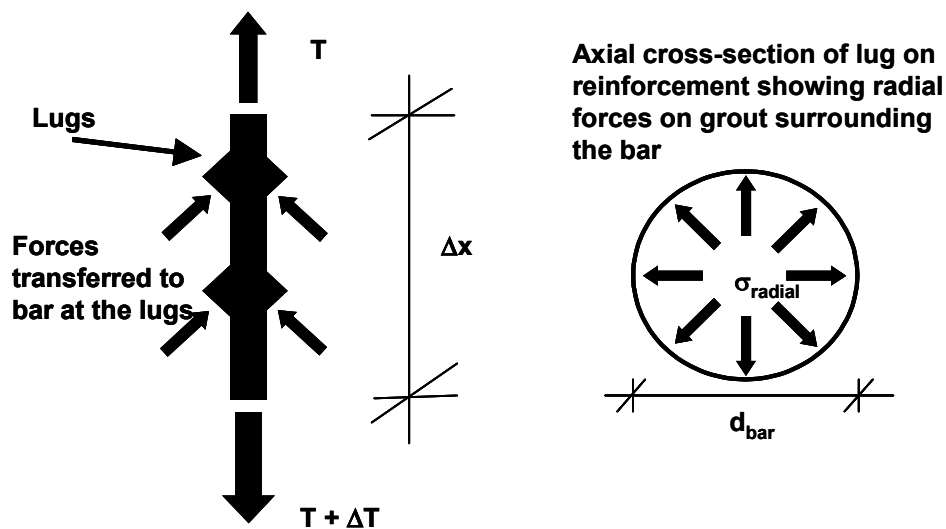


*Figure A.37 Free-body diagram of longitudinal bar with all load transferred through lugs and pressure generated in the surrounding grout*

For design convenience the bond stress can be expressed as a function of shear as shown in Equation (A.27). This relationship is valid in cases where the bond between grout and reinforcement remains intact. Generally bond is broken after the reinforcement yields, therefore this development does not apply to cases where a plastic hinge may form. For practical reasons this analysis based on Equation (A.27) is limited to out-of-plane loading. Since the resultant force acting on the lugs acts at about 45 degrees, the radial stresses,  $\sigma_{radial}$  are also equal to the bond stress,  $u$ , as shown in Equation (A.28).

$$u = \frac{\Delta T}{\pi d_{bar} \cdot \Delta x} = \frac{\Delta M}{jd \cdot \pi d_{bar} \cdot \Delta x} = \frac{V}{jd \cdot \pi d_{bar}} \quad \text{Equation (A.27)}$$

$$\sigma_{radial} = u = \frac{V}{jd \cdot \pi d_{bar}} \quad \text{Equation (A.28)}$$

These radial forces cause splitting tensile stresses along a section through the wall at the center of the grouted core. Because the AAC has only about 15% of the splitting tensile strength of the grout, its tensile strength is neglected. A uniform distribution of splitting stresses across any section through the diameter of the grout core is assumed as shown in Figure A.38a. Since the radial stresses are symmetric about the centerline of the core (Figure A.38a), the net resultant of those radial stresses perpendicular to the centerline is zero. The splitting tensile stresses are resisted by the splitting tensile capacity of a section of grout, whose area is the length of grout shown in Figure A.38b, multiplied by the length of a section  $\Delta x$ . The resistance to the splitting tensile stresses is expressed in Equation (A.29). The resistance is increased by increasing the diameter of the core, decreasing the diameter of the bar, or increasing the tensile strength of the grout.

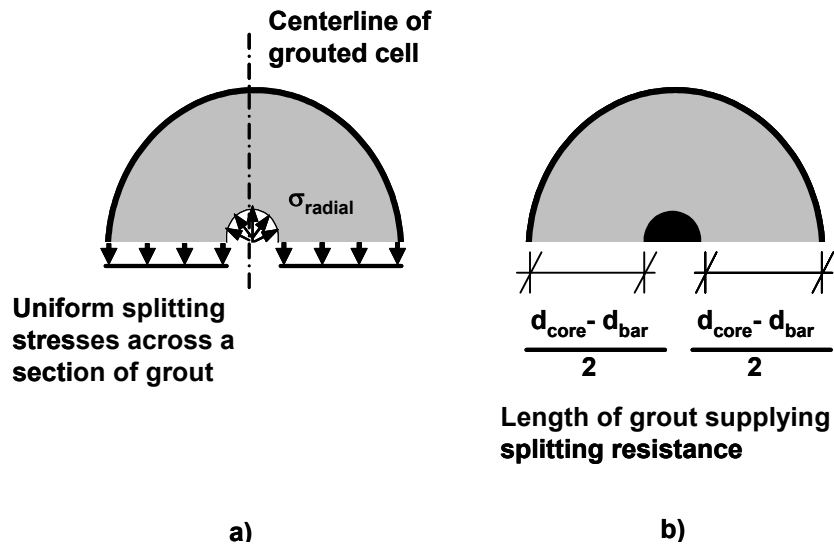


**Figure A.38** Stresses generated perpendicular to a cut along the diameter of a grouted cell

$$F_{resistance} = f_t (d_{core} - d_{bar}) \Delta x \quad \text{Equation (A.29)}$$

The uniform splitting stress across a section of grout as shown in Figure A.38a is calculated by integration. Figure A.39a shows the radial stress acting at the interface between the bar and grout. The vertical component of stress which corresponds to a uniform splitting stress is calculated using geometry for a differential section of the arc,  $ds$  (Figure A.39b). Integrating this expression for the vertical component of force between angles of  $0$  and  $\pi$  yields the expression for the total force generated by the splitting stress shown in Equation (A.30). If the resultant of the uniform splitting tensile stress is set equal to the total force supplied by the resistance of the grout (Figure A.38), Equation (A.31) is generated. The splitting tensile strength,  $f_t$ , is expressed in terms of the bond stress in Equation (A.32).

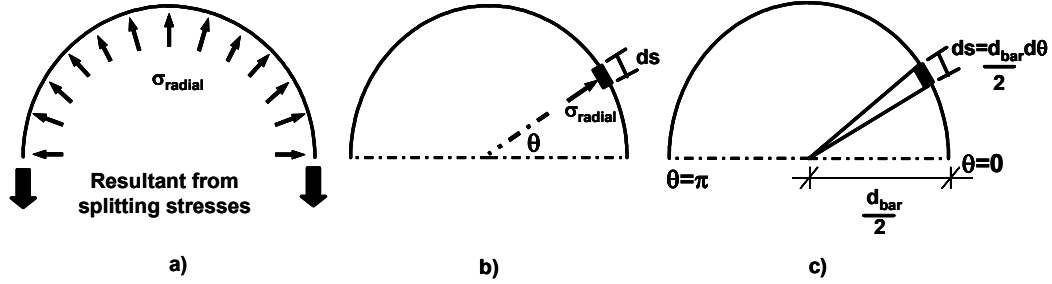


**Figure A.39 Calculation of force corresponding to the splitting tensile stresses across a section of grout**

$$F_{splitting} = \int_0^{\pi} \sigma_{radial} \Delta x \sin \theta \cdot ds = \int_0^{\pi} \sigma_{radial} \Delta x \sin \theta \cdot \frac{d_{bar}}{2} d\theta = \sigma_{radial} d_{bar} \Delta x \quad \text{Equation (A.30)}$$

$$f_t (d_{core} - d_{bar}) \Delta x = \sigma_{radial} d_{bar} \Delta x \quad \text{Equation (A.31)}$$

$$f_{t,reqd} = \frac{\sigma_{radial} d_{bar}}{(d_{core} - d_{bar})} = \frac{u d_{bar}}{(d_{core} - d_{bar})} = \frac{V d_{bar}}{j d \cdot d_{bar} \cdot (d_{core} - d_{bar})} \quad \text{Equation (A.32)}$$

Based on this analysis, for reinforcement in the elastic stress range, the acting splitting tensile stress can be calculated. In such a case the area ratio of longitudinal steel may be increased beyond the proposed value of 3% for the design provisions of Section A.2.8. These proposed design provisions permit area ratios of longitudinal steel to grouted core up to 4.5%, provided that the splitting tensile stress generated in the core (Equation (A.32)) is less than the available splitting tensile strength. A detailed example of these calculations is presented in a design example involving walls subject to out-of-plane loading. The proposed design provisions in ACI 318-02 Code language are as follows:



**12.1.3** – *The maximum ratio of vertical reinforcement to area of a grouted cell shall be 3%. It shall be permitted to use ratios of vertical reinforcement up to 4.5% if the reinforcement remains elastic throughout its entire length and the available splitting tensile strength of the grout is greater than the acting splitting tensile strength as defined by Equation (12-xx)*

$$f_t = \frac{Vd_{bar}}{jd \cdot d_{bar} \cdot (d_{core} - d_{bar})} \quad \text{Equation (12-xx)}$$

*The splitting tensile strength of the grout shall be taken as  $4\sqrt{f'_g}$ . If  $f'_g$  is not specified it shall be permitted to be taken as 2000 psi.*

## **A.2.8 Analysis of the Maximum Permissible Area Ratio in a Plastic Hinge Zone**

If the reinforcement is located in a plastic hinge zone, compatibility of strains no longer exists between the reinforcement and the surrounding grout, and the splitting tensile stress cannot be determined using Equation (A.32). Based on the cracking observed along the flexural reinforcement in the flexure-dominated specimens (Section A.2.4), the proposed design provisions limit the area ratio to 3% in areas where a plastic hinge may form.

## **A.3 DESIGN EXAMPLES**

### **A.3.1 Design of an AAC shear wall**

Design the following two-story AAC shear wall. Material properties, factored loads, and geometry are:

PAAC-5

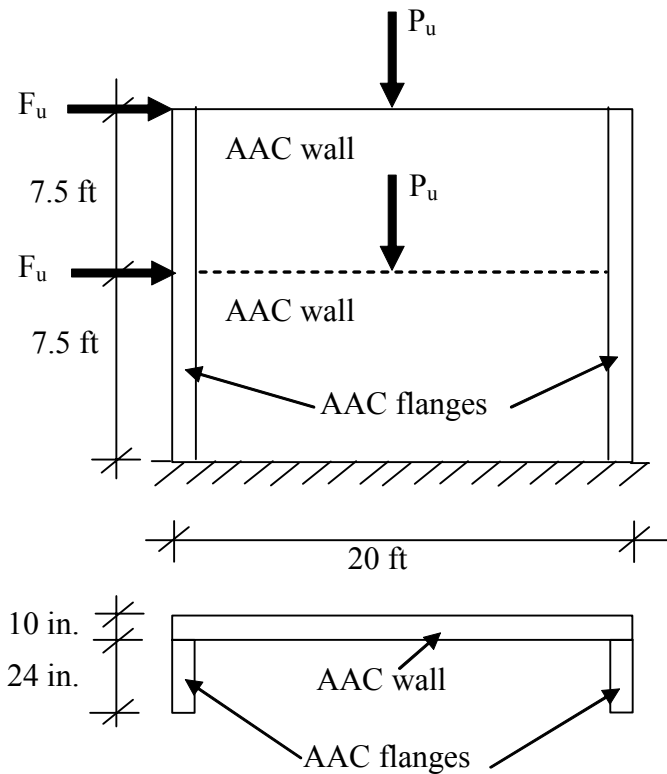
$$f'_{AAC} = 580 \text{ psi}$$

$$f_y = 60,000 \text{ psi (flexural reinforcement)}$$

$E_s = 29,000 \text{ Ksi}$

Factored axial load at each story,  $P_u = 35,000 \text{ lbs}$

Factored lateral load at each story,  $F_u = 18,000 \text{ lbs}$

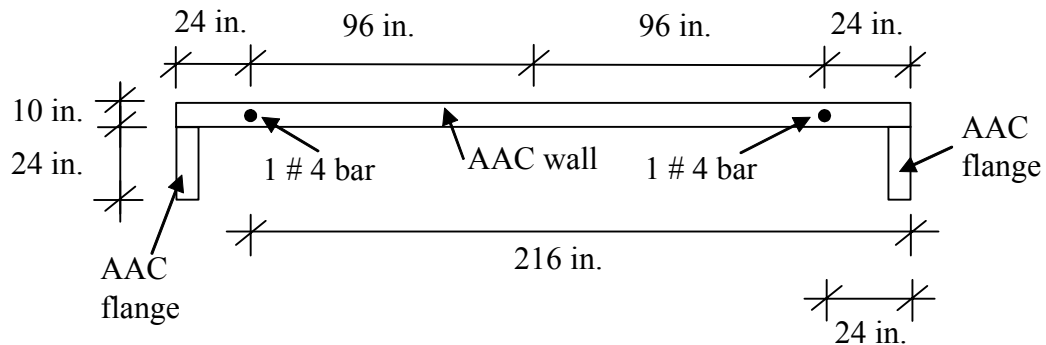


#### ***A.3.1.1 Flexural capacity***

Determine factored bending moment at the base of the wall:

$$M_u = 18,000 (15)(12) + 18,000 (7.5)(12) = 4,860,000 \text{ lbs-in.}$$

Determine flexural capacity at the base of the wall. Assume flexural reinforcement at wall ends only, equal to 1 # 4 bar, located 24 in. from the wall ends.



Calculate forces in bars ( $T_1$  and  $T_2$ ) assuming that both bars are yielding:

$$T_1 = T_2 = A_s f_y = 0.2 (60,000) = 12,000 \text{ lbs}$$

For equilibrium:

$$C = N_u + T_1 + T_2$$

$$N_u = 2 (P_u) = 35,000 + 35,000 = 70,000 \text{ lbs}$$

$$C = 0.85 f'_{AAC} a b$$

$$a = \frac{C}{0.85 f'_{AAC} b} = \frac{70,000 + 12,000 (2)}{0.85 (580) (10 + 24)} = 5.6 \text{ in.}$$

$$M_n = T_1 \left( 216 - \frac{l_w}{2} \right) - T_2 \left( \frac{l_w}{2} - 24 \right) + C \left( \frac{l_w - a}{2} \right)$$

$$M_n = 12,000 \left( 216 - \frac{240}{2} \right) - 12,000 \left( \frac{240}{2} - 24 \right) + 94,000 \left( \frac{240 - 5.6}{2} \right) = 11,020,000 \text{ lbs}$$

$$\phi M_n = 0.9 (11,020,000) = 9,900,000 \text{ lbs}$$

$$\phi M_n = 9,900,000 \text{ lbs-in.} > M_u = 4,860,000 \text{ lbs-in.} \quad \text{OK}$$

Check if right bar ( $T_2$ ) is yielding.

$$c = \frac{a}{\beta_1} = \frac{5.6}{0.67} = 8.4 \text{ in.}$$

$$\varepsilon_2 = \frac{24}{8.4} (\varepsilon_{AAC}) = \frac{24}{8.4} (0.003) = 0.0086$$

$$\varepsilon_y = \frac{f_y}{E_s} = \frac{60,000}{29,000,000} = 0.0021$$

$$\varepsilon_2 = 0.0086 > \varepsilon_y = 0.0021 \quad \text{OK}$$

### A.3.1.2 Shear capacity

Determine factored shear force and axial force at the base of the wall:

$$V_u = 2 F_u = 2 (18,000) = 36,000 \text{ lbs}$$

$$N_u = 70,000 \text{ lbs}$$

Determine shear capacity at the base of the wall (web shear cracking):

$$\phi V_{AAC} = \phi 0.9 t l_w \sqrt{f'_{AAC}} \sqrt{1 + \frac{N_u}{2.4 \sqrt{f'_{AAC}} t l_w}}$$

$$\phi V_{AAC} = 0.75 (0.9) (10) (240) \sqrt{580} \sqrt{1 + \frac{70,000}{2.4 \sqrt{580} (10) (240)}} = 47,850 \text{ lbs}$$

$$\phi V_{AAC} = 47,850 \text{ lbs} > V_u = 36,000 \text{ lbs} \quad \text{OK}$$

Determine factored shear force and axial force at 7.5 ft from the base of the wall:

$$V_u = F_u = 18,000 \text{ lbs}$$

$$P_u = N_u = 35,000 \text{ lbs}$$

Determine shear capacity at 7.5 ft from the base of the wall (web shear cracking):

$$\phi V_{AAC} = 0.75 (0.9)(10)(240)\sqrt{580} \sqrt{1 + \frac{35,000}{2.4 \sqrt{580} (10)(240)}} = 43,700 \text{ lbs}$$

$$\phi V_{AAC} = 43,700 \text{ lbs} > V_u = 18,000 \text{ lbs} \quad \text{OK}$$

Determine shear capacity of bottom wall (crushing of the diagonal strut):

$$\phi V_{AAC} = 0.75 (0.9) f'_{AAC} t w_{\text{strut}} \frac{h \left( \frac{3l_w}{4} \right)}{h^2 + \left( \frac{3l_w}{4} \right)^2}$$

$$w_{\text{strut}} = \frac{l_w}{4} = \frac{240}{4} = 60 \text{ in}$$

$$\phi V_{AAC} = 0.75 (0.9)(580)(10)(60) \frac{90 \left( \frac{3(240)}{4} \right)}{90^2 + \left( \frac{3(240)}{4} \right)^2} = 93,960 \text{ lbs}$$

$$\phi V_{AAC} = 93,960 \text{ lbs} > V_u = 36,000 \text{ lbs} \quad \text{OK}$$

Determine sliding shear capacity of bottom wall and a thin-bed mortar joint:

$\mu = 1$  at a leveling bed joint

$$\phi V_{ss} = \phi (\mu N_u)$$

Neglect additional force in tensile steel:

$$\phi V_{ss} = 0.75 ( (1)(70,000) ) = 52,500 \text{ lbs}$$

$$\phi V_{ss} = 52,500 \text{ lbs} > V_u = 36,000 \text{ lbs} \quad \text{OK}$$

$\mu = 0.75$  at AAC to AAC joint

$$\phi V_{ss} = \phi ( \mu N_u )$$

Neglect additional force in tensile steel.

$$\phi V_{ss} = 0.75 ( (0.75)(70,000) ) = 39,375 \text{ lbs}$$

$$\phi V_{ss} = 39,375 \text{ lbs} > V_u = 36,000 \text{ lbs} \quad \text{OK}$$

### **A.3.2 Design an AAC Shear Wall for Out-of-plane loads**

PAAC-5

$$f'_{AAC} = 580 \text{ psi}$$

$f_y = 60,000 \text{ psi}$  (flexural reinforcement)

$$E_s = 29,000 \text{ ksi}$$

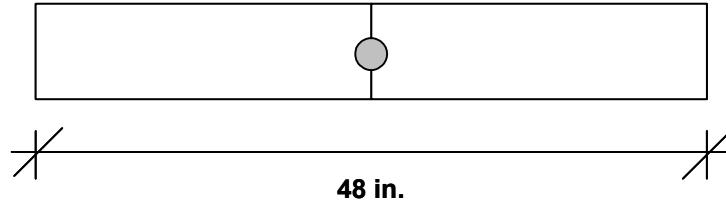
Factored wind load on wall  $\rho_u = 110 \text{ lbs/ft}^2$

Reinforcement in a 3 in. grouted cell at 4 ft. on center

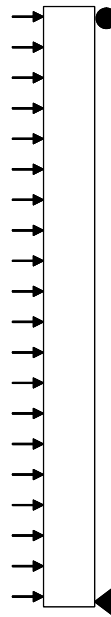
$h = 10 \text{ ft}$

$t = 10 \text{ in.}$

Plan view of 4 ft. section of wall



Elevation of shear wall simply supported at top and bottom



#### ***A.3.2.1 Flexural capacity***

Determine acting moment:

$$w_u = \rho \cdot \text{width} = 110 \text{ lb/ft}^2 \cdot 4\text{ft} = 440 \text{ lb/ft}$$

$$M_u = \frac{wl^2}{8} = \frac{440 \cdot (10)^2}{8} = 5,500 \text{ lb-ft} = 66,000 \text{ lb-in.}$$

Try #4 bar:

$$T = A_s f_y = 0.2 \cdot 60,000 = 12,000 \text{ lb}$$

$$a = \frac{T}{0.85 f_{AC} 'b} = \frac{12,000}{0.85 \cdot 580 \cdot 48} = 0.5 \text{ in}$$

$$M_n = A_s \cdot f_y \cdot (d - \frac{a}{2}) = 12 \cdot (5 - \frac{0.5}{2}) = 57,000 \text{ lb-in}$$

$$\phi M_n = 0.9 \cdot 57,000 \text{ lb-in} = 51,300 \text{ lb-in} < M_u \quad \text{Not Good}$$

Try #5 bar:

$$T = A_s f_y = 0.31 \cdot 60,000 = 18,600 \text{ lb}$$

$$a = \frac{T}{0.85 f_{AC} 'b} = \frac{18,600}{0.85 \cdot 580 \cdot 48} = 0.8 \text{ in}$$

$$M_n = A_s \cdot f_y \cdot (d - \frac{a}{2}) = 18.6 \cdot (5 - \frac{0.8}{2}) = 85,700 \text{ lb-in}$$

$$\phi M_n = 0.9 \cdot 85,700 \text{ lb-in} = 77,130 \text{ lb-in} > M_u \quad \text{O.K.}$$

Check strain limits for this case:

$$c = a / \beta_1 = 0.8 / 0.67 = 1.2$$

$$d = 5$$

$$\epsilon_s = 0.003 \cdot (d - c) / c = 0.0095 > 1.3 \epsilon_y = 1.3 \cdot 1.25 \cdot f_y / E_s = 0.0033$$

Use a #5 bar

$$A_{\text{steel}} / A_{\text{grout}} = 0.31 / 7.1 = 0.044 = 4.4\% > 3\%$$

Perform an analysis to check the bond stress. In the case of out-of-plane loads the reinforcement in the wall does not yield and no plastic hinge forms. In this example, the classical bond stress analysis shown in the example can be used.

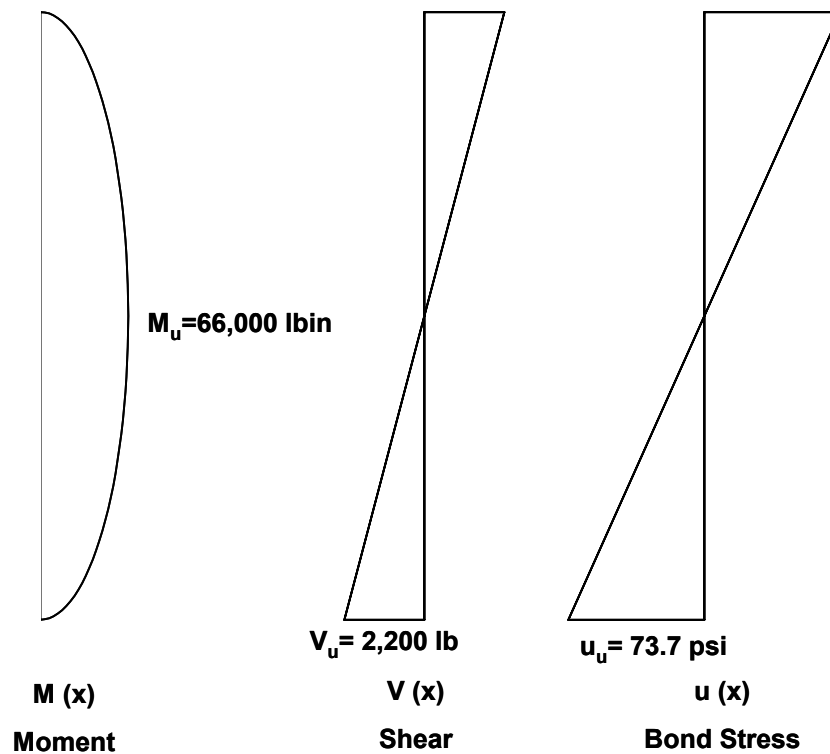
Check bond stress:



Determine if reinforcement is yielding:

$\phi M_n = 0.9 * 85,700 \text{ lb-in} = 77,130 \text{ lb-in} > M_u = 66,000 \text{ lb-in}$ , reinforcement will not be yielding. Since reinforcement will not be yielding consider case where bond remains intact and express bond stress as a function of shear.

Determine shear and bond stress along the length of the wall. Based on the bond stress determine the splitting tensile stress in the wall and compare to the splitting tensile strength of the grout.



$$V_u = \frac{440 \cdot 10}{2} = 2200 \text{ lbs}$$

$$u_u = \frac{V}{\text{arm} \cdot \pi d_{\text{bar}}} = \frac{2200}{0.8 \cdot 5 \cdot \pi \cdot 0.625} = 280 \text{ psi}$$

$$f_{\text{reqd}} = \frac{u d_{\text{bar}}}{(d_{\text{core}} - d_{\text{bar}})} = \frac{280 \cdot 0.625}{(3 - 0.625)} = 73.7 \text{ psi}$$

$$f_{\text{available}} = 4\sqrt{f_g} = 4\sqrt{3000} = 219 \text{ psi}$$

The factored splitting tensile stress is less than the factored tensile strength available. Use  $\phi=0.75$  which corresponds to shear.

$$u_u = 74 \text{ psi} < \phi f_t = 0.75(219) = 164 \text{ psi.}$$

#### ***A.3.2.2 Shear capacity***

Determine factored loads and maximum shear force for a single panel.

$$w_u = 110 \text{ psf}$$

$$V_u = 2 w_u \frac{L}{2} = 2(110) \frac{10}{2} = 1,100 \text{ lbs}$$

Determine shear capacity of floor panel:

$$V_{AAC} = 0.9\sqrt{f'_{AAC}} A_n + 0.05P_u = 0.9\sqrt{580} \cdot 24 \cdot 10 = 5200 \text{ lbs}$$

$$\phi V_{AAC} = 0.75 \cdot (5,200) = 3,900 \text{ lbs} > V_u = 1,100 \text{ lbs} \quad \text{OK}$$

## **APPENDIX B**

### **ACI 523.5R-xx Guide for using Autoclaved Aerated Concrete Panels**

#### **B.1 INTRODUCTION**

Appendix B consists of the first several draft chapters in a *Guide for using Autoclaved Aerated Concrete Panels*, under development in ACI Committee 523A, Cellular Concrete. Much of the material in that draft chapter was extensively rewritten for inclusion in the MS thesis of Argudo (2003). It is presented here to give the reader basic background information on AAC.

##### **B.1.1 Definition of Autoclaved Aerated Concrete**

Autoclaved Aerated Concrete (AAC) is a low-density cementitious product of calcium silicate hydrates in which the low density is obtained by the formation of macroscopic air bubbles, mainly by chemical reactions within the mass during the liquid or plastic phase. The air bubbles are uniformly distributed and are retained in the matrix on setting, hardening, and subsequent curing with high-pressure steam in an autoclave, to produce a cellular structure (Figure B.1). Material specifications for this product are prescribed in ASTM C 1386.



*Figure B.1 Cellular structure of AAC*

### **B.1.2 Typical Mechanical and Thermal Characteristics of AAC**

In Table B.1, typical mechanical and thermal characteristics of AAC are compared with those of conventional concrete, including conventional concrete made with lightweight aggregates. AAC typically has one-sixth to one-third the density of conventional concrete, and about the same ratio of compressive strength, making it potentially suitable for cladding and infills, and for bearing-wall components of low- to medium-rise structures. Its thermal conductivity is one-sixth or less that of concrete, making it potentially energy-efficient. Its fire rating is slightly longer than that of conventional concrete of the same thickness, making it potentially useful in applications where fire resistance is important. Because of its internal porosity, AAC has very low sound transmission, making it potentially useful acoustically.

**Table B.1 Typical mechanical and thermal characteristics of AAC**

<b>Characteristic</b>	<b>AAC</b>	<b>Conventional Concrete</b>
density, pcf (kg/m <sup>3</sup> )	25 - 50 (400 - 800)	80 - 150 (1280 - 2400)
compressive strength, $f_c$ , psi (MPa)	360 - 1090 (2.5 - 7.5)	1000 - 10000 (6.9 - 69)
thermal conductivity, Btu- in/ft <sup>2</sup> -hr-F	0.75 - 1.20	6.0 - 10
fire rating, hours	≤ 8	≤ 6

### **B.1.3 Historical Background of AAC**

AAC was first produced commercially in Sweden, in 1923. Since that time, its production and use have spread to more than 40 countries on all continents, including North America, Central and South America, Europe, the Middle East, the Far East, and Australia. This wide experience has produced many case studies of use in different climates, and under different building codes.

In the US, modern uses of AAC began in 1990, for residential and commercial projects in the southeastern states. US production of plain and reinforced AAC started in 1995 in the southeast, and has since spread to other parts of the country. A nationwide group of AAC manufacturers was formed in 1998 as the Autoclaved Aerated Concrete Products Association. This *Guide* is an effort by the AAC technical community, including manufacturers, designers and

researchers, to propose national design guidelines that could later be developed into code provisions.

#### **B.1.4 Applications of AAC Panels**

AAC can be used to make unreinforced, masonry-type units, and also factory-reinforced floor panels, roof panels, wall panels, lintels, beams, and other special shapes (Figure B.2). These elements can be used in a variety of applications including residential, commercial and industrial construction. Reinforced wall panels can be used as cladding systems as well as load-bearing and non-loadbearing exterior and interior wall systems. Reinforced floor and roof panels can be efficiently used to provide the horizontal diaphragm system while supporting the necessary gravity loads.

#### **B.1.5 Scope and Objectives of this *Guide***

This *Guide* is limited to AAC with a density of 50 lb/ft<sup>3</sup> (800 kg/m<sup>3</sup>) or less. This *Guide* is written for structural designers. It addresses design using factory-reinforced AAC elements. Design of AAC masonry is addressed in other documents.

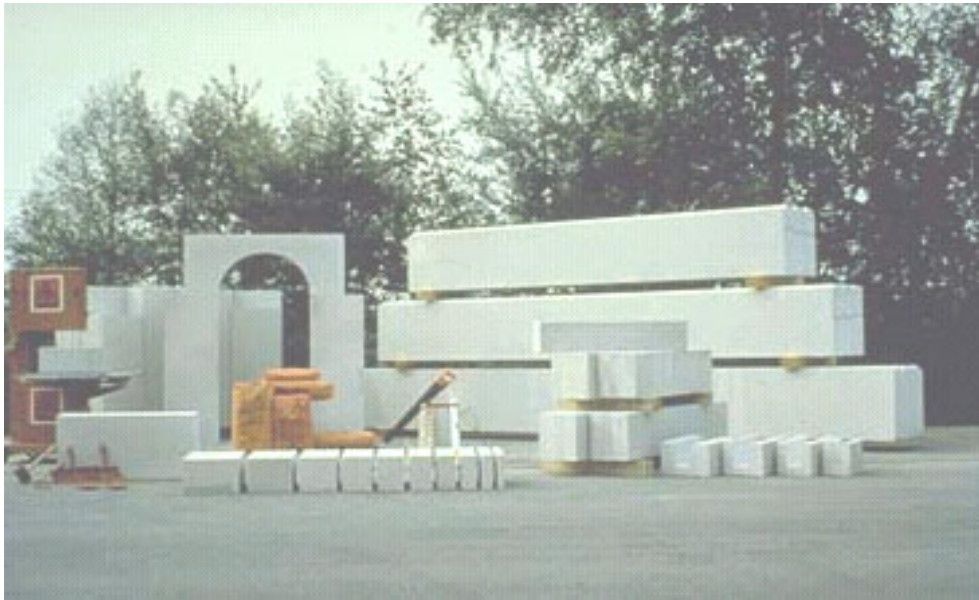


***Figure B.2 Examples of AAC structural elements***

Design documents produced by ACI technical committees are classified as standards or non-standards. The latter include “guides,” which are intended to present directions for analysis, design, construction, materials, or testing on a general basis. Their language is non-mandatory, permitting the user latitude in judgment concerning particular needs.

The specific objectives of this *Guide* are:

- a) To review the basic characteristics of AAC
- b) To provide a capsule history of structural applications of AAC
- c) To review the fabrication of AAC elements
- d) To recommend structural design procedures for factory-reinforced AAC elements
- e) To recommend construction details for use with factory-reinforced AAC elements

The structural design procedures and construction details recommended here are intended to result in AAC elements with adequate structural capacity, durability, appearance and overall serviceability.

## **B.2 TYPICAL MATERIALS AND MANUFACTURE OF AAC**

### **B.2.1 Materials Used in AAC**

Materials for AAC vary with manufacture and location, and are specified in ASTM C1386. They include some or all of the following:

- a) Fine silica sand (ASTM C33, C144 or C332);
- b) Class F fly ash (ASTM C618) with up to 12% loss on ignition (LOI);
- c) Hydraulic cements (ASTM C150 or C595);
- d) Calcined lime (ASTM C110);
- e) Gypsum (ASTM C22);
- f) Expansive agent, such as finely ground aluminum powder;
- g) Mixing water (clean and free of deleterious substances); and
- h) Reinforcement (ASTM A82), welded to form cages, with corrosion-inhibiting coating.

### **B.2.2 Manufacture of AAC**

Overall steps in the manufacture of AAC are shown in Figure B.3.

#### ***B.2.2.1 Preparation, Batching and Mixing of Raw Materials***

Sand is ground to the required fineness in a ball mill, if necessary, and is stored along with other raw materials. The raw materials are then batched by



weight and delivered to the mixer. Measured amounts of water and expansive agent are added to the mixer, and the cementitious slurry is mixed.

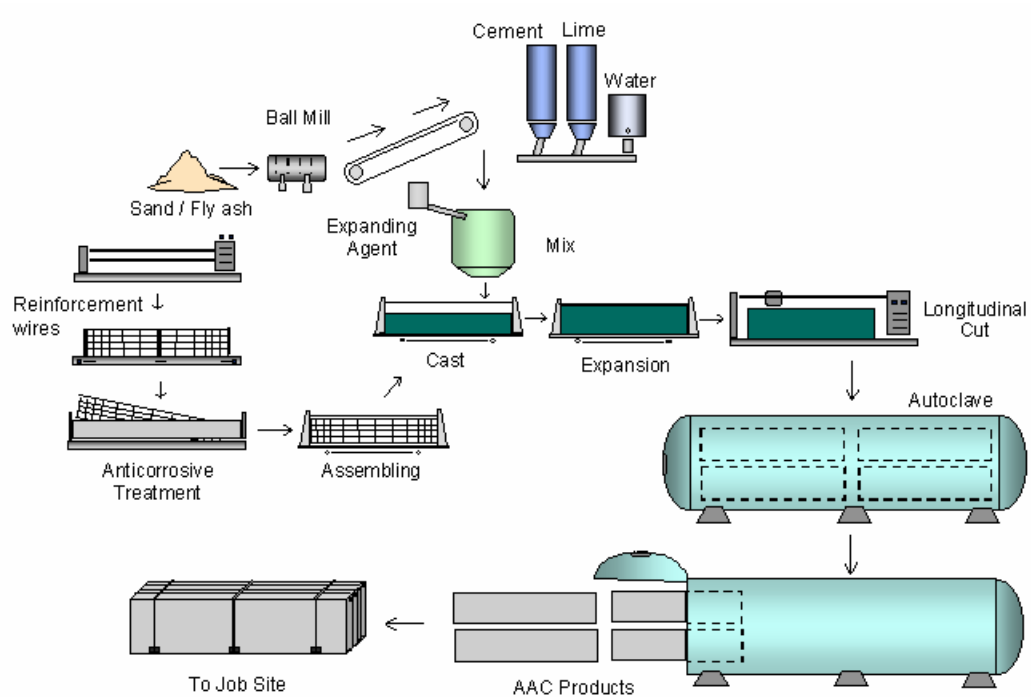


**Figure B.3 Overall steps in manufacture of AAC**

### ***B.2.2.2 Casting, Expansion and Initial Hydration***

Steel molds are prepared to receive the fresh AAC. If reinforced AAC panels are to be produced, steel reinforcing cages are secured within the molds. After mixing, the slurry is poured into the molds. The expansive agent creates small, finely dispersed voids in the fresh mixture, which approximately triples in volume in less than an hour in the molds.

### ***B.2.2.3 Cutting***

Within a few hours after casting, the initial hydration of cementitious compounds in the AAC gives it sufficient strength to hold its shape and support its own weight. The material is removed from the molds (Figure B.4) and fed into a cutting machine, which, using wires, sections the blocks and panels into the required sizes and shapes (Figure B.5). After cutting, the units remain in their original positions in the larger AAC block.



***Figure B.4 Fresh AAC after removal of molds***



*Figure B.5 Cutting AAC into desired shapes*

#### ***B.2.2.4 Autoclaving***

After cutting, the aerated concrete product is transported to a large autoclave, where the curing process is completed (Figure B.6). Autoclaving is required to achieve the desired structural properties and dimensional stability. The process takes about 8 – 12 hours under a pressure of about 174 psi (12 Bars) and a temperature of about 360 °F (180 °C) depending on the grade of material produced. During autoclaving, the wire-cut units remain in their original positions in the AAC block. After autoclaving, they are separated for packaging.

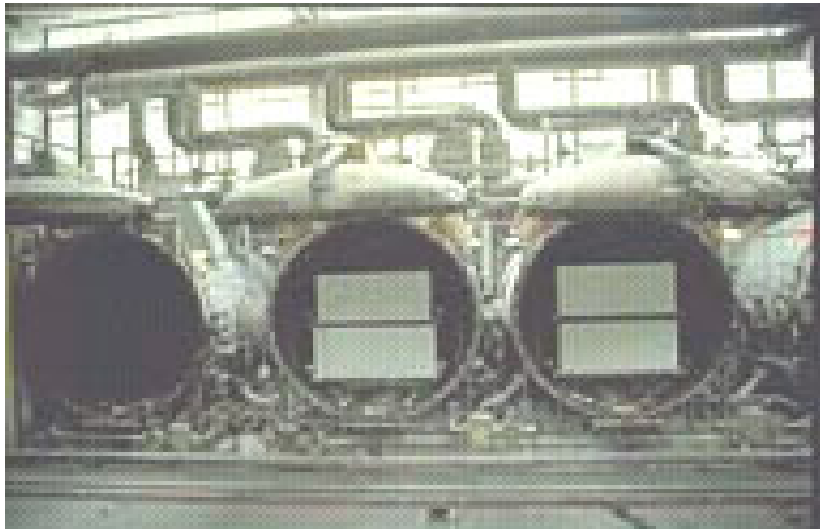


*Figure B.6 Autoclaving AAC*

#### ***B.2.2.5 Packaging***

AAC units are normally placed on pallets for shipping. Unreinforced units are typically shrink-wrapped, while reinforced elements are banded only, using corner guards to minimize potential localized damage that might be caused by the banding.



*Figure B.7 Packaging of finished AAC units*

#### ***B.2.2.6 AAC Strength Classes***

AAC is produced in different densities and corresponding compressive strengths, in accordance with ASTM C1386 (Precast Autoclaved Aerated Concrete Wall Construction Units) and ASTM C 1452 (Standard Specification for Reinforced Autoclaved Aerated Concrete Elements). Densities and corresponding strengths are described in terms of “strength classes.” In each case, the strength class corresponds to the specified compressive strength in MPa.

**Table B.2 Material characteristics of AAC in different strength classes**

<b>Strength Class</b>	<b>Specified Compressive Strength lb/in<sup>2</sup> (MPa)</b>	<b>Average Compressive Strength</b>	<b>Nominal Dry Bulk Density lb/ft<sup>3</sup> (kg/m<sup>3</sup>)</b>	<b>Density Limits lb/ft<sup>3</sup> (kg/m<sup>3</sup>)</b>
AAC 2.0	290 (2.0)	360 (2.5)	25 (400) 31 (500)	22 (350) - 28 (450) 28 (450) - 34 (550)
AAC 3.3	478 (3.3)		31 (500) 37 (600)	28 (450) - 34 (550) 34 (550) - 41 (650)
AAC 4.0	580 (4.0)	720 (5.0)	31 (500) 37 (600) 44 (700) 50 (800)	28 (450) - 34 (550) 34 (550) - 41 (650) 41 (650) - 47 (750) 47 (750) - 53 (850)
AAC 4.4	638 (4.4)		37 (600) 44 (700)	34 (550) - 41 (650) 41 (650) - 47 (750)
AAC 6.0	870 (6.0)	1090 (7.5)	44 (700) 50 (800)	41 (650) - 47 (750) 47 (750) - 53 (850)

### **B.2.3 Typical Dimensions of AAC Units**

#### ***B.2.3.1 Plain AAC Wall Units***

Typical dimensions for plain AAC wall units (masonry-type units) are shown in Table B.3.

***Table B.3 Dimensions of plain AAC wall units***

<b>AAC Unit Type</b>	<b>Width, in. (mm)</b>	<b>Height, in. (mm)</b>	<b>Length, in. (mm)</b>
Standard Block	2 - 15 (50 - 375)	8 (200)	24 (610)
Jumbo Block	4 - 15 (100 - 375)	16 - 24 (400 - 610)	24 - 40 (610 - 1050)

***B.2.3.2 Reinforced AAC Units***

Dimensional tolerances, requirements for reinforcement, and other requirements for reinforced AAC panels are specified in ASTM C1452, which also cites C1386. Typical dimensions for reinforced AAC wall units (panels) are shown in Table B.4.

***Table B.4 Dimensions of reinforced AAC wall units***

<b>Product Type</b>	<b>Thickness, in. (mm)</b>	<b>Height or Width, in. (mm)</b>	<b>Typical Length, ft (mm)</b>
Wall Panel	2 -15 (50 - 375)	24 (610)	20 (6090)
Floor Panel	4 -15 (100 - 375)	24 (610)	20 (6090)
Lintel / Beam	4 -15 (100 - 375)	8 - 24 (200 - 610)	20 (6090)

#### **B.2.4 Dimensional Tolerances**

In accordance with ASTM C1386, dimensional tolerances for plain AAC wall units are 1/8 in. (3 mm) in each dimension. Dimensional tolerances for reinforced elements are given in ASTM C1452, and are listed in Table B.5.

*Table B.5 Dimensional tolerances for reinforced AAC units*

<b>Dimension</b>	<b>Floor or Roof Panels, in. (mm)</b>	<b>Wall Panels, in. (mm)</b>
Length	$\pm 0.20 (\pm 5)$	$\pm 0.20 (\pm 5)$
Width	$\pm 0.12 (\pm 3)$	$\pm 0.12 (\pm 3)$
Thickness	$\pm 0.12 (\pm 3)$	$\pm 0.12 (\pm 3)$
Tongue	$\pm 0.12 (\pm 3)$	$\pm 0.12 (\pm 3)$
Groove	$\pm 0.12 (\pm 3)$	$\pm 0.12 (\pm 3)$

#### **B.2.5 Identification and Marking of AAC Units**

All reinforced AAC units should bear identifying symbol to include a mark indicating the strength class, production identification code, and position number for reinforced panels. Pallets of unreinforced AAC units should be labeled with strength class, production identification code and size of units.



## **B.3 STRUCTURAL DESIGN OF REINFORCED AAC ELEMENTS**

### **B.3.1 Introductory Remarks regarding Design Provisions**

This document is a guide. Its design provisions are non-mandatory, and are a synthesis of design recommendations from the Autoclaved Aerated Concrete Products Association, and from the results of research conducted at the University of Alabama at Birmingham (UAB), the University of Texas at Austin (UT Austin), and elsewhere.

In this chapter, the proposed design provisions are introduced in narrative form. In Appendix C (Argudo 2003), more information is presented regarding specific design provisions, and a commentary on those provisions.

The specific design provisions and their associated commentary of Appendix C (Argudo 2003), are intended to be compatible in organization, numbering and form with the design provisions of ACI 318, in order to facilitate their use by concrete designers, and also to facilitate their future consideration, in mandatory form, by ACI Committee 318. For that reason, the provisions are arranged to refer directly to ACI 318-02. Additions and exceptions are specifically noted. New subcategories are inserted for new design provisions.

Loads for structural design of AAC elements should be taken from appropriate load codes, such as ASCE 7. Understrength factors ( $\Phi$ -factors) for AAC elements depend on the actions under consideration. They reflect the statistical variability of the capacity, and the accuracy of the capacity-calculation formulas. When failure is governed by yield and fracture of tensile reinforcement,  $\Phi$ -factors are justifiably identical to those used for reinforced

concrete. When failure is governed by crushing or diagonal tension of the AAC itself,  $\Phi$ -factors are similar to those used for concrete. They may even be higher, because the factory production of AAC leads to decreased variability in its mechanical characteristics compared to conventional concrete.

The design provisions of this *Guide* are not intended for use with unreinforced, masonry-type units. Design of those units is covered by provisions currently under development within the Masonry Standards Joint Committee.

## **B.3.2 Proposed Design Provisions for Reinforced AAC Panels**

### ***B.3.2.1 Basic Design Assumptions***

The proposed design provisions for reinforced AAC panels are based on the same principles used for strength design of conventional reinforced concrete elements: strain compatibility between AAC and reinforcement (with some modifications as noted below); stress-strain behavior of AAC and reinforcement; and equilibrium. The design strength of AAC in compression is based on a specified design compressive strength,  $f_{AAC}'$ . Compliance with that specified compressive strength is verified by compressive strength testing, using ASTM C1386, when the AAC panels are fabricated. The design strength of AAC in tension is proposed as a function of the specified compressive strength. The design strength of reinforcement in tension is proposed as the specified yield strength.

### ***B.3.2.2 Combinations of Flexure and Axial Load***

AAC panels are designed for combinations of flexural and axial load using principles identical to those for conventional reinforcement. Nominal capacity is computed assuming plane sections; tensile reinforcement is assumed to be yielded; the stress in compressive reinforcement is computed based on its strain and its stress-strain behavior; and the distribution of compressive stress in the AAC is approximated by an equivalent rectangular stress block.

Because reinforced AAC panels usually have equal areas of tensile and compressive reinforcement, flexural capacity is usually “tension-controlled” (in the terminology of ACI 318-02. Sections are under-reinforced (in the terminology of ACI 318-99).

### ***B.3.2.3 Bond and Development of Reinforcement***

Reinforcement in AAC panels consists of welded-wire mesh installed when the panels are produced, and deformed reinforcement installed in 3- to 4- in. grouted cores as the panels are erected.

Bond and development requirements for deformed reinforcement in grout are identical to those used for concrete or masonry construction. Given the small sizes of deformed bars used in AAC construction, bond between the grout and the AAC itself does not govern the bond capacity.

Bond and development requirements for welded-wire fabric embedded in AAC are quite different from those for conventional concrete, however. Because the welded-wire fabric has a corrosion-resistant coating, bond strength between the coated wire and the AAC itself is negligible. Bond strength comes from

bearing of the cross wires against the AAC. For typical cross-wire spacings, local crushing of the AAC under the cross wires can be assumed to redistribute the bearing stresses under the cross wires, leading to a uniform bearing strength of  $f_{AAC'}$  under every cross-wire. Multiplying this stress by the number of cross wires and by the bearing area of each cross-wire gives the maximum force that can be developed in the welded wire fabric (Figure B.8).

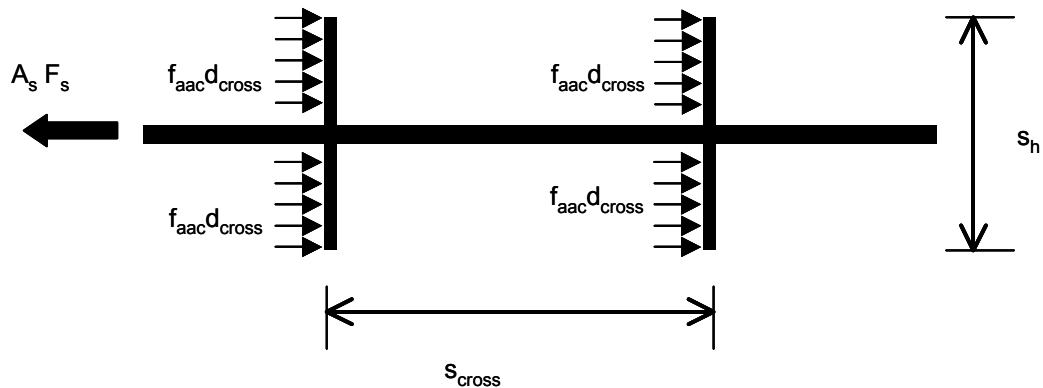


**Figure B.8 Bond mechanism of welded-wire fabric in AAC**

This maximum force in the welded-wire mesh can limit the flexural capacity of a reinforced AAC panel.

#### **B.3.2.4 Shear**

As with conventional reinforced concrete elements, the shear resistance of AAC elements is computed as the summation of a shear resistance due to the AAC itself ( $V_{AAC}$ ), and a shear resistance due to reinforcement oriented parallel to the direction of the shear.

The shear resistance due to the AAC itself ( $V_{AAC}$ ) is computed using the web-shear approach of ACI 318-02. The diagonal tension resistance of the AAC is expressed in terms of its specified compressive strength, and principal tensile stresses, including the effects of axial loads, are equated with this strength. This produces an expression for  $V_{AAC}$  in terms of the diagonal tension resistance of the AAC, and the axial load on the element.

The shear resistance due to transverse reinforcement is computed based on the cross-sectional area of the transverse reinforcement crossing a hypothetical 45-degree crack in the AAC. As explained in the previous subsection, it may also be limited by bond and development of the reinforcement.

#### ***B.3.2.5 Bearing***

To prevent local crushing of the AAC, nominal stresses in it are limited to  $f_{AAC}'$ . When AAC floor or roof panels bear on AAC walls, shear failure of the edge of the wall is also possible. This is handled by limiting the shear stress on potential inclined failure surfaces.

## **B.4 HANDLING, ERECTION AND CONSTRUCTION WITH AAC UNITS**

### **B.4.1 Handling of AAC Panels**

AAC panels should be stored on suitably prepared supports, so that they are prevented from warping. They should be carefully placed in their final position without being overstressed or damaged. Instructions from the manufacturer on how to handle the units should be followed. Special equipment is usually used or recommended by the manufacturer to assist in the transportation and erection of the units.

### **B.4.2 Erection of AAC Wall Panels**

AAC panels are lifted and placed using specially designed clamps, and are aligned using alignment bars.

#### ***B.4.2.1 Erection of AAC Cladding Systems***

AAC panels can be used as non-load bearing cladding systems. This application usually involves horizontally oriented panels attached to steel or reinforced concrete frame. Erection of such panels follows these steps:

- a) Ensure that supporting columns are plumb and true.
- b) Set the bottom panel against the supporting columns and over the floor slab or slab on ground, on top of a bed joint of conventional masonry mortar. Make sure that the panel is true and level.

- c) Immediately after placing the first panel, fasten a wall anchor plate to the column (using a dovetail or mechanically locking connector), and nail the plate to the AAC panel. The back face of the panel should be flush with the outer face of the column.
- d) Place subsequent panels on top of the first one. The top and bottom faces of the horizontal wall panels can have either a tongue and groove profile, or a flat profile. Tongue and groove joints do not require mortar. Flat joints are mortared with thin-bed mortar.
- e) Seal horizontal and vertical joints with flexible sealant.

#### ***B.4.2.2 Erection of Vertical AAC Panels for Bearing-Wall Systems***

Vertical AAC panels may also be used as a load-bearing wall system. In such cases, the floor roof systems are usually designed and detailed as horizontal diaphragms to transfer lateral loads to shear walls. The tops of the panels are connected to the floor or roof diaphragms using a cast-in-place reinforced concrete ring beam. This and many other structural details are addressed in the next chapter.

When vertical wall panels are used in this way, they are set on a bedding joint of conventional masonry mortar, with or without a waterproofing admixture. Vertical wall panels are usually mortared together with thin-bed mortar.

### **B.4.3 Erection of AAC Floor and Roof Panels**

AAC floor and roof panels can be erected on concrete, steel or masonry construction. All bearing surfaces should be level and minimum required bearing areas (to prevent local crushing) should be maintained.

As in any precast construction system, care must be exercised in the installation of the first panel to ensure correct alignment of the remaining panels. All floor and roof anchors should be installed prior to placement of the panels, thus streamlining and expediting panel installation.

Most floor and roof panels are connected by keyed joints that are reinforced and filled with grout to lock the panels together and provide diaphragm action to resist lateral loads. A cast-in-place reinforced concrete ring beam is normally placed along the perimeter of the diaphragm, completing the system.

### **B.4.4 Electrical and Plumbing Installations in AAC**

Electrical and plumbing installations in AAC are placed in routed chases. Care should be taken when laying out chases to ensure that the structural integrity of the AAC elements is maintained. Do not cut reinforcing steel or reduce the structural thickness of the AAC elements in critical areas. When analyzing the AAC element is intended to span vertically, horizontal routing should be permitted only in areas with low flexural and compressive stresses. In contrast, when the AAC element is intended to span horizontally, vertical routing should be minimized. When possible, it may be advantageous to provide designated chases for large quantities of conduit or plumbing.



#### **B.4.5 Exterior Finishes for AAC**

Unprotected exterior AAC deteriorates when exposed to cycles of freezing and thawing while saturated. To prevent such freeze-thaw deterioration, and to enhance the aesthetics and abrasion resistance of AAC, exterior finishes should be used. They should be compatible with the underlying AAC in terms of thermal expansion and modulus of elasticity, and should be vapor permeable. Many different types of exterior finishes are available, and the most common are discussed here.

##### ***B.4.5.1 Polymer-Modified Stuccos, Paints or Finish Systems***

Polymer-modified stuccos, paints or finish systems are the most common exterior finish for AAC. They increase the AAC's water-penetration resistance while allowing the passage of water vapor. Heavy acrylic-based paints containing aggregates are also used to increase abrasion resistance. There is generally no need to level the surface, and horizontal and vertical joints may be chamfered as an architectural feature, or may be filled.

##### ***B.4.5.2 Masonry Veneer***

Masonry veneer may be used over AAC panels in much the same way that it is used over other materials. The veneer is attached to the AAC wall using masonry ties. The space between the AAC and the masonry can be left open (forming a drainage wall), or can be filled with mortar.

##### ***B.4.5.3 Finishes for Basement Walls***

When AAC panels are used in contact with moist or saturated soil (for example, in basement walls, the surface in contact with the soil should be coated with a waterproof material or membrane. The interior surface should either remain uncoated, or be coated with a vapor-permeable interior finish.

## **B.4.6 Interior Finishes for AAC Panels**

Interior finishes are used to enhance the aesthetics and durability of AAC. They should be compatible with the underlying AAC in terms of thermal expansion and modulus of elasticity, and should be vapor permeable. Many different types of interior finishes are available, and the most common are discussed here.

### ***B.4.6.1 Interior Plasters***

Interior AAC wall panels may have a thin coat of a mineral-based plaster to achieve a smooth finished surface. Lightweight interior gypsum-based plaster may provide a thicker coating to level and straighten walls, and to provide a base for decorative interior paints or wall finishes. Interior plasters have bonding agents to enhance their adhesion and flexibility, and are commonly installed by either spraying or troweling.

### ***B.4.6.2 Gypsum Board***

When applied to the interior surface of exterior AAC walls, gypsum board should be attached using pressure-treated furring strips. When applied to interior walls, moisture-resistant gypsum board can be applied directly to the AAC surface.

### ***B.4.6.3 High-Durability Finishes for Commercial Applications***

For commercial applications requiring high durability and low maintenance, acrylic-based coatings are often used. Some contain aggregates to enhance abrasion resistance.

#### ***B.4.6.4 Ceramic Tile***

When ceramic wall tile is to be applied over AAC, surface preparation is normally necessary only when the AAC surface requires leveling. In such cases, a Portland cement- or gypsum-based parge coat is applied to the AAC surface before setting the ceramic tile. The ceramic tile should then be adhered to the parged wall using either a cement-based thin-set mortar or an organic adhesive. In moist areas such as showers, only a Portland cement-based parge coat should be used, and the ceramic tile should be set with cement-based thin-set mortar only.

## REFERENCES

1. Argudo 2003: Argudo, J., "Design Provisions for Reinforced AAC panels", M.S. thesis, Dept. of Civil Engineering, The University of Texas at Austin, August 2003.
2. ACI 318 2002: Building Code Requirements for Structural Concrete Code and Commentary, American Concrete Institute, Farmington Hills, MI.
3. ASTM C 476 (2002): Standard Specification for Grout for Masonry, American Society for Testing and Materials, West Conshohocken, PA, 2002.
4. ASTM C 1006 (2001): Standard Specification for Splitting Tensile Strength of Masonry Units, American Society for Testing and Materials, West Conshohocken, PA, 2001.
5. ASTM C 1386 (1998): Standard Specification for Precast Autoclaved Aerated Concrete (PAAC) Wall Construction Units, American Society for Testing and Materials, West Conshohocken, PA, 1998.
6. Drysdale, Hamid and Baker 1994: Drysdale, R. G., A. A. Hamid, L. R. Baker, *Masonry Structures, Behavior and Design*, Prentice-Hall, Englewood Cliffs, NJ, 1994.
7. Hsu and Mau 1992: Hsu, T. C., S. T. Mau, *Concrete Shear in Earthquakes*, Elsevier Applied Science, New York, NY, 1992.
8. Meyer 1998: Meyer C., *Modelling and Analysis of Reinforced Concrete Structures for Dynamic Loading*, Springer Wien, New York, NY, 1998.
9. Mo 1994: Mo, Y. L., *Dynamic Behavior of Concrete Structures*, Elsevier, New York, NY, 1994.
10. Park and Paulay 1975: Park R., T. Paulay, *Reinforced Concrete Structures*, John Wiley & Sons, New York, NY, 1975.
11. RILEM 1993: *Autoclaved Aerated Concrete: Properties, Testing and Design*, RILEM Recommended Practice, RILEM Technical Committees 78-MCA and 51-ALC, E & FN Spon, London.

12. Tanner 2003: Tanner, J. E., "Design Provisions for Autoclaved Aerated Concrete (AAC) Structural Systems" Ph.D. dissertation, Dept. of Civil Engineering, The University of Texas at Austin, May 2003.
13. Varela 2003: Varela, J. L., "Proposed Values of R and  $C_d$  for AAC Structural Systems" Ph.D. dissertation, Dept. of Civil Engineering, The University of Texas at Austin, May 2003.

## VITA

Ulises Max Cancino was born on March 4, 1971 in Santiago, Chile. He earned his Bachelors of Science in Engineering in 1996. During 1997 and 2002 he worked as a structural engineer in different structural design offices in Santiago and Temuco. This experience involved the design of reinforced concrete buildings, malls, houses and factories. He became a Master's degree candidate at The University of Texas at Austin in 2002.

Permanent address: El Rosedal # 1983  
Comuna: Santiago  
Santiago, Chile

This thesis was typed by the author.